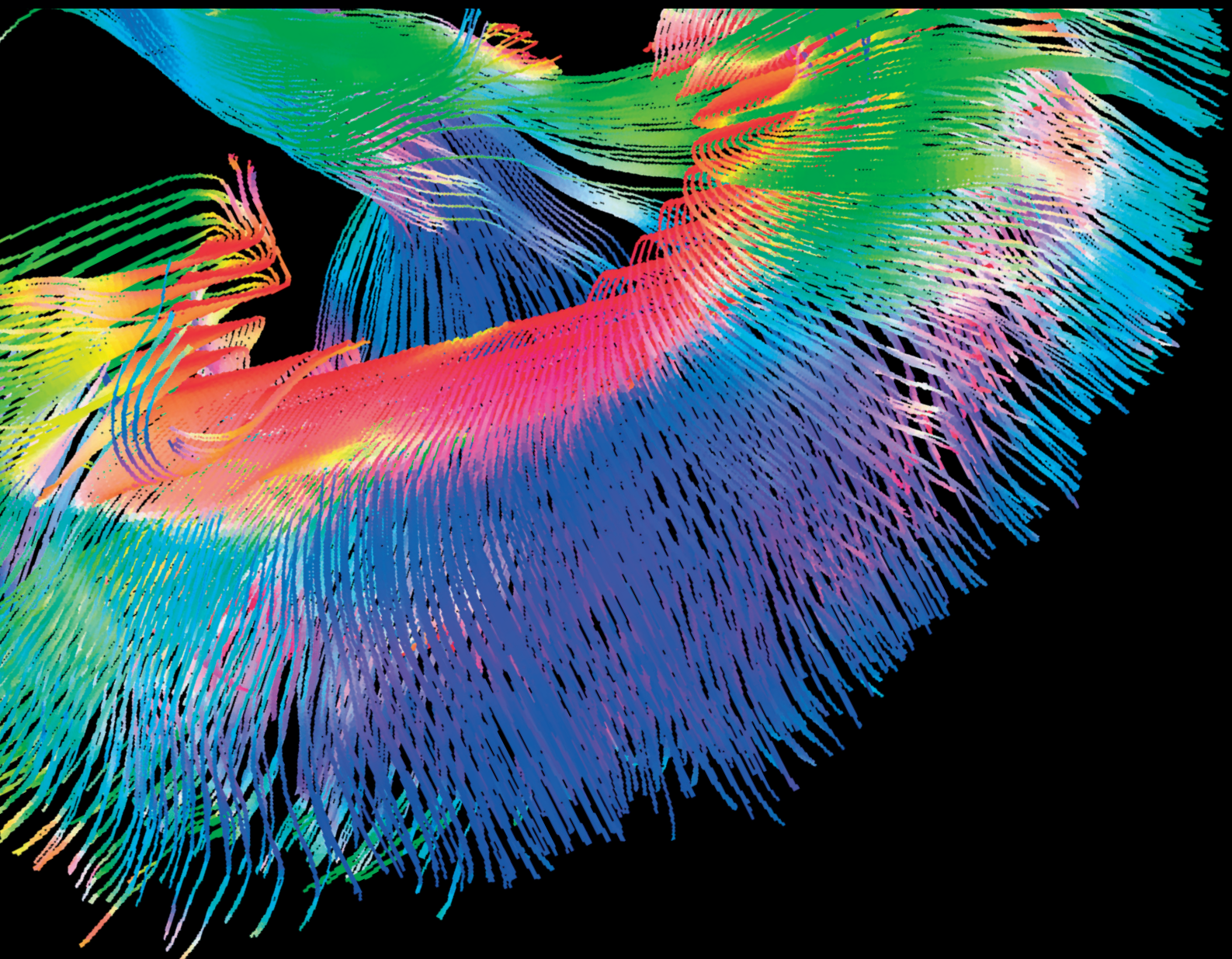


Recent Advances in Quantitative Nuclear Medicine and Molecular Imaging

Lead Guest Editor: Yun Zhou

Guest Editors: Jie Lu, Chongzhao Ran, and Jianhua Zhang



Recent Advances in Quantitative Nuclear Medicine and Molecular Imaging

Contrast Media & Molecular Imaging

Recent Advances in Quantitative Nuclear Medicine and Molecular Imaging

Lead Guest Editor: Yun Zhou

Guest Editors: Jie Lu, Chongzhao Ran, and Jianhua Zhang



Copyright © 2018 Hindawi. All rights reserved.

This is a special issue published in "Contrast Media & Molecular Imaging." All articles are open access articles distributed under the Creative Commons Attribution License, which permits unrestricted use, distribution, and reproduction in any medium, provided the original work is properly cited.

Editorial Board

Ali Azhdarinia, USA	Alexey P. Kostikov, Canada	Giuseppe Rubini, Italy
Peter Bannas, Germany	Françoise Kraeber-Bodéré, France	Barbara Salvatore, Italy
Giorgio Biasiotto, Italy	Gaurav Malviya, UK	Ralf Schirrmacher, Canada
André L. B. de Barros, Brazil	Barbara Palumbo, Italy	Giorgio Treglia, Switzerland
Dinesh K. Deelchand, USA	Giancarlo Pascali, Australia	Reza Vali, Canada
Paul Edison, UK	Maria Joao Ribeiro, France	Changning Wang, USA
Guillermina Ferro-Flores, Mexico	Laurent M. Riou, France	Luc Zimmer, France
María L. García-Martín, Spain	Anne Roivainen, Finland	
Hao Hong, USA	Pedro Rosa-Neto, Canada	

Contents

Recent Advances in Quantitative Nuclear Medicine and Molecular Imaging

Yun Zhou , Jie Lu , Chongzhao Ran, and Jianhua Zhang
Editorial (2 pages), Article ID 3613156, Volume 2018 (2018)

Comparison among Reconstruction Algorithms for Quantitative Analysis of ^{11}C -Acetate Cardiac PET Imaging

Ximin Shi , Nan Li , Haiyan Ding , Yonghong Dang , Guilan Hu, Shuai Liu , Jie Cui ,
Yue Zhang , Fang Li , Hui Zhang, and Li Huo 
Research Article (10 pages), Article ID 9193403, Volume 2018 (2018)

Clinical and Prognostic Value of PET/CT Imaging with Combination of ^{68}Ga -DOTATATE and ^{18}F -FDG in Gastroenteropancreatic Neuroendocrine Neoplasms

Panpan Zhang, Jiangyuan Yu, Jie Li, Lin Shen , Nan Li, Hua Zhu, Shizhen Zhai, Yan Zhang, Zhi Yang ,
and Ming Lu 
Research Article (9 pages), Article ID 2340389, Volume 2018 (2018)

Prognostic Value of Volume-Based Positron Emission Tomography/Computed Tomography in Nasopharyngeal Carcinoma Patients after Comprehensive Therapy

Yueli Tian, Khamis Hassan Bakari, Shanshan Liao, Xiaotian Xia, Xun Sun, Chunxia Qin, Yongxue Zhang ,
and Xiaoli Lan 
Research Article (8 pages), Article ID 1384281, Volume 2018 (2018)

Do TSH, FT3, and FT4 Impact BAT Visualization of Clinical FDG-PET/CT Images?

Ryuichi Nishii , Shigeki Nagamachi, Youichi Mizutani, Tamasa Terada, Syogo Kiyohara,
Hideyuki Wakamatsu, Seigo Fujita, Tatsuya Higashi, Keiichiro Yoshinaga, Tsuneo Saga,
and Toshinori Hirai
Research Article (9 pages), Article ID 4898365, Volume 2018 (2018)

Study of the Influence of Age in ^{18}F -FDG PET Images Using a Data-Driven Approach and Its Evaluation in Alzheimer's Disease

Jiehui Jiang, Yiwu Sun , Hucheng Zhou , Shaoping Li , Zhemin Huang, Ping Wu, Kuangyu Shi ,
Chuantao Zuo , and Alzheimer's Disease Neuroimaging Initiative
Research Article (16 pages), Article ID 3786083, Volume 2018 (2018)

Automated Whole-Body Bone Lesion Detection for Multiple Myeloma on ^{68}Ga -Pentixafor PET/CT Imaging Using Deep Learning Methods

Lina Xu , Giles Tetteh, Jana Lipkova, Yu Zhao, Hongwei Li, Patrick Christ, Marie Piraud ,
Andreas Buck, Kuangyu Shi , and Bjoern H. Menze
Research Article (11 pages), Article ID 2391925, Volume 2018 (2018)

Spectral Unmixing Imaging for Differentiating Brown Adipose Tissue Mass and Its Activation

Jing Yang, Jian Yang, and Chongzhao Ran 
Research Article (7 pages), Article ID 6134186, Volume 2018 (2018)

Associations between ^{18}F -FDG-PET, DWI, and DCE Parameters in Patients with Head and Neck Squamous Cell Carcinoma Depend on Tumor Grading

Leonard Leifels, Sandra Purz, Patrick Stumpp, Stefan Schob, Hans Jonas Meyer, Thomas Kahn, Osama Sabri, and Alexey Surov

Research Article (8 pages), Article ID 5369625, Volume 2017 (2018)

Detecting Triple-Vessel Disease with Cadmium Zinc Telluride-Based Single-Photon Emission Computed Tomography Using the Intensity Signal-to-Noise Ratio between Rest and Stress Studies

Yu-Hua Dean Fang, Tzu-Pei Su, Chi-Jen Chang, Kung-Chu Ho, May Su, and Tzu-Chen Yen

Research Article (8 pages), Article ID 4945680, Volume 2017 (2018)

Post Mortem Leukocyte Scintigraphy in Juvenile Pigs with Experimentally Induced Osteomyelitis

Pia Afzelius, Ole Lerberg Nielsen, Svend Borup Jensen, and Aage Kristian Olsen Alstrup

Research Article (6 pages), Article ID 3603929, Volume 2017 (2018)

Editorial

Recent Advances in Quantitative Nuclear Medicine and Molecular Imaging

Yun Zhou¹, Jie Lu², Chongzhao Ran³, and Jianhua Zhang⁴

¹The Russell H. Morgan Department of Radiology and Radiological Science, Johns Hopkins University School of Medicine, Baltimore, MD 21287, USA

²Department of Radiology, Xuanwu Hospital, Capital Medical University, Beijing, China

³Martinos Center for Biomedical Imaging, Harvard Medical School, Boston, MA 02129, USA

⁴Department of Nuclear Medicine, Peking University First Hospital, Beijing, China

Correspondence should be addressed to Yun Zhou; yunzhou@jhmi.edu

Received 27 May 2018; Accepted 27 May 2018; Published 25 June 2018

Copyright © 2018 Yun Zhou et al. This is an open access article distributed under the Creative Commons Attribution License, which permits unrestricted use, distribution, and reproduction in any medium, provided the original work is properly cited.

Whole-body PET-CT, simultaneous whole-body PET-MRI, and multimodal molecular imaging system are the recent milestone development in nuclear medicine and molecular imaging. These high-end molecular imaging scanners with probes or tracers provide the potential to significantly improve the accuracy in localization and quantification of biological processes at cellular and molecular levels in humans and other living systems. However, there are many challenges in image processing and mathematical and statistical modeling to extract physiological and biochemical information from these multimodal image data. Tremendous efforts have been made recently in the evaluation of the advanced imaging system, extracting physiological and biochemical parameters from multimodal images, integration of multiparametric images, and exploring the applications of the advanced quantitative molecular imaging in clinical nuclear medicine and biology. This special issue invited a number of papers to update the recent advances by those investigators in quantitative nuclear medicine and molecular imaging.

Reconstruction methods play a vital role for the quality and quantification of PET imaging. Time of flight (TOF) and point spread function (PSF) with ordered subset expectation maximization (OSEM) are implemented in most advanced PET-CT and PET-MRI scanners to improve image quality. In the first paper, the effects of image reconstruction algorithms on the kinetic modeling of ¹¹C-acetate PET imaging for myocardium assessment were studied. The study found that the image quality from OSEM/TOF/(TOF + PSF) was significantly better than that from the classical image reconstruction method with filtered backprojection.

To extract multiphysiological or biochemical information from multimodal image data and integrate with the mathematical and statistical model is a key to improve the clinical diagnosis accuracy. In the second paper, the combination of ⁶⁸Ga-DOTATATE and ¹⁸F-FDG could provide better clinical and prognostic evaluation for gastroenteropancreatic neuroendocrine neoplasms (GEP-NENs). They found that the sensitivity of PET/CT imaging with the dual tracers was well associated with cell differentiation, as evidenced by a significant correlation between Ki-67 and SUVmax of PET-CT with both tracers. In the third paper, the researchers assessed the prognostic value of standardized uptake value (SUV), whole-body metabolic tumor volume (WBMTV), and whole-body total lesion glycolysis (WBTLG) for patients with nasopharyngeal carcinoma (NPC) after therapy using FDG PET-CT. Receiver operating characteristic curves were used for the evaluation. They concluded that WBMTV could be used to improve the detection rate of metastatic lesions, and WBTLG could be used as an independent prognostic indicator for NPC after therapy. In the eighth paper, the researchers use ¹⁸F-FDG PET, diffusion-weighted imaging (DWI), and dynamic contrast-enhanced (DCE) imaging to study the relationship among the quantitative measurements of tumor ¹⁸F-FDG SUV, apparent diffusion coefficient (ADC), volume transfer constant k_{trans} , volume of the extravascular extracellular leakage space V_e , and the parameter k_e for diffusion of the contrast medium from the EES back to the plasma, for grading head and neck squamous cell carcinoma (HNSCC). They found that the associations among those parameters were dependent on the stages of HNSCC. The results provide the potential to

improve the accuracy of HNSCC grading. In the ninth article, a novel quantitative parameter, the stress-to-rest ratio of the signal-to-noise ratio (RSNR), was proposed to quantify the myocardial perfusion image generated from a cadmium-zinc-telluride (CZT) single-photon emission computed tomography (SPECT) scanner. Results from the study demonstrated that the RSNR was a useful index to assist the diagnosis of triple-vessel disease.

Now, more and more physicians and scientists are interested to use artificial intelligence technologies such as deep learning for assistance in medical image-based diagnosis. In the sixth paper, the authors proposed to use two convolutional neural networks (CNNs), V-Net and W-Net, for lesion detection on ^{68}Ga -Pentixafor PET/CT images. The deep learning method was evaluated by phantom-based simulation data and multiple myeloma ^{68}Ga -Pentixafor PET/CT patient study. Traditional machine learning methods for tumor detection including random forest classifier (RF), k-nearest neighbors (k-NN), and support vector machine (SVM) were also applied to the same data sets for comparison. Results from the study showed that the proposed deep learning method with PET and CT provided highest lesion detection accuracy.

Functional MRI of the brain's (FMRIB's) linked independent component analysis (FLICA) is a data-driven approach for multimodal image data analysis. The authors in the fifth paper applied FLICA to FDG PET images collected from Huashan Hospital and multicenter Alzheimer's Disease Neuroimaging Initiative (ADNI) studies. They found that some brain regions were negatively correlated with age, and the correlations between those brain regional SUVRs and 3 clinical assessments were significantly improved if age correction was applied to SUVRs.

In the past years, brown adipose tissue (BAT) has been considered as an important and potential therapeutic target for obesity and diabetes. Reportedly, results of BAT imaging can be varied under different conditions such as cold exposure and thyroid hormone levels. In this special issue, two groups have reported their results from preclinical mouse imaging or human imaging. The authors in the seventh paper showed that spectral unmixing imaging with a near-infrared fluorescent probe could be used to dissect the imaging signal from BAT activation and BAT mass. In addition, the authors in the fourth paper showed that elevated TSH condition before RIT, hyperthyroidism, or hypothyroidism had no significant impact on BAT visualization with FDG PET-CT imaging.

The researchers in the tenth paper previously demonstrated that ^{111}In -labeled autologous leukocyte scintigraphy could be used to detect osteomyelitis in living juvenile pigs. To further confirm the exact location and better image interpretation, imaging after euthanasia is always necessary. In this paper, they indicated that SPECT/CT with the same imaging probe at 24 hours after euthanasia could provide the same detectability of osteomyelytic lesions as in living pigs.

Yun Zhou
Jie Lu
Chongzhao Ran
Jianhua Zhang

Research Article

Comparison among Reconstruction Algorithms for Quantitative Analysis of ^{11}C -Acetate Cardiac PET Imaging

Ximin Shi ,¹ Nan Li ,² Haiyan Ding ,³ Yonghong Dang ,¹ Guilan Hu,¹ Shuai Liu ,³ Jie Cui ,² Yue Zhang ,² Fang Li ,¹ Hui Zhang,⁴ and Li Huo ,¹

¹Department of Nuclear Medicine, Peking Union Medical College Hospital, Chinese Academy of Medical Science and Peking Union Medical College, 1 Shuaifuyuan, Dongcheng District, Beijing 100730, China

²Sinounion Healthcare Inc., Building 3-B, Zhongguancun Dong Sheng International Pioneer Park, 1 Yongtaizhuang North Road, Haidian District, Beijing 100192, China

³Center for Biomedical Imaging Research, Department of Biomedical Engineering, School of Medicine, Tsinghua University, Beijing 100084, China

⁴Department of Biomedical Engineering, School of Medicine, Tsinghua University, Beijing 100084, China

Correspondence should be addressed to Li Huo; huoli@pumch.cn

Received 28 July 2017; Revised 12 December 2017; Accepted 30 January 2018; Published 28 February 2018

Academic Editor: Chongzhao Ran

Copyright © 2018 Ximin Shi et al. This is an open access article distributed under the Creative Commons Attribution License, which permits unrestricted use, distribution, and reproduction in any medium, provided the original work is properly cited.

Objective. Kinetic modeling of dynamic ^{11}C -acetate PET imaging provides quantitative information for myocardium assessment. The quality and quantitation of PET images are known to be dependent on PET reconstruction methods. This study aims to investigate the impacts of reconstruction algorithms on the quantitative analysis of dynamic ^{11}C -acetate cardiac PET imaging. **Methods.** Suspected alcoholic cardiomyopathy patients ($N = 24$) underwent ^{11}C -acetate dynamic PET imaging after low dose CT scan. PET images were reconstructed using four algorithms: filtered backprojection (FBP), ordered subsets expectation maximization (OSEM), OSEM with time-of-flight (TOF), and OSEM with both time-of-flight and point-spread-function (TPSF). Standardized uptake values (SUVs) at different time points were compared among images reconstructed using the four algorithms. Time-activity curves (TACs) in myocardium and blood pools of ventricles were generated from the dynamic image series. Kinetic parameters K_1 and k_2 were derived using a 1-tissue-compartment model for kinetic modeling of cardiac flow from ^{11}C -acetate PET images. **Results.** Significant image quality improvement was found in the images reconstructed using iterative OSEM-type algorithms (OSME, TOF, and TPSF) compared with FBP. However, no statistical differences in SUVs were observed among the four reconstruction methods at the selected time points. Kinetic parameters K_1 and k_2 also exhibited no statistical difference among the four reconstruction algorithms in terms of mean value and standard deviation. However, for the correlation analysis, OSEM reconstruction presented relatively higher residual in correlation with FBP reconstruction compared with TOF and TPSF reconstruction, and TOF and TPSF reconstruction were highly correlated with each other. **Conclusion.** All the tested reconstruction algorithms performed similarly for quantitative analysis of ^{11}C -acetate cardiac PET imaging. TOF and TPSF yielded highly consistent kinetic parameter results with superior image quality compared with FBP. OSEM was relatively less reliable. Both TOF and TPSF were recommended for cardiac ^{11}C -acetate kinetic analysis.

1. Introduction

Dynamic PET imaging with kinetic analysis provides more quantitative information compared with the commonly used standardized uptake value (SUV) [1, 2]. Time-activity curves (TACs) in user-defined regions-of-interest (ROIs) can be extracted from a series of images and then applied onto

the compartment kinetic models. Derived parameters reflect radiotracer exchange rate in the kinetic process and are considered as fully quantitative measurement of radiotracer metabolism [3, 4]. Fully quantitative analysis is currently limited in clinical research and drug development because of their complexity in terms of both experimental design and pharmacokinetic modeling methodology [5, 6].

Since TACs are generated from dynamic image series, the image quality is crucial to ensure the accurate and reliable quantitative analysis. The image quality is dependent on the choice of reconstruction algorithm. Classical analytical filtered backprojection algorithm (FBP) is straightforward but rarely used in clinic due to its poor image quality. Most current PET/CT systems employ fully 3D OSEM iterative reconstructions, which allow the corrections for random events, scatter events, normalization, dead time, and photon attenuations [7]. Utilizing more accurate physical system model, OSEM can greatly reduce the noise in the reconstruction and significantly improve the image quality [8, 9]. Recently, progress has been made on OSEM-type reconstruction by combining with time-of-flight (TOF) information [10, 11] and point-spread-function (PSF) kernel [12, 13] in the iterative reconstruction process. These new techniques substantially improve image quality and reduce the partial volume effect (PVE) [14].

Myocardial perfusion PET imaging provides quantitative information for myocardium assessment. Previous work has demonstrated that three-dimensional (3D) acquisition combined with attenuation-weighted ordered subsets expectation maximization (OSEM) reconstruction not only improves the image quality but also keeps the quantitative accuracy in cardiac ¹⁸F-FDG PET studies [15]. The quantitative influence of including TOF and PSF in OSEM algorithms as well as reconstruction parameters (subsets × iteration product; filters) for ⁸²RB PET/CT perfusion studies is also investigated recently [16].

Among the variety of radiotracers, ¹¹C-acetate is unique to measure the regional myocardial oxygen consumption and thus enables noninvasive quantification of the pathophysiology of cardiac metabolic alterations [17]. After bolus injection of ¹¹C-acetate, myocytes extract ¹¹C-acetate rapidly from the blood and then, via the tricarboxylic acid cycle in myocytes, the principal metabolite of acetate, ¹¹CO₂, is cleared from the myocardium. Accordingly, the TAC ascends rapidly and then declines. Using 1-tissue-compartment model, K_1 and k_2 can be calculated to represent the rate of uptake and washout of ¹¹C-acetate. In addition, ¹¹C-acetate has a physical half life of 20 min, and, combined with different frame lengths in the dynamic study, there is much difference in the count statistics in each frame in the acquired imaging data compared with ¹⁸F-FDG and ⁸²RB PET studies, where different image reconstruction techniques may play a role in terms of quantitation. However, there are few studies that systematically investigate the quantitation performance of different reconstruction methods for cardiac ¹¹C-acetate imaging.

The aim of this study was to explore the reconstruction-dependent image quality and their influences on kinetic analysis of ¹¹C-acetate imaging. Image quality, semiquantitative analysis with SUV, and fully quantitative analysis with kinetic modeling parameters from four reconstruction algorithms were investigated: FBP, OSEM, OSEM method with time-of-flight information (TOF), and OSEM method modeled with both time-of-flight information and point-spread-function (TPSF).

2. Method

2.1. Patient and Scan Procedure. The study was approved by the Ethics Committee of Peking Union Medical College Hospital (PUMCH). Patients with suspected alcoholic cardiomyopathy ($N = 24$, male, age range, 48.3 ± 11.6 yrs) were enrolled in the study during January to June 2017. Written informed consent was obtained from all subjects.

All imaging was performed on a clinical PET-CT system [18] (PoleStar m660, Sinounion Healthcare Inc., Beijing, China) at PUMCH. ¹¹C-acetate was synthesized as described in literature [19, 20]. After a low dose CT scan, a total of about 740 MBq ¹¹C-acetate was administered intravenously to the subject and a 40 min dynamic PET scan was acquired for each patient.

2.2. Image Reconstruction. Each dynamic PET scan was sorted into 53 frames (15×10 s, 15×30 s, 16×60 s, and 7×120 s), and images were reconstructed with an object space of $192 \times 192 \times 117$ and a voxel size of $3.15 \times 3.15 \times 1.87$ mm³. Filtered backprojection (FBP) reconstruction and three iterative reconstruction methods, that is, OSEM, OSEM with time-of-flight, and OSEM with both time-of-flight and point-spread-function, were performed for each study. The four reconstruction methods were named as FBP, OSEM, TOF, and TPSF, respectively, for the comparison in this study. Necessary corrections such as random, attenuation, scatter, normalization, dead time, and decay corrections were applied. For the FBP method, scatters and randoms were directly subtracted from projections while, for the iterative methods, they were included in the iteration. The iterative equation used in the ordinary Poisson OSEM-type algorithms was [7]

$$f_j^{(k,q+1)} = \frac{f_j^{(k,q)}}{\sum_{i \in S_q} A_{ij}} \sum_{i \in S_q} \frac{A_{ij} p_i}{\sum_{l=1}^M A_{il} f_l^{(k,q)} + r_i + s_i}, \quad (1)$$

where $f = [f_1, f_2, \dots, f_M]^T$ was the estimated tracer intensities in a finite discrete object space. The sinogram data, $p = [p_1, p_2, \dots, p_N]^T$, was a collection of detected coincidence events with independent Poisson statistical distributions. In (1), k is the iteration number and q is the subset index. The whole sinogram data was divided into several subsets, denoted as $\{S_q\}$, in order to increase the convergence speed. In general, subsets are evenly distributed with angular bins. In the case of both TOF and TPSF, time-of-flight information was treated as an additional dimension of time-of-flight bin in the sinogram space. r and s represented expectations of additive random and scatter events. A was the discrete system response function defined by the physical characteristics of imaging system, which in practice was factorized as a product of normalized correction matrix, attenuation correction matrix, and geometrical modeling matrix. For the TPSF, an additional product of the point-spread-function matrix was added to simulate the depth of interaction in crystals [21, 22].

In iterative reconstructions, the image quality was controlled by the combination of subsets and iterations, which can be simplified as expectation maximization equivalent

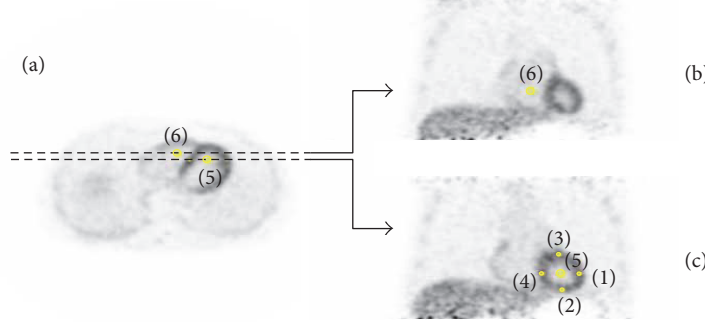


FIGURE 1: PET images reconstructed by TOF protocol: a transversal slice (a), a coronal slice along the higher dashed line (b), a coronal slice along the lower dashed line (c). The iterative reconstruction was performed with 10 iterations and 10 subsets, and a 5 mm (FWHM) Gaussian filter was applied (axial and transaxial) after reconstruction. The scan started 450 seconds after ^{11}C -acetate injection with the scan duration of 30 seconds. The four myocardial ROIs with 5 mm in diameter were evenly distributed along the myocardial wall (ROI (1)–(4)) and the two blood-pool ROIs with 10 mm in diameter were located in the center of the left ventricle (ROI (5)) and right ventricle (ROI (6)).

(EM-equivalent) iterations (the product of iterations and subsets) [23]. More EM-equivalent iterations result in less blurred and noisier reconstructed images. The optimization of EM-equivalent iterations depends on a variety of variables, such as activity distribution, the use of time-of-flight information, point-spread-function modeling, and noise equivalent counts in data.

To better analyze the effects of EM-equivalent iterations on the characteristics of the reconstructed images, we estimated the noise level in the myocardium and the contrast obtained between myocardium and blood pool in LV. One patient was randomly selected and a 30 s PET acquisition (the 21st frame) was used for the evaluation. For simplicity, the subsets were fixed to be 10 in the study. Mean myocardial counts (signal mean) and related standard deviations (signal SD) were calculated from the myocardial ROIs. Background mean counts (background mean) were defined as the average from the blood-pool ROI in LV. The definitions of ROIs were detailed in the next section. The contrast and noise properties in three iterative reconstructions were evaluated as a function of the number of iterations. The coefficient of variance (CV) and contrast were calculated as follows [23]:

$$\begin{aligned} \text{CV} &= \frac{\text{signal SD}}{\text{signal mean}} \\ \text{contrast} &= \frac{\text{signal mean} - \text{background mean}}{\text{background mean}}. \end{aligned} \quad (2)$$

Furthermore, the convergence performances of the fitted kinetic parameters for the three iterative reconstruction methods were explored. In the analysis, the entire image frames were used to minimize the effect of noise in the reconstructed images. In the study, the same patient study data as mentioned above was used and the subsets in the reconstructions were fixed to be 10 as well.

Based on the convergence behaviors with respect to image quality and kinetic parameters, the optimum iterations were determined, respectively, for the three iterative reconstruction methods. The post-filter also affects image

quality and the FWHM of post-filter were adjusted separately for different reconstruction methods to obtain similar image quality.

2.3. Image Analysis, Kinetic Modeling, and Statistics. Spherical regions-of-interest (ROIs) were manually drawn in the reconstructed images by experienced clinicians. As shown in Figure 1, four spherical ROIs (indexes (1)–(4)) with a diameter of 5 mm were drawn to calculate myocardium uptake and they were evenly distributed around LV myocardium and close to epicardium to avoid possible contamination from the blood pool. It is worthwhile to note that, for myocardial ROI analysis in this study, statistics were obtained by averaging the four 5 mm spherical ROIs to reduce the influences of partial volume effect (PVE), statistical noise, and potential motion artifacts.

In order to explore the influence of different reconstruction methods on the quantitation of dynamic cardiac PET images, SUVs of the myocardial ROI at different times after tracer injection were first analyzed. For each reconstruction, four discrete time points were selected representing the high (2 min), moderate (5 min and 10 min), and low (30 min) myocardium activity concentrations, respectively. As explained earlier in the text, mean activity concentration for each time point was obtained by averaging the four 5 mm myocardial ROIs. The corresponding SUV was defined as SUV_{mean} in later comparison and analysis.

Kinetic analysis was also performed on the dynamic image series with different reconstruction methods. Kinetic analysis requires an accurate input function to estimate tracer activity concentration of blood. The gold standard is to collect blood samples by arterial cannulation in order to have direct activity concentration measurement. However, this approach induces patient discomfort as well as complexity during scan. In the study, a 1-tissue-compartment model [24], as shown in Figure 2, was used for kinetic modeling of ^{11}C -acetate cardiac flow from PET images as a feasible and noninvasive alternative to arterial cannulation. A spherical ROI with a diameter of 10 mm (index (5) in Figure 1) was manually

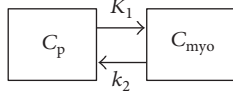


FIGURE 2: The 1-tissue-compartment model for kinetic modeling of ^{11}C -acetate cardiac flow from PET images. C_p and C_{myo} represent the tracer concentration in plasma and myocardial tissue, respectively. K_1 is proportional to perfusion value and k_2 is related to oxidative metabolism.

drawn inside the left ventricle (LV) blood pool to calculate the tracer concentration in plasma. For each reconstruction method, corresponding blood and myocardial time-activity curves (TACs) were extracted from the dynamic image series as the image-derived input functions for kinetic analysis. Also to note is that the myocardial TAC was obtained by averaging the four 5 mm myocardial ROIs as explained earlier.

Kinetic modeling was performed on TACs in LV blood-pool ROI and averaged myocardial ROI using the PMOD software (PMOD Technologies, Zurich, Switzerland). The 1-tissue-compartment model for ^{11}C -acetate cardiac flow implemented in PMOD was adopted to calculate the K_1 and k_2 parameters of ^{11}C -acetate, where K_1 is proportional to perfusion value and k_2 is related to oxidative metabolism. For the purpose of spillover correction, a 10 mm diameter spherical ROI (index (6) in Figure 1) was manually drawn inside the right ventricle (RV) blood pool. This RV blood-pool ROI and LV blood-pool ROI were used by the PMOD software for automatic correction of the spillover from LV and RV into the myocardium [25].

Correlation relationships among kinetic parameters were investigated using linear regression. Group mean (μ) and standard deviation (σ) of kinetic parameters and SUVs for all subjects were compared among different reconstructions. Statistical analysis was performed using paired, two-sample Student's t -test (or Welch's t -test) [26] with a significance level α of 0.05.

3. Results

3.1. Iterations Optimization. Figure 3 showed the convergence behaviors of image noise and contrast for the three iterative algorithms plotted against EM-equivalent iteration. Note that all the iterative reconstructions in this study were performed with 10 subsets. Compared with OSEM, TOF increased speed of reconstruction algorithm convergence, which is in accordance with previous study in [10]. The incorporation of PSF modeling into reconstruction affected the convergence speed of image noise more than contrast. In this study, to ensure good contrast convergence and then the minimum noise property, the number of EM-equivalent iterations of 200 (corresponding to the iteration number of 20) was chosen for the OSEM method while the number of EM-equivalent iterations of 100 (corresponding to the iteration number of 10) was chosen for the TOF and TPSF methods. Furthermore, in order to minimize the difference in CV and obtain similar image qualities, a 3D Gaussian filter of 5.0 mm in FWHM was applied to both TOF and TPSF images,

while a 3D Gaussian filter of 6.5 mm in FWHM was applied to OSEM images.

Visual qualitative assessments on the reconstructed images were performed by experienced clinicians using double blinded study. The contour of LV wall, ^{11}C -acetate distribution in ventricular myocardium, and streak artifacts in cardiac region, especially in LV cavity, were carefully examined.

The determinations of EM-equivalent iteration were further verified in the convergence analysis of kinetic parameters. Figure 4 displayed the convergence behaviors of kinetic parameters (K_1 and k_2) as a function of EM-equivalent iterations for the three iterative reconstruction algorithms. As shown in the figure, the EM-equivalent iterations of 100 ensured the convergence of the kinetic parameters for both TOF and TPSF cases. Although K_1 and k_2 for OSEM converged slowly, the number of EM-equivalent iterations of 200 was still large enough to obtain the stable values.

3.2. Reconstruction Images. Figure 5 showed the representative coronal PET images reconstructed using FBP, OSEM, TOF, and TPSF, respectively. The image frame started at 450 seconds after ^{11}C -acetate injection with a duration of 30 seconds. FBP method exhibited the poorest image quality with streak artifacts, especially in low count regions. As a comparison, iterative OSEM-type algorithms (OSEM, TOF, and TPSF) showed significant improvements in terms of image quality. Residual activity in the LV was obvious in the OSEM method, and the LV myocardium uptake exhibited much nonhomogeneity. The incorporation of time-of-flight information in the reconstruction could greatly reduce the activity bias and led to a more continuous contour of ventricles and homogeneous myocardium uptake, as demonstrated in the TOF and TPSF images. Furthermore, time-of-flight reconstruction leads to improved convergence in cold region, resulting in much more clear blood pools in the LV in the TOF and TPSF images. Similar image qualities were observed between TOF and TPSF methods, suggesting that the incorporation of PSF does not contribute significantly to cardiac PET images.

3.3. SUV and Kinetic Analysis. Figure 6 showed the magnified reconstructed images with different reconstruction methods at 2 min, 5 min, 10 min, and 30 min after tracer injection. For each reconstruction method, the group mean and standard variation (SD) of SUV_{mean} from all the patients were shown in Figure 7. SD with the FBP method was the largest while the SDs with the three OSEM-type methods were similar. The OSEM method exhibited the largest bias on the mean value. Overall, similar performances were observed in the TOF and TPSF methods. At 30 min after injection, with a scan duration of 120 s, the four methods displayed almost the same SUV_{mean} due to the excellent SNR in measurement.

Figure 6 also showed the TACs of the myocardium tissue and the blood pools in the LV and RV extracted with the four reconstruction methods. The FBP method generated much oscillation in the TACs especially in the early frames due to its intrinsic sensitivity to statistical noise. The nonnegative

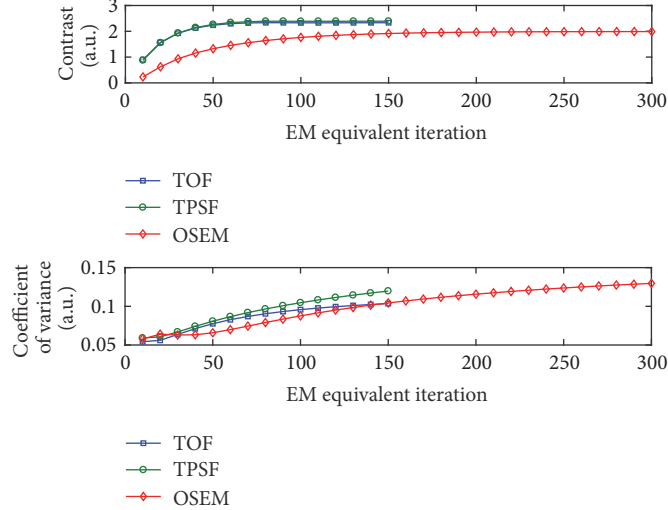


FIGURE 3: The contrast and noise level measured by the coefficient of variance as a function of EM-equivalent iterations for iterative reconstructions.

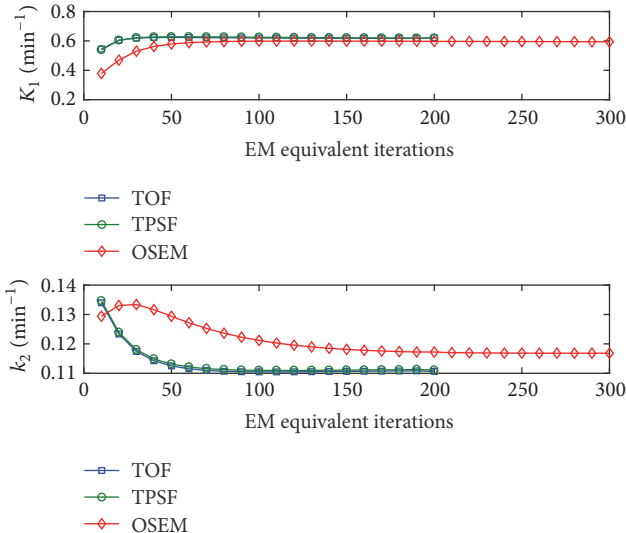


FIGURE 4: The kinetic parameters (K_1 and k_2) as a function of EM-equivalent iterations for iterative reconstructions.

constraints in iterative OSEM-type methods led to positive biased estimation on the regional activity concentration in low count PET data, while the FBP method yields both positive and negative values. Thus the TACs of the iterative methods always lied on the top of the TAC of the FBP method. The incorporation of time-of-flight information in the TOF and TPSF methods could greatly reduce the influence of statistical noise, resulting in much less divergent TACs compared with the OSEM method. The TACs of the TOF and TPSF methods were very similar and, again, the benefit of incorporating PSF was not obvious.

Figures 8 and 9 illustrated the linear regressions of all the kinetic parameters K_1 and k_2 , using the TACs shown in Figure 6. Overall, kinetic parameters derived from FBP reconstruction were the least relevant to those from the

OSEM-type reconstructions. This was because FBP approach produced divergent TACs due to the statistical noise and thus introduced extra variations in curve fitting and kinetic modeling. Both TOF and TPSF methods had excellent linear correlations for all kinetic parameters, and they had slightly less correlations with OSEM method.

Group comparison of the mean values and standard deviations of myocardiums K_1 and k_2 were shown in Figure 10. Consistent kinetic parameters were obtained from the TOF and TPSF methods. The kinetic parameters derived from the FBP method had comparable mean values but relatively the largest SD for K_1 .

The statistic analysis for kinetic parameters was summarized in Table 1. No significant difference was found among different reconstruction approaches. In terms of parameters K_1 and k_2 , the OSEM method presented relatively higher residual in correlation with the FBP method compared with the TOF and TPSF methods. The TOF and TPSF methods were highly correlated with each other with the largest P values. No significant difference was found among all the reconstruction methods in the SUV_{mean} test (Table 2). The results implied that all the reconstruction methods reported similar SUVs in the PET images.

4. Discussion

In the presented work, ^{11}C -acetate cardiac dynamic PET imaging studies were carried out. Data were acquired and reconstructed offline with FBP, OSEM, TOF, and TPSF methods. Both SUVs and kinetic parameters were investigated to evaluate the impacts of different reconstruction approach. It is well known that iterative reconstruction leads to significant improvement in image quality compared with FBP reconstruction, as demonstrated in Figures 5 and 6. However, FBP is much faster in calculation and may be attractive in dynamic studies where iterative methods usually take hours to reconstruct the dynamic image series. Moreover, FBP is linear and does not produce noise-induced positive



FIGURE 5: Coronal PET images reconstructed by FBP (a), OSEM (b), TOF (c), and TPSF (d). OSEM reconstruction was performed with 20 iterations and 10 subsets, with application of a 6.5 mm (FWHM) Gaussian post-filter. Both TOF and TPSF reconstructions were performed with 10 iterations and 10 subsets, with application of a 5 mm (FWHM) Gaussian post-filter. The scan started at 450 seconds after ^{11}C -acetate injection with scan duration of 30 seconds.

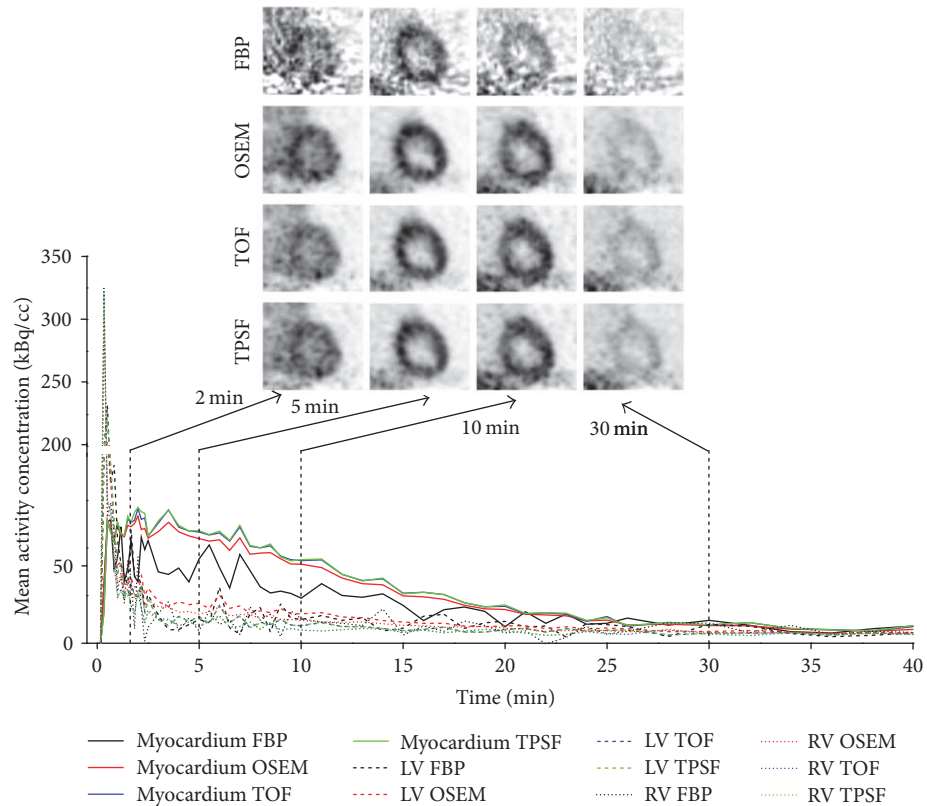


FIGURE 6: Representative heart images reconstructed from four methods at different time points, as well as the corresponding TACs from myocardium (in solid lines), the LV (in dashed lines), and the RV (in dotted lines) after the injection of ^{11}C -acetate.

TABLE 1: Paired two-sample Welch's T -test Results for kinetic parameters with respect to combinations of every two reconstruction approaches.

	FBP-OSEM	FBP-TOF	FBP-TPSF	OSEM-TOF	OSEM-TPSF	TOF-TPSF
K_1	0.92	0.74	0.59	0.63	0.48	0.81
k_2	0.55	0.21	0.25	0.08	0.10	0.93

TABLE 2: Paired two-sample Welch's T -test results for SUV_{mean} at four time points with respect to combinations of every two reconstruction approaches.

	FBP-OSEM	FBP-TOF	FBP-TPSF	OSEM-TOF	OSEM-TPSF	TOF-TPSF
2 min	0.40	0.74	0.64	0.53	0.64	0.87
5 min	0.34	0.66	0.55	0.59	0.71	0.87
10 min	0.86	0.98	0.73	0.87	0.86	0.85
30 min	0.91	0.94	0.80	0.85	0.90	0.94

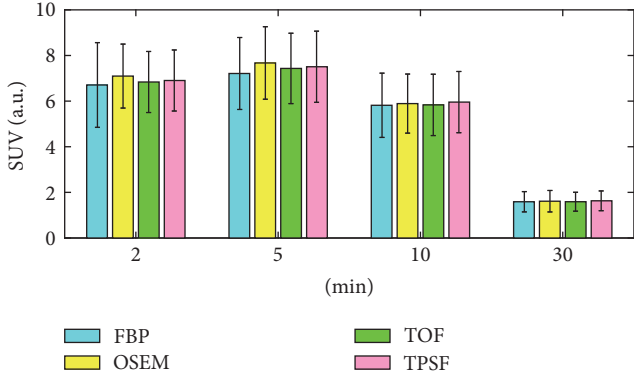


FIGURE 7: Means and standard deviations of semiquantitative ROI-based SUV from four reconstruction methods at 2 min, 5 min, 10 min, and 30 min after radiotracer injection.

bias. Despite its poor image quality and visual artifacts, FBP images can be quantitatively accurate in mean values when the ROI is chosen to be large enough to be less affected by PVE, that is, spill-in and spill-out effects due to variable intense activity surrounding tissues [6]. In this study, all the voxels in the myocardial ROIs were averaged to reduce the noise effect and thus counteract the contributions of positive and negative pulses on closer neighboring streaks. In low count PET images, the SUVs were diverged by the noise, but the group average of SUV_{mean} could be considered accurate due to the linear noise property and the permit of negative values. In comparison, OSEM-type methods had some remaining positive bias in case of very noisy data due to the inherent nonnegativity constraint. The group comparison on SUV among different reconstructions showed that FBP reconstruction had the largest standard variation. TOF reconstruction behaved more similar to FBP reconstruction for all the time point results in terms of mean value of SUV, especially at early frames, which implies that TOF reconstruction is insensitive to the statistic noise. No statistical significance was found from all the time point SUVs of all the reconstructions. TOF reconstruction was better than the other iterative method such as OSEM or TPSF.

SUV_{mean} was chosen in this study instead of SUV_{peak} or SUV_{max} [27]. Using mean values in ROIs reduces the dependency on the statistical quality of the images, but the averaging process also causes loss of sensitivity to hot spot. For clinical examination, the peak values are normally used where hot spots usually attract more attention. However, for kinetic analysis, mean values appear to be more appropriate in order to be less sensitive to statistical noise normally seen in the dynamic acquisition.

In this study, the influence of different reconstruction methods on the kinetic analysis was also investigated. It is known that the noise level in the TAC will affect the robustness of the kinetic parameter estimation. As shown in Figure 6, the TACs from FBP reconstruction exhibited much oscillation, especially in the early frames, leading to the largest standard variation and the worst correlation in terms of kinetic parameters compared with other reconstruction methods.

Compared with FBP, TACs from iterative methods were much smoother. For the kinetic parameter k_2 , differences were seen in the OSEM method compared with both TOF and TPSF methods. OSEM reconstruction has been widely accepted by clinics and has been incorporated in most commercial PET/CT scanners. However, in this study, we found that OSEM method performed poorly in the quantitative analysis of cardiac imaging. One possible reason is that the blood pools in the OSEM reconstructed images exhibit residual activities, which affects the blood input function for the kinetic modeling. The incorporation of time-of-flight information could reduce the noise and lead to much less divergence in the TACs compared with the OSEM method. With time-of-flight information, the positions of annihilation along lines of response can be approximately determined. With this additional information, the reconstructed PET images could achieve better image quality and low count recovery, thus improving the accuracy of regional activity quantification.

In this study, the advantage of incorporating point-spread-function in the reconstruction was not obvious in the quantitative analysis. The point-spread-function describes the detector response of incident photon. The implementation of point-spread-function kernel in the reconstruction often helps to improve the spatial resolution and reduce the partial volume effect. And usually it helps to delineate boundaries with sharp intensity transitions. However, in this study, the defined ROIs were surrounded by almost uniform activity in myocardium and there were no sharp activity transitions along the ROI boundaries. In addition, the partial volume effect had been largely reduced since the size of ROIs was approximately twice the spatial resolution of PET scanner. As a result, similar TACs and good correlations in all the kinetic parameters were found between the TPSF and TOF results. And the two methods generated consistent mean values for all the kinetic parameters with small standard deviations. Similar results were also seen in terms of image quality between the two reconstruction methods.

In this study, neither cardiac nor respiratory gating was used during data acquisition due to the high counts statistical variance especially in early frames, which will become worse as the data are further divided into phases for the gating process. However, the possible unconscious body motion still causes concern for the 40 min long dynamic data acquisition. It is worthwhile to note that, in the ROI analysis in this study, ROIs were manually defined on a single frame and applied to all the image series for each patient. It was possible that the myocardium ROIs partially entered the blood pool in some image series due to patient's unconscious motion. For simplicity these motions were not corrected frame by frame in the study. In order to evaluate the motion effect, data of one patient with obvious movement was examined and two myocardium TACs were generated using fixed ROI positions across image frames as well as manually adjusting ROI positions when necessary to move myocardium ROIs away from the blood pool. The two sets of kinetic parameters derived from the two TACs were compared and results were shown in Table 3. No significant differences were observed for iterative reconstruction methods, while, for the FBP method,

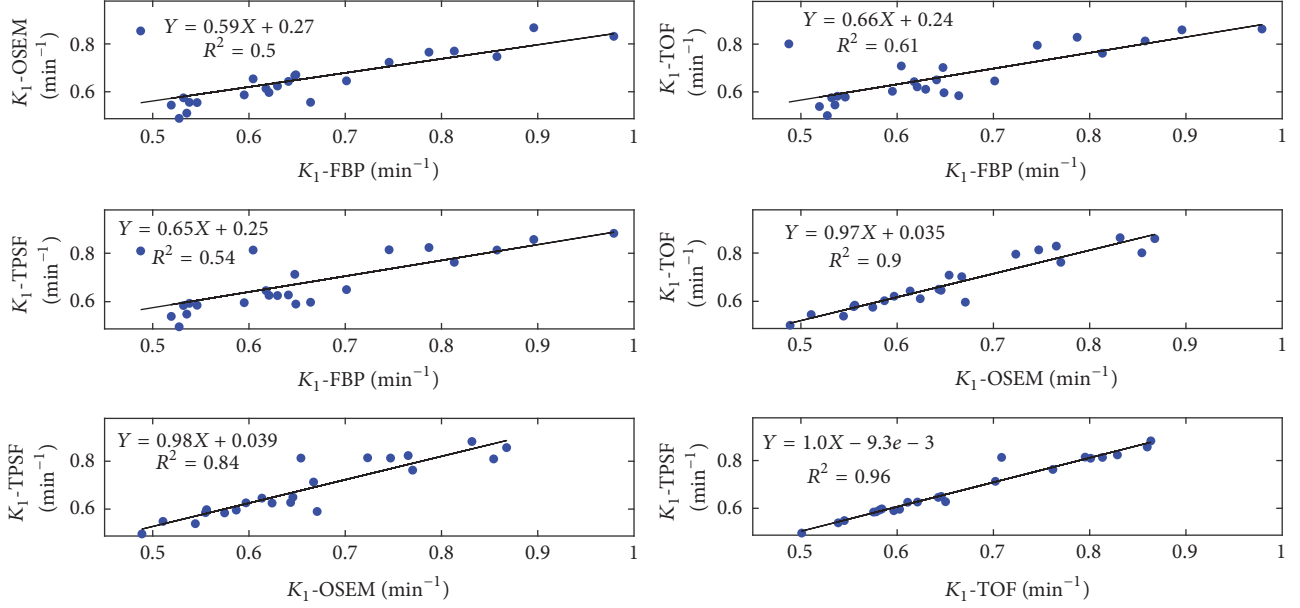


FIGURE 8: Linear regressions of myocardium K_1 calculated from reconstruction methods. Each point represented the corresponding kinetic parameter in myocardium ROI of one patient. Linear function with slope rate, intercept, and squares of Pearson correlation coefficients were indicated.

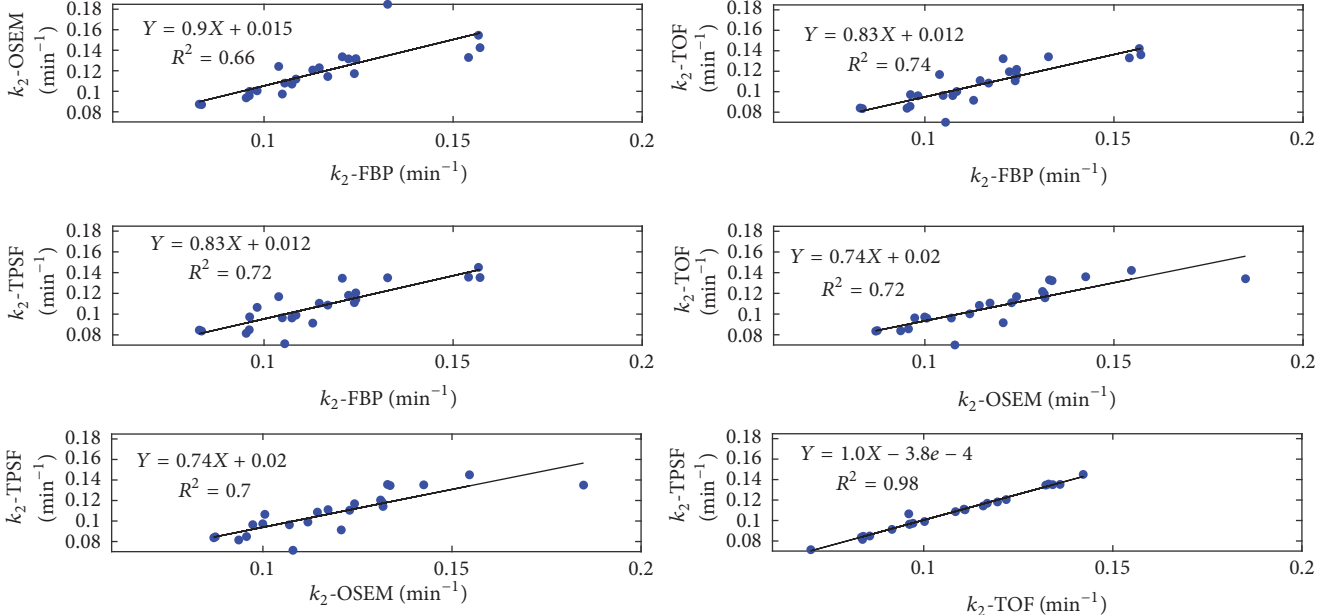


FIGURE 9: Linear regressions of myocardium k_2 calculated from reconstruction methods. Each point represented the corresponding kinetic parameter in myocardium ROI of one patient. Linear function with slope rate, intercept, and squares of Pearson correlation coefficients were indicated.

the difference was more obvious. The possible reason may be that kinetic parameters derived from the divergent TAC from the FBP method are more sensitive to deviations in the curve. However, since patient's unconscious motion was not evident in most cases, ROI with fixed positions was used in the evaluation for all reconstruction methods including FBP in the study.

5. Conclusion

All the tested PET reconstruction algorithms performed similarly in the SUV analysis at the selected time points. Kinetic parameters K_1 and k_2 also exhibited no statistical difference among the four reconstruction algorithms in terms of mean value and standard deviation. However, for the

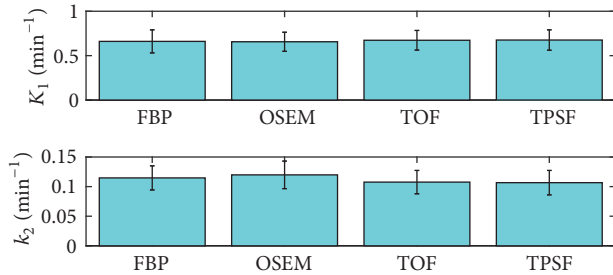


FIGURE 10: Means and standard deviations of myocardium K_1 and k_2 calculated using image-derived input functions for 24 patients with respect to four reconstruction methods of FBP, OSEM, TOF, and TPSF.

TABLE 3: Comparisons of kinetic parameters with and without ROI movements by four reconstruction approaches¹.

	FBP	OSEM	TOF	TPSF
K_1	0.71	0.85	0.80	0.81
	0.59	0.86	0.79	0.80
k_2	0.13	0.18	0.13	0.14
	0.10	0.17	0.14	0.14

¹The parameters with/without ROI movements are shown in bold/italic tables.

correlation analysis, OSEM reconstruction presented relative higher residual in correlation with FBP reconstruction compared with TOF and TPSF reconstruction. TOF and TPSF reconstruction were highly correlated with each other and led to highly consistent kinetic results with superior image quality. As a result, both TOF and TPSF are suitable for cardiac ^{11}C -acetate kinetic analysis. This conclusion needs to be further validated in the future study when arterial blood sampling is provided to measure the true time-activity curve as input function for kinetic modeling.

Conflicts of Interest

The authors declare that they have no conflicts of interest.

Acknowledgments

This work was sponsored in part by the National Natural Science Foundation of China (Grant no. 81571713), Beijing Municipal Science & Technology Commission (Grant no. Z151100003915133), CAMS Innovation Fund for Medical Sciences (CIFMS) (Grant no. 2016-I2 M-4-003), Beijing Municipal Commission of Health and Family Plan (Grant no. 2016-2-40115), and China Scholarship Council (CSC no. 201708110098).

References

- [1] G. Tomasi, F. Turkheimer, and E. Aboagye, "Importance of quantification for the analysis of PET data in oncology: review of current methods and trends for the future," *Molecular Imaging and Biology*, vol. 14, no. 2, pp. 131–136, 2012.
- [2] B. Bai, J. Bading, and P. S. Conti, "Tumor quantification in clinical positron emission tomography," *Theranostics*, vol. 3, no. 10, pp. 787–801, 2013.
- [3] G. Germano, D. S. Berman, and P. Slomka, "Technical Aspects of Cardiac PET Imaging and Recent Advances," *Cardiology Clinics*, vol. 34, no. 1, pp. 13–23, 2016.
- [4] P. Cheebsumon, "Measuring response to therapy using FDG PET: Semi-quantitative and full kinetic analysis," *European Journal of Nuclear Medicine & Molecular Imaging*, vol. 38, no. 5, pp. 832–842, 2011.
- [5] F. A. Kotasidis, C. Tsoumpas, and A. Rahmim, "Advanced kinetic modelling strategies: Towards adoption in clinical PET imaging," *Clinical and Translational Imaging*, vol. 2, no. 3, pp. 219–237, 2014.
- [6] J. B. Moody, B. C. Lee, J. R. Corbett, E. P. Ficaro, and V. L. Murthy, "Precision and accuracy of clinical quantification of myocardial blood flow by dynamic PET: A technical perspective," *Journal of Nuclear Cardiology*, vol. 22, no. 5, pp. 935–951, 2015.
- [7] J. Qi and R. M. Leahy, "Iterative reconstruction techniques in emission computed tomography," *Physics in Medicine and Biology*, vol. 51, no. 15, article no. R01, pp. R541–R578, 2006.
- [8] L. A. Shepp and Y. Vardi, "Maximum likelihood reconstruction for emission tomography," *IEEE Transactions on Medical Imaging*, vol. 1, no. 2, pp. 113–122, 1982.
- [9] H. M. Hudson and R. S. Larkin, "Accelerated image reconstruction using ordered subsets of projection data," *IEEE Transactions on Medical Imaging*, vol. 13, no. 4, pp. 601–609, 1994.
- [10] S. Vandenberghe, E. Mikhaylova, E. D'Hoe, P. Mollet, and J. S. Karp, "Recent developments in time-of-flight PET," *EJNMMI Physics*, vol. 3, no. 1, article no. 3, 2016.
- [11] S. Surti and J. S. Karp, "Advances in time-of-flight PET," *Physica Medica*, vol. 32, no. 1, pp. 12–22, 2016.
- [12] C. C. Watson, "Estimating effective model kernel widths for PSF reconstruction in PET," in *Proceedings of the 2011 IEEE Nuclear Science Symposium and Medical Imaging Conference, NSS/MIC 2011*, pp. 2368–2374, Spain, October 2011.
- [13] M. S. Tohme and J. Qi, "Iterative image reconstruction for positron emission tomography based on a detector response function estimated from point source measurements," *Physics in Medicine and Biology*, vol. 54, no. 12, pp. 3709–3725, 2009.
- [14] E. Prieto, I. Domínguez-Prado, M. J. García-Veloso, I. Peñuelas, J. Á. Richter, and J. M. Martí-Climent, "Impact of time-of-flight and point-spread-function in SUV quantification for oncological PET," *Clinical Nuclear Medicine*, vol. 38, no. 2, pp. 103–109, 2013.
- [15] M. Lubberink, R. Boellaard, A. P. Van Der Weerd, F. C. Visser, and A. A. Lammertsma, "Quantitative comparison of analytic and iterative reconstruction methods in 2- and 3-dimensional dynamic cardiac ^{18}F -FDG PET," *Journal of Nuclear Medicine*, vol. 45, no. 12, pp. 2008–2015, 2004.
- [16] P. Chilra, S. Gnesin, G. Allenbach et al., "Cardiac PET/CT with Rb-82: optimization of image acquisition and reconstruction parameters," *EJNMMI Physics*, vol. 4, no. 1, article 10, 2017.
- [17] F. C. Visser, "Imaging of cardiac metabolism using radiolabelled glucose, fatty acids and acetate," in *Coronary Artery Disease*, Supplement 1, 2001.
- [18] L. Huo, R. Cui, H. Xing, N. Li, C. Zhu, and H. Wu, "Performance evaluation of a new high-sensitivity TOF clinical PET/CT system," *The Journal of Nuclear Medicine*, 2015.

- [19] L. Huo, J. Guo, and Y. Dang, "Kinetic analysis of dynamic ^{11}C -acetate PET/CT imaging as a potential method for differentiation of hepatocellular carcinoma and benign liver lesions," *Theranostics*, vol. 5, no. 4, pp. 371–377, 2015.
- [20] M. Mitterhauser et al., "New aspects on the preparation of $[^{11}\text{C}]$ acetate—a simple and fast approach via distillation," *Applied Radiation & Isotopes Including Data Instrumentation & Methods for Use in Agriculture Industry & Medicine*, vol. 61, no. 6, pp. 1147–1150, 2004.
- [21] J. Qi, R. M. Leahy, S. R. Cherry, A. Chatzioannou, and T. H. Farquhar, "High-resolution 3D bayesian image reconstruction using the microPET small-animal scanner," *Physics in Medicine and Biology*, vol. 43, no. 4, pp. 1001–1013, 1998.
- [22] Q. Jinyi, M. L. Richard, H. Ching-Han, H. F. Thomas, and C. Simon, "Fully 3D bayesian image reconstruction for the ecat exact HR+ I," *Nuclear Science*, vol. 45, pp. 1096–1103, 1998.
- [23] L. Ceriani, T. Ruberto, A. B. Delaloye, J. O. Prior, and L. Giovanella, "Three-Dimensional ordered-subset expectation maximization iterative protocol for evaluation of left ventricular volumes and function by quantitative gated SPECT: A Dynamic phantom study," *Journal of Nuclear Medicine Technology*, vol. 38, no. 1, pp. 18–23, 2010.
- [24] J. van den Hoff, W. Burchert, A.-R. Börner et al., "[^{1-11}C]acetate as a quantitative perfusion tracer in myocardial PET," *Journal of Nuclear Medicine*, vol. 42, no. 8, pp. 1174–1182, 2001.
- [25] PMOD Cardiac PET Modeling Tool (PCARDP), <http://doc.pmod.com/pcardp/pcardp.htm>.
- [26] J. A. Rice, *Mathematical Statistics and Data Analysis*, Duxbury Advanced, 3rd edition, 2006.
- [27] M. A. Lodge, "Repeatability of standardized uptake value in oncologic (^{18}F -FDG PET)," *Journal of Nuclear Medicine Official Publication Society of Nuclear Medicine*, vol. 116, article 186353, 2017.

Research Article

Clinical and Prognostic Value of PET/CT Imaging with Combination of ^{68}Ga -DOTATATE and ^{18}F -FDG in Gastroenteropancreatic Neuroendocrine Neoplasms

Panpan Zhang,¹ Jiangyuan Yu,² Jie Li,¹ Lin Shen ,¹ Nan Li,² Hua Zhu,² Shizhen Zhai,² Yan Zhang,² Zhi Yang ,² and Ming Lu ,¹

¹Department of Gastrointestinal Oncology, Key Laboratory of Carcinogenesis and Translational Research, Ministry of Education, Peking University School of Oncology, Beijing Cancer Hospital and Institute, Beijing, China

²Department of Nuclear Medicine, Key Laboratory of Carcinogenesis and Translational Research, Ministry of Education, Peking University School of Oncology, Beijing Cancer Hospital and Institute, Beijing, China

Correspondence should be addressed to Zhi Yang; pekyz@163.com and Ming Lu; qiminglu_mail@126.com

Received 25 July 2017; Revised 22 October 2017; Accepted 16 January 2018; Published 26 February 2018

Academic Editor: Chongzhao Ran

Copyright © 2018 Panpan Zhang et al. This is an open access article distributed under the Creative Commons Attribution License, which permits unrestricted use, distribution, and reproduction in any medium, provided the original work is properly cited.

Background. To evaluate the clinical and prognostic value of PET/CT with combination of ^{68}Ga -DOTATATE and ^{18}F -FDG in gastroenteropancreatic neuroendocrine neoplasms (GEP-NENs). **Method.** 83 patients of GEP-NENs who underwent ^{68}Ga -DOTATATE and ^{18}F -FDG PET/CT were enrolled between June 2013 and December 2016. Well-differentiated (WD) NETs are divided into group A ($\text{Ki-67} < 10\%$) and group B ($\text{Ki-67} \geq 10\%$), and poorly differentiated (PD) NECs are defined as group C. The relationship between PET/CT results and clinicopathological characteristics was retrospectively investigated. **Result.** For groups A/B/C, the sensitivities of ^{68}Ga -DOTATATE and ^{18}F -FDG were 78.8%/83.3%/37.5% and 52.0%/72.2%/100.0%. A negative correlation between Ki-67 and SUV_{\max} of ^{68}Ga -DOTATATE ($R = -0.415$; $P \leq 0.001$) was observed, while a positive correlation was noted between Ki-67 and SUV_{\max} of ^{18}F -FDG ($R = 0.683$; $P \leq 0.001$). 62.5% (5/8) of patients showed significantly more lesions in the bone if ^{68}Ga -DOTATATE was used, and 22.7% (5/22) of patients showed more lymph node metastases if ^{18}F -FDG was used. **Conclusions.** The sensitivity of dual tracers was correlated with cell differentiation, and a correlation between Ki-67 and both SUV_{\max} of PET-CTs could be observed. ^{68}Ga -DOTATATE is suggested for WD-NET and ^{18}F -FDG is probably suitable for patients with $\text{Ki-67} \geq 10\%$.

1. Introduction

Gastroenteropancreatic neuroendocrine neoplasms (GEP-NENs) are a heterogeneous group of neoplasms that arise from cells of the endocrine system [1]. GEP-NENs are rare and present many clinical challenges. Because of their unpredictable biologic behaviors, the diagnosis usually takes place only after the condition has become advanced. Treatment regimens rely mainly on histological grading via biopsy; however, tumor heterogeneity cannot be fully assessed by tumor biopsy [2, 3]. Although Ki-67 staining has been shown to have prognostic significance in GEP-NENs, pitfalls may lead clinicians to misjudge the tumor grades. Specifically, first, the current gold-standard method, in which 2000 cells

are counted, is heavily dependent on the skill and expertise of the reporting pathologist [4]. Second, the limited tissue in some cases may impede accurate assessment of Ki-67 given the potential for heterogeneity of Ki-67 expression within tumors. Finally, the Ki-67 index may vary over time in the same patient, with changes possible both in response to treatment [5] and over the progression of the disease [6]. We believe that combined dual-tracer PET/CT imaging offers distinct advantages to overcome the above pitfalls.

DOTA-peptides specifically bind to somatostatin receptors 2, 3, and 5 and are usually overexpressed on the surfaces neuroendocrine cells [7, 8]. ^{68}Ga -DOTATATE has been shown to be useful for staging, restaging, surveillance, determining SSTR-based therapy, and monitoring responses

to treatments in NENs [9, 10]. ^{18}F -FDG is a glucose analogue, and PET/CT imaging with this tracer has been shown to be correlated with NENs aggressiveness. The presence of increased glucose in NENs highlights an increased propensity for invasion and metastasis, and PET imaging with ^{18}F -FDG accordingly has higher sensitivity, especially in aggressive and high-grade tumors [11, 12]. Therefore, we believe that PET/CT imaging with combination of ^{68}Ga -DOTATATE and ^{18}F -FDG PET/CT is a highly efficient whole-body imaging method, and it could be complementary to conventional imaging methods.

A large number of previous studies have evaluated the diagnostic accuracy of both tracers in the presence of a relative shortage of information, regarding the correlation to pathological findings and prognostic value. Only a few studies have compared the clinical impact of both ^{68}Ga -DOTATATE and ^{18}F -FDG PET tracers on NENs [13, 14]. The present study aimed to determine the clinical value of the complementary PET/CT imaging method in a large histologically proven NENs population.

2. Materials and Methods

We analyzed the data from 83 (50 males and 33 females) consecutive patients with pathologically proven NENs who underwent contemporaneous PET/CT imaging with ^{68}Ga -DOTATATE and ^{18}F -FDG between June 2013 and December 2016. ^{68}Ga -DOTATATE and ^{18}F -FDG PET/CT scans were performed within an interval of no more than 2 weeks. No patients were treated during this interval. All NENs were classified according to the histopathological reports, which are based on recent consensus statements of the European Neuroendocrine Tumor Society. According to the grade of differentiation, proliferation index (Ki-67), and mitotic count, the well-differentiated (WD) neoplasms are herein defined as NET and graded G1 (Ki-67 $\leq 2\%$) or G2 (Ki-67 3–20%) and G3a (Ki-67 $> 20\%$); the poorly differentiated (PD) neoplasms are defined as NEC and G3b. G2 patients were further divided into 2 groups as G2a (3–9%) and G2b (10–20%).

2.1. PET/CT Acquisition. Patients fasted for at least 6 h before PET/CT scan. Images were acquired 1 h after injection of 3.7 MBq/kg ^{18}F -FDG or 1 h after the injection of 100–200 MBq ^{68}Ga -DOTATATE. Whole-body scan (brain to mid-thigh) was performed with the patient in the supine position. CT exposure factors for all scans were 120 kV and 100 mA. PET/CT images were reported in consensus by two experienced nuclear medicine physicians who were blinded to the findings of the structural imaging. Any nonphysiological focus of ^{68}Ga -DOTATATE or ^{18}F -FDG uptake greater than the normal liver background was considered positive. At the same time, CT imaging was used to differentiate between lesions and physiological uptake. The maximum standardized uptake value (SUV_{\max}) of primary and metastatic lesions was calculated. SUV_{\max} generated from each patient was used in the final analysis. The SUV ratio of the tumor relative to the maximal liver uptake was calculated by dividing SUV_{\max} of the tumor by SUV_{\max} of the liver ($\text{SUV}_{T/L}$). The ratio between

TABLE 1: Patient characteristics.

Characteristics	NET (%)	NEC (%)	All (%)
Gender			
Female (<i>n</i>)	26 (51.0)	7 (21.9)	33 (39.7)
Male (<i>n</i>)	25 (49.0)	25 (78.1)	50 (60.3)
Primary sites (<i>n</i>)			
Pancreas	19 (37.3)	8 (25.0)	27 (32.5)
Gastrointestinal	24 (47.0)	19 (59.4)	43 (51.8)
Primary unknown	8 (15.7)	5 (15.6)	13 (15.7)
Metastatic sites (<i>n</i>)			
Liver	36 (70.6)	13 (40.6)	49 (59.0)
Lymph nodes	21 (41.2)	27 (84.4)	48 (57.8)
Bone	9 (17.6)	10 (31.3)	19 (22.9)
Lung	4 (7.8)	1 (3.1)	5 (6.0)
Other	6 (11.7)	7 (21.9)	13 (15.7)

NET, neuroendocrine tumor; NEC, neuroendocrine carcinoma.

SUV_{\max} of ^{68}Ga -DOTATATE and that of ^{18}F -FDG (SUV_{\max} ratio) was also calculated.

2.2. Statistical Analysis. Descriptive analyses are presented using mean and SD for normally distributed variables, but median, minimum, and maximum values were used for those that were nonnormally distributed. Analyses were performed using SPSS (version 21.0; IBM). The paired Student's *t*-test was used for the related nonnormally distributed variables. Correlation of SUV_{\max} values of ^{68}Ga -DOTATATE and ^{18}F -FDG with Ki-67 index was assessed using Spearman's correlation coefficient. Overall survival (OS) was calculated from the date of diagnosis to the last day of follow-up or death. Kaplan-Meier survival analysis was performed to assess the prognostic value regarding OS, and differences between groups were analyzed using the log-rank test. $P < 0.05$ was considered as statistical significance.

3. Results

3.1. Patient Characteristics. A total of 83 (50 males and 33 females) patients were included in the study, with a median age of 56 years (range: 27–77 years). The primary tumors were located in the pancreas in 27 patients (32.5%), gastrointestinal tract in 43 patients (51.8%), and unknown locations in 13 patients (15.7%). Among the subjects, 48 patients (57.8%) had lymph node involvement and 60 patients (72.3%) had distant metastases. Pathological evaluation showed that 51 patients (61.4%) had WD-NET and 32 patients (38.6%) had PD-NEC. Among WD-NETs, there were 14 patients (16.9%) in G1 ($\leq 2\%$), 19 patients (22.9%) in G2a (3–9%), 9 patients (10.8%) in G2b (10–20%), and 28 patients (33.7%) in G3a ($> 20\%$) (Table 1).

3.2. Complementary PET/CT Qualitative Evaluation

3.2.1. Comparison in Sensitivity. For all patients, ^{68}Ga -DOTATATE was positive in 53 cases and negative in 30 cases, while ^{18}F -FDG PET/CT was positive in 62 cases and

TABLE 2: Sensitivity and uptake of ^{68}Ga -DOTATATE and ^{18}F -FDG PET/CT for different primary sites and grades.

	Sensitivity (%)		SUV_{\max} (mean \pm SD)	
	^{68}Ga -DOTATATE	^{18}F -FDG PET/CT	^{68}Ga -DOTATATE	^{18}F -FDG PET/CT
Primary lesion				
Gastrointestinal tract	55.8%	74.4%	16.75 ± 2.62	7.56 ± 0.87
Pancreas	85.2%	66.7%	29.87 ± 4.77	6.51 ± 0.78
WD NET	80.4%	58.8%	28.87 ± 3.52	4.51 ± 0.45
Gastrointestinal NET	75.0%	54.2%	22.68 ± 2.77	3.71 ± 0.45
Pancreatic NET	89.5%	52.6%	31.19 ± 4.25	5.13 ± 0.93
PD NEC	37.5%	100.0%	10.86 ± 1.78	11.46 ± 0.75
Gastrointestinal NEC	31.6%	100.0%	9.26 ± 1.25	12.44 ± 1.11
Pancreatic NEC	75.0%	100.0%	18.23 ± 5.93	10.23 ± 0.67

WD, well-differentiated; PD, poorly differentiated; NET, neuroendocrine tumor; NEC, neuroendocrine carcinoma.

negative in 21 cases. Overall, ^{18}F -FDG assessment was found to have a better sensitivity (74.7%) compared with ^{68}Ga -DOTATATE (63.8%), although it is not statistically significant ($P = 0.593$). Remarkably, we found that the sensitivity of dual tracers (94.0%) was significantly higher than that with ^{68}Ga -DOTATATE or ^{18}F -FDG alone ($P < 0.01$). For NET and NEC, the sensitivity was 80.39% (41/51) and 37.5% (12/32) with ^{68}Ga -DOTATATE and was 58.82% (30/51) and 100% (32/32) with ^{18}F -FDG. Separating from the primary sites, the sensitivity of ^{68}Ga -DOTATATE in pancreatic NET was higher than that in gastrointestinal NET (NET: 89.5% versus 75.0%, $P = 0.034$; NEC: 75.0% versus 31.6%, $P = 0.027$). However, ^{18}F -FDG showed no difference between pancreatic and gastrointestinal NENs in terms of sensitivity.

3.2.2. Complementary PET/CT Semiquantitative Evaluation. Table 2 illustrates the sensitivities and SUV_{\max} in correlation with primary sites and grades. The uptake values of ^{68}Ga -DOTATATE in PanNENs were significantly higher than those in GI-NEN (29.87 \pm 4.78 versus 16.76 \pm 2.62, $P = 0.011$). The values of ^{18}F -FDG PET/CT in PanNEN had a trend toward a lower SUV than that in GI-NEN (6.51 \pm 0.77 versus 7.57 \pm 0.86, $P = 0.067$) (Figure 1).

3.2.3. Comparison in Different Pathological Groups. The sensitivity of ^{68}Ga -DOTATATE and ^{18}F -FDG in G1/G2a/G2b/G3a/G3b was 78.6%/73.3%/88.9%/77.8%/37.5% and 50.0%/52.6%/66.7%/77.8%/100.0%. ^{68}Ga -DOTATATE imaging provided a sensitivity of >73% in WD-NET (G1-G3a) and only 37.5% in PD-NEC (G3b). For G1 and G2a (Ki-67 < 10%), a statistically significant positive correlation between Ki-67 and the sensitivity with ^{18}F -FDG could be found, and the sensitivity in G1 and G2a (Ki-67 < 10%) was about 50%, increasing dramatically when the Ki-67 index was over 10%. The sensitivity in G3a reached 77.8% and that in G3b was 100%. The patients were divided into 3 groups: group A (G1 + G2a), group B (G2b + G3a), and group C (G3b). With this grouping, the sensitivity of ^{68}Ga -DOTATATE and ^{18}F -FDG in group A/B/C was 78.8%/83.3%/37.5% and 52.0%/72.2%/100.0%. Importantly, we found that the sensitivities of imaging with dual tracers in groups A/B/C

were 84.8%/100%/100%, which were significantly higher than that with the single tracer. There was a significant negative correlation between Ki-67 and ^{68}Ga -DOTATATE SUV_{\max} ($R = -0.415$; $P \leq 0.001$), while a positive correlation was noted between Ki-67 and ^{18}F -FDG SUV_{\max} value ($R = 0.683$; $P \leq 0.001$). Moreover, ^{68}Ga -DOTATATE $\text{SUV}_{T/L}$ showed a negative correlation with Ki-67 index ($R = -0.357$; $P = 0.001$). However, ^{18}F -FDG $\text{SUV}_{T/L}$ was positively correlated with Ki-67 index ($R = 0.617$; $P \leq 0.001$) (Figure 1).

3.2.4. Concordant and Discordant Findings. When combining the results of the dual-tracer PET/CT, 37 patients were positive in both tracers, and 16 patients were ^{68}Ga -DOTATATE-positive and ^{18}F -FDG-negative, while 25 patients were ^{18}F -FDG-positive and ^{68}Ga -DOTATATE-negative. 5 patients were negative in both tracers (Table 3).

^{68}Ga -DOTATATE and ^{18}F -FDG PET/CT findings were concordant in 37 patients with 25 WD-NETs and in 12 PD-NECs. Only 1 patient was diagnosed as localized duodenal NEN. The remaining 36 patients had regional lymph node metastasis, distant metastasis, or both mainly occurring in liver or bone. Of 27 patients with liver metastases, 8 patients (29.6%) examined via ^{68}Ga -DOTATATE showed heterogeneity in SSTR expression. Of 8 patients with bone metastases, imaging findings of 5 patients (62.5%) demonstrated that ^{68}Ga -DOTATATE highlighted more bone lesions than ^{18}F -FDG PET/CT. Of 22 patients with lymph node involvement, the dual tracers with 5 patients (22.7%) showed that ^{18}F -FDG findings could be more prominent than those with ^{68}Ga -DOTATATE (Figure 2).

5 patients showed negative results in both two tracers, with a histological diagnosis of group A. 1 patient was diagnosed as duodenal NET G2 (Ki-67: 3%) with multiple liver metastases (largest lesion: 7.2 cm \times 4.7 cm). The remaining 4 patients had rectal or gastric NET (G1/2) with lesions smaller than 5 mm.

3.3. Treatment and Follow-Up. Of the 83 patients, 26 performed radical surgery; 57 (31 NET and 26 NEC) unresectable patients were treated with palliative surgery, SSA, chemotherapy, and TACE. The median follow-up was 21

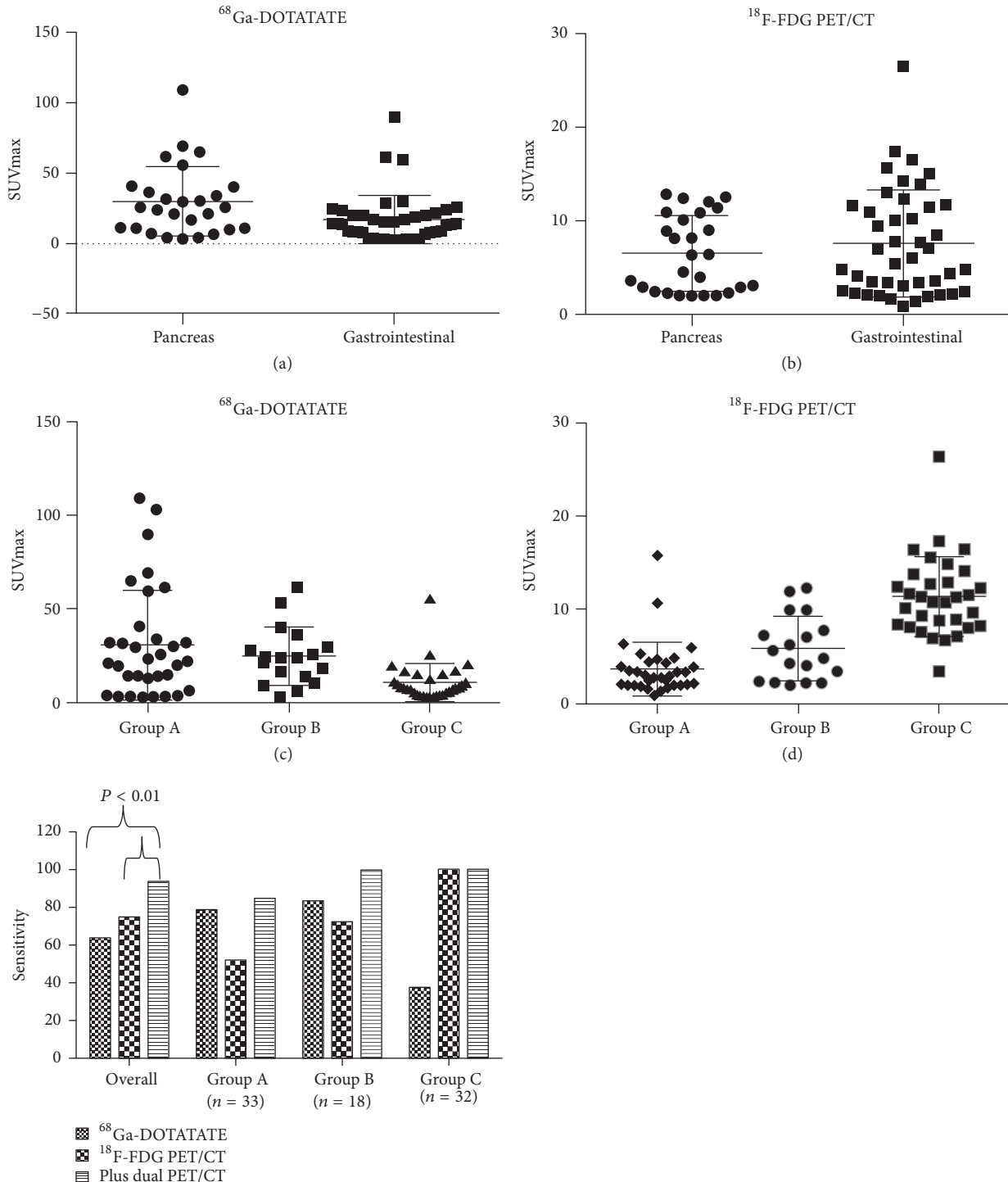


FIGURE 1: Comparison of SUV_{max} of PET/CT according to primary sites ((a) and (b)) and tumor grade ((c) and (d)). The sensitivity of group A (G1 + G2a = Ki-67 < 10%), group B (G2b + G3a = well-differentiated neoplasms with Ki-67 ≥ 10%), and group C (G3b = poorly differentiated neoplasms with Ki-67 > 20%) in PET/CT imaging.

months (in the range of 2–62 months). During the follow-up period, 9 (6 NEC and 3 NET) patients died of the progressive disease. Unresectable patients with positive results solely with ^{18}F -FDG showed the worst prognosis, while those positive solely with ^{68}Ga -DOTATATE showed the best prognosis.

For unresectable patients with NET ($n = 31$), being ^{68}Ga -DOTATATE-negative was associated with worse prognosis (HR: 10.4; 95% CI: 1.5–78.2; $P \leq 0.001$), and being ^{18}F -FDG-positive tended to be correlated with a worse prognosis (HR: 3.6; 95% CI: 0.7–9.8; $P = 0.158$). For unresectable patients

TABLE 3: Concordant and discordant findings.

⁶⁸ Ga-DOTATATE	Positive	Positive	Negative	Negative
¹⁸ F-FDG PET/CT	Positive	Negative	Positive	Negative
Primary lesion (<i>n</i>)				
Pancreas	14	9	4	0
Gastrointestinal tract	18	6	14	5
CUP	5	1	7	0
Metastatic sites				
Liver	27	11	9	1
Lymph node	22	7	18	0
Bone	8	2	8	0
Ki-67 range				
Group A (<i>n</i> = 33)	15 (45.5%)	11 (33.3%)	2 (6.1%)	5 (15.1%)
Group B (<i>n</i> = 18)	10 (55.5%)	5 (27.8%)	3 (16.7%)	0
Group C (<i>n</i> = 32)	12 (37.5%)	0	20 (62.5%)	0

CUP, Cancer of unknown primary.

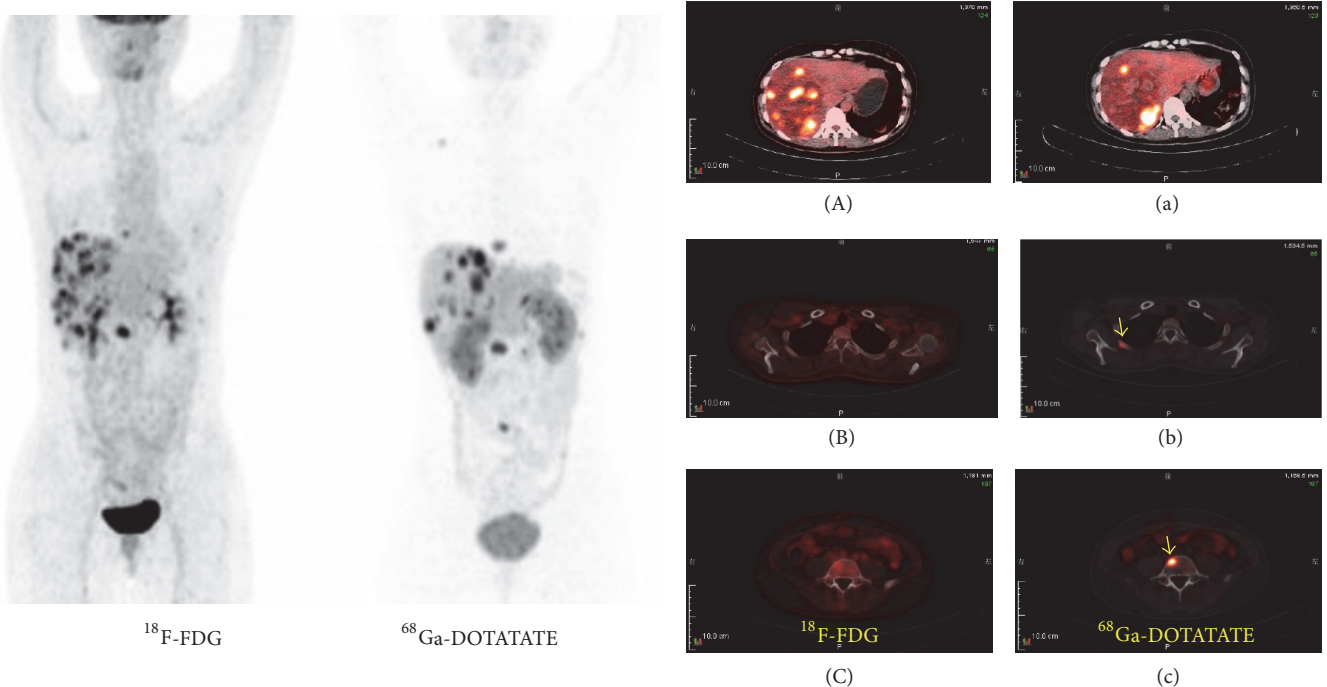


FIGURE 2: A 37-year-old women with pancreatic NEC G3 (Ki-67 = 80%) and lymph node, liver, and bone metastases, from whom the primary lesion has been resected.¹⁸F-FDG PET/CT showed more liver lesions, while ⁶⁸Ga-DOTATATE detected more bone lesions. ((A) and (a)) Liver lesions showed heterogeneity in SSTR expression. ((B) and (b) and (C) and (c)) ¹⁸F-FDG PET/CT failed to show bone metastases in rib and lumbar vertebra.

with NEC (*n* = 26), being ⁶⁸Ga-DOTATATE-negative also tended to be associated with a worse prognosis (HR: 2.4; 95% CI: 0.3–5.4; *P* = 0.382) (Figure 3).

4. Discussion

⁶⁸Ga-DOTATATE and ¹⁸F-FDG PET/CT play a crucial role in the diagnosis and clinical management of NENs with morphologic and functional information. ⁶⁸Ga-DOTATATE was found to be superior to ¹⁸F-FDG in WD-NET, whereas

¹⁸F-FDG was more sensitive in PD-NEC [15]. Considering the costs of molecular imaging, choosing the selected patients for the specific PET/CT imaging is of vital importance. Analyzing the results produced using both tracers for different grades and primary sites could be a balanced approach. The aim of the present study was to compare ⁶⁸Ga-DOTATATE and ¹⁸F-FDG PET/CT in GEP-NENs and to investigate the relationship between the complementary PET/CT results and histopathologic findings in clinical and prognostic values in a large, histologically confirmed NEN population.

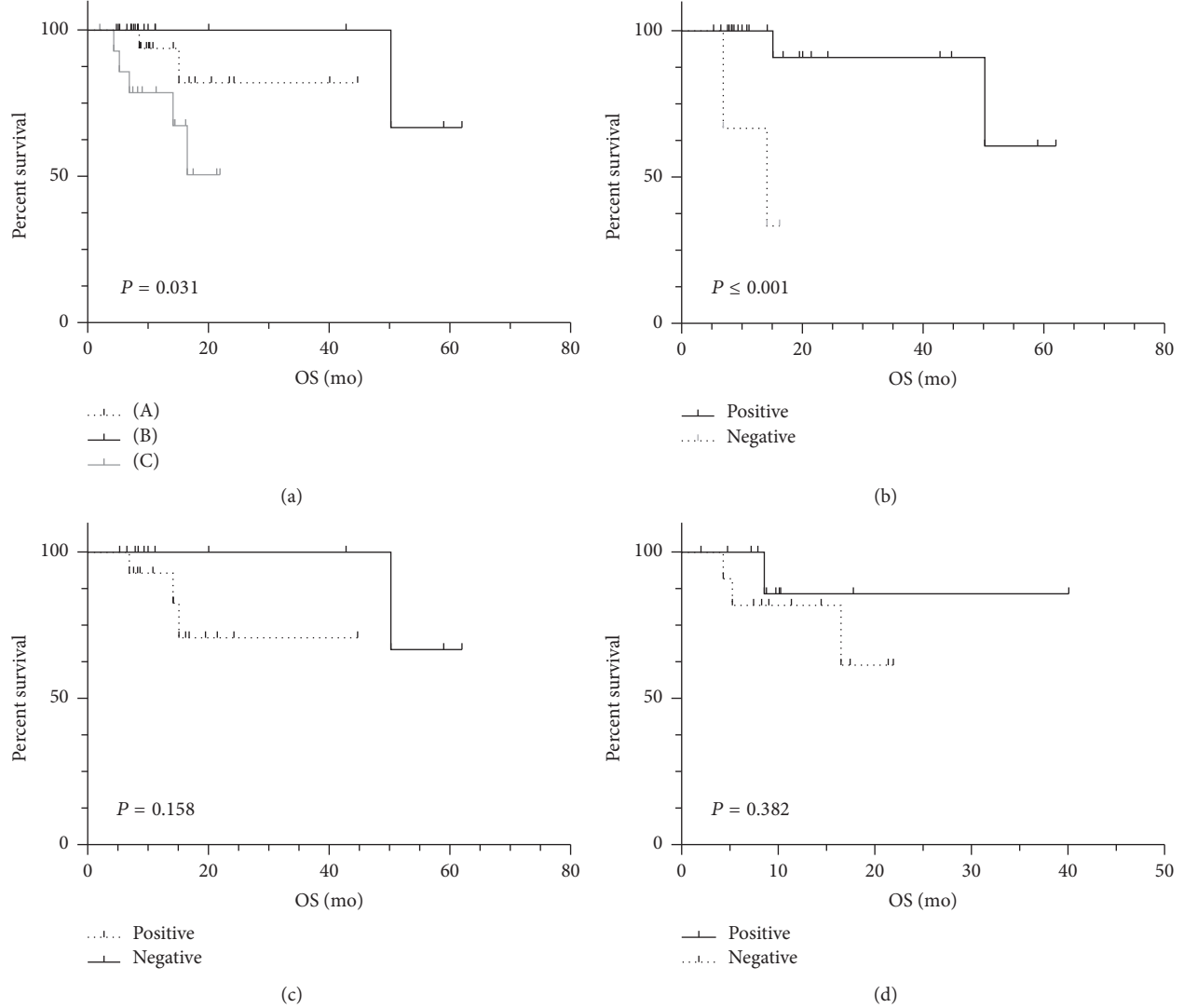


FIGURE 3: The overall survival of unresectable patients detected with dual tracers: (a) Kaplan-Meier survival curve for unresectable patients, (A) positive for both tracers, (B) ⁶⁸Ga-DOTA-TATE only, and (C) ¹⁸F-FDG only; (b) unresectable NET patients with ⁶⁸Ga-DOTA-TATE results (positive or negative); (c) unresectable NET patients with ¹⁸F-FDG results (positive or negative); (d) unresectable NEC patients with ⁶⁸Ga-DOTA-TATE results (positive or negative).

⁶⁸Ga-DOTATATE imaging and ¹⁸F-FDG PET/CT imaging have been compared in several studies which have been shown to have variable sensitivities in detecting NENs with a relatively small number of patients. Naswa et al. [16] reported that the sensitivity of ⁶⁸Ga-DOTANOC and ¹⁸F-FDG was 91.4% and 42.5%, respectively. Koukouraki et al. [17] demonstrated that the sensitivity of ⁶⁸Ga-DOTATOC and ¹⁸F-FDG was 90% and 68%, respectively, and ⁶⁸Ga-DOTANOC was more sensitive in the detection of primary sites or metastasis than ¹⁸F-FDG [18]. Notably the patients included in this study were mainly WD-NETs with lower glucose metabolism. In the present study, the sensitivity of ⁶⁸Ga-DOTATATE and ¹⁸F-FDG PET/CT was 63.85% and 74.70%, respectively. Subgroup analysis showed that the sensitivity of ⁶⁸Ga-DOTATATE was mainly correlated with the degree of differentiation, instead of correlation with

Ki-67 index. The sensitivity of ¹⁸F-FDG showed a positive correlation with the Ki-67 index and differentiation. From ¹⁸F-FDG imaging, the sensitivity was under 53% for patients with Ki-67 < 10% and 100% for PD-NEC. SUV_{max} of patients with NEC was low even for those who had positive results under ⁶⁸Ga-DOTATATE. We also observed that patients with Ki-67 < 10% showed low uptake in ¹⁸F-FDG PET/CT. On consideration of the weak significance of ⁶⁸Ga-DOTATATE for PD-NEC and ¹⁸F-FDG PET/CT for lower-grade NET, our study demonstrated that ¹⁸F-FDG is more suitable for patients with Ki-67 ≥ 10%, and ⁶⁸Ga-DOTATATE is less advantageous in PD-NEC and should be tailored to the individual patients.

Our study demonstrated that PET/CT uptake was statistically significantly different between subgroups of GEP-NENs according to grading. The cohort was separated into

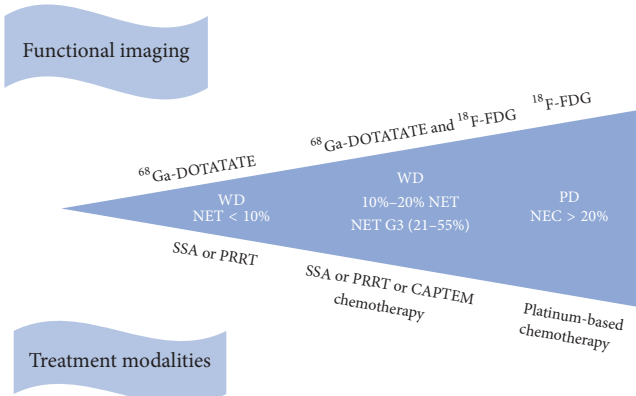


FIGURE 4: PET/CT imaging and treatment regime.

3 groups: A (G1 + G2a), B (G2b + G3a), and C (G3b). Group B showed higher sensitivity for ¹⁸F-FDG than group A, and the median SUV_{max} increased significantly, indicating relatively quick proliferation rate associated with Ki-67 index. Strosberg [19] proposed chemotherapy as a treatment option for tumors with Ki-67 ≥ 10%, especially those with higher ¹⁸F-FDG activity. Such tumors showed high proliferative capacity and aggressive behavior and are recommended for chemotherapy after PRRT or somatostatin therapy. In this way, ¹⁸F-FDG PET/CT may be suitable for identifying patients with aggressive conditions in group B who could benefit from chemotherapy. Thus, PET/CT imaging may establish the missing link between histopathologic findings and the treatment regimen.

Based on our results, dual tracers' assessment is recommended for WD-NET with Ki-67 ≥ 10% (G2b and G3a). ⁶⁸Ga-DOTATATE and ¹⁸F-FDG were complementary in detecting lesions and dual-trace PET/CT showed an advantage in the assessment of SSA, PRRT, and chemotherapy. We proposed that WD-NET patients with Ki-67 ≥ 10% should be examined using dual tracers upon diagnosis. We also suggest that ⁶⁸Ga-DOTATATE should be performed solely in WD-NET patients with Ki-67 < 10% and ¹⁸F-FDG is sufficient for PD NEC. Moreover, repeated PET/CT is warranted when disease progresses rapidly, considering the heterogeneous expression and complementary findings to histopathology (Figure 4).

We investigated the correlations between dual tracers and Ki-67 index. SUV_{max} or SUV_{T/L} was positively correlated with Ki-67 index with respect to ¹⁸F-FDG PET/CT and negatively correlated with Ki-67 index with respect to ⁶⁸Ga-DOTATATE. SUV_{max} of PET/CT may be a suitable biomarker for evaluation of the biological behavior of NENs. The relationship between SUV_{T/L} and Ki-67 index was weak, but it showed a consistency with SUV_{max}. However, SUV_{max} may be influenced by technical elements, while SUV_{T/L} could reduce the differences attributable to equipment and operation to some extent.

GEP-NENs are a heterogeneous group of neoplasms that display great variability in biological behaviors and clinical outcomes [20]. This requires accurate diagnostic techniques for precise staging and choice of therapy. The standard

grading is mainly based on the immunohistochemistry of the proliferation marker Ki-67. However, there are many lesions with variable tracer uptake at different parts of the tumor. Especially within the same organ, these lesions may prevent the biopsy from being a comprehensive reflection of tumor heterogeneity *in vivo*, leading to inaccurate Ki-67 index results. Therefore, dual-trace PET/CT, which is a whole-body noninvasive alternative, is warranted to overcome the shortcomings of histopathologic grading. The findings of this study included the ability of ⁶⁸Ga-DOTATATE to detect heterogeneity in tumors and variable expression in primary sites. SUV_{max} of PanNEN was higher than that of GI-NENs, which was consistent with prior studies [21, 22], where the investigators found higher levels of messenger RNA expression of SSTR2 and SSTR5 in pancreatic than in gastrointestinal NENs. In this way, ⁶⁸Ga-DOTATATE is more sensitive in PanNEN, but it may miss some lesions in GI-NEN. However, SUV_{max} of PanNEN and GI-NEN showed no difference for ¹⁸F-FDG, which is complementary to ⁶⁸Ga DOTATATE. Another finding of the present study was that ⁶⁸Ga DOTATATE has a superb ability to detect heterogeneity in metastatic lesions, which is beneficial for us to select the optimal protocol. We believe that complementary PET/CT can evaluate the tumors' heterogeneity and influence treatment options.

The morphological findings and Ki-67 index are considered important prognostic markers in NENs. One major limitation of these histopathological parameters as prognostic markers is the requirement for tissue sampling, which is not always feasible. A few studies have demonstrated the prognostic value of ¹⁸F-FDG and ⁶⁸Ga-DOTATATE PET/CT in patients with NENs. ¹⁸F-FDG was an independent predictor of PFS [23, 24]. ¹⁸F-FDG SUV_{max} > 3 was demonstrated to be independent predictor of disease progression, superior to conventional prognostic factors such as Ki-67 index and serum CgA [25]. SSTR expression was found to be a positive prognostic factor, and it was therefore expected that SSTR-base PET/CT would also have prognostic value in NENs [26]. Sharma et al. [27] demonstrated the prognostic value of SUV_{max} measured with ⁶⁸Ga DOTATATE in 37 patients with NET. SUV_{max} ≥ 14.5 was found to distinguish patients with progressive and those with nonprogressive disease. A major limitation of the prior studies was that most of the patients included were WD-NET, which may involve selection bias. Our study enrolled 57 unresectable patients (31 NET and 26 NEC). Unresectable patients positive with ¹⁸F-FDG alone showed the worst prognosis, while those positive with ⁶⁸Ga-DOTATATE alone had the best prognosis. NET patients with predominant ¹⁸F-FDG uptake and a negative ⁶⁸Ga-DOTATATE scans had worse prognosis. There is a strong association between high ¹⁸F-FDG uptake and worse outcome even in patients with WD-NETs. However, PD-NEC with negative ⁶⁸Ga-DOTATATE uptake may lead to worse prognosis. The present study has several limitations. First, our study is retrospective, and the second limitation is that the follow-up time was not long enough to assess treatment response, considering the relatively inert biological behavior of NENs.

Noninvasive dual-tracer imaging with ^{68}Ga -DOTATATE and ^{18}F -FDG PET/CT seems promising as an alternative to tissue sampling, due to its capacity to reflect two different aspects of tumor biology, SSTR expression and glucose metabolism, respectively. Accordingly, imaging with dual tracer is recommended for WD-NET patients with Ki-67 $\geq 10\%$, providing information for selection of SSA, PRRT, and chemotherapy. Taking the advantages of dual-tracer imaging in detecting lesions is useful for accurate clinical management. Dual-tracer imaging also shows a clearly linear correlation between SUV_{max} and Ki-67 index. On consideration of heterogeneous expression and complementary findings to histopathology, our results suggested that repeated dual-tracer imaging is warranted to evaluate dynamic biological behavior and prognosis.

Abbreviations

GEP-NENs:	Gastroenteropancreatic neoplasms
PD:	Poorly differentiated
WD:	Well-differentiated
OS:	Overall survival
NET:	Neuroendocrine tumor
NEC:	Neuroendocrine carcinoma
PRRT:	Peptide receptor radionuclide therapy

Conflicts of Interest

The authors declare that there are no conflicts of interest that could be perceived as prejudicing the impartiality of the research reported.

Authors' Contributions

Panpan Zhang and Jiangyuan Yu contributed equally to this work. Panpan Zhang and Jiangyuan Yu wrote the manuscript and analyzed the data. Jie Li, Lin Shen, Nan Li, Hua Zhu, Shizhen Zhai, and Yan Zhang collected patient data and technical information. Zhi Yang and Ming Lu reviewed and helped revise the manuscript.

References

- R. Garcia-Carbonero, J. Capdevila, G. Crespo-Herrero et al., "Incidence, patterns of care and prognostic factors for outcome of gastroenteropancreatic neuroendocrine tumors (GEP-NETs): results from the national cancer registry of Spain (RGETNE)," *Annals of Oncology*, vol. 21, no. 9, pp. 1794–1803, 2010.
- D. S. Klimstra, I. R. Modlin, N. V. Adsay et al., "Pathology reporting of neuroendocrine tumors: Application of the delphic consensus process to the development of a minimum pathology data set," *The American Journal of Surgical Pathology*, vol. 34, no. 3, pp. 300–313, 2010.
- G. Carliniante, P. Baccarini, D. Beretti et al., "Ki-67 cytological index can distinguish well-differentiated from poorly differentiated pancreatic neuroendocrine tumors: A comparative cytohistological study of 53 cases," *Virchows Archiv*, vol. 465, no. 1, pp. 49–55, 2014.
- G. Rindi, G. Klöppel, A. Couvelard et al., "TNM staging of midgut and hindgut (neuro) endocrine tumors: A consensus proposal including a grading system," *Virchows Archiv*, vol. 451, no. 4, pp. 757–762, 2007.
- J. C. Yao, A. T. Phan, D. Z. Chang et al., "Efficacy of RAD001 (everolimus) and octreotide LAR in advanced low- to intermediate-grade neuroendocrine tumors: results of a phase II study," *Journal of Clinical Oncology*, vol. 26, no. 26, pp. 4311–4318, 2008.
- S. Singh, J. Hallet, C. Rowsell, and C. H. L. Law, "Variability of Ki67 labeling index in multiple neuroendocrine tumors specimens over the course of the disease," *European Journal of Surgical Oncology*, vol. 40, no. 11, pp. 1517–1522, 2014.
- E. Grande, J. J. Díez, V. Pachón, and A. Carrato, "Advances in the therapy of gastroenteropancreatic-neuroendocrine tumours (GEP-NETs)," *Clinical and Translational Oncology*, vol. 12, no. 7, pp. 481–492, 2010.
- M. Miederer, S. Seidl, A. Buck et al., "Correlation of immunohistopathological expression of somatostatin receptor 2 with standardised uptake values in ^{68}Ga -DOTATOC PET/CT," *European Journal of Nuclear Medicine and Molecular Imaging*, vol. 36, no. 1, pp. 48–52, 2009.
- W. A. P. Breeman, E. de Blois, H. Sze Chan, M. Konijnenberg, D. J. Kwekkeboom, and E. P. Krenning, " ^{68}Ga -labeled DOTA-peptides and ^{68}Ga -labeled radiopharmaceuticals for positron emission tomography: current status of research, clinical applications, and future perspectives," *Seminars in Nuclear Medicine*, vol. 41, no. 4, pp. 314–321, 2011.
- N. Naswa, P. Sharma, A. Kumar et al., "Gallium-68-DOTANOC PET/CT of patients with gastroenteropancreatic neuroendocrine tumors: A prospective single-center study," *American Journal of Roentgenology*, vol. 197, no. 5, pp. 1221–1228, 2011.
- I. Kayani, J. B. Bomanji, A. Groves et al., "Functional imaging of neuroendocrine tumors with combined PET/CT using ^{68}Ga -DOTATATE (Dota-DPhE₁, Tyr3-octreotate) and ^{18}F -FDG," *Cancer*, vol. 112, no. 11, pp. 2447–2455, 2008.
- R. Abgral, S. Leboulleux, D. Déandreibs et al., "Performance of 18fluorodeoxyglucose-positron emission tomography and somatostatin receptor scintigraphy for high Ki67 ($\geq 10\%$) well-differentiated endocrine carcinoma staging," *The Journal of Clinical Endocrinology & Metabolism*, vol. 96, no. 3, pp. 665–671, 2011.
- D. H. Simsek, S. Kuyumcu, C. Turkmen et al., "Can complementary ^{68}Ga -dotataate and ^{18}F -FDG PET/CT establish the missing link between histopathology and therapeutic approach in gastroenteropancreatic neuroendocrine tumors?" *Journal of Nuclear Medicine*, vol. 55, no. 11, pp. 1811–1817, 2014.
- E. Panagiotidis, A. Alshammari, S. Michopoulos et al., "Comparison of the impact of ^{68}Ga -DOTATATE and ^{18}F -FDG PET/CT on clinical management in patients with Neuroendocrine tumors," *Journal of Nuclear Medicine*, vol. 58, no. 1, pp. 91–96, 2017.
- M. H. Squires, N. Volkan Adsay, D. M. Schuster et al., "Octreoscan Versus FDG-PET for Neuroendocrine Tumor Staging: A Biological Approach," *Annals of Surgical Oncology*, vol. 22, no. 7, pp. 2295–2301, 2015.
- N. Naswa, P. Sharma, S. K. Gupta et al., "Dual tracer functional imaging of gastroenteropancreatic neuroendocrine tumors using ^{68}Ga -DOTA-NOC PET-CT and ^{18}F -FDG PET-CT: Competitive or complimentary?" *Clinical Nuclear Medicine*, vol. 39, no. 1, pp. e27–e34, 2014.
- S. Koukouraki, L. G. Strauss, V. Georgoulias, M. Eisenhut, U. Haberkorn, and A. Dimitrakopoulou-Strauss, "Comparison of the pharmacokinetics of ^{68}Ga -DOTATOC and [^{18}F]FDG in

- patients with metastatic neuroendocrine tumors scheduled for ^{90}Y -DOTATOC therapy," *European Journal of Nuclear Medicine and Molecular Imaging*, vol. 33, no. 10, pp. 1115–1122, 2006.
- [18] V. Ambrosini, D. Campana, L. Bodei et al., "68Ga-DOTANOC PET/CT clinical impact in patients with neuroendocrine tumors," *Journal of nuclear medicine : official publication, Society of Nuclear Medicine*, vol. 51, no. 5, pp. 669–673, 2010.
- [19] J. R. Strosberg, "Systemic treatment of gastroenteropancreatic neuroendocrine tumors (GEP-NETs): Current approaches and future options," *Endocrine Practice*, vol. 20, no. 2, pp. 167–175, 2014.
- [20] Z. Yang, L. H. Tang, and D. S. Klimstra, "Effect of tumor heterogeneity on the assessment of Ki67 labeling index in well-differentiated neuroendocrine tumors metastatic to the liver: Implications for prognostic stratification," *The American Journal of Surgical Pathology*, vol. 35, no. 6, pp. 853–860, 2011.
- [21] D. Campana, V. Ambrosini, R. Pezzilli et al., "Standardized uptake values of 68Ga-DOTANOC PET: a promising prognostic tool in neuroendocrine tumors," *Journal of Nuclear Medicine*, vol. 51, no. 3, pp. 353–359, 2010.
- [22] D. O'Toole, A. Saveanu, A. Couvelard et al., "The analysis of quantitative expression of somatostatin and dopamine receptors in gastro-entero-pancreatic tumours opens new therapeutic strategies," *European Journal of Endocrinology*, vol. 155, no. 6, pp. 849–857, 2006.
- [23] A. Sundin and A. Rockall, "Therapeutic monitoring of gastroenteropancreatic neuroendocrine tumors: The challenges ahead," *Neuroendocrinology*, vol. 96, no. 4, pp. 261–271, 2012.
- [24] E. Garin, F. Le Jeune, A. Devillers et al., "Predictive value of 18F-FDG PET and somatostatin receptor scintigraphy in patients with metastatic endocrine tumors," *Journal of Nuclear Medicine*, vol. 50, no. 6, pp. 858–864, 2009.
- [25] T. Binderup, U. Knigge, A. Loft, B. Federspiel, and A. Kjaer, " ^{18}F -fluorodeoxyglucose positron emission tomography predicts survival of patients with neuroendocrine tumors," *Clinical Cancer Research*, vol. 16, no. 3, pp. 978–985, 2010.
- [26] H. S. Kim, H. S. Lee, and W. H. Kim, "Clinical significance of protein expression of cyclooxygenase-2 and somatostatin receptors in gastroenteropancreatic neuroendocrine tumors," *Cancer Research and Treatment*, vol. 43, no. 3, pp. 181–188, 2011.
- [27] P. Sharma, N. Naswa, S. S. KC et al., "Comparison of the prognostic values of ^{68}Ga -DOTANOC PET/CT and ^{18}F -FDG PET/CT in patients with well-differentiated neuroendocrine tumor," *European Journal of Nuclear Medicine and Molecular Imaging*, vol. 41, no. 12, pp. 2194–2202, 2014.

Research Article

Prognostic Value of Volume-Based Positron Emission Tomography/Computed Tomography in Nasopharyngeal Carcinoma Patients after Comprehensive Therapy

Yueli Tian,^{1,2} Khamis Hassan Bakari,^{1,2} Shanshan Liao,^{1,2} Xiaotian Xia,^{1,2} Xun Sun,^{1,2} Chunxia Qin,^{1,2} Yongxue Zhang ,^{1,2} and Xiaoli Lan ,^{1,2}

¹Department of Nuclear Medicine, Union Hospital, Tongji Medical College, Huazhong University of Science and Technology, Wuhan 430022, China

²Hubei Key Laboratory of Molecular Imaging, Union Hospital, Tongji Medical College, Huazhong University of Science and Technology, Wuhan 430022, China

Correspondence should be addressed to Xiaoli Lan; lxl730724@hotmail.com

Received 28 July 2017; Revised 14 December 2017; Accepted 26 December 2017; Published 21 February 2018

Academic Editor: Jianhua Zhang

Copyright © 2018 Yueli Tian et al. This is an open access article distributed under the Creative Commons Attribution License, which permits unrestricted use, distribution, and reproduction in any medium, provided the original work is properly cited.

Objective. We assessed the prognostic value of standardized uptake value (SUV) and volume-based methods including whole-body metabolic tumor volume (WBMTV) and whole-body total lesion glycolysis (WBTLG) using ¹⁸F-fluorodeoxyglucose positron emission tomography/computed tomography (PET/CT) of patients with nasopharyngeal carcinoma (NPC) after therapy. **Methods.** A total of 221 posttherapy NPC cases were enrolled, all of whom had undergone PET/CT scanning and follow-up in this retrospective study. The diagnostic results of PET/CT were analyzed and compared with histopathological diagnosis or clinical follow-up. Receiver operator characteristic curves, the Kaplan-Meier method, and the log-rank test were used to assess the optimal cutoff values for WBMTV and WBTLG to identify independent predictors of survival. **Results.** The detection rates of the threshold SUV were 2.5, 20%, and 40%, and SUV background methods were 65.6% (378/576), 80.2% (462/576), 71.5% (412/576), and 90.4% (521/576), respectively ($P < 0.005$). Patients with a WBMTV < 8.10 and/or a WBTLG < 35.58 had significantly better 5-year overall survival than those above the cutoffs (90.7% versus 51.2%, $P < 0.001$; 91.7% versus 50.4%, $P < 0.001$), respectively. Multivariate Cox regression modeling showed both WBTLG (RR, 1.002; $P = 0.004$) and age (RR, 1.046; $P = 0.006$) could be used to predict overall survival. WBTLG (RR, 1.003; $P < 0.001$) may have predictive relevance in estimating disease-free survival. **Conclusions.** SUV volume-based threshold background methodology had a significantly higher detection rate for metastatic lesions. WBTLG could be used as an independent prognostic indicator for posttherapy NPC.

1. Introduction

Nasopharyngeal carcinoma (NPC) is one of the commonest epithelial-derived malignant tumors of the head and neck, and it is associated with the highest incidence of nodal and/or distant metastases [1–3]. As a chemo- and radiosensitive tumor, the current standard treatment for locally advanced NPC is concurrent chemoradiotherapy [4, 5], which can result in 5-year survival and disease-free rates up to 70% [6, 7]. However, recurrence of the disease may occur [7, 8]. Known prognostic factors of NPC include a history of smoking, TNM stage classification, clinical and molecular

prognostic variables, and elevated plasma Epstein-Barr virus DNA [9]. Clinically, none of them can accurately define the prognosis of NPC patients.

¹⁸F-Fluorodeoxyglucose positron emission tomography/computed tomography (¹⁸F-FDG PET/CT) is suitable for the evaluation of various types of cancers including NPC. Being noninvasive, the tool has the ability to visualize and measure physiological function and biochemical processes (metabolism) of most cancers and has been widely used in the diagnosis, staging, management, monitoring of treatment response, and recurrence detection of many malignancies [10]. ¹⁸F-FDG PET parameters that are used as

independent prognostic factors during or after chemotherapy and radiotherapy include maximum standardized uptake value (SUVmax), metabolic tumor volume (MTV), and total lesion glycolysis (TLG) [11–13]. Multiple reports have shown that SUVmax, defined as the maximum SUV in a region of interest (ROI) containing the tumor, is one prognostic factor in some cancers [11, 14, 15]. In addition to SUVmax, MTV and TLG have also been widely used as tumor metabolic and volumetric parameters in ¹⁸F-FDG PET/CT. The volume of tumor tissue with active ¹⁸F-FDG uptake is defined as MTV [16–18]. TLG is the median SUV in an ROI multiplied by the MTV. The utilization of MTV and TLG is crucial in dealing with metabolically active lesions and tumor invasiveness [19].

Different thresholds such as the absolute, relative, and background relative thresholds have been frequently applied in lesion segmentation but it is still a contentious matter as to which threshold should be designated for segmenting the volume of lesion. Incongruent results of the prognostic importance of SUVmax, MTV, and TLG in NPC patients have been reported by previous studies [20, 21]. The importance of volumetric ¹⁸F-FDG PET parameters has not been fully assessed, thus making it difficult to accurately identify the best predictors of treatment outcome. The aim of this study was to investigate the prognostic value of WBMTV and WBTLG obtained from ¹⁸F-FDG PET/CT images in NPC patients after comprehensive therapy. Four different threshold methods were assessed and an optimal threshold for segmentation of recurrent metastatic lesions was selected.

2. Patients and Methods

2.1. Patients. Permission to conduct this study was granted by the institution review board of Tongji Medical College, Huazhong University of Science and Technology, and informed consent was obtained from all patients. A total of 221 patients (169 males [76.4%] and 52 females [23.5%]; median age 46 ± 12 y, range: 17–75 y) were retrospectively analyzed. All patients had performed ¹⁸F-FDG PET/CT imaging in the PET Center of Union Hospital, Tongji Medical College of Huazhong University of Science and Technology, between September 2003 and May 2013 after treatment. All patients had received surgery and/or definitive intensity-modulated radiotherapy (IMRT) and/or adjuvant platinum-based chemotherapy. Inclusion criteria were as follows: (1) histologically proven nasopharyngeal carcinoma; (2) complete clinical and imaging data; (3) the patients receiving therapy before the PET/CT scan. Exclusion criteria were as follows: (1) diabetes and pregnancy; (2) absence of other malignant lesions or borderline lesions. Follow-up time was 34.4 ± 24.8 months (range: 5–120 months) and ended in October 2013. The time of death in patients signifies the endpoint of follow-up.

2.2. ¹⁸F-FDG PET/CT Imaging. All patients fasted for at least 6 h before the examination and were injected intravenously with 3.74 MBq (0.10 mCi)/Kg ¹⁸F-FDG. All patients had their blood glucose concentration measured and established to be <6.6 mmol/L. Patients then rested for 45–60 minutes

in a quiet, dark environment and later drank 300–500 mL of water to empty their bladder before PET/CT scanning. ¹⁸F-FDG PET imaging was performed using a Discovery LS PET/CT system (GE Medical Systems). A CT scan was acquired for attenuation correction using the following parameters: a tube voltage of 120 kV, a tube current of 80 mA, and 4.25 mm section collimation. Immediately after the CT, a PET scan was then obtained from the level of the head to the upper part of the legs at 3 minutes per bed position, usually 6–8 bed positions depending on the height of the patient. Reconstruction of the PET data was performed with the ordered set expectation maximization algorithm. A Xeleris workstation (GE Medical System) was used for evaluation of data obtained from both CT and PET.

2.3. Measurement of MTV and TLG. Two experienced nuclear medicine physicians analyzed all the images independently on Xeleris workstations to identify all definite cancer-related lesions. The lesions' locations were recorded to produce target volumes from PET/CT results. RT image, a free software program developed by the Department of Radiation Oncology and MIPS at Stanford University, was deployed to read all the primary CT and PET DICOM data. Each lesion was selected on PET images and segmented automatically using a 3D-area growing algorithm.

Four thresholds were chosen for delineation: (1) The absolute threshold (Th2.5) was calculated as SUVmax = 2.5 marking all voxels inside foci with SUVs > 2.5 as tumor tissue. (2) The relative threshold (Th20) was calculated as SUV = 20% × SUVmax, meaning that all voxels inside the lesion with SUV higher than 20% of the SUVmax of the lesion were labeled as tumor tissue. (3) The relative threshold (Th40) was calculated as SUV = 40% × SUVmax, indicating that all voxels inside the lesion with an SUV > 40% SUVmax of the lesion would be labeled as tumor tissue. (4) The relative background dependent threshold (Thbgd) was calculated as SUV = SUVbgd + 20% (SUVmax – SUVbgd), where SUVbgd was described as the mean SUVmax of the surrounding background of the ROI, that is, ten randomly outlined regions in the background around the lesion where their mean was SUVbgd. SUVmax ROI is indicated as the SUVmax of the lesion [22]. The volume and SUVmean of each lesion were calculated by the software. The MTV of each slice was then calculated by multiplying the area within the threshold margin. The sum of the MTVs of every lesion in a patient is the WBMTV. TLG is calculated by multiplying the MTV by the SUVmean [23]. The sum of the TLGs of each lesion is the whole-body TLG (WBTLG).

2.4. Statistical Analysis. We used SPSS statistical software version 17.0 (SPSS Inc., Chicago, IL, USA) for statistical analysis. We also used chi-square analysis and Fisher's exact test to determine differences in the lesion detection rate among the four threshold methods. The optimal SUV threshold method was then performed to calculate WBMTV and WBTLG. Receiver operating characteristics (ROC) curves were generated to assess the area under the curve (AUC) and the optimal cutoff value for WBMTV and WBTLG. The

TABLE 1: Characteristics of 221 patients.

Characteristic	Number of patients	Constituent ratio (%)
<i>Age</i>		
Median	46 ± 12	
Range	17~75	
<i>Gender</i>		
Male	169	76.4
Female	52	23.5
<i>Treatment</i>		
Radiotherapy	89	40.3
Radiotherapy & chemotherapy	119	53.8
Surgery & radiotherapy & chemotherapy	10	4.5
Surgery & radiotherapy	1	0.5
Chemotherapy	1	0.5
Surgical	1	0.5
<i>Patient status</i>		
No evidence of disease	156	70.6
Alive with disease	28	12.7
Dead	37	16.7

Kaplan-Meier method and the log-rank test were used to evaluate and compare survival rates. Overall survival (OS) and disease-free survival (DFS) were chosen as endpoints and were measured from the date of radiotherapy initiation to the date of death or recurrence. The prognostic significance of SUVmax, WBMTV, WBTLG, and other pathological variables for OS and DFS was assessed by Cox proportional hazards regression analysis.

3. Results

3.1. Patients. The characteristics of the patients are summarized in Table 1. Of 221 patients, recurrence and metastasis were confirmed in 28 patients. A total of 37 had died at the last follow-up. A total of 156 patients enjoyed DFS, which includes 90 normal and 66 residual cases. Five-year OS and mean survival time of all patients were 71.6% and 90.9 ± 0.6 months, respectively.

3.2. Comparison among the Four Thresholds. The 221 patients had a total of 576 lesions (Table 2). Figure 1 shows a case of NPC after comprehensive therapy, where the four threshold methods were used for segmentation. The detection rates of the threshold Th2.5, Th20, Th40, and Thbgd method were 65.6% (378/576), 80.2% (462/576), 71.5% (412/576), and 90.4% (521/576), respectively. The Thbgd threshold delineated significantly more lesions than the Th2.5, Th20, and Th40 methods ($P < 0.001$), while statistical differences could be seen among the Th2.5, Th20, and Th40 methods ($P < 0.05$). Th2.5, Th20, and Th40 thresholds mainly failed to segment lesions in the nasopharynx, the skull base, cervical

TABLE 2: Location of definitive lesions in the included patients.

Position	Number
Nasopharynx	86
The skull nearby nasopharynx	92
Lymph nodes in neck/axilla/thorax	278
Pleura	3
Lung	36
Liver	20
Bone	61
Total	576

TABLE 3: Lesions unable to be segmented using different thresholds.

Location	Lesion numbers			
	Th2.5	Th20	Th40	Thbgd
Nasopharynx	31	25	28	2
The skull nearby nasopharynx	38	11	29	5
Lymph nodes in neck/axilla/thorax	58	28	41	15
Pleura	0	0	0	0
Lung	28	18	25	11
Liver	11	7	9	6
Bone	32	25	32	16
Total	198	114	164	55

lymph nodes, lung, abdomen, pelvis, liver, and bone; the Thbgd threshold mainly failed to delineate lesions in the lung, liver, and bone (Table 3).

3.3. WBMTV, WBTLG, and Prognostic Factors. WBMTV and WBTLG were calculated according to the Thbgd threshold, which segmented most of the metastatic lesions. The mean values of SUVmax, WBMTV, and WBTLG were 5.57 ± 5.5 (range, 1.7–24.9), $15.2 \pm 21.1 \text{ cm}^3$ (range, 0–159.3 cm^3), and 88.6 ± 127.9 (range, 0–900.9), respectively. From ROC curves, the cutoff values of WBMTV and WBTLG were 8.10 and 35.58 (Figure 2(a)), respectively. AUCs were 0.733 ± 0.037 and 0.736 ± 0.035 , respectively. Patients with WBMTV < 8.10 had significantly better 5-year OS (90.7% versus 51.2%, $\chi^2 = 18.0$, $P < 0.001$) than patients with a WBMTV ≥ 8.10 . Patients with WBTLG < 35.58 had significantly better 5-year OS (91.7% versus 50.4%, $\chi^2 = 21.8$, $P < 0.001$) than patients with a WBTLG ≥ 35.58 (Figures 2(b) and 2(c)). A Cox proportional hazards multivariate model of OS and DFS outcome was constructed to evaluate the age, gender, treatment, lesion number, SUVmax, WBMTV, and WBTLG as predictors of disease progression and survival. The results indicated that both WBTLG (RR, 1.002; $P = 0.004$) and age (RR, 1.046; $P = 0.006$) could be used to predict OS (Table 4). For DFS, WBTLG (RR, 1.003; $P < 0.001$) may have predictive relevance.

4. Discussion

The current standard treatment for NPC is radiotherapy. The treatment has effects such as edema, loss of tissue

TABLE 4: Cox proportional hazards regression analysis for OS of different factors.

Factors	P	HR	95% CI*	
			Lower	Upper
Age	0.006	1.046	1.001	1.245
Gender	0.319	0.681	0.621	1.008
Treatment	0.523	1.078	0.801	1.107
Focus number	0.681	1.101	0.568	1.814
SUVmax	0.356	1.032	0.758	1.072
WBMTV	0.254	0.853	0.824	1.082
WBTLG	0.004	1.002	1.002	1.236

P < 0.05. CI indicates confidence interval.

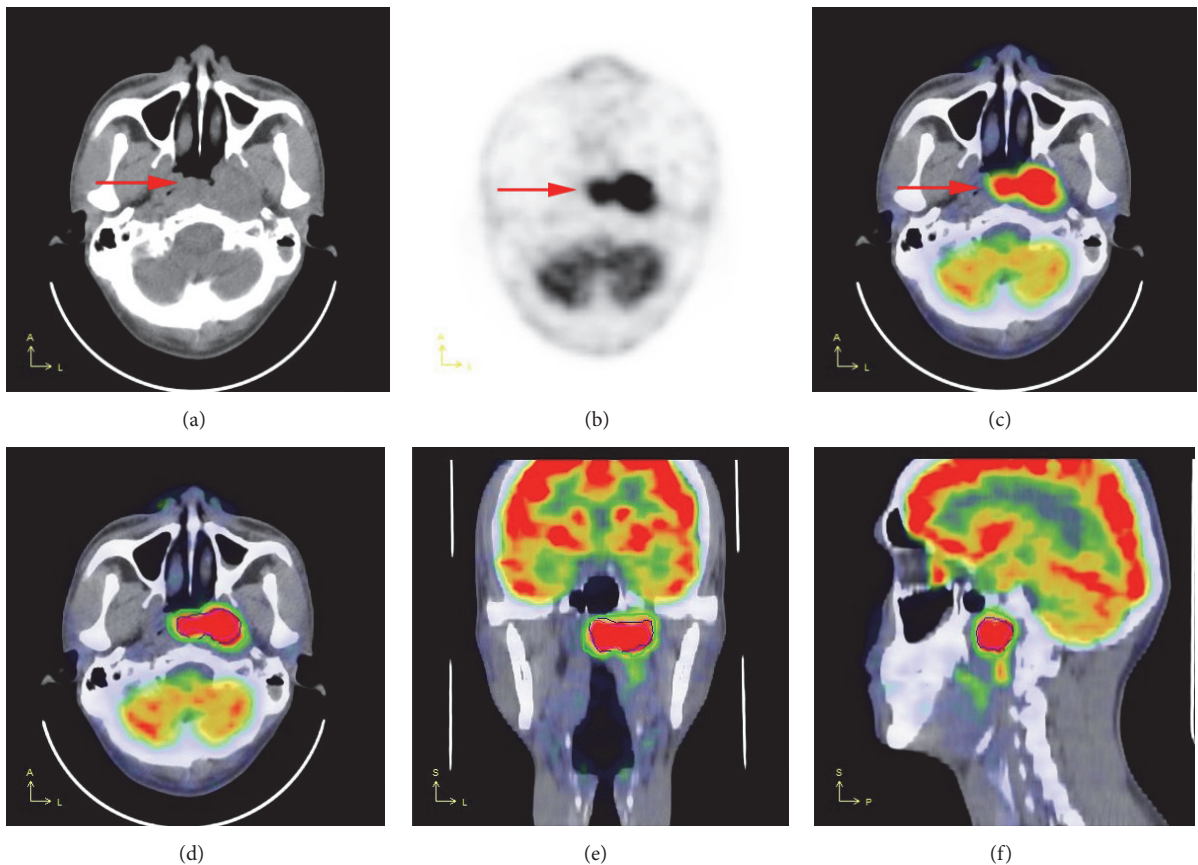


FIGURE 1: A 59-year-old male with NPC after comprehensive therapy. CT (a), PET (b), and fused (c) images show a mass lesion in nasopharyngeal posterior wall and left lateral wall (red arrow). Results of segmentation using the four described thresholds are shown on transaxial (d), coronal (e), and sagittal views (f). The light red, purple, blue, and green areas were segmented using SUVmax = 2.5, Th20, Th40, and Th_{bgd} thresholds, respectively.

planes, fibrosis, mucositis, and scarring [24] resulting in serious complications to the patient and causing interference with the detection of local recurrent or persistent NPC. Accurate prediction of prognosis is vital for therapy planning. Identification of predictors associated with poor outcomes is of paramount importance before selecting appropriate candidates for such treatment modalities. ¹⁸F-FDG PET/CT is a noninvasive imaging modality which has the ability to visualize and quantify the glucose metabolism of malignancies

including NPC. The purpose of our study was to investigate a number of PET-based functional indices and their relationship with the prognosis in NPC patients after comprehensive therapy. In our study, we found that the background threshold for segmentation of malignant lesions was much better than Th2.5, Th20, and Th40. WBTLG, a parameter that includes information on both tumor function and volume, was an important independent factor to predict the prognosis. However, WBMTV was found to be unrelated to the prognosis.

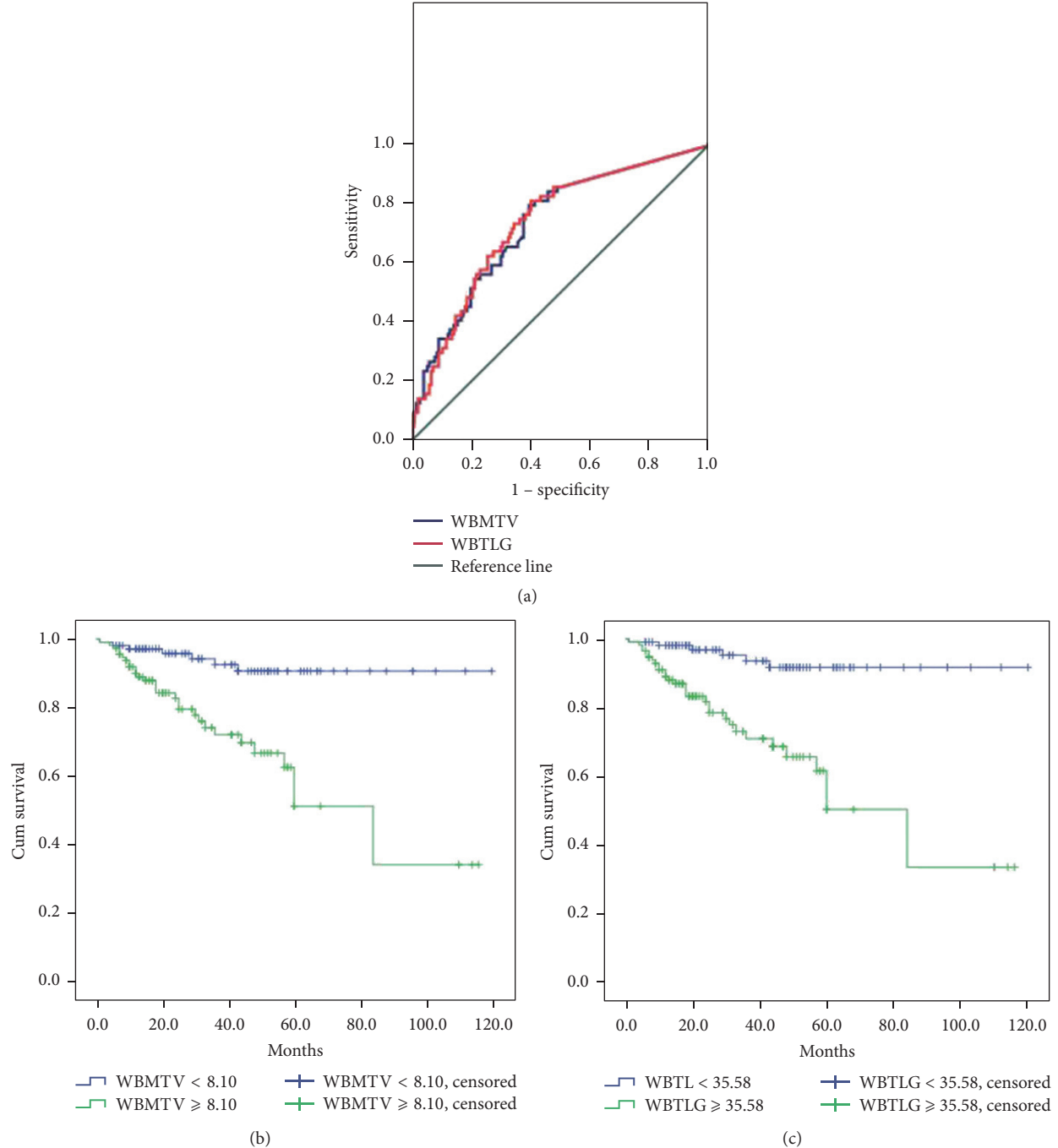


FIGURE 2: (a) The cutoff value of WBMTV and WBTLG was 8.10 and 35.58, respectively, from ROC analysis. (b) Five-year OS stratified by WBMTV (log-rank test, $P < 0.001$). (c) Five-year OS stratified by WBTLG (log-rank test, $P < 0.001$).

Tumor volume analysis was based on a set of thresholds. We selected four different thresholds for comparison in this study. Only 65.6% of lesions were segmented when the threshold was selected as $\text{SUV} = 2.5$. This is mainly because sometimes the background around the lesion was >2.5 ; while the computer was selecting the lesion area, the surrounding background might have been segmented as a lesion, hence making it harder in differentiating the tumor lesions from the surrounding normal tissue. Th20 and Th40 were

rendered inadequate methods by some low-uptake lesions that could not be segmented (such as lung and liver) when the thresholds were lower than the surrounding background SUV. Significant FDG accumulation was always visible in some head-neck inflammatory areas resulting in excessive segmentation with the surrounding background. Using the background method to segment volume, the lesion detection rate reached 90.4%. The main advantage of this method is the inclusion of the surrounding background into the calculation

of threshold, taking full account of the high FDG uptake area and the surrounding normal tissue. Yu et al. observed that the background method is able to predict primary lesion of esophageal cancer [22]. Liao et al. reported that the detection rate of lesions using the background method to calculate the threshold was significantly higher than that of using SUV 2.5 in epithelial-derived ovarian cancer patients after surgery [25].

Clinically, SUVmax, a metabolic index, is frequently used to assess tumor activity because it is an observer-independent measurement. Prior studies have documented the importance of SUVmax in predicting treatment response and survival in patients presenting with head and neck cancer and other types of malignancies [26, 27]. SUVmax, as a single voxel value, is susceptible to noise and therefore it may not accurately reproduce the overall tumor burden [28]. A previous study of NPC patients treated with radiotherapy or CCRT suggested that the SUVmax of the primary tumor was not an independent prognostic factor [29]. These findings are similar to those of an earlier published report, which observed that SUVmax of the primary tumor was not only a poor independent prognostic factor for survival but also a poor predictor of treatment response [30]. Therefore, adequate methods of identifying patients who are at risk and who may be candidates for aggressive initial treatment are crucial.

Chan et al. suggested that MTV is a prognostic factor in patients with head and neck cancer. Furthermore, they indicated that MTV appears to be an independent risk factor in advanced NPC patients [31]. Other studies focusing on lung cancer and lymphoma reported similar findings by showing that MTV is an accurate predictor of disease and death and thus is independent of other recognized prognostic factors [31]. A cutoff value of 30 cm^3 for metabolic volume and 130 for metabolic index has been suggested to differentiate between favorable and unfavorable outcomes [32]. In our study, we discovered that 8.10 cm^3 was the most discriminative cutoff for WBMTV. On further analysis, we found that patients with tumors with lower WBMTVs had higher 5-year OS than those patients with higher WBMTVs. However, there was no statistical significance in multivariate analysis due to the fact that all the patients in our study had received surgery or radiotherapy/chemotherapy resulting in inadequate statistical significance in the relationship with survival time. Thus, the current evidence highlights weaknesses of SUVmax and WBMTV.

TLG, which is derived from SUVmean and MTV, is regarded as an ideal metabolic variable in reflecting total tumor volume. TLG incorporates both anatomic (tumor volume) and biological (glucose metabolism) data, making it a more accurate predictor than either MTV or SUV [31]. An earlier report by Chan et al. suggested that TLG was more predictive than MTV for OS and DFS [31]. TLG has also been shown to be able to predict the response of epithelial-derived ovarian cancer patients to treatment [23]. Similar findings in the generation of prognosis by using diameter-SUVindex were found by Roedl et al. [33]. Both TLG and MTV have been found to be independent predictors of prognosis in groups of patients with malignant mesothelioma

and oropharyngeal squamous cell carcinoma [34, 35]. Kim et al., in their study of 140 patients with diffuse large B cell lymphoma, showed that TLG with a 50% margin threshold was an independent prognostic factor for survival [36]. Consistent with this finding, we discovered that the value 35.58 was the most discriminative cutoff. A principal finding of this study is that WBTLG is strongly correlated with OS and DFS in patients with NPC after comprehensive therapy, and thus it is a better predictor of long-term survival than WBMTV and SUVmax alone. In our opinion, high WBTLG represents a tumor's aggressiveness.

Our study has some limitations. The low number of patients evaluated and the retrospective nature of our study restrict the magnitude at which our results can be applicable in a large-scale setting. The other limitation is the heterogeneity of the patients and different treatments protocols. The different time interval of PET acquisitions and variations of lesions locations were other added limitations. Furthermore, the possible risk factors, such as Epstein-Barr virus status and DNA level, were not included in the analysis due to limited cases with available data in our setting. Long-term prospective validation studies of large populations are necessary to confirm our findings.

4.1. Conclusion. By quantitatively analyzing ^{18}F -FDG PET/CT images of NPC patients after comprehensive therapy, the SUV threshold background method had a significantly higher detection rate of metastatic lesions than using an SUV cutoff of 2.5, Th20, or Th40. WBTLG calculated from the Thbgd threshold could be used as an independent prognostic factor for patients with NPC postcomprehensive therapy. A prospective study with a large sample size is needed to further validate the reliability of this study.

Ethical Approval

This retrospective study of existing patient data and images was approved by the institutional review board of Union Hospital, Tongji Medical College, Huazhong University of Science and Technology.

Conflicts of Interest

The authors declare that there are no conflicts of interest regarding the publication of this paper.

Acknowledgments

This work was supported by the National Natural Science Foundation of China (no. 81630049) and the Clinical Research Physician Program of Tongji Medical College, Huazhong University of Science and Technology (no. 5001530008).

References

- [1] S. G. Jeng Tang, F. J. Lin, M. S. Chen, C. C. Liaw, W. M. Leung, and J. H. Hong, "Prognostic factors of nasopharyngeal

- carcinoma: A multivariate analysis," *International Journal of Radiation Oncology Biology Physics*, vol. 19, no. 5, pp. 1143–1149, 1990.
- [2] P. M. L. Teo, W. H. Kwan, W. Y. Lee, S. F. Leung, and P. J. Johnson, "Prognosticators determining survival subsequent to distant metastasis from nasopharyngeal carcinoma," *Cancer*, vol. 77, no. 12, pp. 2423–2431, 1996.
- [3] A. W. M. Lee, Y. F. Poon, W. Foo et al., "Retrospective analysis of 5037 patients with nasopharyngeal carcinoma treated during 1976–1985: overall survival and patterns of failure," *International Journal of Radiation Oncology Biology Physics*, vol. 23, no. 2, pp. 261–270, 1992.
- [4] Y. Kim, B. Kim, S. Jung et al., "Radiation Therapy Combined with (or without) Cisplatin-based Chemotherapy for Patients with Nasopharyngeal Cancer: 15-years Experience of a Single Institution in Korea," *Cancer Research and Treatment*, vol. 40, no. 4, p. 155, 2008.
- [5] L. Zhang, C. Zhao, B. Ghimire et al., "The role of concurrent chemoradiotherapy in the treatment of locoregionally advanced nasopharyngeal carcinoma among endemic population: a meta-analysis of the phase iii randomized trials," *BMC Cancer*, vol. 10, article 558, 2010.
- [6] M. Al-Sarraf, M. LeBlanc, P. G. S. Giri et al., "Chemoradiotherapy versus radiotherapy in patients with advanced nasopharyngeal cancer: phase III randomized Intergroup study 0099," *Journal of Clinical Oncology*, vol. 16, no. 4, pp. 1310–1317, 1998.
- [7] J.-C. Lin, J.-S. Jan, C.-Y. Hsu, W.-M. Liang, R.-S. Jiang, and W.-Y. Wang, "Phase III study of concurrent chemoradiotherapy versus radiotherapy alone for advanced nasopharyngeal carcinoma: positive effect on overall and progression-free survival," *Journal of Clinical Oncology*, vol. 21, no. 4, pp. 631–637, 2003.
- [8] A. W. M. Lee, W. M. Sze, J. S. K. Au et al., "Treatment results for nasopharyngeal carcinoma in the modern era: The Hong Kong experience," *International Journal of Radiation Oncology Biology Physics*, vol. 61, no. 4, pp. 1107–1116, 2005.
- [9] M. L. K. Chua, J. T. S. Wee, E. P. Hui, and A. T. C. Chan, "Nasopharyngeal carcinoma," *The Lancet*, vol. 387, no. 10022, pp. 1012–1024, 2016.
- [10] J. W. Fletcher, B. Djulbegovic, H. P. Soares et al., "Recommendations on the use of ^{18}F -FDG PET in oncology," *Journal of Nuclear Medicine*, vol. 49, no. 3, pp. 480–508, 2008.
- [11] A. Gallamini, C. Zwarthoed, and A. Borra, "Positron emission tomography (PET) in oncology," *Cancers*, vol. 6, no. 4, pp. 1821–1889, 2014.
- [12] V. Paidipally, A. Chirindel, C. H. Chung et al., "FDG volumetric parameters and survival outcomes after definitive chemoradiotherapy in patients with recurrent head and neck squamous cell carcinoma," *American Journal of Roentgenology*, vol. 203, no. 2, pp. W139–W145, 2014.
- [13] M. K. Chung, H.-S. Jeong, S. G. Park et al., "Metabolic tumor volume of $[^{18}\text{F}]$ -fluorodeoxyglucose positron emission tomography/computed tomography predicts short-term outcome to radiotherapy with or without chemotherapy in pharyngeal cancer," *Clinical Cancer Research*, vol. 15, no. 18, pp. 5861–5868, 2009.
- [14] H. Doi, K. Kitajima, K. Fukushima et al., "SUVmax on FDG-PET is a predictor of prognosis in patients with maxillary sinus cancer," *Japanese Journal of Radiology*, vol. 34, no. 5, pp. 349–355, 2016.
- [15] T. Rahman, T. Tsujikawa, M. Yamamoto et al., "Different prognostic implications of 18 F -FDG PET between histological subtypes in patients with cervical cancer," *Medicine (United States)*, vol. 95, no. 9, Article ID e3017, 2016.
- [16] R. Boellaard, R. Delgado-Bolton, W. J. G. Oyen et al., "FDG PET/CT: EANM procedure guidelines for tumour imaging: version 2.0," *European Journal of Nuclear Medicine and Molecular Imaging*, vol. 42, no. 2, pp. 328–354, 2014.
- [17] J. W. Lee, C. M. Kang, H. J. Choi et al., "Prognostic value of metabolic tumor volume and total lesion glycolysis on preoperative (1)(8) F -FDG PET/CT in patients with pancreatic cancer," *Journal of Nuclear Medicine*, vol. 55, no. 6, pp. 898–904, 2014.
- [18] J. A. Husby, B. C. Reitan, M. Biermann et al., "Metabolic tumor volume on 18 F -FDG PET/CT improves preoperative identification of high-risk endometrial carcinoma patients," *Journal of Nuclear Medicine*, vol. 56, no. 8, pp. 1191–1198, 2015.
- [19] J. Davison, G. Mercier, G. Russo, and R. M. Subramaniam, "PET-based primary tumor volumetric parameters and survival of patients with non-small cell lung carcinoma," *American Journal of Roentgenology*, vol. 200, no. 3, pp. 635–640, 2013.
- [20] W. Xiao, A. Xu, F. Han et al., "Positron emission tomography-computed tomography before treatment is highly prognostic of distant metastasis in nasopharyngeal carcinoma patients after intensity-modulated radiotherapy treatment: A prospective study with long-term follow-up," *Oral Oncology*, vol. 51, no. 4, pp. 363–369, 2015.
- [21] S. H. Moon, J. Y. Choi, H. J. Lee et al., "Prognostic value of volume-based positron emission tomography/computed tomography in patients with nasopharyngeal carcinoma treated with concurrent chemoradiotherapy," *Clinical and Experimental Otorhinolaryngology*, vol. 8, no. 2, pp. 142–148, 2015.
- [22] W. Yu, X.-L. Fu, Y.-J. Zhang et al., "GTV spatial conformity between different delineation methods by 18FDG PET/CT and pathology in esophageal cancer," *Radiotherapy & Oncology*, vol. 93, no. 3, pp. 441–446, 2009.
- [23] H. H. Chung, H. W. Kwon, and K. W. Kang, "Prognostic value of preoperative metabolic tumor volume and total lesion glycolysis in patients with epithelial ovarian cancer," *Annals of Surgical Oncology*, vol. 19, no. 6, pp. 1966–1972, 2012.
- [24] S.-H. Ng, S.-C. Chan, T.-C. Yen et al., "Comprehensive imaging of residual/recurrent nasopharyngeal carcinoma using whole-body MRI at 3 T compared with FDG-PET-CT," *European Radiology*, vol. 20, no. 9, pp. 2229–2240, 2010.
- [25] S. Liao, X. Lan, G. Cao, H. Yuan, and Y. Zhang, "Prognostic predictive value of total lesion glycolysis from 18F-FDG PET/CT in post-surgical patients with epithelial ovarian cancer," *Clinical Nuclear Medicine*, vol. 38, no. 9, pp. 715–720, 2013.
- [26] R. Sasaki, R. Komaki, H. Macapinlac et al., "[^{18}F]fluorodeoxyglucose uptake by positron emission tomography predicts outcome of non-small-cell lung cancer," *Journal of Clinical Oncology*, vol. 23, no. 6, pp. 1136–1143, 2005.
- [27] K. A. Higgins, J. K. Hoang, M. C. Roach et al., "Analysis of pretreatment FDG-PET SUV parameters in head-and-neck cancer: Tumor SUV mean has superior prognostic value," *International Journal of Radiation Oncology Biology Physics*, vol. 82, no. 2, pp. 548–553, 2012.
- [28] M. Soret, S. L. Bacharach, and I. Buvat, "Partial-volume effect in PET tumor imaging," *Journal of Nuclear Medicine*, vol. 48, no. 6, pp. 932–945, 2007.
- [29] W.-S. Liu, M.-F. Wu, H.-C. Tseng et al., "The role of pretreatment FDG-PET in nasopharyngeal carcinoma treated with intensity-modulated radiotherapy," *International Journal of Radiation Oncology Biology Physics*, vol. 82, no. 2, pp. 561–566, 2012.

- [30] T. H. La, E. J. Filion, B. B. Turnbull et al., "Metabolic Tumor Volume Predicts for Recurrence and Death in Head-and-Neck Cancer," *International Journal of Radiation Oncology Biology Physics*, vol. 74, no. 5, pp. 1335–1341, 2009.
- [31] S.-C. Chan, J. T. Chang, C.-Y. Lin et al., "Clinical utility of ¹⁸F-FDG PET parameters in patients with advanced nasopharyngeal carcinoma: Predictive role for different survival endpoints and impact on prognostic stratification," *Nuclear Medicine Communications*, vol. 32, no. 11, pp. 989–996, 2011.
- [32] P. Xie, J.-B. Yue, H.-X. Zhao et al., "Prognostic value of ¹⁸F-FDG PET-CT metabolic index for nasopharyngeal carcinoma," *Journal of Cancer Research and Clinical Oncology*, vol. 136, no. 6, pp. 883–889, 2010.
- [33] J. B. Roedl, E. F. Halpern, R. R. Colen, D. V. Sahani, A. J. Fischman, and M. A. Blake, "Metabolic tumor width parameters as determined on PET/CT predict disease-free survival and treatment response in squamous cell carcinoma of the esophagus," *Molecular Imaging and Biology*, vol. 11, no. 1, pp. 54–60, 2009.
- [34] R. Lim, A. Eaton, N. Y. Lee et al., "18F-FDG PET/CT metabolic tumor volume and total lesion glycolysis predict outcome in oropharyngeal squamous cell carcinoma," *Journal of Nuclear Medicine*, vol. 53, no. 10, pp. 1506–1513, 2012.
- [35] S. J. Lee, J. Y. Choi, H. J. Lee et al., "Prognostic value of volume-based 18F-fluorodeoxyglucose PET/CT parameters in patients with clinically node-negative oral tongue squamous cell carcinoma," *Korean Journal of Radiology*, vol. 13, no. 6, pp. 752–759, 2012.
- [36] T. M. Kim, J. C. Paeng, I. K. Chun et al., "Total lesion glycolysis in positron emission tomography is a better predictor of outcome than the International Prognostic Index for patients with diffuse large B cell lymphoma," *Cancer*, vol. 119, no. 6, pp. 1195–1202, 2013.

Research Article

Do TSH, FT3, and FT4 Impact BAT Visualization of Clinical FDG-PET/CT Images?

Ryuichi Nishii ,^{1,2} Shigeki Nagamachi,^{2,3} Youichi Mizutani,² Tamasa Terada,² Syogo Kiyohara,² Hideyuki Wakamatsu,² Seigo Fujita,² Tatsuya Higashi,¹ Keiichiro Yoshinaga,¹ Tsuneo Saga,⁴ and Toshinori Hirai²

¹Department of Molecular Imaging and Theranostics, National Institute of Radiological Sciences (NIRS), QST, 4-9-1 Anagawa, Inage-ku, Chiba-shi, Chiba 263-8555, Japan

²Department of Radiology, Faculty of Medicine, University of Miyazaki, 5200 Kihara, Kiyotake-cho, Miyazaki-shi, Miyazaki 889-1692, Japan

³Department of Radiology, Faculty of Medicine, Fukuoka University, 7-45-1 Nanakuma, Jonan-ku, Fukuoka 814-0180, Japan

⁴Department of Diagnostic Imaging and Nuclear Medicine, Kyoto University, Graduate School of Medicine, No. 54, ShogoinKawahara-cho, Sakyo-ku, Kyoto, Kyoto 606-8507, Japan

Correspondence should be addressed to Ryuichi Nishii; nishii.ryuichi@qst.go.jp

Received 12 September 2017; Revised 29 December 2017; Accepted 4 January 2018; Published 13 February 2018

Academic Editor: Chongzhao Ran

Copyright © 2018 Ryuichi Nishii et al. This is an open access article distributed under the Creative Commons Attribution License, which permits unrestricted use, distribution, and reproduction in any medium, provided the original work is properly cited.

Objective. We retrospectively analyzed activated BAT visualization on FDG-PET/CT in patients with various conditions and TH levels to clarify the relationships between visualization of BAT on FDG-PET/CT and the effect of TH. **Methods.** Patients who underwent clinical FDG-PET/CT were reviewed and we categorized patients into 5 groups: (i) thyroid hormone withdrawal (THW) group; (ii) recombinant human thyrotropin (rhTSH) group; (iii) hypothyroidism group; (iv) hyperthyroidism group; and (v) BAT group. A total of sixty-two FDG-PET/CT imaging studies in fifty-nine patients were performed. To compare each group, gender; age; body weight; serum TSH, FT3, and FT4 levels; and outside temperature were evaluated. **Results.** No significant visualization of BAT was noted in any of the images in the THW, rhTSH, hypothyroidism, and hyperthyroidism groups. All patients in the BAT group were in a euthyroid state. When the BAT-negative and BAT-positive patient groups were compared, it was noted that the minimum and maximum temperature on the day of the PET study and maximum temperature of the one day before the PET study were significantly lower in BAT-positive group than in all those of other groups. **Conclusions.** Elevated TSH condition before RIT, hyperthyroidism, or hypothyroidism did not significantly impact BAT visualization of clinical FDG-PET/CT images.

1. Introduction

Detection of ¹⁸F-2-fluoro-2-deoxy-D-glucose (FDG) uptake on positron emission tomography (PET) is commonly used for the diagnostic imaging of a variety of tumors. Currently, FDG-PET or FDG-PET/CT is the first-choice modality for functional imaging in clinical oncology [1]. However, the visualization of hypermetabolic brown adipose tissue (BAT) on FDG-PET/CT is a known cause of both false-positive and false-negative findings. Therefore, the high FDG avidity of BAT should be taken into account on FDG-PET/CT for

oncologic imaging because misidentifying BAT as cancer metastasis may alter clinical decisions.

There are significant BAT depots from the anterior neck to the thorax of adults, not just in that of newborns and young children [2]. Uncoupling protein 1 (UCP1) has been identified as a biological landmark of BAT that mediates nonshivering thermogenesis. Jeanguillaume et al. reported a relationship between activated BAT on FDG-PET and UCP1 expression in mice [3]. In addition, type 2 iodothyronine deiodinase (D2) is the primary enzyme responsible for the rapid increases in intracellular T3 and preservation of T3 as serum T4 decreases,

which is essential for adaptive thermogenesis of BAT [4]. D2 is considered to be important for the synergism of thyroid hormone (TH) and is required to generate T3 from T4 in BAT, which maintains normal acute thermogenic function [5]. Since possible stimulation of thermogenesis in BAT by thyroid-stimulating hormone (TSH) was described in 1975 [6], several studies have confirmed the relationship between TSH or TH and the activation of thermogenesis in BAT [4, 5, 7]. However, relatively few papers have reported the relationship between TH and BAT visualization by clinical FDG-PET/CT. Lahesmaa et al. found that hyperthyroidism promotes BAT metabolism in humans using FDG-PET/CT [8]; however, contradicting results were reported by Connolly et al. in 2015 [9]. Furthermore, a case report of MRI and infrared thermal imaging regarding the presence of BAT in an adolescent with primary hypothyroidism was recently published [9]. Nonetheless, to date, details about the relationship between visualization of BAT on FDG-PET/CT and the effect of TH remain unknown. Therefore, identification of a possible mechanism of TH-induced BAT activation is considered to be important to interpret FDG-PET/CT imaging, especially of the neck region.

This study is the first to retrospectively analyze BAT visualization on FDG-PET/CT in patients with various conditions and TH levels.

2. Materials and Methods

2.1. Patients. We retrospectively reviewed images from all patients who underwent clinical FDG-PET/CT studies in our facility from October 2010 to July 2015. Patients younger than 20 years were excluded from this study. All patients who met the criteria for inclusion in any of the following five groups were enrolled in this study: (i) a TH withdrawal (THW) group, which included patients who were examined by FDG-PET/CT during a hypothyroid state with TH withdrawal and low-iodine diet prior to radioiodine therapy for metastasis after total thyroidectomy. A hypothyroid state was confirmed by serum TSH, FT3, and FT4 measured within 3 days of FDG-PET/CT; (ii) a recombinant human thyrotropin (rhTSH) group, which included patients who were examined by FDG-PET/CT after two consecutive daily intramuscular injections of rhTSH (0.9 mg of Thyrogen; Genzyme Co., Cambridge, MA) at 48 and 24 h prior to the FDG-PET/CT study, during low-iodine diet prior to radioiodine thyroid remnant ablation after total thyroidectomy. FT3, FT4, and elevated TSH levels were confirmed by blood tests on the day of FDG-PET/CT imaging; (iii) a hypothyroidism group; (iv) a hyperthyroidism group, which included patients who received treatment for hypothyroidism and were examined by FDG-PET/CT for detection of malignancy. A hypothyroid state was confirmed by an endocrinologist and serum TSH, FT3, and FT4 measured within 14 days of FDG-PET/CT; and (v) a BAT group, which included patients who were examined by FDG-PET/CT for the detection of malignancy with findings of BAT uptake and serum TSH, FT3, and FT4 levels measured within 3 months of FDG-PET/CT imaging.

This retrospective investigation was approved by institutional review board and all enrolled patients provided written

informed consent that was approved by our institutional review board.

2.2. ^{18}F -FDG-PET/CT Imaging. Commercially available FDG (185 MBq) in 2 ml of saline solution was purchased from Nihon Medi-physics Co. Ltd. (Tokyo, Japan). All patients were examined by whole-body PET with an integrated 16-slice multidetector CT (Siemens Biograph-16 PET/CT, Nashville, TN, USA).

The patients fasted for more than 5 h before receiving an intravenous injection of FDG (185 MBq). Whole-body PET/CT images (head to upper thigh) were acquired after 60 min for each patient in using 5 or 6 bed positions, depending on subject's height. Emission images were acquired for 2 min per bed position. The data was reconstructed using the ordered subsets expectation maximization (OSEM) method using eight subsets, two iterations, and an array size of 256×256 . For the attenuation correction of PET/CT fusion images, the CT component was performed according to a standard protocol with the following parameters: 140 kV; 50 mAs; tube rotation time, 0.5 s per rotation; slice thickness, 5 mm; and gap, 2 mm. The E-soft workstation (Siemens, Nashville, TN, USA) was used to construct PET/CT fusion images.

2.3. Data Analysis. The parameters of gender; age; body weight; serum TSH, FT3, and FT4 levels; minimum and maximum temperature on the day of FDG-PET/CT imaging and maximum temperature one day before; and the deference of temperature were compared. Based on an in-house reference value, the normal range of the value of each blood hormone was set as follows: TSH, 0.35–4.94 $\mu\text{IU}/\text{mL}$; FT3, 1.71–3.71 pg/mL; and FT4, 0.70–1.48 ng/dL. Temperature obtained from local weather records was referenced. Differences in temperature were calculated as follows: (maximum temperature one day before) – (minimum temperature on the day of examination) ($^{\circ}\text{C}$).

PET/CT images were interpreted and visually assessed by one or two of the five experienced nuclear medicine physicians (SN, RN, YM, SK, and HW) with access to all available clinical information to determine whether visualization of activated BAT was apparent in the neck, shoulder, back, paravertebral, and/or other soft tissues. A final diagnosis was made by consensus.

2.4. Statistical Analysis. All values are expressed as the mean \pm standard deviation. All statistical analyses were performed using JMP ver. 12 statistical software (SAS Institute, Cary, NC, USA). A probability (p) value < 0.01 was considered statistically significant. Comparisons between groups were made using the Wilcoxon rank-sum test.

3. Results

As summarized in Table 1, 62 FDG-PET/CT images of 59 patients were reviewed in this retrospective study, as follows: (i) THW group: 21 images; mean age, 61.6 ± 14.9 years; seven males and 14 females; (ii) rhTSH group: eight images; mean age, 48.4 ± 14.1 years; four males and four females;

TABLE 1: Patient characteristics and summary of each group.

Group	THW	rhTSH	Hypothyroidism	Hyperthyroidism	BAT	p value
N	21	8	9	14	10	
BAT uptake	0	0	0	0	10	
Age (y-o)	61.6 ± 14.9	48.4 ± 14.1	65.8 ± 17.5	50.0 ± 13.3	52.5 ± 22.9	n.s.
Gender (M : F)	7 : 14	4 : 4	4 : 5	6 : 8	2 : 8	n.s.
Body weight (kg)	62.7 ± 14.6	66.6 ± 18.7	50.7 ± 12.6	60.0 ± 18.0	50.1 ± 9.4	n.s.
TSH (μ IU/mL)	50.79 ± 34.54	191.80 ± 73.97	23.02 ± 27.77	0.03 ± 0.04	2.58 ± 2.72	<0.0001
FT3 (pg/mL)	1.54 ± 0.27	2.85 ± 0.33	1.99 ± 0.39	7.11 ± 7.92	2.74 ± 0.11	<0.0001
FT4 (ng/dL)	0.48 ± 0.08	1.29 ± 0.12	0.87 ± 0.28	1.89 ± 1.17	1.22 ± 0.03	<0.0001
T-Chol (mg/dL)	244 ± 44	165 ± 26	156 ± 46	146 ± 41	203 ± 28	<0.0001
Min. temp. of the day (°C)	14.2 ± 8.0	18.0 ± 5.5	19.9 ± 6.3	14.9 ± 8.2	5.1 ± 7.1	<0.01
Max. temp. of the day (°C)	23.0 ± 6.2	25.1 ± 5.0	28.4 ± 4.2	21.9 ± 6.2	13.8 ± 5.5	<0.01
Max. temp. of 1 day before (°C)	23.2 ± 6.3	24.9 ± 3.8	28.6 ± 3.6	21.6 ± 7.6	13.9 ± 4.4	<0.01
Difference temp. (°C)	9.0 ± 3.4	6.9 ± 3.9	8.7 ± 3.4	6.8 ± 4.2	8.8 ± 1.1	n.s.

Data: expressed as mean ± s.d.

(iii) hypothyroidism group: nine images; mean age, 65.8 ± 17.5 years; four males and five females; (iv) hyperthyroidism group: 14 images; mean age, 50.0 ± 13.3 years; six males and eight females; and (v) BAT group: 10 images; mean age 52.5 ± 22.9 years; two males and eight females. A total of 9,273 whole-body FDG-PET/CT imaging study was performed in this study period. Among them, BAT visualization was found in 85 FDG-PET/CT imaging studies (0.92%). Among them 10 out of these 85 imaging studies whose serum TSH, FT3, and FT4 levels were able to be measured were analyzed in this study.

No significant visualization of BAT was noted in any of the images included in the THW, rhTSH, hypothyroidism, and hyperthyroidism groups (Table 1 and Figure 1). Serum TSH level was significantly high in the rhTSH group and significantly low in the hyperthyroidism group. Elevated serum TSH was noted in the THW and hypothyroidism groups. All patients in the BAT group were in a euthyroid state (Table 2). Serum total cholesterol was significantly elevated in the THW group because of hypometabolism caused by hypothyroidism due to TH withdrawal.

Comparisons of BAT-negative and BAT-positive patients are shown in Table 3. The minimum and maximum temperature on the day of the PET study and maximum temperature one day before were significantly lower in BAT-positive patients, whereas there was no difference between maximum temperature one day before and minimum temperature on the day of the PET study.

Representative whole-body maximum intensity projection and FDG-PET/CT axial images of various conditions associated with TH are shown in Figures 1(a)–1(d). A representative case of visualized BAT on a FDG-PET/CT image is shown in Figure 1(e). Patients (a), (b), and (c) had high serum TSH levels at the time of FDG-PET/CT examinations, whereas patient (d) had suppressed serum TSH and patient (e) exhibited a euthyroid state. As FDG-PET/CT imaging of patient (e) was performed to identify the primary tumor site and, for the staging of gastric cancer, a focal increased uptake of FDG was detected in the left upper abdomen showing the

primary site of the gastric cancer. Multiple foci of FDG uptake by BAT were seen in the neck, shoulder, back, and paravertebral regions. However, no abnormal uptake of FDG by a suspected metastatic lesion was detected.

There was also no significant higher glucose uptake in the supraclavicular subcutaneous fat and/or in the skeletal muscle in the hyperthyroidism group compared with the BAT group, as shown in the supplement file.

4. Discussion

TH plays a key role in the regulation of basal metabolic rate and adaptive thermogenesis, both of which have significant impacts on body weight [10]. Adrenergic stimulation is required for adaptive thermogenesis as a result of direct actions on gene regulation and indirectly by stimulation of D2 activity. In BAT, adrenergic signaling through the β 3-adrenergic receptor (β 3-AR) stimulates UCP1 gene expression through the activation of protein kinase A and D2 via deubiquitination and promotes thermogenesis and weight loss. In this metabolic process, FT3 is also required to induce UCP1 gene upregulation [11].

There are several types of iodothyronine deiodinases, including two activating enzymes (D1 and D2) and one inactivating enzyme (D3). D1 is expressed at high levels in the liver, kidney, and thyroid; D2 in the brain, pituitary, thyroid, and BAT; and D3 in the skin and vascular tissue. D2 is the primary enzyme responsible for the rapid increases in intracellular T3 in specific tissues as well as the primary producer of serum T3 in humans [4]. The D2 enzyme has a short half-life due to ubiquitination and subsequent proteasome degradation [12, 13]. Deubiquitination, which increases D2 activity, is stimulated by adrenergic activation or by low levels of serum T4 [14, 15]. D2 is expressed in key TH-responsive tissues, such as the brain, skeletal muscle, and BAT. FT3 is preserved in these tissues as serum FT4 levels decrease. The FT3 generated intracellularly by D2 is transferred to the nucleus for the regulation of gene transcription. D2 activity is critical for the synergism of TH and

TABLE 2: Visualization of BAT on ^{18}F -FDG-PET/CT and related parameters.

#	Gender	Age	Body weight (kg)	Brown fat uptake	TSH ($\mu\text{IU}/\text{mL}$)	FT3 (pg/mL)	FT4 (ng/dL)	T-Chol (mg/dL)	min. temp. of the day ($^{\circ}\text{C}$)	max temp. of the day before ($^{\circ}\text{C}$)	Difference of temp. ($^{\circ}\text{C}$) [*]
(1)	F	29	65.0	negative	77.67	1.26	0.40	237	25	30	5
(2)	F	32	63.9	negative	20.44	1.51	0.40	255	14	19	5
(3)	F	42	48.7	negative	93.51	1.78	0.53	-	17	26	9
(4)	F	49	54.0	negative	124.48	1.60	0.46	287	12	22	10
(5)	M	50	84.0	negative	24.42	1.53	0.52	-	25	31	6
(6)	F	55	91.0	negative	13.43	2.06	0.54	296	12	20	8
(7)	F	56	52.0	negative	67.10	1.69	0.42	239	2	12	10
(8)	F	56	88.7	negative	18.92	1.67	0.46	-	20	26	6
(9)	M	64	64.0	negative	56.75	2.04	0.48	265	12	21	9
(10)	M	65	70.2	negative	64.25	1.64	0.47	175	22	29	7
(11)	F	65	51.6	negative	54.47	1.36	0.44	251	15	25	10
(12)	M	66	67.2	negative	122.54	1.00	0.40	207	-1	18	19
(13)	F	68	57.2	negative	72.49	1.40	0.40	342	14	21	7
(14)	M	68	57.6	negative	8.01	1.63	0.57	-	6	14	8
(15)	F	69	37.7	negative	19.94	1.35	0.56	287	22	34	12
(16)	F	70	47.6	negative	35.78	1.06	0.51	-	3	19	16
(17)	F	72	49.0	negative	58.63	1.58	0.40	225	18	27	9
(18)	M	75	84.2	negative	25.74	1.65	0.65	209	21	28	7
(19)	F	77	68.0	negative	35.08	1.34	0.41	271	25	32	7
(20)	F	78	51.4	negative	10.13	1.44	0.67	200	12	19	7
(21)	M	87	63.7	negative	62.88	1.71	0.49	204	3	14	11
(22)	F	20	53.9	negative	151.24	2.44	1.21	217	15	19	4
(23)	M	41	100.4	negative	87.31	3.20	1.17	147	14	25	11

TABLE 2: Continued.

#	Gender	Age	Body weight (kg)	Brown fat uptake	TSH (μ IU/mL)	FT3 (pg/mL)	FT4 (ng/dL)	T-Chol (mg/dL)	min. temp. of the day ($^{\circ}$ C)	max. temp. of the day before the day ($^{\circ}$ C)	Difference of temp. ($^{\circ}$ C)*
(24)	M	45	51.8	negative	175.22	2.55	1.48	165	20	27	7
(25)	M	47	81.0	negative	158.08	2.85	1.15	155	21	23	2
(26)	F	50	67.0	negative	149.42	3.31	1.27	175	11	24	13
(27)	F	59	78.4	negative	223.90	2.67	1.45	161	25	28	3
(28)	F	60	45.6	negative	281.10	3.14	1.26	217	13	22	9
(29)	M	65	54.8	negative	308.10	2.67	1.34	139	25	31	6
(30)	M	25	43.0	negative	24.83	2.21	0.98	-	23	31	8
(31)	F	56	71.7	negative	5.56	2.11	1.18	256	23	28	5
(32)	M	60	46.1	negative	9.88	2.17	0.94	193	23	30	7
(33)	F	70	45.9	negative	5.26	2.35	0.96	184	6	23	17
(34)	F	70	46.0	negative	3.78	1.56	1.12	136	24	31	7
(35)	M	73	58.8	negative	77.99	1.14	0.40	132	14	23	9
(36)	F	77	37.8	negative	5.07	2.15	0.87	127	21	29	8
(37)	F	78	38.2	negative	12.41	1.98	1.00	131	26	34	8
(38)	M	83	68.7	negative	62.36	2.26	0.40	121	19	28	9
(39)	F	32	46.2	negative	Hyperthyroidism	3.22	1.93	120	6	16	10
(40)	M	33	63.6	negative		4.76	1.67	124	26	30	4
(41)	M	38	49.1	negative		30.00	4.89	161	19	29	10
(42)	M	38	102.5	negative		4.59	0.98	-	-1	9	10

TABLE 2: Continued.

#	Gender	Age	Body weight (kg)	Brown fat uptake	TSH (μ IU/mL)	FT3 (pg/mL)	FT4 (ng/dL)	T-Chol (mg/dL)	min. temp. of the day ($^{\circ}$ C)	max. temp. of the day before the day ($^{\circ}$ C)	Difference of temp. ($^{\circ}$ C)*
(43)	F	39	44.0	negative	0.01	3.33	1.02	-	19	22	3
(44)	F	51	62.4	negative	0.05	3.98	1.74	141	16	20	4
(45)	F	52	83.0	negative	0.01	8.42	2.11	149	3	14	11
(46)	F	52	37.9	negative	0.01	4.41	0.95	94	17	30	13
(47)	F	52	51.2	negative	0.01	3.59	1.42	205	17	28	11
(48)	F	53	81.5	negative	0.01	3.90	1.17	-	25	28	3
(49)	M	54	58.5	negative	0.01	19.72	3.99	107	11	19	8
(50)	M	62	57.0	negative	0.13	2.32	1.34	-	18	18	0
(51)	M	64	59.8	negative	0.01	4.90	2.12	121	9	10	1
(52)	F	80	43.4	negative	0.01	2.38	1.11	210	23	30	7
				BAT							
(53)	F	24	60.6	positive	3.58	2.49	1.07	-	3	13	10
(54)	F	27	35.2	positive	0.48	2.94	1.29	-	0	12	12
(55)	M	27	67.0	positive	1.16	3.55	1.13	211	21	23	2
(56)	F	41	49.7	positive	0.49	3.19	1.25	244	2	9	7
(57)	F	50	50.0	positive	4.88	2.35	1.32	200	6	17	11
(58)	F	50	36.6	positive	1.13	2.45	1.31	168	9	15	6
(59)	F	70	51.8	positive	9.19	2.76	1.30	212	12	18	6
(60)	M	71	50.2	positive	2.55	3.15	0.96	-	-1	11	12
(61)	F	82	50.0	positive	1.16	2.36	1.36	177	0	10	10
(62)	F	83	50.0	positive	1.15	2.12	1.25	175	-1	11	12

* not determined. * Difference of temperature: (max. temp. of the day) ($^{\circ}$ C); normal range of TSH: 0.35–4.94 μ IU/mL, FT3: 1.71–3.71 pg/mL, and FT4: 0.70–1.48 ng/dL, T-Chol: 129–238 mg/dL.

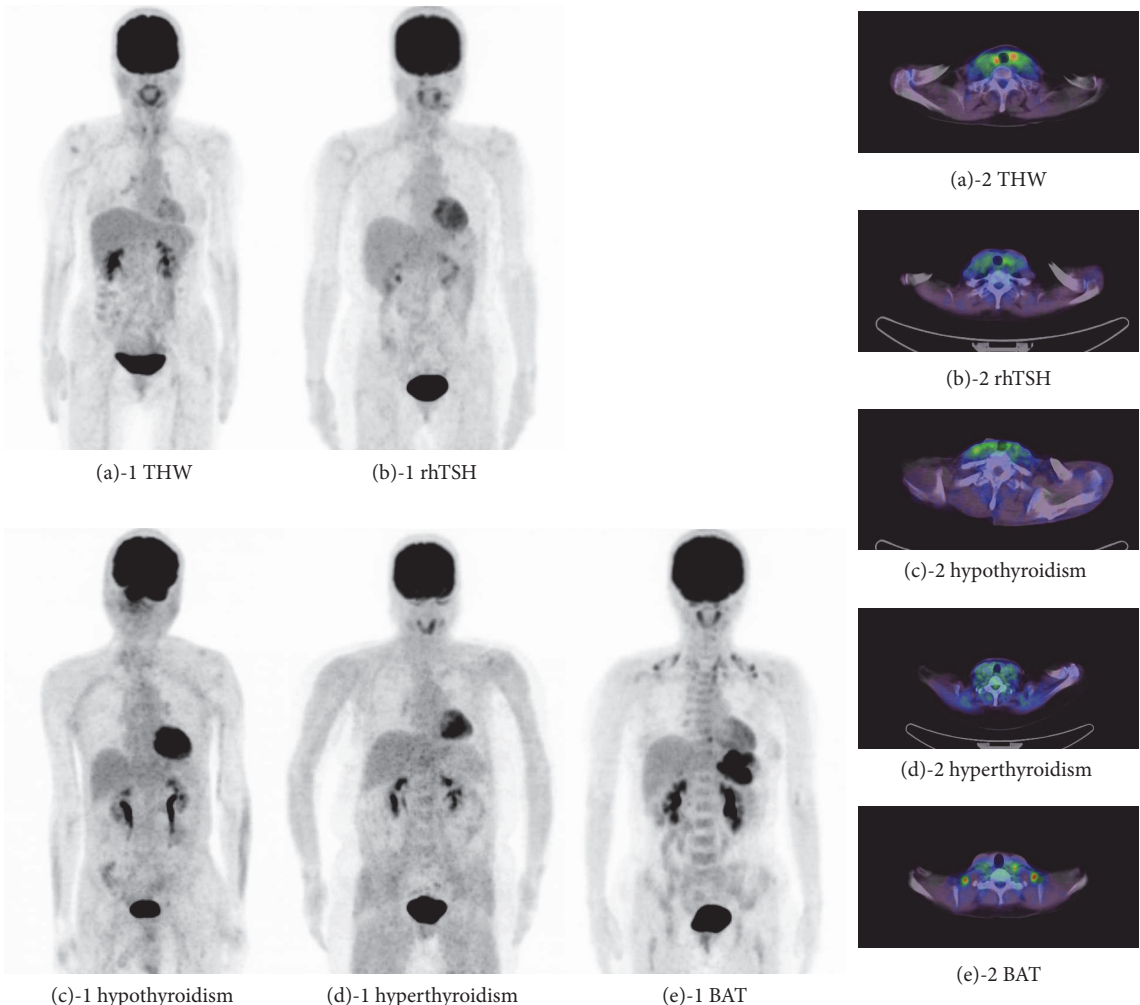


FIGURE 1: Representative whole-body maximum intensity projection and FDG-PET/CT axial images of various conditions associated with TH. Images (a) to (d) were without any uptake of BAT, but (e) showed BAT uptake in the neck, the shoulder, the back, and the paravertebral region. (a) Forty-nine-year-old female who was in THW state before radioiodine therapy (case #(4)); (b) fifty-year-old female who received rhTSH before thyroidal ablation (case #(26)); (c) seventy-three-year-old male who underwent FDG-PET for screening of recurrence after surgery for hypopharyngeal carcinoma (case #(37)); (d) fifty-two-year-old female who had a diagnosis of hyperthyroidism (case #(45)); and (e) forty-one-year-old female who received FDG-PET for gastric cancer (case #(56)).

TABLE 3: Comparison of parameters between BAT negative and BAT positive in this study population.

	BAT negative	BAT positive	<i>p</i> value
<i>N</i>	52	10	
Age (y-o)	57.2 ± 16.0	52.5 ± 22.9	n.s.
Gender (M:F)	21:31	2:8	n.s.
Body weight (kg)	60.5 ± 16.3	50.1 ± 9.4	n.s.
TSH (μ IU/mL)	54.00 ± 72.74	2.58 ± 2.73	n.s.
FT3 (pg/mL)	3.32 ± 4.65	2.74 ± 0.46	n.s.
FT4 (ng/dL)	1.05 ± 0.84	1.22 ± 0.13	n.s.
T-Chol (mg/dL)	189 ± 59	203 ± 28	n.s.
Min. temp. of the day (°C)	16.0 ± 7.6	5.1 ± 7.1	<0.01
Max. temp. of the day (°C)	24.0 ± 6.1	13.8 ± 5.5	<0.01
Max. temp. of 1 day before (°C)	23.7 ± 6.5	13.9 ± 4.4	<0.01
Difference temp. (°C)	8.0 ± 3.8	8.8 ± 3.4	n.s.

Data: expressed as mean \pm s.d.; if p value is less than 0.01, it is as significant; Wilcoxon rank-sum χ^2 -square test.

signaling for the regulation of thermogenesis in BAT [16]. Forty years ago, Doniach proposed a possible mechanism for the stimulation of thermogenesis in BAT by TSH [6]. Furthermore, a more recent mouse study demonstrated that D2 was essential for thyroid-sympathetic synergism required for thermal homeostasis in BAT, and the deletion of the TSH receptor resulted in impaired BAT thermogenesis [5]. In an FDG-PET imaging study of mice, Jeanguillaume et al. confirmed that increased glucose uptake in fat is, generally, an indication of the presence of UCP1-positive BAT [3].

TSH increases basal and FT3-stimulated UCP1 and Dio2 expression as well as D2 activity. TSH can increase basal UCP1 levels, which is synergized by the effect of T3 on UCP1 [17]. In this study, the authors also proposed TSH activity as an alternative pathway in thermogenesis regulation by BAT. Endo and Kobayashi reported that TSH was involved in the regulation of UCP1 expression and thermogenesis in BAT to protect against a further decrease in body temperature in a mouse hypothyroid model [7].

Although several reports have discussed the correlation between serum TH levels and the visualization of BAT on FDG-PET or PET/CT, there is no definite consensus on this association. Lahesmaa et al. evaluated 10 patients with hyperthyroidism and healthy and euthyroid individuals by FDG-PET and found greater glucose uptake in BAT of hyperthyroid patients than that of controls [8]. On the other hand, a recently published controversial report claims that nine of 10 study subjects with Graves' disease had no detectable active BAT on FDG-PET/CT [18]. This group also reported significantly lower FT3 and FT4 levels in 75 BAT-positive subjects than in BAT-negative subjects and proposed the lower levels of TH needed for higher BAT thermogenesis as a possible cause. Furthermore, there is a recent case report about BAT visualization on FDG-PET/CT in severe primary hypothyroidism that suggested a potential role of TSH and TRH as regulators of BAT activation [19].

In radioiodine therapy (RIT) for metastasis after total thyroidectomy for differentiated thyroid carcinoma, patients were instructed to adhere to a low-iodine diet and discontinue TH supplementation for at least 2-3 weeks before RIT so that the patients would tend to exhibit temporary hypothyroidism (low FT3 and FT4 and elevated TSH). In thyroidal ablation therapy after total thyroidectomy for differentiated thyroid carcinoma, patients were instructed to adhere to a low-iodine diet and received injections of rhTSH 1 and 2 days before RIT instead of TH withdrawal to temporally elevate serum TSH. FT3 and FT4 levels tended to be within the normal range in most patients who underwent thyroidal ablation because of continuous TH replacement, as in this study. Our results showed that temporarily or continuously elevated TSH did not have a significant influence on BAT visualization on whole-body FDG-PET/CT imaging. In addition, we found that suppression of serum TSH in the hyperthyroidism group had no significant effect on the visualization of activated BAT on FDG-PET/CT imaging. Only temperature either on the day on or the day before FDG-PET/CT imaging was a significant parameter impacting the visualization of BAT, as described before [20-24].

In the current study, the small number of subjects and the lack of a cooling protocol to stimulate BAT group were major study limitations. Since this study was a retrospective one, it was not easy to register enrollees who confirmed serum TSH, FT3, and FT4 in the BAT group. Further studies with prospective design and basic research might be needed to clarify the association between BAT visualization and thyroid hormones.

In summary, we investigated the influence of TH on the visualization of activated BAT on FDG-PET/CT images of patients with various conditions. Although TH was considered to be associated with thermogenesis through UCP1 gene expression and D2 in BAT, elevated TSH status before RIT, hyperthyroidism, or hypothyroidism did not significantly impact BAT visualization and the interpretation of clinical FDG-PET/CT images.

Disclosure

The manuscript was presented as an abstract in the following link. http://jnm.snmjournals.org/content/57/supplement_2/44.short

Conflicts of Interest

The authors declare that they have no conflicts of interest regarding the publication of this article.

Supplementary Materials

Supplementary 1. Whole-body maximum intensity projection images of FDG-PET/CT of the hyperthyroidism group. Each image corresponds to patients #(39)–#(52) of Table 2.

Supplementary 2. Whole-body maximum intensity projection images of FDG-PET/CT of the BAT group. Each image corresponds to patients #(53)–#(62) of Table 2.

References

- [1] T. D. Poeppel, B. J. Krause, T. A. Heusner, C. Boy, A. Bockisch, and G. Antoch, "PET/CT for the staging and follow-up of patients with malignancies," *European Journal of Radiology*, vol. 70, no. 3, pp. 382–392, 2009.
- [2] H. Sacks and M. E. Symonds, "Anatomical locations of human brown adipose tissue: Functional relevance and implications in obesity and type 2 diabetes," *Diabetes*, vol. 62, no. 6, pp. 1783–1790, 2013.
- [3] C. Jeanguillaume, G. Metrard, D. Ricquier et al., "Visualization of Activated BAT in Mice, with FDG-PET and Its Relation to UCP1," *Advances in Molecular Imaging*, vol. 03, no. 03, pp. 19–22, 2013.
- [4] A. L. Maia, B. W. Kim, S. A. Huang, J. W. Harney, and P. R. Larsen, "Type 2 iodothyronine deiodinase is the major source of plasma T3 in euthyroid humans," *The Journal of Clinical Investigation*, vol. 115, no. 9, pp. 2524–2533, 2005.
- [5] L. A. De Jesus, S. D. Carvalho, M. O. Ribeiro et al., "The type 2 iodothyronine deiodinase is essential for adaptive thermogenesis in brown adipose tissue," *The Journal of Clinical Investigation*, vol. 108, no. 9, pp. 1379–1385, 2001.

- [6] D. Doniach, "Possible stimulation of thermogenesis in brown adipose tissue by thyroid-stimulating hormone," *The Lancet*, vol. 306, no. 7926, pp. 160-161, 1975.
- [7] T. Endo and T. Kobayashi, "Thyroid-stimulating hormone receptor in brown adipose tissue is involved in the regulation of thermogenesis," *American Journal of Physiology-Endocrinology and Metabolism*, vol. 295, no. 2, pp. E514-E518, 2008.
- [8] M. Lahesmaa, J. Orava, C. Schalin-Jäntti et al., "Hyperthyroidism increases brown fat metabolism in humans," *The Journal of Clinical Endocrinology & Metabolism*, vol. 99, no. 1, pp. E28-E35, 2014.
- [9] R. M. Connolly, J. P. Leal, M. P. Goetz et al., "TBCRC 008: Early change in 18F-FDG uptake on PET predicts response to pre-operative systemic therapy in human epidermal growth factor receptor 2-negative primary operable breast cancer," *Journal of Nuclear Medicine*, vol. 56, no. 1, pp. 31-37, 2015.
- [10] D. G. Nicholls and R. M. Locke, "Thermogenic mechanisms in brown fat," *Physiological Reviews*, vol. 64, no. 1, pp. 1-64, 1984.
- [11] R. Mullur, Y.-Y. Liu, and G. A. Brent, "Thyroid hormone regulation of metabolism," *Physiological Reviews*, vol. 94, no. 2, pp. 355-382, 2014.
- [12] R. Arrojo E Drigo and A. C. Bianco, "Type 2 deiodinase at the crossroads of thyroid hormone action," *The International Journal of Biochemistry & Cell Biology*, vol. 43, no. 10, pp. 1432-1441, 2011.
- [13] B. Gereben, A. M. Zavacki, S. Ribich et al., "Cellular and molecular basis of deiodinase-regulated thyroid hormone signaling," *Endocrine Reviews*, vol. 29, no. 7, pp. 898-938, 2008.
- [14] B. Gereben, A. Zeöld, M. Dentice, D. Salvatore, and A. C. Bianco, "Activation and inactivation of thyroid hormone by deiodinases: Local action with general consequences," *Cellular and Molecular Life Sciences*, vol. 65, no. 4, pp. 570-590, 2008.
- [15] G. D. V. Sagar, B. Gereben, I. Callebaut et al., "Ubiquitination-induced conformational change within the deiodinase dimer is a switch regulating enzyme activity," *Molecular and Cellular Biology*, vol. 27, no. 13, pp. 4774-4783, 2007.
- [16] J. E. Silva and S. D. C. Bianco, "Thyroid-adrenergic interactions: Physiological and clinical implications," *Thyroid*, vol. 18, no. 2, pp. 157-165, 2008.
- [17] R. Martinez-deMena, A. Anedda, S. Cadena, and M.-J. Obregon, "TSH effects on thermogenesis in rat brown adipocytes," *Molecular and Cellular Endocrinology*, vol. 404, pp. 151-158, 2015.
- [18] Q. Zhang, Q. Miao, H. Ye et al., "The effects of thyroid hormones on brown adipose tissue in humans: A PET-CT study," *Diabetes/Metabolism Research and Reviews*, vol. 30, no. 6, pp. 513-520, 2014.
- [19] M. S. Kim, H. H. Hu, P. C. Aggabao, M. E. Geffner, and V. Gil-sanz, "Presence of brown adipose tissue in an adolescent with severe primary hypothyroidism," *The Journal of Clinical Endocrinology & Metabolism*, vol. 99, no. 9, pp. E1686-E1690, 2014.
- [20] A. A. J. van der Lans, R. Wierts, M. J. Vosselman, P. Schrauwen, B. Brans, and W. D. van Marken Lichtenbelt, "Cold-activated brown adipose tissue in human adults: Methodological issues," *American Journal of Physiology-Regulatory, Integrative and Comparative Physiology*, vol. 307, no. 2, pp. R103-R113, 2014.
- [21] A. Skillen, G. M. Currie, and J. M. Wheat, "Thermal control of brown adipose tissue in 18F-FDG PET," *Journal of Nuclear Medicine Technology*, vol. 40, no. 2, pp. 99-103, 2012.
- [22] M. Saito, Y. Okamatsu-Ogura, and M. Matsushita, "High incidence of metabolically active brown adipose tissue in healthy adult humans: effects of cold exposure and adiposity," *Diabetes*, vol. 58, no. 7, pp. 1526-1531, 2009.
- [23] C. Cohade, K. A. Mountzikos, and R. L. Wahl, "'USA-Fat': prevalence is related to ambient outdoor temperature—evaluation with 18F-FDG PET/CT," *Journal of Nuclear Medicine*, vol. 44, no. 8, pp. 1267-1270, 2003.
- [24] N. J. Rothwell and M. J. Stock, "Influence of environmental temperature on energy balance, diet-induced thermogenesis and brown fat activity in 'cafeteria'-fed rats," *British Journal of Nutrition*, vol. 56, no. 01, p. 123, 1986.

Research Article

Study of the Influence of Age in ^{18}F -FDG PET Images Using a Data-Driven Approach and Its Evaluation in Alzheimer's Disease

Jiehui Jiang,¹ Yiwu Sun ,¹ Hucheng Zhou ,¹ Shaoping Li ,¹ Zhemin Huang,² Ping Wu,² Kuangyu Shi ,³ Chuantao Zuo ,^{2,4} and Alzheimer's Disease Neuroimaging Initiative

¹*Shanghai Institute for Advanced Communication and Data Science, Shanghai University, Shanghai, China*

²*PET Center, Huashan Hospital, Fudan University, Shanghai, China*

³*Department of Nuclear Medicine, Technische Universität München, Munich, Germany*

⁴*Institute of Functional and Molecular Medical Imaging, Fudan University, Shanghai, China*

Correspondence should be addressed to Chuantao Zuo; 18939922532@163.com

Received 24 August 2017; Revised 18 November 2017; Accepted 18 December 2017; Published 8 February 2018

Academic Editor: Jie Lu

Copyright © 2018 Jiehui Jiang et al. This is an open access article distributed under the Creative Commons Attribution License, which permits unrestricted use, distribution, and reproduction in any medium, provided the original work is properly cited.

Objectives. ^{18}F -FDG PET scan is one of the most frequently used neural imaging scans. However, the influence of age has proven to be the greatest interfering factor for many clinical dementia diagnoses when analyzing ^{18}F -FDG PET images, since radiologists encounter difficulties when deciding whether the abnormalities in specific regions correlate with normal aging, disease, or both. In the present paper, the authors aimed to define specific brain regions and determine an age-correction mathematical model. **Methods.** A data-driven approach was used based on 255 healthy subjects. **Results.** The inferior frontal gyrus, the left medial part and the left medial orbital part of superior frontal gyrus, the right insula, the left anterior cingulate, the left median cingulate, and paracingulate gyri, and bilateral superior temporal gyri were found to have a strong negative correlation with age. For evaluation, an age-correction model was applied to 262 healthy subjects and 50 AD subjects selected from the ADNI database, and partial correlations between SUVR mean and three clinical results were carried out before and after age correction. **Conclusion.** All correlation coefficients were significantly improved after the age correction. The proposed model was effective in the age correction of both healthy and AD subjects.

1. Introduction

The influence of age has been proven to be the greatest interfering factor for many clinical dementia diagnoses [1]. For Alzheimer's disease (AD), the most common (60%–70%) form of chronic neurodegenerative dementia in the elderly [2], advanced age is commonly associated with adverse changes in the brain that are reflected in different imaging modalities such as magnetic resonance imaging (MRI), functional MRI (fMRI), and positron emission tomography (PET) [3–6]. Thus, it is important for clinics to eliminate the influence of age in order to determine whether the abnormalities in specific regions correlate with normal aging, disease or both. For instance, several research studies have reported that the grey matter volume and cortical thickness within

certain regions-of-interest (ROIs) such as the hippocampus, the inferior frontal, superior frontal, middle frontal, and temporal cortices decreased with aging, based on the findings of structural magnetic resonance imaging (MRI) [7–10]. The amyloid β level, as measured by the standardized uptake value ratio (SUVR) in ^{11}C -Pittsburgh Compound B (PiB) PET scans was found to increase abnormally after the age of 70 in apolipoprotein E (APOE) $\epsilon 4$ Genotype carriers [11]. The important parameter of fractional anisotropy (FA, a measure of the degree of anisotropy of a diffusion process) was found to exhibit a negative linear correlation with age in most white matter regions, in particular in the superior corona radiata [7].

Currently, ^{18}F -Fluorodeoxyglucose (FDG) PET is regarded as a "Gold Standard" for AD diagnosis, since its predictive

value enables detection of abnormal cerebral metabolism during the earliest stages of dementia or even before the dementia is present [4, 12–14]. It is a major challenge for radiologists to eliminate the influence of age from ^{18}F -FDG PET images. For this purpose, a few research groups have investigated the manner in which age-influenced brain metabolism occurs and within which brain regions. For example, strong negative correlations were found between metabolism and normal aging mainly in the frontal and temporal lobes [15–22], suggesting that tissue shrinkage or loss and glucose metabolism reduction could be accelerated by normal aging. In other studies [23–25], regions within a default mode network (DMN) including the temporal, parietal, and prefrontal areas and the posterior cingulate cortex were found to be significantly reduced with age. In view of these findings, it is reasonable to suggest that image intensity of certain regions, especially the prefrontal and temporal areas, may exhibit double the effect of normal aging.

More specifically, in [26], the authors applied an age-correction criterion [27] based on the results of the Montreal Cognitive Assessment (MoCA) according to the circumstance that predetermined the age range of the patient. Similar criteria can be found in [28]. Although these corrections were not based directly on brain images, the line of thought was illuminating. Subsequently, [29] using MRI, a simple linear model was proposed to correct the effect of age on grey matter (GM) voxel values by determining a regression coefficient β_C between age and each voxel coordinate of the separate healthy control group. This β_C value indicated the declination speed of the corresponding voxel with increasing age. The same model was used for the MRI GM voxel values and the ^{18}F -FDG PET intensity values by [14]. Moreover, as proposed in previous studies, it was unnecessary to apply the linear correction model to all the voxels within the images, because not all regions correlated significantly with age [17, 19–21]. However, there have been a lack of studies investigating the exact brain regions in ^{18}F -FDG PET images that have negative relationships with age, and these have defined any age-correction mathematical models.

Therefore, the present study aimed to (1) use a data-driven method to explore brain regions that have a strong negative linear relationship with age in ^{18}F -FDG PET images and to then define an age-correction mathematical model. Subsequently, the intent was to (2) validate those brain regions and the mathematical model using statistical analysis on both healthy and AD subjects.

2. Materials and Methods

2.1. Datasets. The two datasets used in this study were as follows: (1) 255 healthy control ^{18}F -FDG PET images were from Huashan Hospital, Fudan University, Shanghai, China; (2) 262 healthy control and 50 AD ^{18}F -FDG PET images were selected from Alzheimer's Disease Neuroimaging Initiative (ADNI).

For the first dataset, data collection was approved by the Medical Ethics Committee of Huashan Hospital, Fudan University, Shanghai, China. All subjects signed agreements

to participate in this study. The sample group was comprised of 127 female and 128 male healthy subjects (ages: 20–79), who had no current axis I psychiatric disorder, no psychotropic medication use or hormone use within the prior 6 months, and no history of head injury or alcohol abuse. These subjects received brain ^{18}F -FDG PET scans. No occult ^{18}F -FDG-avid carcinoma was determined in any of the included subjects, based on the brain PET examination. Blood glucose levels were monitored prior to ^{18}F -FDG injection (5.5 ± 0.8 mm for males and 5.3 ± 0.9 mm for females).

The 131 male and 131 female healthy subjects (age: 56.5–80) were selected from the ADNI database. Furthermore, the 25 male and 25 female AD subjects (ages: 59.3–79.8) were also selected from the ADNI database. Table 1 shows the basic information for the datasets.

2.2. Image Acquisition. All subjects who underwent ^{18}F -FDG PET brain scans at Huashan Hospital were in a resting state. The ^{18}F -FDG PET whole-body scans followed the brain scans in case of these subjects (1.5 min/bed, 5 beds). A 222–296 MBq injection of ^{18}F -FDG was administered intravenously under standardized conditions (in a quiet, dimly lit room with the patient's eyes open). A 10 min 3-dimensional brain emission scan was acquired at 45 min after injection with a state-of-the-art PET scanner (Siemens Biograph 64 HD PET/CT, Siemens, Germany). During the scanning procedure, the subjects' heads were immobilized using a head holder. Attenuation correction was performed using a low-dose CT (150 mAs, 120 kV, Acq. 64×0.6 mm) prior to the emission scan. Following corrections for scatter, dead time, and random coincidences, PET images were reconstructed by 3-dimensional filtered backprojection and a Gaussian Filter (FWHM 3.5 mm), providing 64 contiguous transaxial slices of 5 mm thick spacing.

For images downloaded from the ADNI database, detailed information regarding the data acquisition protocol is publicly available on the LONI website (<https://ida.loni.usc.edu/login.jsp>). Briefly, PET images from the ADNI database were acquired from a variety of scanners nationwide using either a 30-minute six frame scan or a static 30-minute single frame scan, both acquired 30–60 minutes after injection. For the former case, the dynamic scans were coregistered with the first frame and averaged to create a single average image.

2.3. Image Preprocessing. The aim of preprocessing was to remove unwanted distortions such as low-frequency background noise, to spatially normalize the images into a standard space defined by template images and to enhance important image features prior to further computational processing. In the present study, all of the images were preprocessed using Statistical Parametric Mapping 8 (SPM8), a Statistical Parametric Mapping software package designed for the analysis of brain imaging data sequences (<http://www.fil.ion.ucl.ac.uk/spm/software/spm8/>), implemented in MATLAB R2014a. The preprocessing was mainly composed of normalization and smoothing. The details of image preprocessing can be found in the following paragraph.

TABLE 1: Demographic data and cognitive performance of the datasets.

Parameter	Healthy (<i>n</i> = 255)	ADNI healthy (<i>n</i> = 262)	ADNI AD (<i>n</i> = 50)
Demographic data			
Age (years)	49.2 ± 16.7	72.9 ± 4.5	73.1 ± 5.6
Age grades			
20–30	44	-	-
31–40	44	-	-
41–50	42	-	-
51–60	45	3	3
61–70	50	80	10
71–80	30	179	37
Sex (M/F)	128/127	131/131	25/25
EDU	-	16.3 ± 2.7	15.1 ± 3.0
ApoE4	-	0.3 ± 0.5	1.0 ± 0.7
Clinical scales			
MMSE	-	29.0 ± 1.2	23.2 ± 2.0
CDRSB	-	0.0 ± 0.2	4.1 ± 1.3
FDG-PET			
FDG	-	1.3 ± 0.1	1.1 ± 0.1

EDU: education; MMSE: minimental state exam; CDRSB: clinical dementia rating sum of boxes; FDG: average FDG-PET of angular, temporal, and posterior cingulate.

All original DICOM images from each subject were combined into one NIfTI format file using a tool in MRIcron called DCM2NII (available at <http://people.cs.sc.edu/rorden/mricron/index.html>). For each subject, the PET image was first normalized to the Montreal Neurological Institute (MNI, McGill University, Montreal, Canada) space through the “Normalize: Estimate and Write” methodology. During this step, a reference PET template provided by SPM software was used as the standard space. The nonlinear warping normalization was carried out automatically following determination of the optimum 12-parameter affine transformation. Subsequently, the normalized images prefixed with a “w” were smoothed using an isotropic Gaussian smoothing kernel with the full-width at half maximum (FWHM) of 10 × 10 × 10 mm³. Thus, the images’ noise-signal ratio can be improved by these standardized processing steps. The resulting images had 91 × 109 × 91 voxels with a voxel size of 2 × 2 × 2 mm³. Next, the preprocessed FDG PET 3D images were concatenated to one 4D image file using the DCM2NII tool in preparation for the following data analysis.

2.4. Exploration of Brain Regions Displaying Negative Relationships with Age. To explore brain regions with negative relationships with age, three steps were used in this section: (1) A data-driven method, Functional MRI of the Brain’s (FMRIB’s) Linked Independent Component Analysis (FLICA), was used to obtain an indication of the initial brain regions that had a strong negative relationship with age. (2) To obtain a more accurate indication of age-related brain regions, different thresholds of voxel values were set and compared correlations between SUVR mean and age using Pearson correlation. (3) Optimized brain regions were defined after the application of suitable threshold voxel values.

2.4.1. Exploration of the Initial Age-Related Brain Regions Using FLICA. To define initial brain regions, a data-driven approach—FLICA—was used. Independent component analysis (ICA) is a computational model for separating a multivariate signal into additive subcomponents. Applied in the spatial dimension, it is efficient for finding meaningful and spatially independent components by assuming that the subcomponents are non-Gaussian distributed spatial sources and thus they are likely to represent real underlying structured features in the dataset. This is because, during linear mixing processes, it is likely that the non-Gaussian independent sources can turn into more Gaussian observed signals. Consequently, seeking non-Gaussian sources can be an unsupervised means of revealing the original independent sources.

FLICA is an advanced independent component analysis (ICA) approach implemented in FSL running as a MATLAB toolbox in the Linux system [30, 31]. FLICA is an entirely data-driven approach that can comodel multiple imaging modalities. Its main goal is to model the imaging data as a set of interpretable features (independent components), most of which characterize biophysically plausible modes of variability across all of the subjects’ images. Unlike in a principal component analysis, the mixing matrix vectors of an ICA are not forced to be orthogonal to each other and thus can explain common variance of variables external to the ICA, such as age [32]. Linked ICA has also been implemented in age studies in earlier papers [32, 33]. (<https://fsl.fmrib.ox.ac.uk/fsl/fslwiki/FLICA>).

In the present study, the dataset from Huashan Hospital was analyzed using FLICA, which was run totally on MATLAB R2014a installed in a Linux environment. The comprehensive library of analysis tools for brain imaging

TABLE 2: Information obtained from an IC output by FLICA.

Parameters	Meaning	Utility in this study
IC value	IC value: representing the weight of each subject's intensity explained by the corresponding IC	Used to find out the IC that has the strongest negative relationship with age (see results in Section 3.1.1)
SI	Spatial information: representing the regions that correspond to each IC (Figure 1)	Used to define initial brain regions
VV	Voxel value: the probability operation results of each voxel within the regions of IC (Figure 1)	-
σ	The thresholds of VV	Used to determine the more accurate age-related regions (see details in Section 2.4.2)

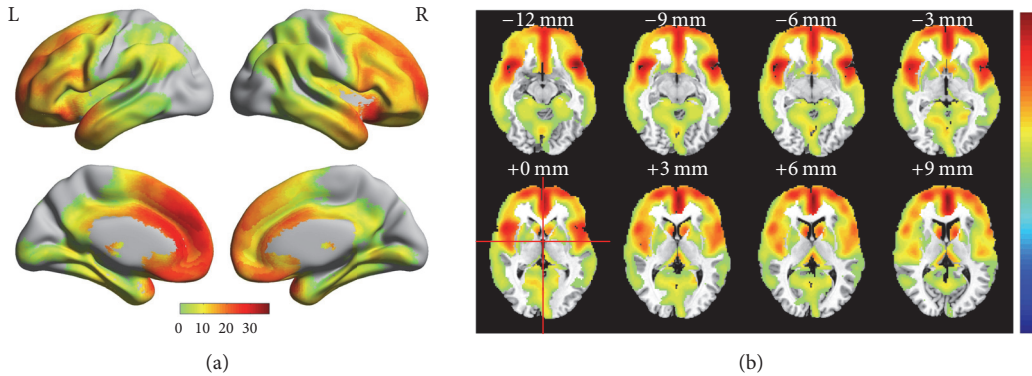


FIGURE 1: Anatomic structure of the brain regions corresponding to the significant age-related IC3 (pseudocolor) obtained across all 255 healthy subjects.

data, FSL, was also required for the procedure. The combined 4D image file was converted to a readable format in FSL (*.nii.gz) by the DCM2NII tool. Following data preparation and creation of the environmental variables and options, the analysis was run with all automatic calculations. When finished, the output was saved safely, including a set of independent components, in a sensible order (either in the order of total energy or to match with a previous similar run), with the relevant spatial maps.

The independent components (ICs) output from FLICA contained three types of information: IC values, spatial information, and voxel values (see Table 2). The IC values were represented as an $M \times N$ matrix where M is the number of the subjects and N is the number of ICs obtained. The spatial information (SI) and corresponding voxel values (VV) of the ICs were combined in a 4D nii formatted file that could be opened and viewed as a common brain image where voxel values can be displayed in pseudocolor (Figure 1). Note that the voxel value is the probability operation result of the coordinate of each voxel. That is, the possibility of the region having a strong relationship with age becomes larger as the voxel values of the corresponding coordinates become larger. Hence, an appropriate threshold of VV, σ , is required to be defined in order to obtain an accurate indication of affected brain regions.

2.4.2. Further Exploration of the Final Age-Related Brain Regions by Defining σ .

Three steps were used to achieve appropriate values of σ :

- (I) Extraction of initial brain regions: for 255 image data from Huashan Hospital, SI corresponding to the IC was extracted as initial brain regions using the Automatic Anatomical Labelling (AAL) template in the Montreal Neurological Institute (MNI) standard space.
- (II) Definition of σ : the initial brain regions were then optimized by setting different thresholds for σ . In particular, σ was set to start as 1 and end as the maximal voxel value, X . To generate an optimized brain region mask for each σ separately, all voxels whose values were no less than σ were set as 1 and others as 0. Next, data from the 255 healthy subjects were utilized to calculate SUVR mean [34] of the targeted brain regions generated with different σ , by using the paracentral lobule (AAL 69 and AAL 70) as the reference regions [35]. The formula to form SUVR mean is [34]

$$\text{SUVR mean} = \frac{I_{\text{avg_ROI}}}{I_{\text{avg_ref}}}, \quad (1)$$

where $I_{\text{avg,ROIC}}$ is the average intensity of the brain regions and $I_{\text{avg,ref}}$ is the average intensity of the reference region.

(III) Comparison experiments: subsequently, Pearson correlation [36] was used to analyze correlations between age and SUVR mean under different σ and the most appropriate σ was selected to achieve the strongest correlations. In order to reduce the influence of accidental factors to a minimum, 250 subjects were selected randomly from a total of 255 subjects for 3,000 times and the Pearson correlation analysis was carried out separately on these data. The statistical results, including the correlation coefficients R and p values, were taken as an average of the 3,000 results.

2.5. Definition of the Age-Correction Mathematical Model. With an appropriate σ , Pearson correlation analysis was carried out again on the same 255 healthy subjects in order to obtain the linear coefficient β_C . The entire process was as follows:

(I) The linear regression coefficient β_C between age and the corresponding set of SUVR means was calculated. Thus, the development of SUVR mean during normal aging can be described as

$$\text{SUVR mean} = \beta_C \times \text{age} + p_2. \quad (2)$$

(II) Similar to Section 2.4.1, the linear regression process was repeated for 3,000 times and the β_C value was taken as an average of the 3,000 results.

(III) Finally, to carry out the age correction, a model similar to the one proposed in [29] was defined, and the amount (Δ) assumed to have been affected by the subject's age since birth (i.e., aged 0) was calculated:

$$\Delta = Y(\text{age}_{\text{subject}}) - Y(\text{age}_0) = \beta_C \times \text{age}. \quad (3)$$

Then the target index was then corrected by subtracting this amount, as follows:

$$\text{Index}_{\text{cor}} = \text{Index}_{\text{tar}} - \Delta. \quad (4)$$

2.6. Evaluation of the Brain Regions and Age-Correction Mathematical Model. To validate the effectiveness of the brain regions and age-correction mathematical model defined in the present study, they were evaluated using another dataset that included 262 healthy subjects and 50 AD subjects from the ADNI. These two datasets were firstly preprocessed using the same approach as in Section 2.3. Following preprocessing, the evaluation was composed of four tests.

(I) In the first test, using 262 healthy subjects, the correlations were calculated between age and SUVR mean in the final brain regions from Section 2.4.2. It was verified whether negative relationships between age and SUVR means also occurred in the new dataset. Pearson correlation analysis was used in this test.

(II) In the second test, 262 healthy subjects were used to test the effectiveness of the age-correction mathematical model. Pearson correlation analysis was also used to compare negative relationships between age and SUVR means before and after correction. As expected, the relationships should be weaker after correlation and the slope should be flat.

(III) In the third test, to visualize the changes before and after corrections, a case study with one healthy and one AD subject was evaluated.

(IV) In the fourth test, to verify whether the age-correction mathematical model can be used for clinical purposes, 50 AD subjects from ADNI were tested. Partial correlation analyses were made between SUVR means and the outcomes of the two clinical scales, MMSE and CDRSB, and an imaging index, FDG (Table 1), and the results of the analyses were compared. During the partial analyses, the effects of education, sex, and ApoE4 status were removed as a set of controlled variables.

(V) In the final test, to verify whether the diagnostic accuracy of AD increased after the age correction in these 50 subjects, we performed principal component analysis (PCA) to extract image features and support vector machine (SVM) for AD classification. For simplification, linear kernel was used for SVM. 50 age-matched healthy subjects were selected from the 262 healthy subjects, and classification was carried out on these altogether 100 subjects before and after the age correction, respectively. The results are represented as the classification accuracy and ROC curves.

3. Results

3.1. Exploration of Brain Regions Displaying Negative Relationships with Age

3.1.1. Exploration of the Initial Age-Related Brain Regions Using FLICA. A total of 29 ICs were obtained from the FLICA blind tests for any other demographics or cognitive factors of the participants. According to the purpose of the present study, there were 10 statistically significant components ($p < 0.05$), as shown in Figure 2. Amongst these, only the third component (IC3) revealed a monotone linear decrease with increasing age (although assessed using a quadratic fit) with a clear practical significance ($R^2 = 0.518$, $p = 1 \times 10^{-40}$). R squared values for all other components were below 0.3. In the present study, both linear and quadratic fits were used to assess the relationship between IC values and age. As a result, the statistics of the quadratic fits were generally better than those of the linear fits. Furthermore, the curves of IC3 plotted with a linear fit and a quadratic fit, respectively, virtually coincide with each other. Thus, only results of quadratic fits are presented here. Moreover, the statistical results (quadratic fits) between the ICs and age in the 6 age groups of the 255 subjects are shown in Table 3. Amongst these, the subgroups of age 51–60 and 61–70 reached

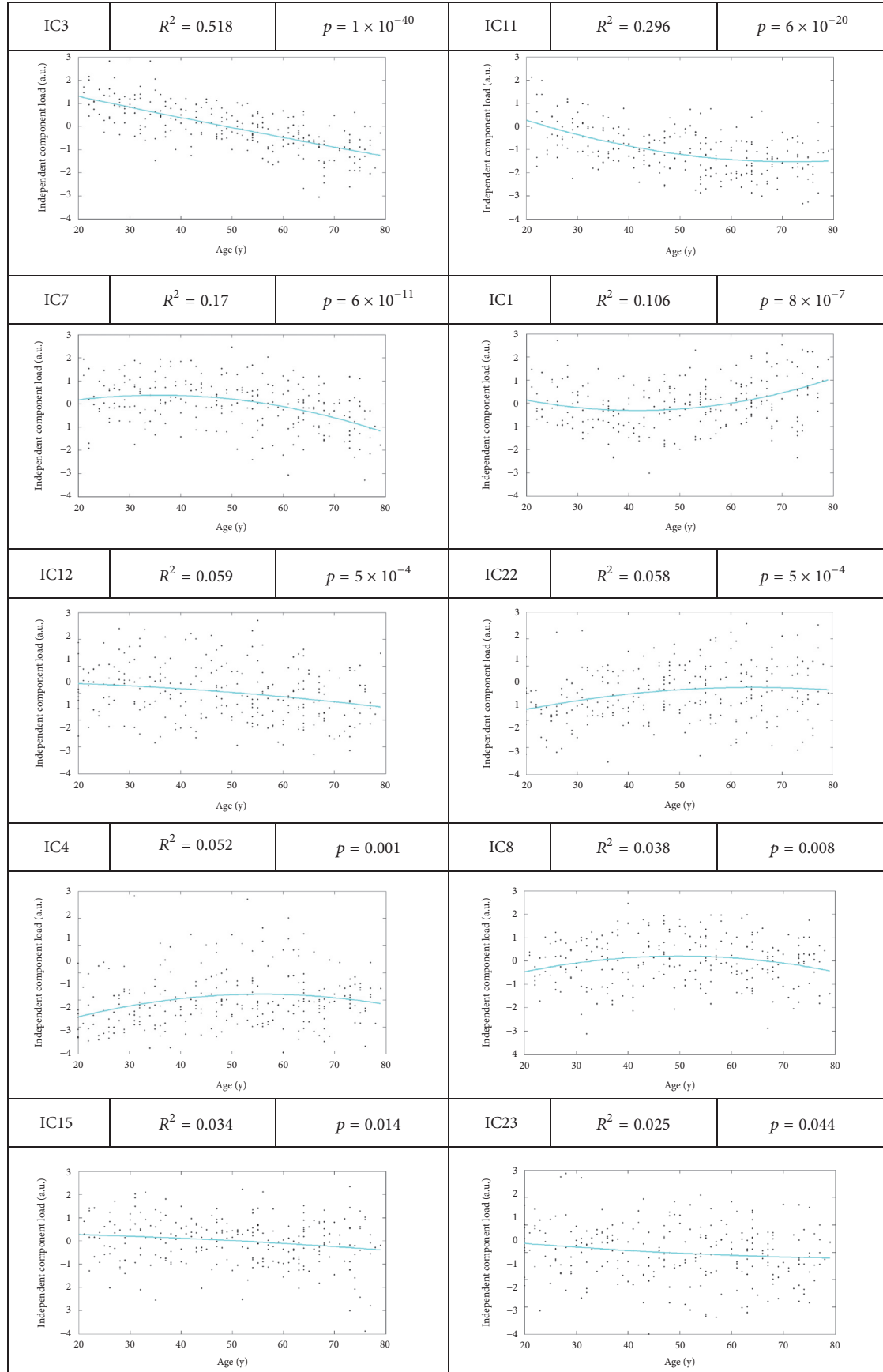


FIGURE 2: Plots of the post hoc relationship between the ICs and age.

TABLE 3: Statistical results (quadratic fits) between IC3 and age in the 6 age groups of the 255 subjects.

	Subgroup			Cumulation		
	Number	p	R	Number	p	R
20–30	44	0.077	0.117	20–30	44	0.077
31–40	44	0.672	0.019	20–40	88	2.49E–04
41–50	42	0.317	0.057	20–50	130	1.11E–09
51–60	45	0.032	0.151	20–60	175	4.37E–18
61–70	50	0.01	0.179	20–70	225	1.56E–31
71–80	30	0.71	0.026	20–80	255	1.22E–40

statistical significance ($p < 0.05$), while from the perspective of cumulation, the correlation reached statistical significance from the second age group 20–40.

Spatially, IC3 covered the regions encompassing: Frontal_Mid, Frontal_Med_Orb, Cingulum_Ant, Cingulum_Post, Parietal_Inf, Temporal_Mid, Temporal_Inf, Frontal_Sup, Frontal_Sup_Orb, Frontal_Mid_Orb, Frontal_Inf_Oper, Frontal_Inf_Tri, Frontal_Inf_Orb, Insula, Cingulum_Ant, Hippocampus, ParaHippocampal, Lingual, Fusiform, Caudate, Temporal_Sup, Temporal_Pole_Sup, and Temporal_Mid (all coordinating with the AAL template within the MNI standard space). The anatomic structure of these regions is shown in Figure 1.

The anatomic structure of the brain regions corresponding to the significant age-related IC3 degradation is illustrated in Figure 1. The voxel values ranged from 1 to 38. The total voxel volume was 128271. Figure 1(a) was visualized using the BrainNet Viewer package (<https://www.nitrc.org/projects/bnv/>). Figure 1(b) was visualized using the RESTplus toolkit (<http://restfmri.net/forum/index.php?q=rest>).

3.1.2. Further Exploration of the Final Age-Related Brain Regions by Defining σ . The automatic results from FLICA showed that IC3 totally contained 128271 voxels, with voxel values ranging from 1 to 38. The cumulative distribution of the 38 voxel values is shown in Figure 3. It can be observed that voxels with values of 1 to 9 occupied more than 50% of the IC3 region. As σ increased, the brain regions narrowed and the high voxel values were mainly concentrated in the Frontal_Inf_Orb, Insula_L, and Temporal_Pole_Sup_L. When σ is 38, the volume of the narrowed brain regions was only 16.

The statistical results of the Pearson correlation analyses between SUVR mean and age under different σ (average of 3,000 times) are shown in Table 4. The correlation coefficients R became larger when σ increased and peaked at $\sigma = 30$ ($R = -0.787$; p value = $1.77E-53$). The fluctuation of R values can be observed when σ is greater than 30. According to previous literature, this may be due to the fact that the SUVR mean value of the IC3 region becomes vulnerable when σ is above the peak [34]. Note that all of these were negative, indicating a negative correlation between SUVR mean and age. In addition, all p values were less than $1.00E - 35$, suggesting that the correlations were strong and statistically significant for every σ from 1 to 38.

According to the analysis results listed in Table 4, 30 was chosen as the best σ due to the strongest correlation. The

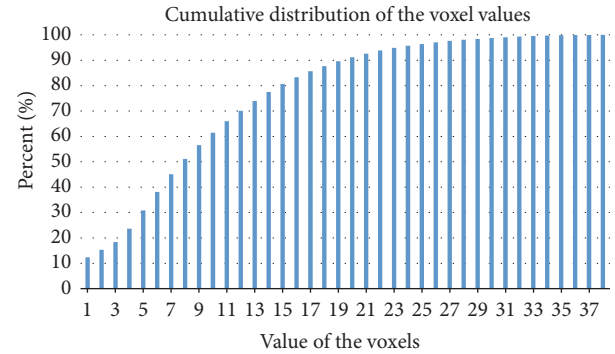


FIGURE 3: Cumulative distribution of the voxel values.

final brain region was then defined. The number of voxels with $\sigma = 30$ was 2031. The AAL regions covered by the final brain region are shown in Table 5. The anatomic structure of the final brain region with $\sigma = 30$ is shown in Figure 4. In particular, areas corresponding to $\sigma = 30$ overlapped with 9 regions in AAL: Frontal_Inf_Orb_L (15), Frontal_Inf_Orb_R (16), Frontal_Sup_Medial_L (23), Frontal_Med_Orb_L (25), Insula_R (30), Cingulum_Ant_L (31), Cingulum_Mid_L (33), Temporal_Pole_Sup_L (83), and Temporal_Pole_Sup_R (84).

The final brain region included the bilateral orbital part of inferior frontal gyrus (AAL 15 and AAL 16), the left medial part of superior frontal gyrus (AAL 23), the left medial orbital part of superior frontal gyrus (AAL 25), the right insula (AAL 30), the left anterior cingulate (AAL 31), the left median cingulate, and paracingulate gyri (AAL 33), and bilateral superior temporal gyri (AAL 83 and AAL 84).

3.2. Definition of the Age-Correction Mathematical Model. The linearity coefficients β_C were calculated to create the corresponding age-correction mathematical model. Similar to the last step, random sampling was used in this step. 3,000 times of random sampling of 250 subjects from 255 healthy subjects were conducted and the linear regression coefficients β_C between their SUVR mean and age were calculated, respectively (the third column in Table 5). Thus, the mathematical model can be described as

$$\text{SUVR mean} = -0.00415 \times \text{age} + p_2, \quad (5)$$

where $\beta_C = -0.00539$ and p_2 was the constant term when conducting the linear regression, which had no effect on the definition of the age-correction model.

TABLE 4: Statistical results of Pearson correlation analyses between SUVR mean and age under different σ .

σ	R	SUVR mean				β_C
		Average	\pm	Average	\pm	
1	-0.69078	0.004314		2.15E - 36	4.63E - 36	-0.00201
2	-0.70248	0.004163		4.04E - 38	9.70E - 38	-0.00211
3	-0.70505	0.004088		1.72E - 38	3.48E - 38	-0.00213
4	-0.70732	0.003972		7.79E - 39	1.28E - 38	-0.00215
5	-0.71126	0.004001		1.98E - 39	3.59E - 39	-0.00219
6	-0.71589	0.003869		3.74E - 40	7.52E - 40	-0.00225
7	-0.71954	0.003853		9.62E - 41	2.11E - 40	-0.00231
8	-0.72191	0.004004		3.85E - 41	9.00E - 41	-0.00237
9	-0.72329	0.00385		2.37E - 41	3.97E - 41	-0.00243
10	-0.72439	0.003884		1.62E - 41	3.12E - 41	-0.00248
11	-0.72653	0.003878		6.94E - 42	1.41E - 41	-0.00254
12	-0.72982	0.003748		2.02E - 42	3.85E - 42	-0.00261
13	-0.73463	0.003733		2.96E - 43	5.12E - 43	-0.00268
14	-0.74075	0.003678		2.45E - 44	4.79E - 44	-0.00277
15	-0.74601	0.003559		3.03E - 45	7.36E - 45	-0.00285
16	-0.75093	0.00336		3.60E - 46	7.28E - 46	-0.00294
17	-0.75519	0.003342		5.89E - 47	1.09E - 46	-0.00303
18	-0.75828	0.003328		1.47E - 47	2.85E - 47	-0.00311
19	-0.76163	0.003282		3.26E - 48	8.33E - 48	-0.0032
20	-0.76479	0.003203		7.59E - 49	1.84E - 48	-0.00329
21	-0.76782	0.00321		1.84E - 49	4.31E - 49	-0.00338
22	-0.77095	0.003207		4.29E - 50	8.36E - 50	-0.00348
23	-0.77505	0.003002		6.17E - 51	1.09E - 50	-0.00359
24	-0.77783	0.003031		1.62E - 51	3.07E - 51	-0.00368
25	-0.78031	0.00297		4.91E - 52	1.11E - 51	-0.00377
26	-0.78164	0.002894		2.62E - 52	5.01E - 52	-0.00384
27	-0.78308	0.00284		1.16E - 52	2.12E - 52	-0.00392
28	-0.78417	0.002848		6.79E - 53	1.70E - 52	-0.00399
29	-0.78584	0.002811		2.76E - 53	6.28E - 53	-0.00408
30	-0.78679	0.002817		1.77E - 53	3.22E - 53	-0.00415
31	-0.7865	0.002822		2.18E - 53	4.26E - 53	-0.0042
32	-0.78558	0.002849		3.41E - 53	6.38E - 53	-0.00425
33	-0.78627	0.002835		2.26E - 53	4.77E - 53	-0.00433
34	-0.78522	0.002819		3.93E - 53	9.98E - 53	-0.00439
35	-0.77836	0.002867		1.15E - 51	2.35E - 51	-0.00441
36	-0.77042	0.002963		5.30E - 50	1.00E - 49	-0.00443
37	-0.76594	0.00296		4.43E - 49	8.09E - 49	-0.00453
38	-0.7343	0.003578		3.35E - 43	7.69E - 43	-0.00443

Note. All the results in Table 5 are the average of the 3000 Pearson correlations between SUVR mean and age.

3.3. Evaluation of the Mathematical Age-Correction Model in Healthy Participants

3.3.1. Evaluation of the Final Brain Region in 262 Healthy Participants. The validation results of the final brain region with the new dataset are shown in Figure 5. The p value was $5.39E - 04$, indicating a statistically significant relationship between SUVR mean and age, and the correlation coefficient $R = -0.212$, indicating a negative correlation (see Figure 5).

3.3.2. Evaluation of the Mathematical Age-Correction Model in 262 Healthy Participants. The validation results are shown in Figure 6 as a scatter plot and fitting curves between SUVR mean and age across the 262 healthy subjects before (red and dashed) and after (green and solid) age correction. The correlation between SUVR mean and age measured using Pearson correlation analysis became weaker after age correction (the Pearson correlation coefficient R declined from 0.212 to 0.027 while the p value rose from $5.39E - 04$

TABLE 5: AAL regions covered by the final brain region with $\sigma = 30$.

Region number	Region name	MNI coordinates (mm)		
		x	y	z
15	Frontal_Inf_Orb_L	-35.98	30.71	-12.11
16	Frontal_Inf_Orb_R	41.22	32.23	-11.91
23	Frontal_Sup_Medial_L	-8.06	15.05	-11.46
25	Frontal_Med_Orb_L	-5.17	54.06	-7.40
30	Insula_R	39.02	6.25	2.08
31	Cingulum_Ant_L	-4.04	35.40	13.95
33	Cingulum_Mid_L	-5.48	-14.92	41.57
83	Temporal_Pole_Sup_L	-39.88	15.14	-20.18
84	Temporal_Pole_Sup_R	48.25	14.75	-16.86

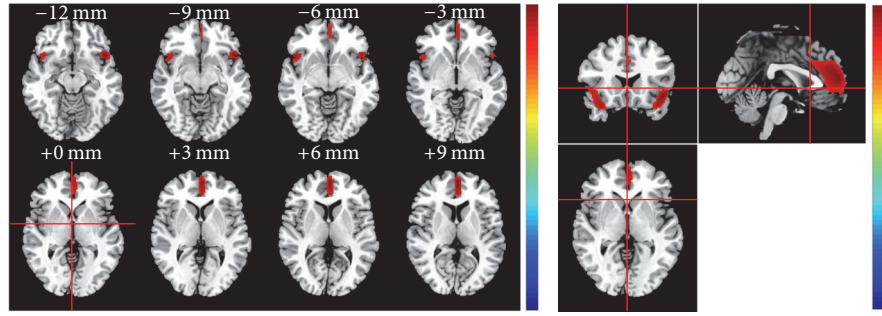
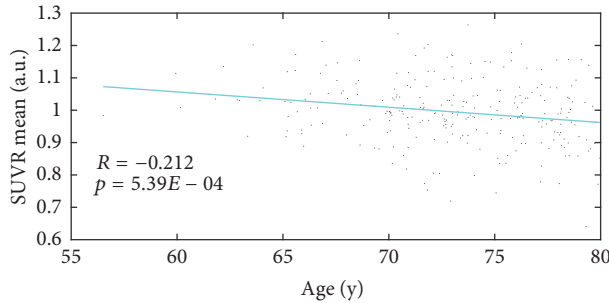
FIGURE 4: Anatomic structure of the final brain region with $\sigma = 30$.

FIGURE 5: Scatter plot and fitting curves between SUVR mean formed from brain regions and age.

to 0.669), indicating that the influence of age on the regions used to form the SUVR mean was weakened as a result of age correction. Simultaneously, after correction, the slope was decreased to almost 0, indicating that the influence of age on the SUVR mean values had been eliminated. In addition, similar changes were found in the p values and Pearson correlation coefficients R in both age groups of the 252 healthy subjects after age correction (the Pearson correlation coefficients R declined from 0.208 to 0.063 for age group 61–70 and from 0.171 to 0.07 for age group 71–80 while the p value rose from 0.059 to 0.573 for age group 61–70 and from 0.022 to 0.353 for age group 71–80).

3.3.3. A Qualitative Case Study. To visually demonstrate the correction results visually, one typical subject was selected

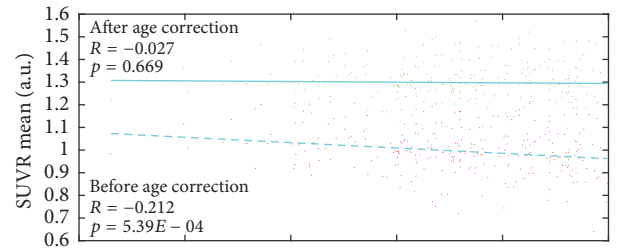


FIGURE 6: Scatter plot and fitting curves between SUVR mean and age across the 262 healthy subjects before (red and dashed) and after (green and solid) age correction. In addition, the statistical results of the age correction in the two age groups of the 252 healthy subjects are presented below.

from each of the two groups (healthy group and AD group) and the age-correction model was applied on all the voxels within the final brain region (the subject selected from the healthy group was aged 78.3 and the other subject selected from the AD group was aged 58.4). As shown in Figures 7(a) and 7(c) the origin anatomic structures of the final brain region are extracted from the healthy and AD subject, respectively. The corrected anatomic structures of the final

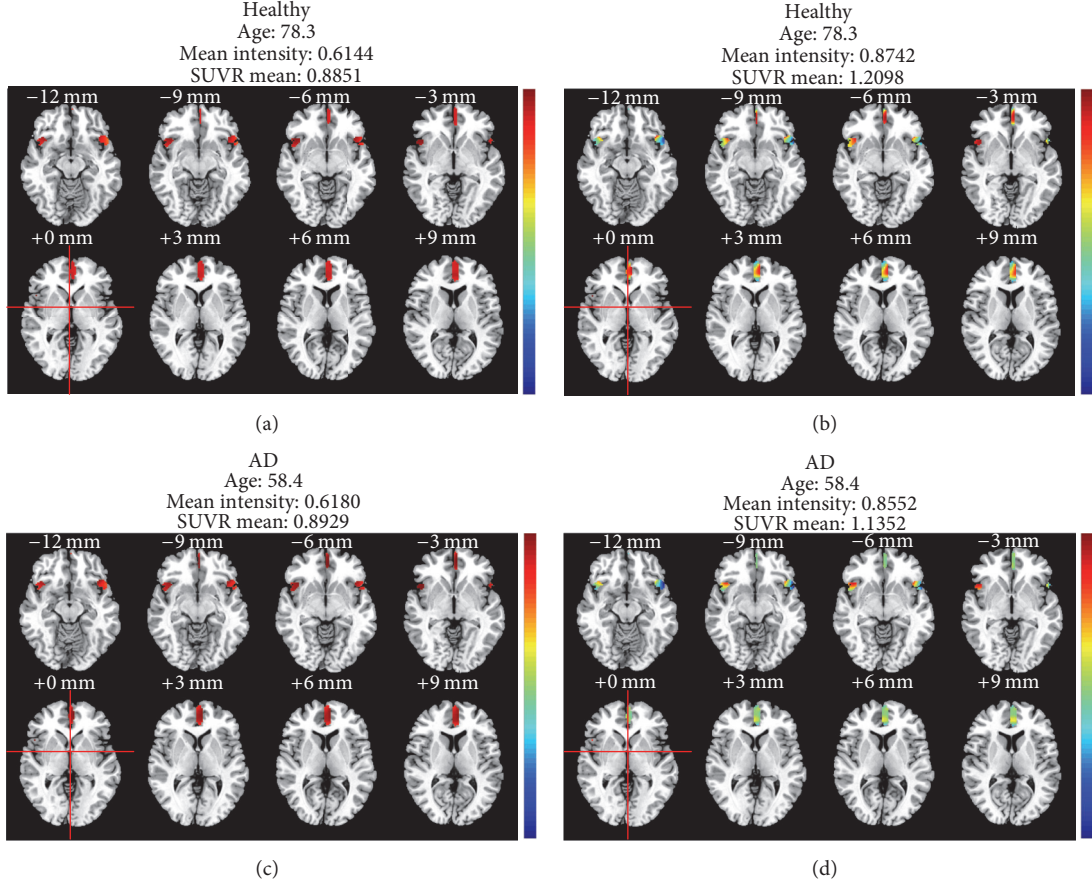


FIGURE 7: Visual result demonstration of a qualitative case study.

brain regions extracted from the healthy and AD subject are shown in Figures 7(b) and 7(d), respectively. The mean intensities of these two subjects were very similar (0.6180 and 0.6144, resp.). The age correction results of the two subjects are shown in Figures 7(b) and 7(d), and the mean intensity of the healthy subject went beyond that of the AD subject (0.8742 and 0.8552, resp.), indicating a healthier status after eliminating the influence of age.

Additionally, the SUVR mean values based on the final brain region of each subjects in both the healthy and AD groups were calculated before and after the age correction and the statistical significance between the two groups was measured by an independent *t*-test. The *p* value declined from $1.706E - 08$ to $1.740E - 10$ after the age correction, indicating that the difference between healthy and AD subjects became more significant after the age correction.

3.3.4. Evaluation of the Mathematical Age-Correction Model in AD Participants. To validate whether the age-correction model can serve to eliminate the confusing factor of age so as to highlight the pathological differences, the model was applied to the dataset of 50 AD patients selected from the ADNI database. The SUVR mean of each subject was generated from the optimal final brain region, and age correction for SUVR mean was then carried out. Before and after the age correction, the partial correlation analysis

was applied between the SUVR mean and the 3 clinical results. As is evident from Figure 8 and Table 6, the *p* value and *R* coefficient were both significantly improved after age correction. The partial correlation coefficients *R* rose from 0.371 to 0.497 for MMSE, -0.422 to -0.512 for CDRSB, and 0.426 to 0.573 for FDG. During the partial analyses, the effect of education, sex, and ApoE4 status was removed as a set of controlled variables. The results showed that the correlations between the SUVR means values and clinical tests were improved after age-correction. Radiologists may find it easier to diagnose AD by analyzing FDG PET images after age-correction.

As shown in Table 6, we can see that, in subgroups 69–73 and 73–78, the relationship between SUVR mean and two of the clinical results (MMSE and CDRSB for subgroup 69–73 and CDRSB and FDG for 73–78) became much stronger after age correction. Apart from that, the relationship between SUVR mean and FDG in subgroup 56–69 also became much stronger after age correction.

Taken together, it can be safely concluded, with the results of Figure 2 and Tables 3 and 6, that the effect of normal aging becomes apparent after approximately age 50 (Figure 2 and Table 3). Meanwhile, the age of early-onset dementia such as AD has been reported to be 60–65 years [11, 23]. As seen from Table 6, the effect of age correction on subgroup 69–73 and 73–78 was obvious since the *p*

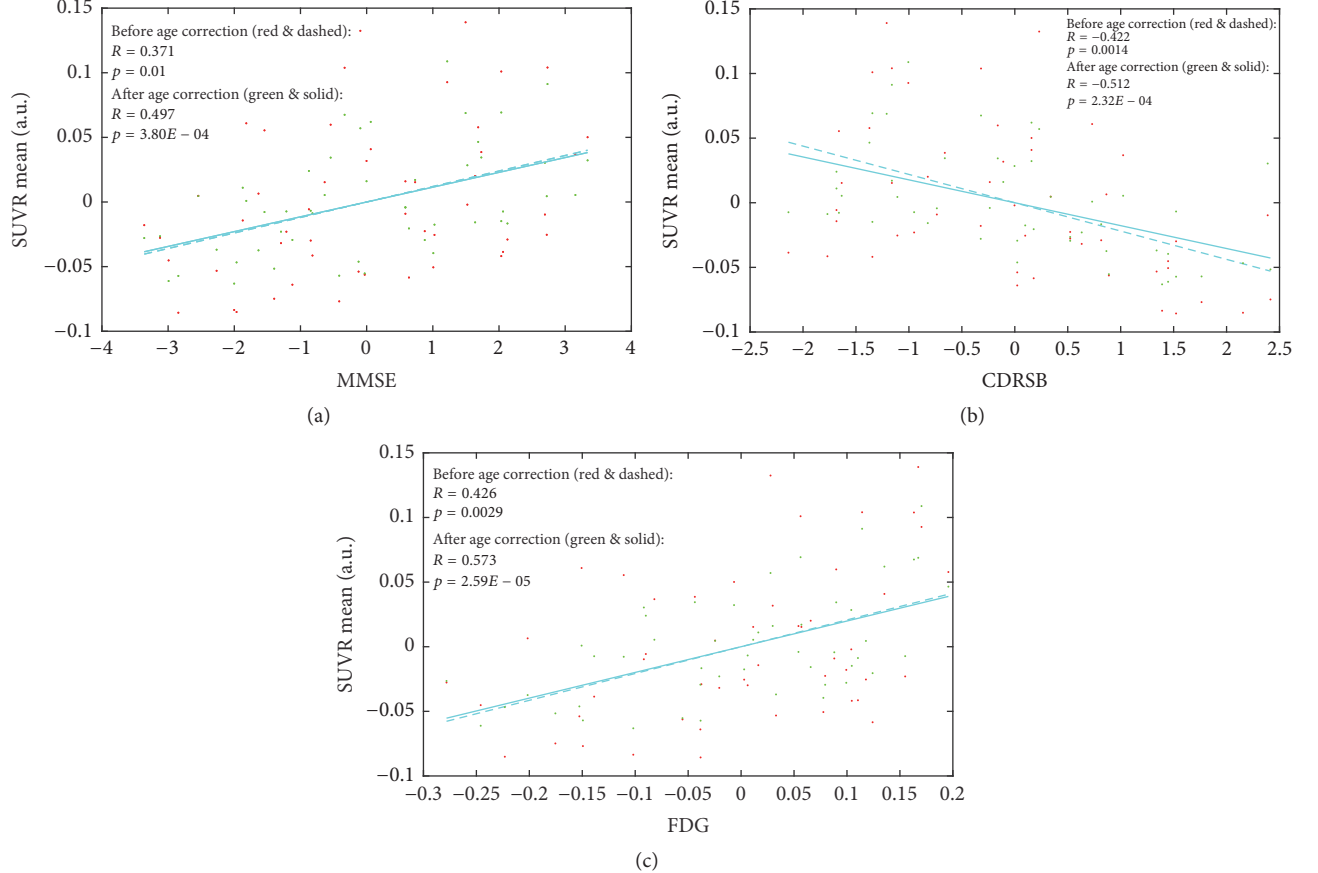


FIGURE 8: Scatter plot and fitting curves between SUVR mean and (a) MMSE, (b) CDRSB, and (c) FDG across the 50 AD subjects before (red dots and dashed lines) and after (green dots and solid lines) age correction.

TABLE 6: Statistical results of the age correction in each age group of the 50 AD subjects.

Age grade	Number	Before correction			After correction			
		MMSE	CDRSB	FDG	MMSE	CDRSB	FDG	
56–69	11	<i>P</i>	0.419	0.166	0.025	<i>P</i>	0.158	0.139
		<i>R</i>	0.272	-0.449	0.668	<i>R</i>	0.456	-0.476
69–73	10	<i>P</i>	0.037	0.04	0.26	<i>P</i>	0.025	0.029
		<i>R</i>	0.663	-0.655	0.394	<i>R</i>	0.699	-0.685
73–78	16	<i>P</i>	0.12	0.034	0.011	<i>P</i>	0.091	0.02
		<i>R</i>	0.404	-0.531	0.615	<i>R</i>	0.436	-0.575
78–80	13	<i>P</i>	0.014	0.067	0.057	<i>P</i>	0.015	0.058
		<i>R</i>	0.663	-0.522	0.539	<i>R</i>	0.658	0.52

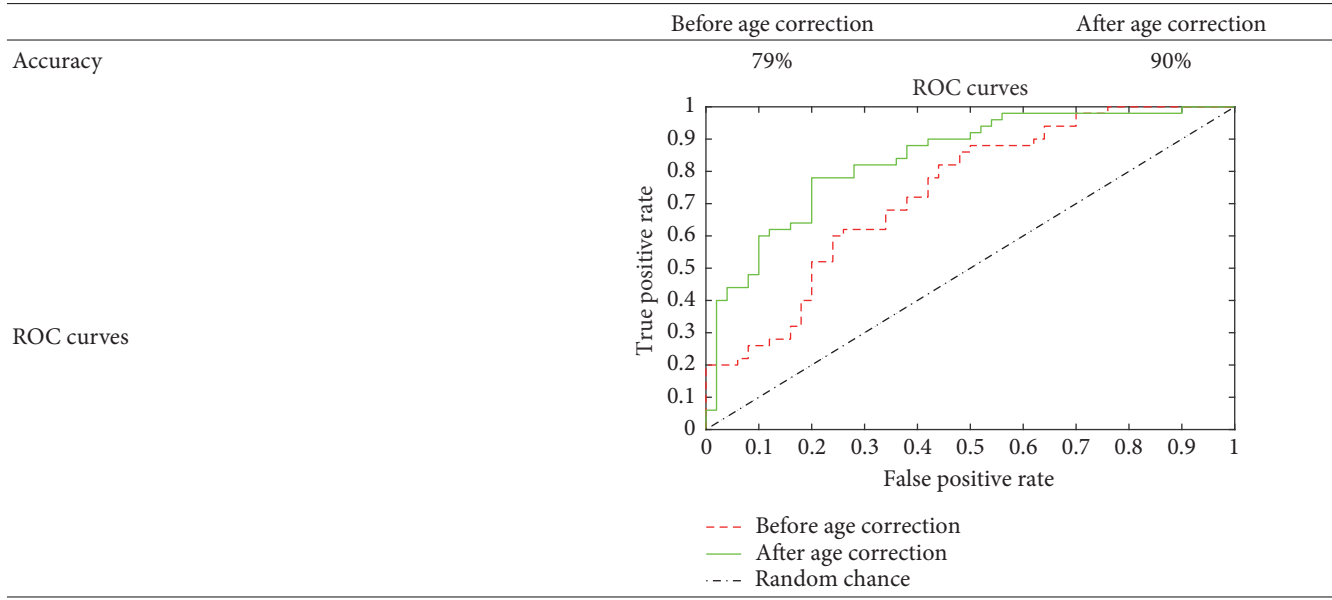
Note. Age groups 69–71 and 71–73 and 73–76 and 76–78 were combined into one group, respectively, because of their insufficient quantity.

values decreases evidently after age correction. We can conclude that the age correction is more effective for ages 69–78.

To verify whether age correction can help to improve the diagnostic accuracy, classification for AD combining PCA and SVM was applied to 50 healthy and 50 AD subjects. Age correction was conducted on the final brain region of IC3 and then the whole brain of each subject was used as the input for

the feature extraction of PCA. Leave-one-out cross validation was used during SVM classification to achieve more reliable results by reducing the influence of stochastic factors. As shown in Table 7, the classification performance was achieved with an accuracy of 79% before age correction and 90% after age correction. Table 7 also shows the ROC curves of the two classifications. The AUC values were 0.735 before age correction and 0.84 after age correction.

TABLE 7: Classification accuracy for AD before and after age correction.



4. Discussion

In the present study, a data-driven analysis of brain glucose metabolism variation across 255 healthy participants revealed a component showing a monotone decrease with an increase in age. According to Figure 4, the regions corresponding to the component IC3 included left inferior and superior frontal gyrus (AAL 15 and AAL 16), the left medial part of superior frontal gyrus (AAL 23), the left medial orbital part of superior frontal gyrus (AAL 25), the right insula (AAL 30), the left anterior cingulate (AAL 31), the left median cingulate, and paracingulate gyri (AAL 33), and bilateral superior temporal gyri (AAL 83 and AAL 84). These findings were mostly in accordance with the typical results that have been reported in most lifespan studies [15–22]. In addition, a set of brain region called the resting state, or default mode network (DMN) of the human brain, which has been suggested by studies of functional connectivity to be relevant to cognitive development, was reported to be significantly related to age [23–25]. This network includes the posterior cingulum (PCC), the precuneus, the left orbital and medial prefrontal cortex (OPFC and MPFC_L), the left orbitofrontal cortex (OFC_L), and the angular gyrus (ANG). As can be observed, the final brain regions overlapped with regions of DMN typically within the left MPFC, OPFC, and medial temporal lobe, which again is in good agreement with the age-related findings of most previous studies described above.

In addition to DMN, the final brain region also covered other areas that have been reported to be related to AD. FDG PET is said to have a predictive value for neurodegeneration at a very early stage [4, 12, 13]. A network was reported to enable FDG PET to detect abnormal metabolism reduction both earlier and at more advanced AD stages than MRI [14]. This network encompassed hippocampal, temporal, parietal, occipital, and posterior caudate regions. It was mostly covered

by the final brain regions identified in the present study, with the exception of the occipital regions and right hippocampal regions. Hence, age correction may be conducive to enhancing the conviction of predictions.

The IC value of IC3 was found to have a negative linear correlation with age (Figure 2 and Table 3). This finding is in good agreement with reports in the literatures of most regions using FDG PET, where there are clear negative correlations with age [15–22]. In addition, comparison of ICs with the literature [7] showed a similar negative correlation trend through other imaging modalities in GM volume, WM volume, and FA between ages 22 and 82, indicating advanced age-related adverse changes in the brain reflected by various imaging modalities. The results of the comparison between the present study and the literature are shown in Figure 9, suggesting that the definition of IC3 in the present study is credible.

The age-correction model was also conducted on 50 AD subjects. Before the correction, a statistically significant positive correlation between SUVR mean and MMSE or FDG and the negative correlation between SUVR mean and CDRSB were in good accordance with the authors' general understanding of the clinical physiological indices (i.e., the severity of AD is indicated by a lower SUVR mean, a lower MMSE score, and a lower FDG, but a higher CDRSB score). After the correction, these correlations remained unchanged, and the correlation coefficient R finally rose to 0.497 for SUVR mean and MMSE, -0.512 for SUVR mean and CDRSB, and 0.573 for SUVR mean and FDG, respectively. The corrected results were compared with those from other studies. In the work by Hatashita [37], the correlation coefficients R reached 0.46 for SUVR and MMSE and -0.44 for SUVR mean and CDRSB, which is numerically similar to the correlations before age correction in the present study (0.371 and -0.422). After the age correction, however, the correlation coefficients

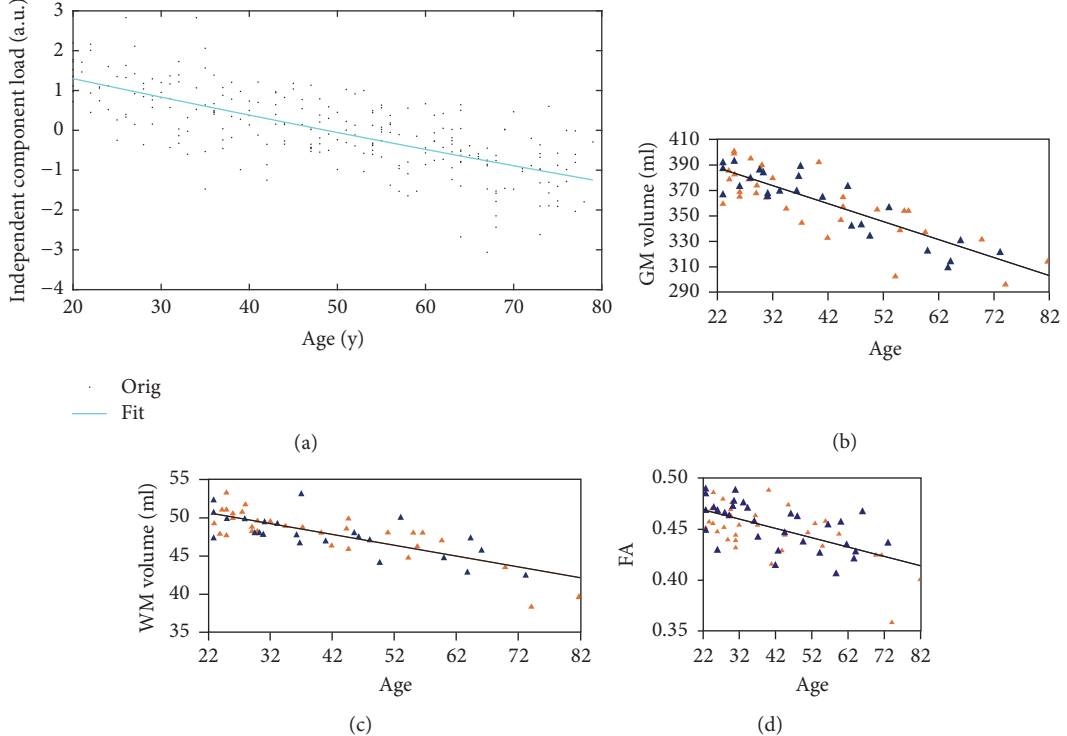


FIGURE 9: Similar linear scatter plots of negative correlations between age and different imaging indices. (a) Results from the present study. Correlation between SUVR mean and age. Correlations between (a) IC value (b; c; d) Results in [7]. Correlations between (b) GM volume, (c) WM volume, and (d) FA and age.

in the present study rose to 0.497 and -0.512 , respectively, indicating a relatively stronger correlation between SUVR and the clinical results. Note that the stronger correlation between SUVR mean and FDG after age correction indicated both potential age- and AD-related responses with areas of angular, temporal, and posterior cingulate indications, which again overlapped with the network of DMN [23–25, 38, 39]. Overall, it can be reasonably concluded that the age correction is valid in clinical AD diagnoses.

The methodological approach used here had two advantages that were crucial in confirming this monotone decreasing component IC3 that revealed a natural decline with age. First, no spatial, age-related, or any other prior information was imposed on the data. Second, the presumption that the components were non-Gaussian independently distributed sources allowed more subtle modes to be detected with respect to abnormal variation and coordinately dominated by certain underlying common features across all subjects. While explaining only a modest amount of the metabolism variation across all 255 healthy subjects (3.7%), the IC3 revealed a strong negative relationship with age (as age explained 51.8% of the spatial variance). Therefore, the FLICA method is very suitable for the present study. In the work by [32], the authors obtained 70 ICs, including IC1, that had an extraordinary relationship with age, for which the R square value was 0.9 across 484 healthy participants along with 3 modals (MRI, vertexwise cortical thickness and surface area). In addition, the authors mainly discussed a symmetrical

inverted-U IC4 with an R square value with age that was 0.5, indicating a mirror effect in age-related brain development. Earlier, in the work by Groves et al. [33], 100 ICs were obtained with a larger dataset that included the same 484 subjects and the three modalities mentioned above, in addition to another three modalities: FA, MD, and MO, all of which were derived from DTI scans. It was understandable that the IC3 obtained during the present study had a lower R squared value due to a relatively smaller and single-modal data size, but its relationship with age was still significant.

In addition, the paracentral lobule (AAL 69 and AAL 70) was set during the present study as the reference region when forming SUVR following the research by Zhang et al. [35]. However, other regions may also be selected as reference regions. In the work by Gardener et al. [40, 41], the whole cerebellar or the whole brain region was used as the reference region, and the cerebellar tonsil (AAL 105 and AAL 106) was also reported by Zhang et al. [35] to be one of the two best regions to be a reference, due to their improvement in the separation of natural age-associated changes from changes in brain metabolism. In the present study, these four regions were taken separately as a reference region and the SUVR mean was calculated under different values of σ . As shown in Figure 10 (all the results in Figure 10 are the average of the 3000 times Pearson correlation between SUVR mean and age), the relationship between age and SUVR mean was strongest when normalized to the paracentral lobule, with the R value climbing up to 0.787 at $\sigma = 30$. However, its

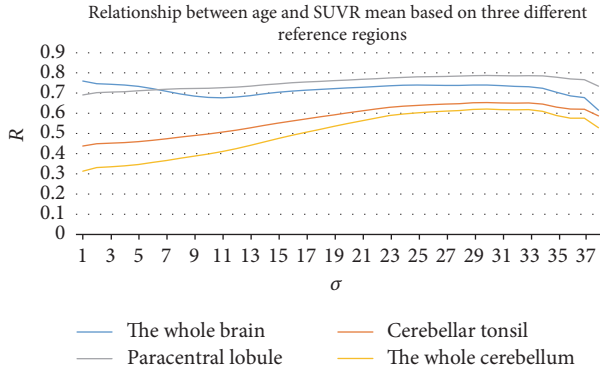


FIGURE 10: Relationship between age and SUVR mean based on four different reference regions: the cerebellum, the cerebellar tonsil, the paracentral lobule, and the whole brain region.

advantage was not obvious when compared with the whole cerebellum ($R = 0.76$ at $\sigma = 1$). This may be due to the limitations inherent to the datasets, such as possible cohort effects and selection bias, which may influence the use of this more rational reference region to some degree. Nevertheless, it could arguably be concluded that the paracentral lobule can be chosen as the reference region when the age influence needs to be discounted.

5. Limitations and Further Considerations

Although certain initial findings regarding brain regions related to age in FDG PET have been explored in the present study, some limitations still exist. First, no cognitive tests such as MMSE or CDRSB have been conducted on subjects at the Huashan Hospital to evaluate their cognitive condition. Further, no partial volume correction (PVC) was performed during the present study due to the lack of MRI data. Both issues should be addressed in future work. Second, the R squared value of IC3 was only 0.518, which is far less than for the similar monotonically decreasing IC obtained by [32] whose R squared value fitting with age was 0.9. The reason for this discrepancy was likely the limitation of the amount of the subjects' image data, since they had a dataset of 484 subjects. Thus, we could only define one age-correction mathematical model during the long age-span of 20–80 years. Without the data deficiency, we would be able to obtain one age-correction model for each age grade, and the effect of the age correction would then be much more precise. Third, only a linear relationship between the IC value and age was taken into account for the definition of the age-correction mathematical model, since IC3 revealed a monotone linear decrease with increasing age via assessment with a quadratic fit (Figure 2 and Table 3). In fact, a nonlinear relationship with age has also been reported in previous literatures as was found in the present study (e.g., IC11). However, a nonlinear age-correction mathematical model was not investigated but will be studied in the near future. Fourth, in the present study, we used the same template from SPM during the image preprocessing steps for both datasets from Huashan Hospital and the ADNI. However, structural

and functional differences between brains in the Chinese and Western elderly populations exist, which may result in various impacts of age on FDG PET scans. Thus, geographical differences between the two datasets from Huashan Hospital and the ADNI will be investigated in the future using different templates. Fifth, in the present study, only FDG PET scans were used for the FLICA. In fact, the FLICA approach can also be used on multimodal data. In addition to FDG PET, the others modals (i.e., other brain imaging techniques) can be MRI, PiB-PET, DTI, and the advanced morphological patterns extracted from these modals, such as FA, MD, and MO from DTI [33], or vertexwise cortical thickness and surface area measures from MRI [32]. Different brain imaging techniques focus on different dementia disorders such as MRI and structural atrophy, PiB-PET and amyloid deposition, and DTI and communication amongst nerve cells in the brain. Thus, combined multimodal analyses can definitely help to increase the number of ICs and obtain more accurate appraisals of brain regions as a result of more integrated information. It is certainly worth comparing the brain regions related to age in these different modals so as to build a corresponding correction template. This approach can also help in the study of differences in how diseases affect each modal of the images. Last of all, the differences in natural brain decline between male and female subjects need to be studied further.

6. Conclusion

In summary, the findings of the present investigation suggest that the inferior frontal gyrus, the left medial part of superior frontal gyrus, the left medial orbital part of superior frontal gyrus, the right insula, the left anterior cingulate, the left median cingulate, and paracingulate gyri, and bilateral superior temporal gyri have a strong negative relationship with age in ^{18}F -FDG PET images. An age-correction model characterizing the rate of decline of the index SUVR mean provides the possibility of correcting analyses for the effect of the confounding variable, age. By applying the age correction to AD subjects, it was determined that the correction could effectively suppress the interference of age on the analysis and bring disease abnormalities nearer to manifestation. Thus, the method can be applied to patients prior to a clinical AD diagnosis, which will help in determining the severity of the underlying disease.

Disclosure

The Alzheimer's Disease Neuroimaging Initiative data used in preparation of this article were obtained from the Alzheimer's Disease Neuroimaging Initiative (ADNI) database (<http://adni.loni.usc.edu/>). As such, the investigators within the ADNI contributed to the design and implementation of ADNI and/or provided data.

Conflicts of Interest

The authors declare that they have no conflicts of interest.

Acknowledgments

This study was supported by grants from the National Science Foundation of China (no. 61603236, no. 81671239, no. 81361120393, and no. 81401135), Shanghai Technology and Science Key Project in Healthcare (no. 17441902100), the Development Fund for Shanghai Talents (no. 201448), and Shanghai Key Laboratory of Psychotic Disorders (no. 13dz2260500). The international cooperation was supported by the Sino-German Institute for Brain Molecular Imaging and Clinical Translation. The authors thank Xinghui Shu, Yupeng Li, and Jun Xu for their kind help with data preprocessing. Data collection and sharing for this project were funded by the Alzheimer's Disease Neuroimaging Initiative (ADNI) (National Institutes of Health Grant U01 AG024904) and DOD ADNI (Department of Defense, Award no. W81XWH-12-2-0012). ADNI is funded by the National Institute of Aging and the National Institute of Biomedical Imaging and Bioengineering and through generous contributions from the following: AbbVie, Alzheimer's Association; Alzheimer's Drug Discovery Foundation; Araclon Biotech; BioClinica, Inc.; Biogen; Bristol-Myers Squibb Company; CereSpir, Inc.; Eisai Inc.; Elan Pharmaceuticals, Inc.; Eli Lilly and Company; EuroImmun; F. Hoffmann-La Roche Ltd. and its affiliated company Genentech, Inc.; Fujirebio; GE Healthcare; IXICO Ltd.; Janssen Alzheimer Immunotherapy Research & Development, LLC.; Johnson & Johnson Pharmaceutical Research & Development LLC.; Lumosity; Lundbeck; Merck & Co., Inc.; Meso Scale Diagnostics, LLC.; NeuroRx Research; Neurotrack Technologies; Novartis Pharmaceuticals Corporation; Pfizer Inc.; Piramal Imaging; Servier; Takeda Pharmaceutical Company; and Transition Therapeutics. The Canadian Institutes of Health Research is providing funds to support ADNI clinical sites in Canada. Private sector contributions are facilitated by the Foundation for the National Institutes of Health (<https://www.fnih.org>). The grantee organization is the Northern California Institute for Research and Education, and the study is coordinated by the Alzheimer's Disease Cooperative Study at the University of California, San Diego. ADNI data are disseminated by the Laboratory for Neuro Imaging at the University of Southern California.

References

- [1] G. M. Savva, S. B. Wharton, and P. G. Ince, "Age, Neuropathology, and Dementia," *The New England Journal of Medicine*, vol. 360, pp. 2302–2309, 2009.
- [2] B. W. Patterson, D. L. Elbert, K. G. Mawuenyega et al., "Age and amyloid effects on human central nervous system amyloid-beta kinetics," *Annals of Neurology*, vol. 78, no. 3, pp. 439–453, 2015.
- [3] G. McKhann, D. Drachman, M. Folstein, R. Katzman, D. Price, and E. M. Stadlan, "Clinical diagnosis of Alzheimer's disease: report of the NINCDS-ADRDA work group under the auspices of department of health and human services task force on alzheimer's disease," *Neurology*, vol. 34, no. 7, pp. 939–944, 1984.
- [4] J. R. Petrella, R. E. Coleman, and P. M. Doraiswamy, "Neuroimaging and early diagnosis of alzheimer disease: A look to the future," *Radiology*, vol. 226, no. 2, pp. 315–336, 2003.
- [5] S. E. Prince, S. Woo, P. M. Doraiswamy, and J. R. Petrella, "Functional MRI in the early diagnosis of Alzheimer's disease: is it time to refocus?" *Expert Review of Neurotherapeutics*, vol. 8, no. 2, pp. 169–175, 2008.
- [6] R. C. Petersen, "Aging, mild cognitive impairment, and Alzheimer's disease," *Neurologic Clinics*, vol. 18, no. 4, pp. 789–805, 2000.
- [7] A. Giorgio, L. Santelli, V. Tomassini et al., "Age-related changes in grey and white matter structure throughout adulthood," *NeuroImage*, vol. 51, no. 3, pp. 943–951, 2010.
- [8] C. D. Good, I. S. Johnsrude, J. Ashburner, R. N. A. Henson, K. J. Friston, and R. S. J. Frackowiak, "A voxel-based morphometric study of ageing in 465 normal adult human brains," in *Proceedings of the 5th IEEE EMBS International Summer School on Biomedical Imaging*, June 2002.
- [9] C. D. Smith, H. Chebrok, D. R. Wekstein, F. A. Schmitt, and W. R. Markesberry, "Age and gender effects on human brain anatomy: a voxel-based morphometric study in healthy elderly," *Neurobiology of Aging*, vol. 28, no. 7, pp. 1075–1087, 2007.
- [10] H. Oh, C. Madison, S. Villeneuve, C. Markley, and W. J. Jagust, "Association of gray matter atrophy with age, β -amyloid, and cognition in aging," *Cerebral Cortex*, vol. 24, no. 6, pp. 1609–1618, 2014.
- [11] C. R. Jack, H. J. Wiste, S. D. Weigand et al., "Age, sex, and APOE $\epsilon 4$ effects on memory, brain structure, and β -Amyloid across the adult life Span," *JAMA Neurology*, vol. 72, no. 5, pp. 511–519, 2015.
- [12] D. H. S. Silverman, S. S. Gambhir, H.-W. C. Huang et al., "Evaluating early dementia with and without assessment of regional cerebral metabolism by PET: A comparison of predicted costs and benefits," *Journal of Nuclear Medicine*, vol. 43, no. 2, pp. 253–266, 2002.
- [13] D. H. S. Silverman, C. T. Truong, S. K. Kim et al., "Prognostic value of regional cerebral metabolism in patients undergoing dementia evaluation: comparison to a quantifying parameter of subsequent cognitive performance and to prognostic assessment without PET," *Molecular Genetics and Metabolism*, vol. 80, no. 3, pp. 350–355, 2003.
- [14] O. Sporns, J. Dukart, F. Kherif et al., "Generative FDG-PET and MRI model of aging and disease progression in Alzheimer's disease," *PLoS Computational Biology*, vol. 9, no. 4, Article ID e1002987, 2013.
- [15] A. Loessner, A. Alavi, K.-U. Lewandrowski, D. Mozley, E. Souder, and R. E. Gur, "Regional cerebral function determined by FDG-PET in healthy volunteers: Normal patterns and changes with age," *Journal of Nuclear Medicine*, vol. 36, no. 7, pp. 1141–1149, 1995.
- [16] J. R. Moeller, T. Ishikawa, V. Dhawan et al., "The metabolic topography of normal aging," *Journal of Cerebral Blood Flow & Metabolism*, vol. 16, no. 3, pp. 385–398, 1996.
- [17] S. Bonte, P. Vandemaele, S. Verleden et al., "Healthy brain aging assessed with 18F-FDG PET and age-dependent recovery factors after partial volume effect correction," *European Journal of Nuclear Medicine and Molecular Imaging*, vol. 44, no. 5, pp. 838–849, 2016.
- [18] G. Zuendorf, N. Kerrouche, K. Herholz, and J.-C. Baron, "Efficient principal component analysis for multivariate 3D voxel-based mapping of brain functional imaging data sets as applied to FDG-PET and normal aging," *Human Brain Mapping*, vol. 18, no. 1, pp. 13–21, 2003.
- [19] E. Iseki, N. Murayama, R. Yamamoto et al., "Construction of a 18F-FDG PET normative database of Japanese healthy elderly

- subjects and its application to demented and mild cognitive impairment patients," *International Journal of Geriatric Psychiatry*, vol. 25, no. 4, pp. 352–361, 2010.
- [20] X. Shen, H. Liu, Z. Hu, H. Hu, and P. Shi, "The relationship between cerebral glucose metabolism and age: report of a large brain pet data set," *PLoS ONE*, vol. 7, no. 12, Article ID e51517, 2012.
- [21] G. Chételat, B. Landeau, E. Salmon et al., "Relationships between brain metabolism decrease in normal aging and changes in structural and functional connectivity," *NeuroImage*, vol. 76, pp. 167–177, 2013.
- [22] C. Lustig, A. Z. Snyder, M. Bhakta et al., "Functional deactivations: change with age and dementia of the Alzheimer type," *Proceedings of the National Academy of Sciences of the United States of America*, vol. 100, no. 2, pp. 14504–14509, 2003.
- [23] K. Herholz, E. Salmon, D. Perani et al., "Discrimination between Alzheimer dementia and controls by automated analysis of multicenter FDG PET," *NeuroImage*, vol. 17, no. 1, pp. 302–316, 2002.
- [24] D. Bittner, G. Grön, H. Schirrmeister, S. N. Reske, and M. W. Riepe, "[¹⁸F]FDG-PET in patients with Alzheimer's disease: Marker of disease spread," *Dementia and Geriatric Cognitive Disorders*, vol. 19, no. 1, pp. 24–30, 2005.
- [25] E. J. Kim, S. S. Cho, Y. Jeong et al., "Glucose metabolism in early onset versus late onset Alzheimer's disease: an SPM analysis of 120 patients," *Brain*, vol. 128, no. 8, pp. 1790–1801, 2005.
- [26] E. Kalbe, P. Calabrese, S. Fengler, and J. Kessler, "DemTect, PANDA, EASY, and MUSIC: Cognitive screening tools with age correction and weighting of subtests according to their sensitivity and specificity," *Journal of Alzheimer's Disease*, vol. 34, no. 4, pp. 813–834, 2013.
- [27] Z. S. Nasreddine, N. A. Phillips, V. Bédirian et al., "The montreal cognitive assessment, MoCA: a brief screening tool for mild cognitive impairment," *Journal of the American Geriatrics Society*, vol. 53, no. 4, pp. 695–699, 2005.
- [28] J. Hessler, O. Tucha, H. Förstl, E. Mösch, and H. Bickel, "Age-correction of test scores reduces the validity of mild cognitive impairment in predicting progression to dementia," *PLoS ONE*, vol. 9, no. 8, Article ID e106284, 2014.
- [29] J. Dukart, M. L. Schroeter, and K. Mueller, "Age correction in Dementia—Matching to a healthy brain," *PLoS ONE*, vol. 6, no. 7, Article ID e22193, 2011.
- [30] S. M. Smith, M. Jenkinson, M. W. Woolrich et al., "Advances in functional and structural MR image analysis and implementation as FSL," *NeuroImage*, vol. 23, supplement 1, pp. S208–S219, 2004.
- [31] A. R. Groves, C. F. Beckmann, S. M. Smith, and M. W. Woolrich, "Linked independent component analysis for multimodal data fusion," *NeuroImage*, vol. 54, no. 3, pp. 2198–2217, 2011.
- [32] G. Douaud, A. R. Groves, C. K. Tamnes et al., "A common brain network links development, aging, and vulnerability to disease," *Proceedings of the National Academy of Sciences of the United States of America*, vol. 111, no. 49, pp. 17648–17653, 2014.
- [33] A. R. Groves, S. M. Smith, A. M. Fjell et al., "Benefits of multi-modal fusion analysis on a large-scale dataset: Life-span patterns of inter-subject variability in cortical morphometry and white matter microstructure," *NeuroImage*, vol. 63, no. 1, pp. 365–380, 2012.
- [34] H. Li, N. Becker, S. Raman, T. C. Y. Chan, and J.-P. Bissonnette, "The value of nodal information in predicting lung cancer relapse using 4DPET/4DCT," *Medical Physics*, vol. 42, no. 8, pp. 4727–4733, 2015.
- [35] H. Zhang, P. Wu, S. I. Ziegler et al., "Data-driven identification of intensity normalization region based on longitudinal coherency of 18F-FDG metabolism in the healthy brain," *NeuroImage*, vol. 146, pp. 589–599, 2017.
- [36] D. Tural, D. K. Salim, H. Mutlu et al., "Is there any relation between PET-CT SUVmax value and prognostic factors in locally advanced breast cancer?" *Journal of B.U.ON.*, vol. 20, no. 5, pp. 1282–1286, 2015.
- [37] S. Hatashita, "Cortical amyloid deposition and glucose metabolism in clinically different stages of Alzheimer's disease," *Alzheimer's Dementia*, vol. 7, no. 4, p. S748, 2011.
- [38] S. Passow, K. Specht, T. C. Adamsen et al., "Default-mode network functional connectivity is closely related to metabolic activity," *Human Brain Mapping*, vol. 36, no. 6, pp. 2027–2038, 2015.
- [39] C. Liguori, A. Chiaravalloti, G. Sancesario et al., "Cerebrospinal fluid lactate levels and brain [¹⁸F]FDG PET hypometabolism within the default mode network in Alzheimer's disease," *European Journal of Nuclear Medicine and Molecular Imaging*, vol. 43, no. 11, pp. 2040–2049, 2016.
- [40] S. L. Gardener, H. R. Sohrabi, K.-K. Shen et al., "Cerebral glucose metabolism is associated with verbal but not visual memory performance in community-dwelling older adults," *Journal of Alzheimer's Disease*, vol. 52, no. 2, pp. 661–672, 2016.
- [41] E. Rodriguez-Vieitez, A. Leuzy, K. Chiots, L. Saint-Aubert, A. Wall, and A. Nordberg, "Comparability of [¹⁸F]THK5317 and [¹¹C]PIB blood flow proxy images with [¹⁸F]FDG positron emission tomography in Alzheimer's disease," *Journal of Cerebral Blood Flow & Metabolism*, vol. 37, no. 2, pp. 740–749, 2016.

Research Article

Automated Whole-Body Bone Lesion Detection for Multiple Myeloma on ^{68}Ga -Pentixafor PET/CT Imaging Using Deep Learning Methods

Lina Xu ,^{1,2} Giles Tetteh,^{1,3} Jana Lipkova,^{1,3} Yu Zhao,^{1,3} Hongwei Li,^{1,3} Patrick Christ,^{1,3} Marie Piraud ,^{1,3} Andreas Buck,⁴ Kuangyu Shi ,² and Bjoern H. Menze^{1,3}

¹Department of Informatics, Technische Universität München, Munich, Germany

²Department of Nuclear Medicine, Klinikum Rechts der Isar, TU München, Munich, Germany

³Institute of Medical Engineering, Technische Universität München, Munich, Germany

⁴Department of Nuclear Medicine, Universität Würzburg, Würzburg, Germany

Correspondence should be addressed to Kuangyu Shi; k.shi@tum.de

Received 28 July 2017; Revised 29 November 2017; Accepted 12 December 2017; Published 8 January 2018

Academic Editor: Yun Zhou

Copyright © 2018 Lina Xu et al. This is an open access article distributed under the Creative Commons Attribution License, which permits unrestricted use, distribution, and reproduction in any medium, provided the original work is properly cited.

The identification of bone lesions is crucial in the diagnostic assessment of multiple myeloma (MM). ^{68}Ga -Pentixafor PET/CT can capture the abnormal molecular expression of CXCR-4 in addition to anatomical changes. However, whole-body detection of dozens of lesions on hybrid imaging is tedious and error prone. It is even more difficult to identify lesions with a large heterogeneity. This study employed deep learning methods to automatically combine characteristics of PET and CT for whole-body MM bone lesion detection in a 3D manner. Two convolutional neural networks (CNNs), V-Net and W-Net, were adopted to segment and detect the lesions. The feasibility of deep learning for lesion detection on ^{68}Ga -Pentixafor PET/CT was first verified on digital phantoms generated using realistic PET simulation methods. Then the proposed methods were evaluated on real ^{68}Ga -Pentixafor PET/CT scans of MM patients. The preliminary results showed that deep learning method can leverage multimodal information for spatial feature representation, and W-Net obtained the best result for segmentation and lesion detection. It also outperformed traditional machine learning methods such as random forest classifier (RF), k -Nearest Neighbors (k -NN), and support vector machine (SVM). The proof-of-concept study encourages further development of deep learning approach for MM lesion detection in population study.

1. Introduction

Multiple myeloma (MM) is a malignancy accounting for 13% of the hematological cases [1–3]. A characteristic hallmark of MM is the proliferation of malignant plasma cells in the bone marrow [4]. Common symptoms of MM are summarized as CRAB: C for hypercalcemia, R for renal failure, A for anemia, and B for bone lesions. Modern treatments have achieved a 5-year survival rate of 45% [5]. Nevertheless, MM remains an incurable disease at the moment and it usually relapses after a period of remission under therapy. The identification of bone lesions plays an important role in the diagnostic and therapeutic assessment of MM.

Radiographic skeletal survey (whole-body X-ray) is traditionally applied in the characterization of bone lesions of MM. However, it can only display lesions when the trabecular bone has already lost more than 30% around the focal, usually leading to underestimation of lesion extent [6]. 3D computed tomography (CT) allows the detection of smaller bone lesions that are not detectable by conventional radiography [7]. Magnetic resonance imaging (MRI) is also more sensitive than skeletal survey in the detection of MM lesions and it can detect diffuse bone marrow infiltration with good soft tissue differentiation [8, 9]. Comparable high sensitivity in the detection of small bone lesions can be achieved using PET/CT by combining metabolic (^{18}F -FDG PET) and anatomical

(CT) information [10–13]. The lesions are usually visualized more clearly with the guidance of hotspots in fused images, which can potentially improve the diagnosis and prognosis of MM [14]. Recently, the overexpression of chemokine (C-X-C motif) receptor 4 (CXCR4) has been verified in a variety of cancers, leading to the development of targeted PET tracer such as ⁶⁸Ga-Pentixafor [15]. This emerging tracer has already demonstrated a higher sensitivity in the visualization of MM lesions [16, 17].

Even with advanced imaging, challenges remain in the identification of MM bone lesions. It is commonly seen that dozens of lesions spread across the whole body. Manual reading of all these distributed lesions is usually tedious for physicians and can result in large interobserver variations [18] and may be prone to errors. Although metabolic lesion volume is a prognostic index for the interpretation of MM PET images [19], it is necessary to identify the lesions before the calculation of characteristic quantities such as the maximum of standardized uptake value within tumor (SUVmax) and total lesion evaluation (TLE) [20, 21].

Computer-aided detection (CAD) has been developed to assist radiologists to resolve the critical information from complex data, which improves the accuracy and robustness of diagnosis [22–25]. Machine learning is the engine for typical CAD approaches. Several methods have been developed for lesion detection or tumor screening in oncological applications [26, 27], in which lesion and nonlesion parts are differentiated and segmented. For hybrid imaging, either is characterized with low spatial resolution in PET or features with low contrast in CT, and a direct detection or cosegmentation of tumors in both modalities is difficult. Based on such concern, in [28, 29] a fuzzy locally adaptive Bayesian algorithm has been developed for volume determination for PET imaging and later applied in lung tumor delineation. In [30–33] Markov Random Field (MRF) and graph-cut based methods were integrated to encode shape and context priors into the model. Simultaneously model delineation of regions using random walk and object/background seed localization method were also being employed in joint segmentation. In [34] modality-specific visibility weighting scheme based on a fuzzy connectedness (FC) image segmentation algorithm was proposed to determine the boundary correspondences of lesions in varied imaging modalities.

In order to tackle the multiple myeloma lesion detection, classification, or other pathological analysis issues for the bone, several methods have been developed. A virtual calcium subtraction method [35] has been adopted to evaluate MM in the spine. The study of [36] focuses on detecting lesions in femur cortical bones, in which a probabilistic, spatially dependent density model has been developed to automatically identify bone marrow infiltration in low-dose CT. In [37] a semiautomatic software was developed to perform pixel thresholding based segmentation for the assessment of bone marrow metabolism while automatic quantification of bone marrow myeloma volume was conducted in [38]. A hybrid iterative reconstruction technique was used to compare the diagnostic performance of conventional radiography (CR) and whole-body low-dose computed

tomography (WBLDCT) with a comparable radiation dose reconstructed for MM staging [39]. However, none of the above-mentioned approaches can be directly transferred to automatically detect systemic bone lesions on PET imaging. As is shown in Figure 1, the ⁶⁸Ga-Pentixafor PET imaging has a large variation in uptake and size even among the lesions in the same patient. Such heterogeneity in lesion size and tracer uptake in the complex context of various nonspecific overexpression makes the whole-body detection of all the lesions extremely difficult. To the best of our knowledge, no effective CAD methods have been presented for automated detection of MM bone lesions in the full body.

The emergence of deep learning methods largely exceeds human perception power in extracting useful information from large amount of data such as images and conventional machine learning methods in many applications [26, 40, 41]. They have already demonstrated advantages in computerized diagnosis on medical images, such as abnormality detection [42, 43]. Convolutional neural networks (CNNs) are the driving force among many network architectures, and the current state-of-the-art work largely relies on CNN approaches to address the common semantic segmentation or detection tasks [44]. The combination of convolutional and deconvolutional layers can well extract high-level contextual and spatial features hierarchically. CNN architecture such as U-Net offers a 2D framework to segment biomedical images by using a contracting path for contextual extraction and a symmetric reversed path for object localization [45]. U-Net has been extended to a 3D version as V-Net [46] and achieves promising results by introducing an optimized objective function to train the model end-to-end. Similar 3D CNNs have been presented in [47] to learn intermediate features for brain lesion segmentation. A cascaded CNN has been developed to first segment the liver and then the liver lesions in [48].

This paper explores the advantages of cascaded CNNs in lesion prediction and segmentation with the aim of detecting MM bone lesion in a full body manner. For the first time, deep learning method is developed to combine anatomical and molecular information of ⁶⁸Ga-Pentixafor PET/CT imaging to support whole-body lesion identification. Besides employing V-Net, two enhanced V-Nets are cascaded to build a W-shaped framework to learn the volumetric feature representation of the skeleton and its lesions from coarse to fine. The whole network requires only minimal preprocessing and no postprocessing. We testify the algorithm on 70 digital phantoms generated by realistic simulation of ⁶⁸Ga-Pentixafor PET images to demonstrate the applicability of deep learning architectures in hierarchically extracting features and predicting the MM bone lesions. For proof-of-concept, the methods were further evaluated on 12 clinical PET/CT data and the results demonstrate the potential to improve MM bone lesion detection. In addition, we compared the proposed approach with several traditional machine learning methods, including random forest classifier, *k*-Nearest Neighbor (*k*-NN) classifier, and support vector machine (SVM) algorithm, in which cases the advantages of deep learning methods are more evidently shown.

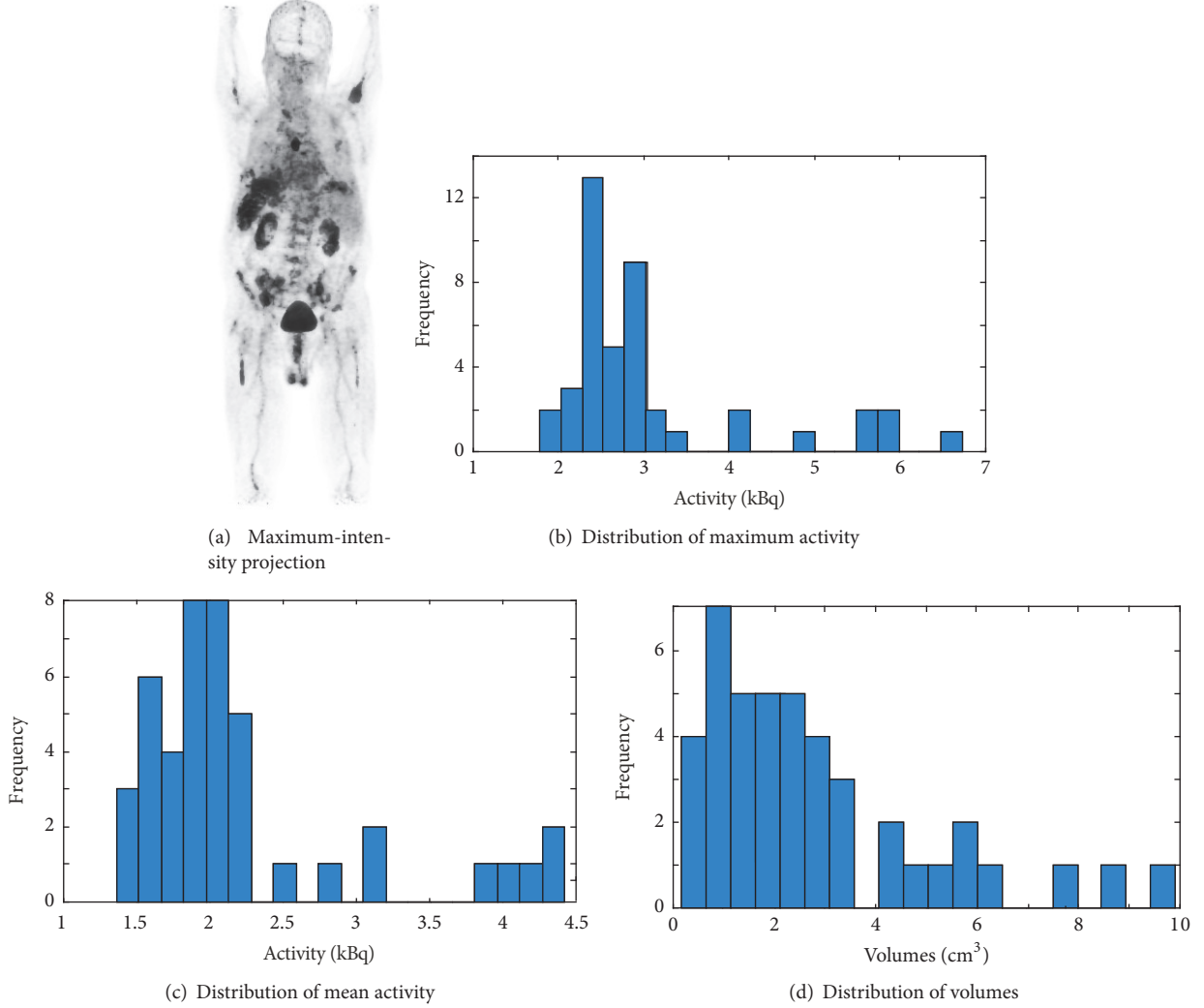


FIGURE 1: Properties of MM lesions of an exemplary patient with ^{68}Ga -Pentixafor PET imaging: (a) maximum-intensity projection of ^{68}Ga -Pentixafor PET; (b) histogram distribution of maximum activity of the lesions; (c) histogram distribution of mean activity of the lesions; (d) histogram distribution of volumes of the lesions.

2. Methods and Materials

2.1. Deep Learning Methods: V-Net and W-Net. In this study, we investigate a widely used CNN-based deep learning architecture, V-Net, for 3D volumetric image segmentation [46] on CT and PET images. 3D convolutions are performed aiming to extract features from both modalities. At the end of each stage, to reduce its resolution by using appropriate stride, the left part of the V-Net consists of a compression path, while the right part decompresses the signal until its original size is reached. Convolutions are all applied with appropriate padding. We assembled PET and CT into two channels of combined images for lesion segmentation.

In particular, we cascaded two V-Nets to form a W-Net architecture to improve the segmentation to bone-specific lesions in this study. As illustrated in Figure 2, there is a compression downward path, followed by an approximately symmetric decompression path inside each V-Net. The former cuts the volumetric size and broadens the receptive field

along the layers, while the latter functions the opposite way to expand the spatial support of the lower resolution feature maps. For both contracting and expanding paths, we use the $3 \times 3 \times 3$ kernel for convolution and a stride of two for max pooling or upsampling. For the first V-Net, only volumetric CT data is fed into the network in order to learn anatomical knowledge about the bone. The outcome builds a binary mask for the skeleton, which adaptively offers geometrical boundary for lesion localization. The second V-Net then adds both PET/CT and the output from the first network as the total input, of which PET/CT provides additional feature information to jointly predict the lesion. Since lesions have comparatively smaller size than the bone, the deeper a network goes, the more detailed information will vanish even if adding concatenations from layers in the contracting path. For the W-Net, we use five layers in the first V-Net and three layers for the second V-Net. For the single V-Net architecture, 3 layers are adopted.

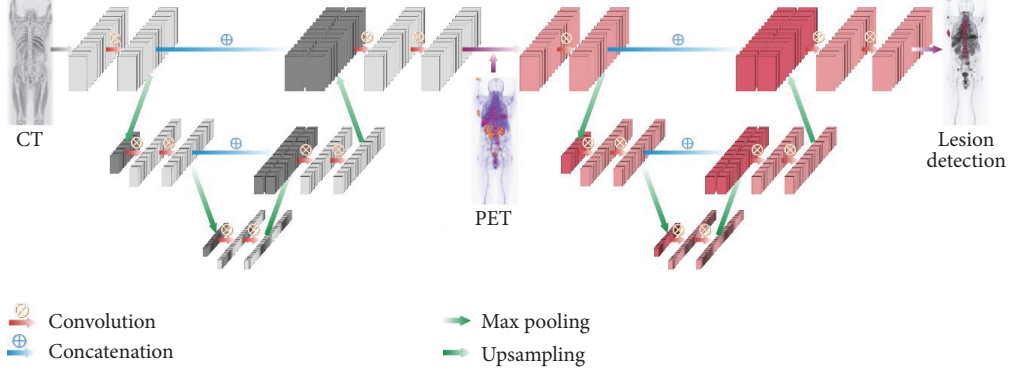


FIGURE 2: Overview of a simplified W-Net architecture.

All the experiments are implemented on Theano using Python 2.7 and all the PET/CT volumes are trained on NVIDIA TITAN X with a GPU memory of 12 GB. We employed 3-fold cross validation to test the prediction accuracy.

There exists high imbalance in the dataset, especially for lesion labels with very small sizes. In order to better track tiny lesions and balance different sizes of the bone systemically, we also adopt a similar weight balance strategy as in [48]. For the input CT volume V and a given voxel i , there is a set of labels containing two values, of which 0 denotes nonbone regions and 1 denotes bones. As for the PET volumes in the binary label set, 0 denotes nonmyeloma part and 1 indicates MM lesions. We define $p(x_i = l \vee V)$ to be the probability that a voxel i is being assigned a label l given the volume V , with the label set $l \in [0, 1]$. Then a cross-entropy loss function L is defined as follows:

$$L = \frac{-1}{N} \sum_{i=1}^N \omega_i^{\text{label}} [\hat{p}_i \log p_i + (1 - \hat{p}_i) \log (1 - p_i)]. \quad (1)$$

In (1), \hat{p}_i is the ground truth while p_i is the probability assigned to voxel i when it belongs to the foreground. ω_i^{label} is set to be inversely proportional to the number of voxels that belong to a certain label.

Besides, we adopt another balance implementation, which is patch-based balance strategy. We subsample the training dataset to bridge the gap between the labels (bone and lesion) and the background. For each patient, we pretrain our network by first extracting patches of size $(64 \times 64 \times 64)$ across the whole patient volume, with an overlap of 5 voxels in all directions. We then select the top 30 patches per patient volume based on the ratio of label to background in each patch. These selected patches improve the total label to background ratio for the bone label from a percentage of 12.35% to 20.16% and for the lesion label from a percentage of 2.54% to 7.01%.

With the class balancing loss function and the patches used in V-Net, we pretrain the network for 1000 iterations. Stochastic gradient descent with a learning rate of 0.001 and a momentum of 0.95 is performed for every 100 iterations. We then use the entire training set to fine-tune the network

until it converges following the same setup as is adopted in the pretraining process. This training scheme is employed for both bone and lesion segmentation tasks.

Dice score was calculated to estimate the segmentation accuracy. In addition, the lesionwise detection accuracies (sensitivity, specification, and precision) were summarized on the segmented results based on the criteria of patch overlapping. Patches of size $9 \times 9 \times 9$ were generated across the lesions with an overlap of 4 voxels being added in all three directions. A lesion was considered as detected when the amount of lesion labels that fell into the patch was above 10%.

We calculate precision and other relevant metrics via patch overlapping, where the annotated ground truth patch is considered positive if at least 10% of the total voxels in the patch are a lesion and negative otherwise.

2.2. Test on Realistic PET Phantoms. To evaluate the performance of deep learning methods for lesion detection, we generated realistic digital phantoms of ^{68}Ga -Pentixafor PET scans. Digital phantoms using physically based simulations provide ground truth to in-depth evaluate the performance of algorithms [49]. Realistic PET activities extracted from patient data were assigned to a whole-body phantom with CT and anatomical labels such as liver, spleen, and kidney. Bone lesions of various sizes, shapes, and uptakes at different locations were generated randomly in skeleton of phantoms to represent a large diversity of lesion presentations. The CT values were modified accordingly by considering severity of lesions. Realistic PET measurements of the phantoms were simulated by a forward projection model following the procedures described in [50]. This model includes object attenuation as well as the system geometry resembling the characteristics of a real clinical scanner (Siemens Biograph mMR [51]). With the scanner geometry described above, scattered events within the phantom and detectors were simulated using GATE V6. These events were sorted out from the GATE output and formed the expectation of scatter sinogram. In this simulation, 30% scattered and 30% uniformly distributed random events were included considering a large positron range of Ga-68. Poisson noise was then generated in each sinogram bin. Finally, a set of sinograms (90 bins and

TABLE 1: Experimental results of phantom study using synthetic PET/CT using V-Net, random forest (RF), k -Nearest Neighbor (k -NN), and support vector machine (SVM).

Performance (%)	Sensitivity	Specificity	Precision	Dice
V-Net	89.71	99.68	88.82	89.26
RF with $n = 20$	99.16	89.49	12.18	21.69
k NN with $k = 15$	98.52	90.38	12.41	23.09
SVM with $C = 0.5$	98.76	92.15	15.60	26.94

160 projections) was generated with the expectation of the total counts to be 1 million. In total, 70 digital phantoms of different lesions were simulated.

2.3. Test on Clinical Data. 12 patients (3 female and 9 male) with histologically proven primary multiple myeloma disease were referred for ^{68}Ga -Pentixafor PET/CT imaging (Siemens Biograph mCT 64; Siemens Medical Solutions, Germany). Approximately 90 to 205 MBq ^{68}Ga -Pentixafor was injected intravenously 1 hour before the scan. A low-dose CT (20 mAs, 120 keV) covering the body from the base of skull to the proximal thighs was acquired for attenuation correction. PET emission data were acquired using a 3D mode with a 200×200 matrix for 3 min emission time per bed position. PET data were corrected for decay and scattering and iteratively reconstructed with attenuation correction. This study was approved by the corresponding ethics committees. Patients were given written informed consent prior to the investigations.

The coregistration of PET and CT was visually inspected using PMOD (PMOD Technologies Ltd., Switzerland). With the fusion of PET and CT, all the lesions were manually annotated under the supervision of experienced radiologist, then each lesion was segmented by local thresholding at half maximum.

2.4. Comparison with Traditional Machine Learning Methods. Traditional machine learning methods [52] including random forest, k -NN, and SVM were employed in this study for the comparison with deep learning methods. The patch-based intensity information was extracted as features for different algorithmic implementation. Multimodality features were obtained by taking the PET and CT intensities patchwise with a size of $3 \times 3 \times 3$ in order that neighbor and intensity information can be encoded. For training, a total of 2000 lesion samples (patches) and 2000 nonlesion samples for each data volume were randomly selected and normalized to form the feature space. Each sample in the training/test set was represented as an intensity-based feature vector of 54 dimensions. Then the principal component analysis (PCA) was applied to reduce the dimensionality to 15 and the grid search with 3-fold cross validation was used to select the parameters. For random forest, the number of trees n was set to 20. For k -NN, the number of neighbors k was set to 15. For SVM, we choose a linear kernel, and the penalty parameter of the error term C was set to 0.5.



FIGURE 3: Synthetic PET data generating from digital phantom and its corresponding CT scan.

3. Results and Discussions

An exemplary coronal slice of simulated ^{68}Ga -Pentixafor PET and its corresponding CT scan are shown in Figure 3. The simulated PET images present visual similarities to real PET measures. The detection results of 3 slices of different body regions in axial plane are shown in Figure 4 and the test results on 70 of these realistic digital phantoms are listed in Table 1. It achieves specificity as high as 99.68% and the Dice score is also remarkable with a value of 89.26%, which confirm that deep learning method has the potential to detect the whole-body MM lesions.

The comparisons between V-Nets and W-Net using clinical dataset are summarized in Table 2. For the deep learning methods, the combination of PET and CT for V-Net improves the Dice score (69.49%) compared to V-Net with CT alone (26.37%) or PET alone (28.51%). For lesionwise accuracy, the combination of PET and CT for V-Net achieves higher specificity (99.51%) than V-Net using CT (94.43%) or PET (96.04%) and lower sensitivity than V-Net with CT alone (73.18%). For V-Net, the combination of CT and PET can improve the lesion segmentation; however, it does not bring much benefit to the sensitivity. This is because CT volume represents good anatomical structure and is sensitive to abnormal structure of lesions. The mixture usage of CT and PET in lesion detection does not increase the possibility of capturing such feature.

TABLE 2: Experimental results of V-Nets and W-Net for MM bone lesion detection. Best results are indicated in italic.

Performance (%)	Sensitivity	Specificity	Precision	Dice
V-Net + CT	73.18	94.43	16.08	26.37
V-Net + PET	61.77	96.04	18.53	28.51
V-Net + PET/CT	71.06	99.51	68.00	69.49
<i>W-Net + PET/CT</i>	<i>73.50</i>	<i>99.59</i>	<i>72.46</i>	<i>72.98</i>

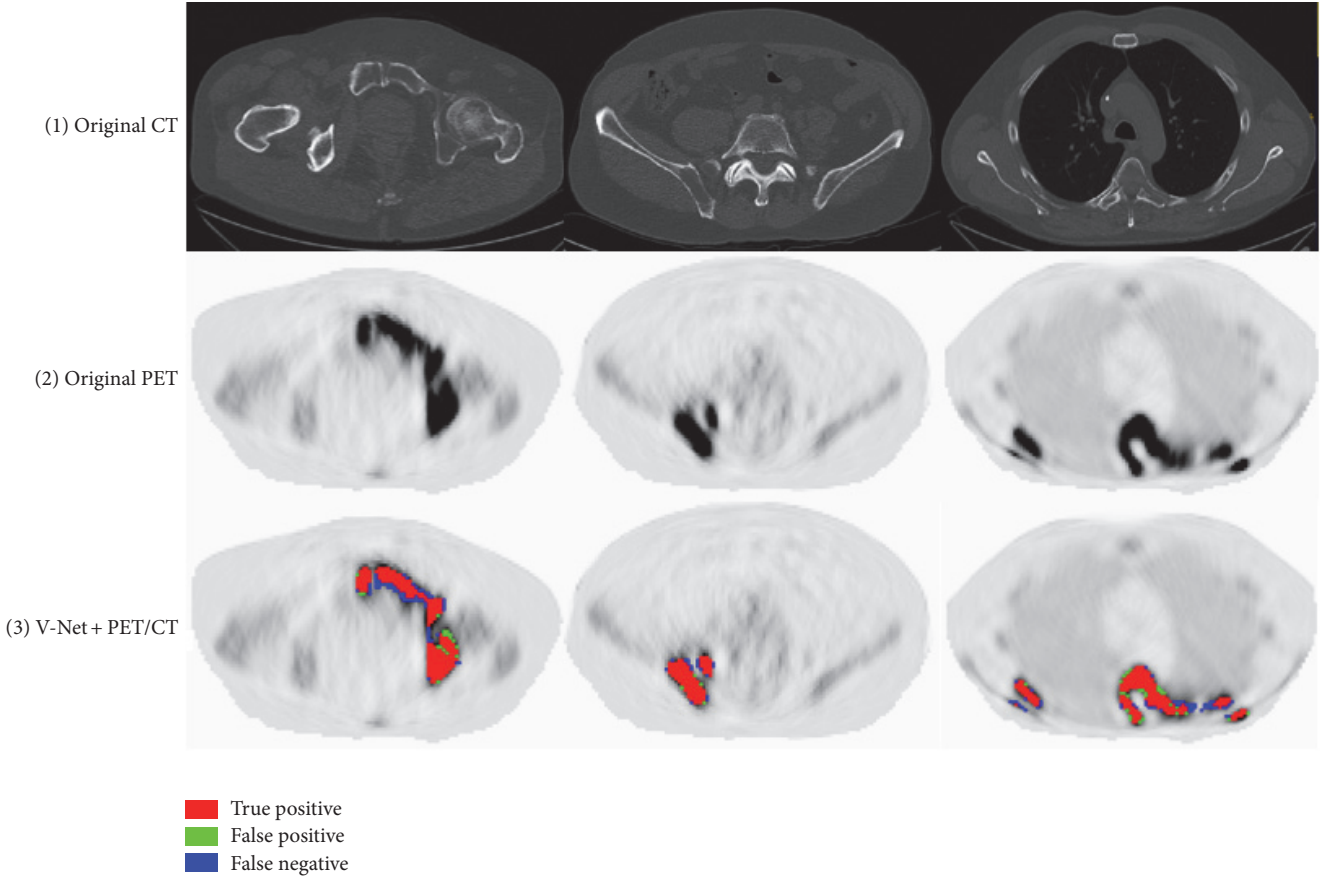


FIGURE 4: Exemplary detection results of phantom study: (1) the original axial CT slices; (2) the corresponding PET slices; (3) MM lesion prediction using V-Net.

W-Net, which also combines PET and CT, reaches the highest segmentation accuracy (Dice score 72.98%) and lesion detection accuracy (sensitivity 73.50%, specificity 99.59%, and precision 72.46%). In contrast to V-Net, W-Net distinguishes the information on CT and PET, and the extracted CT skeleton can be utilized as a type of regularization. The maximization of information utilization improves the segmentation and lesion detection. However, given the expensive computation by adding an extra V-Net, the sophisticated W-Net only slightly improves the performance (around 2% to 4%) compared to V-Net with PET/CT input. This can be elucidated in two aspects. On one hand, the hybrid input already contains anatomic information, which is encoded and learnt as important features by the single V-Net. On the other hand, the overall performance of the W-Net may be restricted by the first V-Net. If the skeleton mask is not

correctly labeled, its segmentation error will be propagated to the second V-Net and once again cause negative effect on subsequent lesion detection. Further improvement of the individual V-Net may improve the overall performance. Besides, all the methods obtain high specificity (true negative rate) of more than 90%, which demonstrate that the deep learning methods can properly exclude nonlesion parts.

Exemplary detection results of 3 slices of different body regions using deep learning methods are visualized in axial plane in Figure 5, where the false positive and false negative are marked out for in-depth comparison. Typically, false negatives occur when the lesion is too small while the contrast is not high enough to identify its presence. False positives are highly intensity driven, which considers the nonspecific high tracer uptake as lesion by mistake. The V-Net with CT or PET alone predicted lesions in low accuracy with

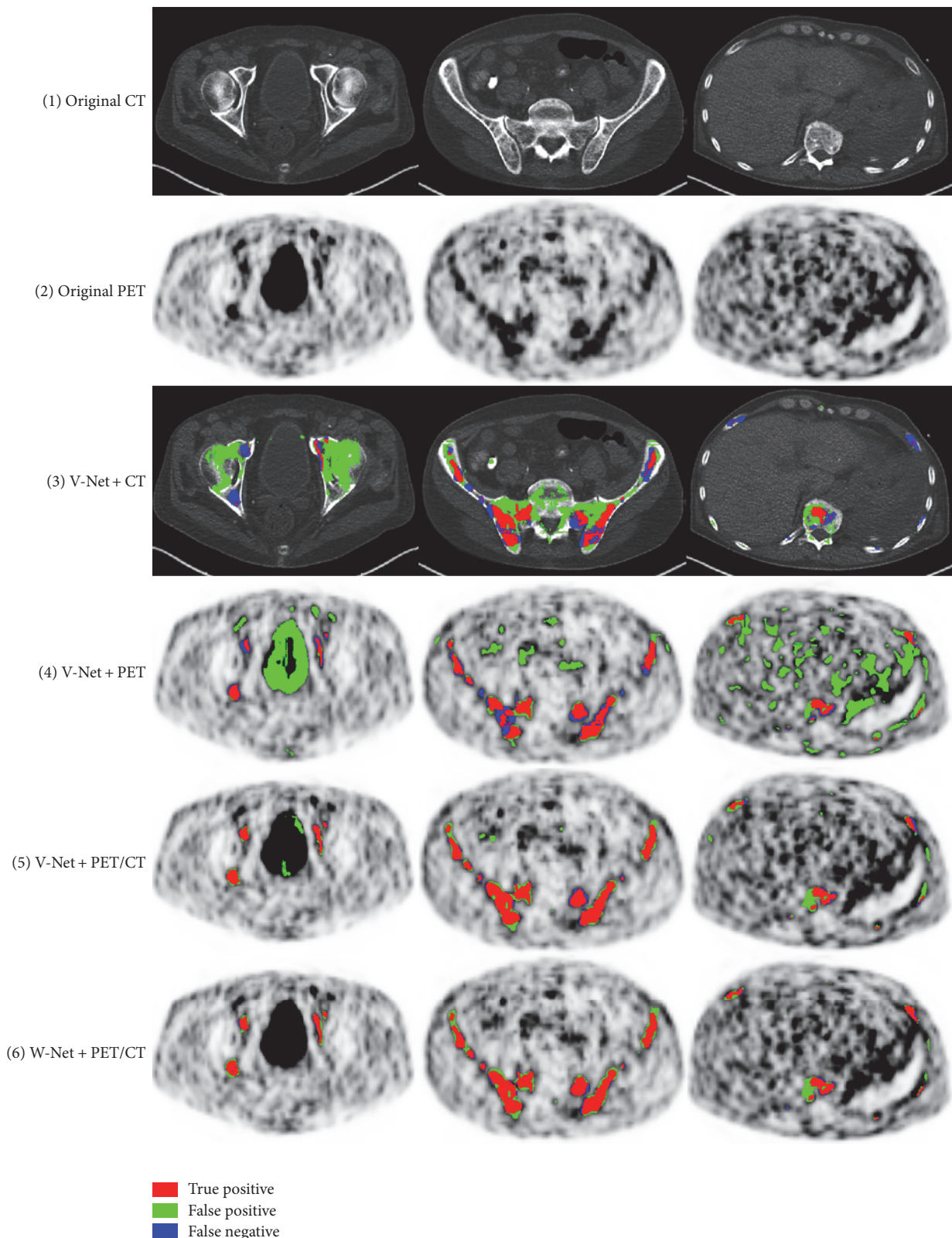


FIGURE 5: Exemplary detection results of V-Nets and W-Net: (1) the original axial CT slices; (2) the corresponding PET slices; (3) MM lesion prediction using CT alone in V-Net; (4) MM lesion prediction using PET alone in V-Net; (5) MM lesion prediction using PET/CT in V-Net; (6) MM lesion detection using W-Net.

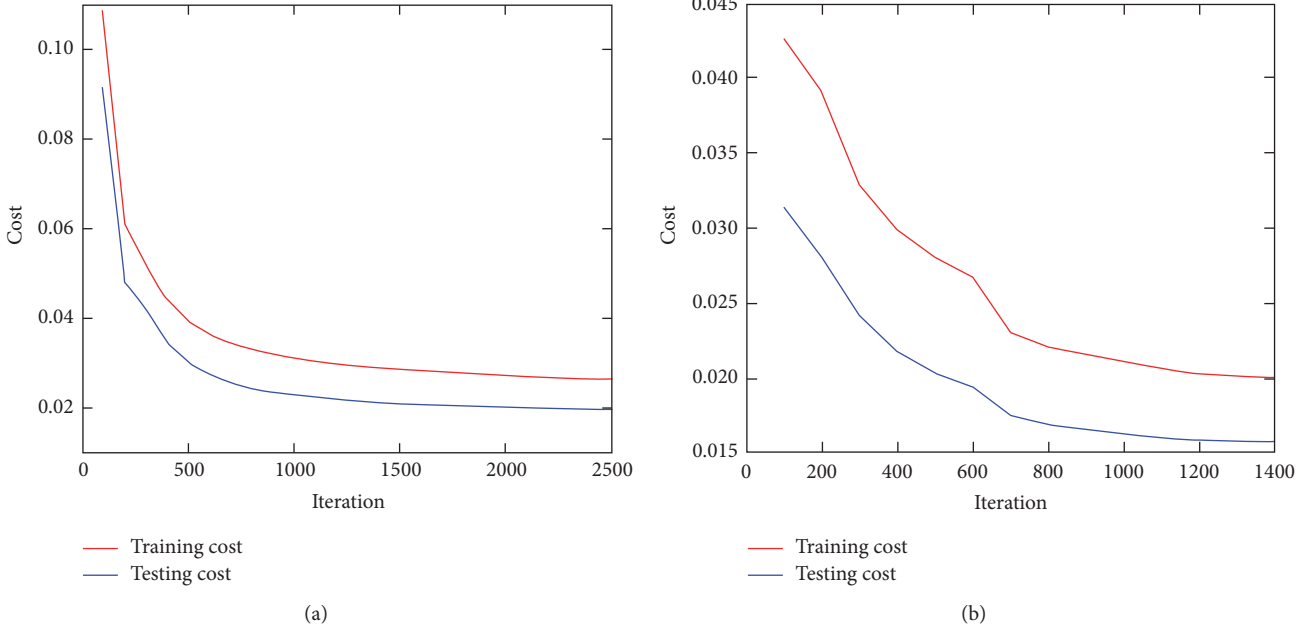


FIGURE 6: Convergence curves of different network architectures, W-Net (a) or V-Net (b).

lots of false negative and false positives. The V-Net with hybrid PET/CT data as input is capable of learning features from both modalities. It can generally prevent false positive prediction to a large extent. For W-Net, the obtained binary skeleton mask is forwarded to the second V-Net together with PET/CT volumes. Therefore, W-Net geometrically offers extra anatomical restrictions and reduces the probability of assigning wrong lesion labels, which further improves the detection performance compared to V-Net of the same input. The convergence curves for different networks are shown in Figure 6.

The experimental results of conventional machine learning methods (RF, k -NN, and SVM) are shown in Table 1. For the traditional methods, all of them achieve comparable good sensitivity and specificity. However, to the exact voxelwise discrimination of correct classes, random forest obtains a Dice score of 21.69%, k -NN gives a Dice score of 23.09%, and SVM shows a Dice score of 26.94%. The outperformance of SVM over random forest and k -NN indicates that SVM is more capable of providing a hyperplane in distinguishing nonlesion regions from lesion regions than the other two. For random forest, it might be explained as that bone lesions are in quite a small quantity compared to the rest of healthy parts of the whole body, which results in the data to be rather sparse and hinders its performance. This is exactly the advantage when applying sparse data to SVM. For k -NN, the reason behind it might be that the pure calculation of Euclidean distance as the features to predict the closeness of testing voxel and the training samples does not fit for bone lesions spread over the full body.

For the first time, this study proposed a deep learning method to automatically detect and segment the whole-body MM bone lesions on CXCR-4 PET/CT imaging. It can

efficiently leverage the potential information inside multimodal imaging instead of extracting handcrafted features that are difficult to identify or reach an evaluation consensus. However, the current study is restricted by small number of patient data. Even though we tried to augment the number of training samples by generating patches, the performance of the deep learning methods is still hampered. Nevertheless, this explorative study demonstrated the potential of deep learning methods in combining multimodal information for lesion detection. The preliminary results support the further development of deep learning methods for whole-body lesion detection. With the evolution of CXCR-4 imaging and therapy in clinical practice, more and more subjects will be enrolled for the tests. The performance of deep learning is expected to be improved with the availability of more data volumes. Besides, we only focus on the detection of bone lesions of multiple myeloma in this proof-of-concept study and lesions outside the bone are not considered. This is not realistic for multiple myeloma patients with possible extramedullary lesions. The W-Net architecture can be naturally extended to the detection of lesions outside the bone by incorporating more labels of other tissue types and lesions. However, this needs sufficient data to make the training and test converge, which may be achieved with an increased number of subjects.

4. Conclusion

This study proposed the first computer-aided MM bone lesion detection approach on whole-body ^{68}Ga -Pentixafor PET/CT imaging. It explored two deep learning architectures, that is, V-Net and W-Net, for lesion segmentation and detection. The deep learning methods can efficiently combine

the information inside multimodal imaging and do not require the extraction of handcrafted features that are difficult to identify with regard to intermodality characteristics. We demonstrate the feasibility of deep learning methods by conducting realistic digital phantom study. Traditional machine learning methods were also compared to further confirm the advantage of deep learning approaches in handling lesion heterogeneities. The preliminary results based on limited number of data support the W-Net, which incorporates additional skeletal information as a kind of regularization for MM bone lesion detection. Increasing the amount of data may further enhance the performance of the proposed deep learning method. The trial of this study makes a step further towards developing an automated tool for the management of multiple myeloma disease.

Conflicts of Interest

The authors declare that they have no conflicts of interest.

Authors' Contributions

Lina Xu, Giles Tetteh, Kuangyu Shi, and Bjoern H. Menze contributed equally to the article.

Acknowledgments

This work was supported by China Scholarship Council under Grant no. 201306890013. This work was also supported by the German Research Foundation (DFG) and the Technical University of Munich (TUM) in the framework of the Open Access Publishing Program. The authors deeply acknowledge NVIDIA Corporation for the donation of the Titan X Pascal GPU for this research.

References

- [1] E. Terpos and N. Kanellias, *Practical Considerations for Bone Health in Multiple Myeloma Personalized Therapy for Multiple Myeloma*, Springer, 2018.
- [2] E. Terpos and M.-A. Dimopoulos, "Myeloma bone disease: Pathophysiology and management," *Annals of Oncology*, vol. 16, no. 8, pp. 1223–1231, 2005.
- [3] C. D. Collins, "Problems monitoring response in multiple myeloma," *Cancer Imaging*, vol. 5, no. special issue A, pp. S119–S126, 2005.
- [4] N. S. Callander and G. D. Roodman, "Myeloma bone disease," *Seminars in Hematology*, vol. 38, no. 3, pp. 276–285, 2001.
- [5] S. Lütje, J. W. J. Rooy, S. Croockewit, E. Koedam, W. J. G. Oyen, and R. A. Raymakers, "Role of radiography, MRI and FDG-PET/CT in diagnosing, staging and therapeutical evaluation of patients with multiple myeloma," *Annals of Hematology*, vol. 88, no. 12, pp. 1161–1168, 2009.
- [6] M. Dimopoulos, E. Terpos, R. L. Comenzo et al., "International myeloma working group consensus statement and guidelines regarding the current role of imaging techniques in the diagnosis and monitoring of multiple Myeloma," *Leukemia*, vol. 23, no. 9, pp. 1545–1556, 2009.
- [7] M. Horger, C. D. Claussen, U. Bross-Bach et al., "Whole-body low-dose multidetector row-CT in the diagnosis of multiple myeloma: an alternative to conventional radiography," *European Journal of Radiology*, vol. 54, no. 2, pp. 289–297, 2005.
- [8] J. C. Dutoit and K. L. Verstraete, "MRI in multiple myeloma: a pictorial review of diagnostic and post-treatment findings," *Insights into Imaging*, vol. 7, no. 4, pp. 553–569, 2016.
- [9] M. A. Dimopoulos, J. Hillengass, S. Usmani et al., "Role of magnetic resonance imaging in the management of patients with multiple myeloma: a consensus statement," *Journal of Clinical Oncology*, vol. 33, no. 6, pp. 657–664, 2015.
- [10] D. Van Lammeren-Venema, J. C. Regelink, I. I. Riphagen, S. Zweegman, O. S. Hoekstra, and J. M. Zijlstra, "18F-fluorodeoxyglucose positron emission tomography in assessment of myeloma-related bone disease: a systematic review," *Cancer*, vol. 118, no. 8, pp. 1971–1981, 2012.
- [11] Y. Nakamoto, "Clinical contribution of PET/CT in myeloma: from the perspective of a radiologist," *Clinical Lymphoma, Myeloma & Leukemia*, vol. 14, no. 1, pp. 10–11, 2014.
- [12] C. F. Healy, J. G. Murray, S. J. Eustace, J. Madewell, P. J. O'Gorman, and P. O'Sullivan, "Multiple myeloma: a review of imaging features and radiological techniques," *Bone Marrow Research*, vol. 2011, pp. 1–9, 2011.
- [13] M. Cavo, E. Terpos, C. Nanni et al., "Role of 18 F-FDG PET/CT in the diagnosis and management of multiple myeloma and other plasma cell disorders: a consensus statement by the International Myeloma Working Group," *The Lancet Oncology*, vol. 18, no. 4, pp. e206–e217, 2017.
- [14] P. Moreau, M. Attal, D. Caillot et al., "Prospective evaluation of magnetic resonance imaging and [18F] fluorodeoxyglucose positron emission tomography-computed tomography at diagnosis and before maintenance therapy in symptomatic patients with multiple myeloma included in the IFM/DFCI 2009 trial: results of the IMAJEM study," *Journal of Clinical Oncology*, vol. 35, no. 25, pp. 2911–2918, 2017.
- [15] T. Vag, C. Gerngross, P. Herhaus et al., "First experience with chemokine receptor CXCR4 Targeted PET imaging of patients with solid cancers," *Journal of Nuclear Medicine*, vol. 57, no. 5, pp. 741–746, 2016.
- [16] K. Philipp-Abbrederis, K. Herrmann, S. Knop et al., "In vivo molecular imaging of chemokine receptor CXCR4 expression in patients with advanced multiple myeloma," *EMBO Molecular Medicine*, vol. 7, no. 4, pp. 477–487, 2015.
- [17] C. Lapa, M. Schreder, A. Schirbel et al., "[68Ga]Pentixafor-PET/CT for imaging of chemokine receptor CXCR4 expression in multiple myeloma—comparison to [18F]FDG and laboratory values," *Theranostics*, vol. 7, no. 1, pp. 205–212, 2017.
- [18] A. L. Belton, S. Saini, K. Liebermann, G. W. Boland, and E. F. Halpern, "Tumour size measurement in an oncology clinical trial: comparison between off-site and on-site measurements," *Clinical Radiology*, vol. 58, no. 4, pp. 311–314, 2003.
- [19] R. Fonti, M. Larobina, S. Del Vecchio et al., "Metabolic tumor volume assessed by 18F-FDG PET/CT for the prediction of outcome in patients with multiple myeloma," *Journal of Nuclear Medicine*, vol. 53, no. 12, pp. 1829–1835, 2012.
- [20] B. Foster, U. Bagci, A. Mansoor, Z. Xu, and D. J. Mollura, "A review on segmentation of positron emission tomography images," *Computers in Biology and Medicine*, vol. 50, pp. 76–96, 2014.

- [21] U. Bagci, J. K. Udupa, N. Mendhiratta et al., "Joint segmentation of anatomical and functional images: applications in quantification of lesions from PET, PET-CT, MRI-PET, and MRI-PET-CT images," *Medical Image Analysis*, vol. 17, no. 8, pp. 929–945, 2013.
- [22] A. T. Taylor and E. V. Garcia, "Computer-assisted diagnosis in renal nuclear medicine: Rationale, methodology, and interpretative criteria for diuretic renography," *Seminars in Nuclear Medicine*, vol. 44, no. 2, pp. 146–158, 2014.
- [23] N. Petrick, B. Sahiner, S. G. Armato III et al., "Evaluation of computer-aided detection and diagnosis systems," *Medical Physics*, vol. 40, no. 8, Article ID 087001, 2013.
- [24] F. J. Gilbert, S. M. Astley, M. G. C. Gillan et al., "Single reading with computer-aided detection for screening mammography," *The New England Journal of Medicine*, vol. 359, no. 16, pp. 1675–1684, 2008.
- [25] L. H. Eadie, P. Taylor, and A. P. Gibson, "A systematic review of computer-assisted diagnosis in diagnostic cancer imaging," *European Journal of Radiology*, vol. 81, no. 1, pp. e70–e76, 2012.
- [26] H. Shin, H. R. Roth, M. Gao et al., "Deep convolutional neural networks for computer-aided detection: CNN architectures, dataset characteristics and transfer learning," *IEEE Transactions on Medical Imaging*, vol. 35, no. 5, pp. 1285–1298, 2016.
- [27] K. Kouros, T. P. Exarchos, K. P. Exarchos, M. V. Karamouzis, and D. I. Fotiadis, "Machine learning applications in cancer prognosis and prediction," *Computational and Structural Biotechnology Journal*, vol. 13, pp. 8–17, 2015.
- [28] M. Halt, C. C. Le Rest, A. Turzo, C. Roux, and D. Visvikis, "A fuzzy locally adaptive Bayesian segmentation approach for volume determination in PET," *IEEE Transactions on Medical Imaging*, vol. 28, no. 6, pp. 881–893, 2009.
- [29] M. Hatt, C. Cheze-Le Rest, A. Van Baardwijk, P. Lambin, O. Pradier, and D. Visvikis, "Impact of tumor size and tracer uptake heterogeneity in 18F-FDG PET and CT non-small cell lung cancer tumor delineation," *Journal of Nuclear Medicine*, vol. 52, no. 11, pp. 1690–1697, 2011.
- [30] Q. Song, M. Chen, J. Bai, M. Sonka, and X. Wu, "Surface-region context in optimal multi-object graph-based segmentation: robust delineation of pulmonary tumors," in *Information Processing in Medical Imaging*, vol. 6801 of *Lecture Notes in Computer Science*, pp. 61–72, Springer, Berlin, Heidelberg, Germany, 2011.
- [31] Q. Song, J. Bai, D. Han et al., "Optimal Co-segmentation of tumor in PET-CT images with context information," *IEEE Transactions on Medical Imaging*, vol. 32, no. 9, pp. 1685–1697, 2013.
- [32] Q. Song, J. Bai, M. K. Garvin, M. Sonka, J. M. Buatti, and X. Wu, "Optimal multiple surface segmentation with shape and context priors," *IEEE Transactions on Medical Imaging*, vol. 32, no. 2, pp. 376–386, 2013.
- [33] W. Ju, D. Xiang, B. Zhang, L. Wang, I. Kopriva, and X. Chen, "Random walk and graph cut for co-segmentation of lung tumor on PET-CT images," *IEEE Transactions on Image Processing*, vol. 24, no. 12, pp. 5854–5867, 2015.
- [34] Z. Xu, U. Bagci, J. K. Udupa, and D. J. Mollura, "Fuzzy connectedness image Co-segmentation for HybridPET/MRI and PET/CT scans," in *Proceedings of the CMMI-MICCAI*, vol. 22, pp. 15–24, Springer, 2015.
- [35] C. Thomas, C. Schabel, B. Krauss et al., "Dual-energy CT: Virtual calcium subtraction for assessment of bone marrow involvement of the spine in multiple myeloma," *American Journal of Roentgenology*, vol. 204, no. 3, pp. W324–W331, 2015.
- [36] F. Martínez-Martínez, J. Kybic, L. Lambert, and Z. Mecková, "Fully automated classification of bone marrow infiltration in low-dose CT of patients with multiple myeloma based on probabilistic density model and supervised learning," *Computers in Biology and Medicine*, vol. 71, pp. 57–66, 2016.
- [37] P. Leydon, M. O'Connell, D. Greene, and K. Curran, *Semi-automatic Bone Marrow Evaluation in PETCT for Multiple Myeloma Annual Conference on Medical Image Understanding and Analysis*, Springer, 2017.
- [38] Y. Nishida, S. Kimura, H. Mizobe et al., "Automatic digital quantification of bone marrow myeloma volume in appendicular skeletons—clinical implications and prognostic significance," *Scientific Reports*, vol. 7, no. 1, article 12885, 2017.
- [39] L. Lambert, P. Ourednicek, Z. Meckova, G. Gavelli, J. Straub, and I. Spicka, "Whole-body low-dose computed tomography in multiple myeloma staging: superior diagnostic performance in the detection of bone lesions, vertebral compression fractures, rib fractures and extraskeletal findings compared to radiography with similar radiation exposure," *Oncology Letters*, vol. 13, no. 4, pp. 2490–2494, 2017.
- [40] D. Silver, A. Huang, C. J. Maddison et al., "Mastering the game of Go with deep neural networks and tree search," *Nature*, vol. 529, no. 7587, pp. 484–489, 2016.
- [41] Y. LeCun, Y. Bengio, and G. Hinton, "Deep learning," *Nature*, vol. 521, no. 7553, pp. 436–444, 2015.
- [42] N. Tajbakhsh, M. B. Gotway, and J. Liang, "Computer-aided pulmonary embolism detection using a novel vessel-aligned multi-planar image representation and convolutional neural networks," in *Proceedings of the International Conference on Medical Image Computing and Computer-Assisted Intervention (MICCAI '15)*, vol. 9350 of *Lecture Notes in Computer Science*, pp. 62–69, Springer, 2015.
- [43] H. R. Roth, L. Lu, and J. Liu, "Improving computer-aided detection using convolutional neural networks and random view aggregation," *IEEE Transactions on Medical Imaging*, vol. 35, no. 5, pp. 1170–1181, 2015.
- [44] J. Long, E. Shelhamer, and T. Darrell, "Fully convolutional networks for semantic segmentation," in *Proceedings of the IEEE Conference on Computer Vision and Pattern Recognition (CVPR '15)*, pp. 3431–3440, IEEE, Boston, MA, USA, June 2015.
- [45] O. Ronneberger, P. Fischer, and T. Brox, "U-net: convolutional networks for biomedical image segmentation," in *Proceedings of the International Conference on Medical Image Computing and Computer-Assisted Intervention and Medical Image Computing and Computer-Assisted Intervention (MICCAI '15)*, vol. 9351 of *Lecture Notes in Computer Science*, pp. 234–241, November 2015.
- [46] F. Milletari, N. Navab, and S.-A. Ahmadi, "V-Net: fully convolutional neural networks for volumetric medical image segmentation," in *Proceedings of the 4th International Conference on 3D Vision (3DV '16)*, pp. 565–571, IEEE, October 2016.
- [47] K. Kamnitsas, C. Ledig, V. F. J. Newcombe et al., "Efficient multi-scale 3D CNN with fully connected CRF for accurate brain lesion segmentation," *Medical Image Analysis*, vol. 36, pp. 61–78, 2017.
- [48] P. F. Christ, M. E. A. Elshaer, F. Ettlinger et al., "Automatic liver and lesion segmentation in CT using cascaded fully convolutional neural networks and 3D conditional random fields," in *Proceedings of the International Conference on Medical Image Computing and Computer-Assisted Intervention (MICCAI '16)*, vol. 9901 of *Lecture Notes in Computer Science*, pp. 415–423, Springer, October 2016.

- [49] M. A. Gavrielides, L. M. Kinnard, K. J. Myers et al., “A resource for the assessment of lung nodule size estimation methods: Database of thoracic CT scans of an anthropomorphic phantom,” *Optics Express*, vol. 18, no. 14, pp. 15244–15255, 2010.
- [50] X. Cheng, Z. Li, Z. Liu et al., “Direct parametric image reconstruction in reduced parameter space for rapid multi-tracer PET imaging,” *IEEE Transactions on Medical Imaging*, vol. 34, no. 7, pp. 1498–1512, 2015.
- [51] G. Delso, S. Fürst, B. Jakoby et al., “Performance measurements of the siemens mMR integrated whole-body PET/MR scanner,” *Journal of Nuclear Medicine*, vol. 52, no. 12, pp. 1914–1922, 2011.
- [52] P. Anbeek, K. L. Vincken, and M. A. Viergever, “Automated MS-lesion segmentation by k-nearest neighbor classification,” *MIDAS Journal*, 2008.

Research Article

Spectral Unmixing Imaging for Differentiating Brown Adipose Tissue Mass and Its Activation

Jing Yang,^{1,2} Jian Yang,^{1,3} and Chongzhao Ran¹ 

¹Molecular Imaging Laboratory, MGH/MIT/HMS Athinoula A. Martinos Center for Biomedical Imaging, Department of Radiology, Massachusetts General Hospital/Harvard Medical School, Room 2301, Building 149, Charlestown, Boston, MA 02129, USA

²School of Pharmacy, Soochow University, Suzhou 215006, China

³Center for Drug Discovery, School of Pharmacy, China Pharmaceutical University, Nanjing 210009, China

Correspondence should be addressed to Chongzhao Ran; cran@nmr.mgh.harvard.edu

Received 30 August 2017; Revised 5 December 2017; Accepted 11 December 2017; Published 4 January 2018

Academic Editor: Giancarlo Pascali

Copyright © 2018 Jing Yang et al. This is an open access article distributed under the Creative Commons Attribution License, which permits unrestricted use, distribution, and reproduction in any medium, provided the original work is properly cited.

Recent large-scale clinical analysis indicates that brown adipose tissue (BAT) mass levels inversely correlate with body-mass index (BMI), suggesting that BAT is associated with metabolic disorders such as obesity and diabetes. PET imaging with ¹⁸F-FDG is the most commonly used method for visualizing BAT. However, this method is not able to differentiate between BAT mass and BAT activation. This task, in fact, presents a tremendous challenge with no currently existing methods to separate BAT mass and BAT activation. Our previous results indicated that BAT could be successfully imaged in mice with near infrared fluorescent (NIRF) curcumin analogues. However, the results from conventional NIRF imaging could not reflect what portion of the NIRF signal from BAT activation contributed to the signal observed. To solve this problem, we used spectral unmixing to separate/unmix NIRF signal from oil droplets in BAT, which represents its mass and NIRF signal from blood, which represents BAT activation. In this report, results from our proof-of-concept investigation demonstrated that spectral unmixing could be used to separate NIRF signal from BAT mass and BAT activation.

1. Introduction

Brown adipose tissue (BAT) has been considered as “good fat,” due to its function of dissipating large amounts of chemical/food energy as heat to maintain the energy balance of the whole body [1–3]. Investigations of BAT have been ongoing for decades, particularly using animals. Reportedly, BAT has been assumed to have no physiologic relevance in adult humans, even though it is highly abundant in embryonic and early postnatal stages. However, this dogmatic opinion has been overturned by large clinical studies. In 2009, Cypess et al. reported that, by analyzing 3640 PET-CT images of 1,972 patients, BMI (body-mass index) inversely correlated with the amount of BAT, strongly suggesting that BAT is an important target in obesity and diabetes [4]. The existence of BAT in adults has been strongly endorsed by other important investigations as well [5–11]. Moreover, since 2009 numerous groundbreaking studies strongly support the significance

and potential benefits of BAT [12–33]. Characteristically, BAT contains a large number of mitochondria, abundant uncoupling protein-1 (UCP-1) expression, numerous small oil droplets in a single cell, and significant vascularization of BAT tissue [4, 34–37]. The above characteristics strongly imply that BAT plays an important role in metabolism and energy expenditure; therefore BAT is a potential target for diabetes and obesity therapy.

The assumption that BAT is “nonexistent” in adults is partially due to the lack of proper imaging methods to “see” the small BAT depots *in vivo*, as only 3%–8% of adult patients’ BAT depots could be clearly visualized with ¹⁸F-FDG if no cold or drug stimulation is applied [38–40]. However, under stimulated conditions, PET-FDG imaging has shown that BAT is still present in 95% health adults in the upper chest, neck, and other locations [4, 6, 8, 34, 35]. This remarkably large difference between unstimulated and stimulated conditions strongly indicates that PET-FDG

imaging only reflects the activation of BAT, but not BAT mass. Therefore, imaging probes that can consistently report BAT mass are highly desirable.

Accurately reporting BAT mass is a tremendous challenge for imaging scientists, due to the fact that BAT mass and BAT activation are intertwined under various conditions. It is obvious that there is no absolute “resting” status of BAT, and BAT activation cannot be “zero” for a living subject. Therefore, dissection of BAT mass and BAT activation is a remarkable challenge. However, most of the current imaging methods often reflect the summed signal from BAT mass and activation. Although PET-FDG imaging has significantly contributed to the “rediscovery” of BAT in adults, it primarily reflects BAT activation, but not BAT mass [41]. Similarly, most of other reported imaging methods are also BAT activation dependent [24, 41–51]. Our group has recently reported that near infrared fluorescence (NIRF) probe CRANAD-X ($X = -2, -3$, and -29) could be used for BAT mass imaging [52], and Cerenkov luminescence imaging with ^{18}F -FDG could be applied to image BAT in mice [53]. Via conventional NIRF imaging with CRANAD-29, BAT mass change in a streptozotocin-induced diabetic mouse model and BAT activation under cold exposure could be reported. In addition, the same method could be used to monitor “browning” of WAT that was induced by β 3-adrenoceptor agonist CL316,243 [52]. However, conventional NIRF imaging is not capable of dissecting the signal from BAT mass and from BAT activation.

To the best of our knowledge, there is no available imaging method for differentiating BAT mass and activation. The key to this challenge is to dissect BAT mass measurement from BAT physiology status (activated or suppressed). It is well known that BAT is highly vascularized, and activation of BAT is tightly closely associated with a significant increase of blood flow. Therefore, the change of blood flow has been considered to be a biomarker for BAT activation [54–56]. For a hydrophobic NIRF probe, its emission spectra are highly dependent on its environments [57]. In a hydrophobic environment such as in oil droplet of BAT mass, its emission spectra would be significantly blue-shifted [57]. Therefore, for the same NIRF probe, there will be apparent difference between the spectra from oil droplets of BAT and the spectra from blood flow. Previously, we have successfully utilized spectral unmixing technique to differentiate bound and free probe in the case of in vivo amyloid beta detection [58]. In this report, we demonstrated that spectral unmixing could be used to dissect NIRF signal from BAT mass and NIRF signal from blood flow [59]. With this technique, it is feasible to accurately report BAT mass and BAT activation/physiological status.

2. Methods and Materials

The reagents used for the synthesis were purchased from Aldrich and used without further purification. CRANAD-29 was synthesized according to our previously reported procedures [52]. All animal experimental procedures were approved by the Institutional Animal Care and Use Committee (IACUC) at Massachusetts General Hospital and carried

out in accordance with the approved guidelines. *In vivo* NIRF imaging was performed using the IVIS® Spectrum animal imaging system (Caliper Life Sciences, Perkin Elmer, Hopkinton, MA), and data analysis was conducted using Living Image® 4.2.1 software. Mice were anesthetized with isoflurane balanced with oxygen during image acquisition (less than 5 minutes for each imaging session).

2.1. Ex Vivo Spectral Unmixing with Dissected BAT and Blood. A two-month-old balb/c mouse was injected intravenously with $100 \mu\text{L}$ CRANAD-29 (0.4 mg/kg, 15% DMSO, 15% Cremophor EL, and 70% PBS pH 7.4). The mouse was sacrificed at 4 hours after the injection. BAT was dissected and 0.1 mL blood was collected. Sequence images were acquired with the following parameters: Ex/Em pairs: 605/660 nm, 640/680 nm, 640/700, 640/720 nm, 675/740 nm, 675/760 nm, and 675/780 nm. Exposure time is auto, FOV = B. Spectral unmixing was performed with Living Image® 4.2.1 software, and manual unmixing method was selected. The generated spectra for autofluorescence, BAT, and blood were saved as a spectral library for CRANAD-29.

2.2. In Vivo Spectral Unmixing of CRANAD-29 in Mice. A two-month-old balb/c mouse was injected intravenously with $100 \mu\text{L}$ CRANAD-29 (0.4 mg/kg, 15% DMSO, 15% Cremophor EL, and 70% PBS pH 7.4) in a 25°C room. Sequence images were captured at 4 hours after CRANAD-29 injection with the following parameters: Ex/Em pairs: 605/660 nm, 640/680 nm, 640/700, 640/720 nm, 675/740 nm, 675/760 nm, and 675/780 nm. Exposure time is auto, FOV = D. Spectral unmixing was performed with Living Image® 4.2.1 software, and Library Unmixing Method was selected.

2.3. In Vivo Spectral Unmixing of CRANAD-29 in Mice under Short Cold Exposure. Two-month-old balb/c mice ($n = 5$) were placed in a 4°C cold room for 2 hours before intravenous injection of CRANAD-29. After CRANAD-29 was totally washed out (about 10 days because of the slow clearance of CRANAD-29), the same group of mice were used as the control group ($n = 5$) and were placed in a 25°C room. Sequence images were acquired at 4 hours after probe injection with the same parameters as above in vivo imaging. For the cold exposure group, the mice were maintained at 4°C for 4 hours after probe injection. Spectral unmixing was performed with Living Image® 4.2.1 software, and Library Unmixing Method was selected. ROIs were manually drawn around the BAT area.

3. Results and Discussions

In our previous report, with conventional NIRF imaging, we demonstrated that CRANAD-29 had significant selectivity for BAT over WAT and could be used to monitor BAT activation and BAT mass changes [52]. For a NIRF probe, its residing environments have significant impact on its fluorescence properties, including intensity, emission spectrum, and lifetime. We hypothesized that the emission spectra of the same NIRF probe were different from oil droplets in BAT mass and from blood flow, due to their different residing

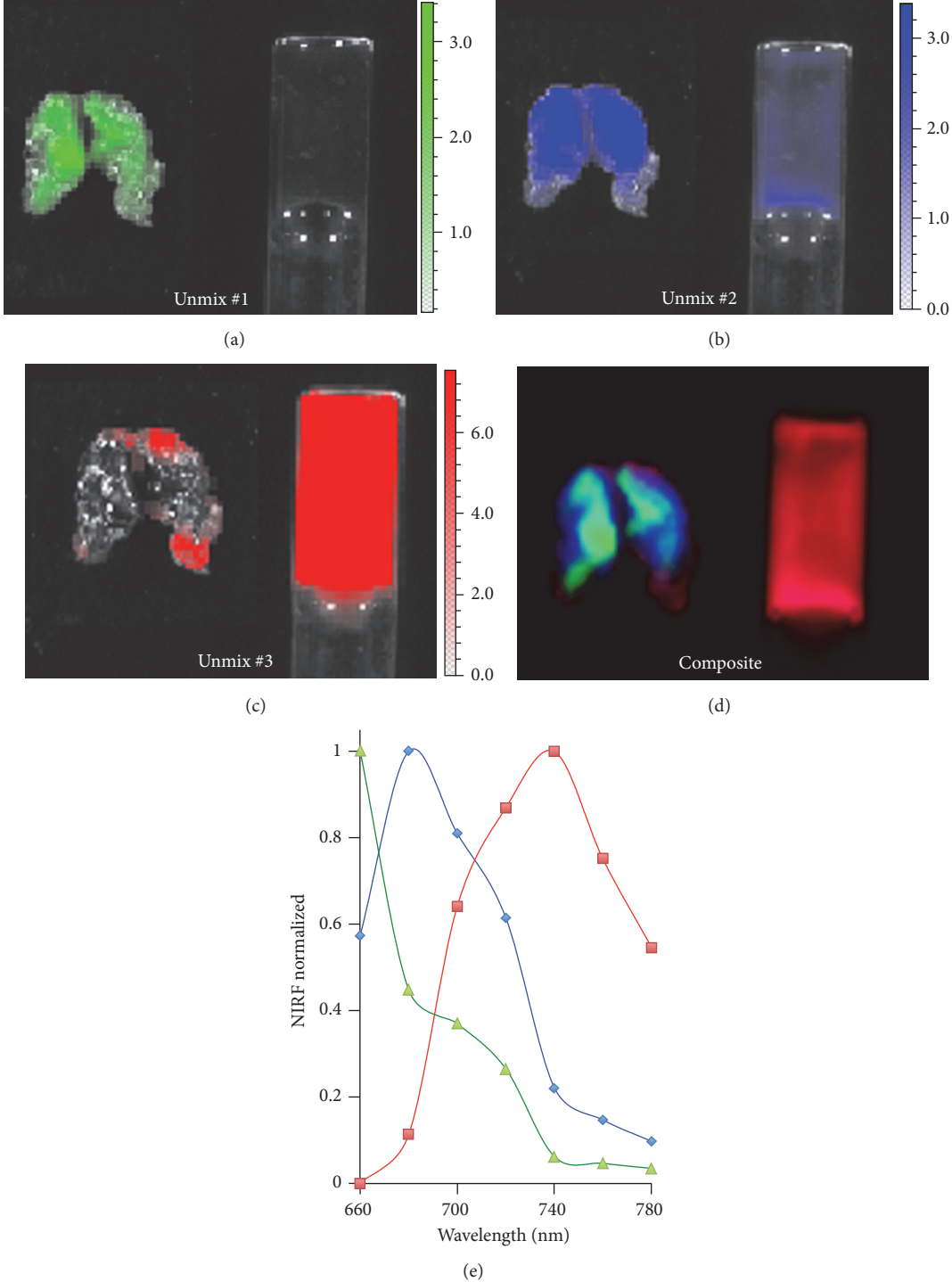


FIGURE 1: Spectral unmixing with CRANAD-29 for ex vivo BAT and blood. (a) Unmixed #1 represents autofluorescence signal and is corresponding to green line spectrum in (e). (b) Unmixed #1 represents NIRF signal from BAT mass and is corresponding to blue line spectrum in (e). (c) Unmixed #2 is for NIRF from blood and red line spectrum in (e). (d) Merged image of unmixed #1, #2, and #3. (e) Ex vivo unmixed spectra for autofluorescence (green), BAT mass (blue), and blood flow (red).

environments, and the spectral difference could be used for spectral unmixing.

To validate our hypothesis, we first conducted spectral unmixing imaging with ex vivo BAT tissue and blood from

a mouse injected with CRANAD-29. Sequence images were acquired with seven Ex/Em pairs, and spectral unmixing was conducted with Living Image® 4.2.1 software. As expected, we were able to differentiate BAT and blood, as evidenced

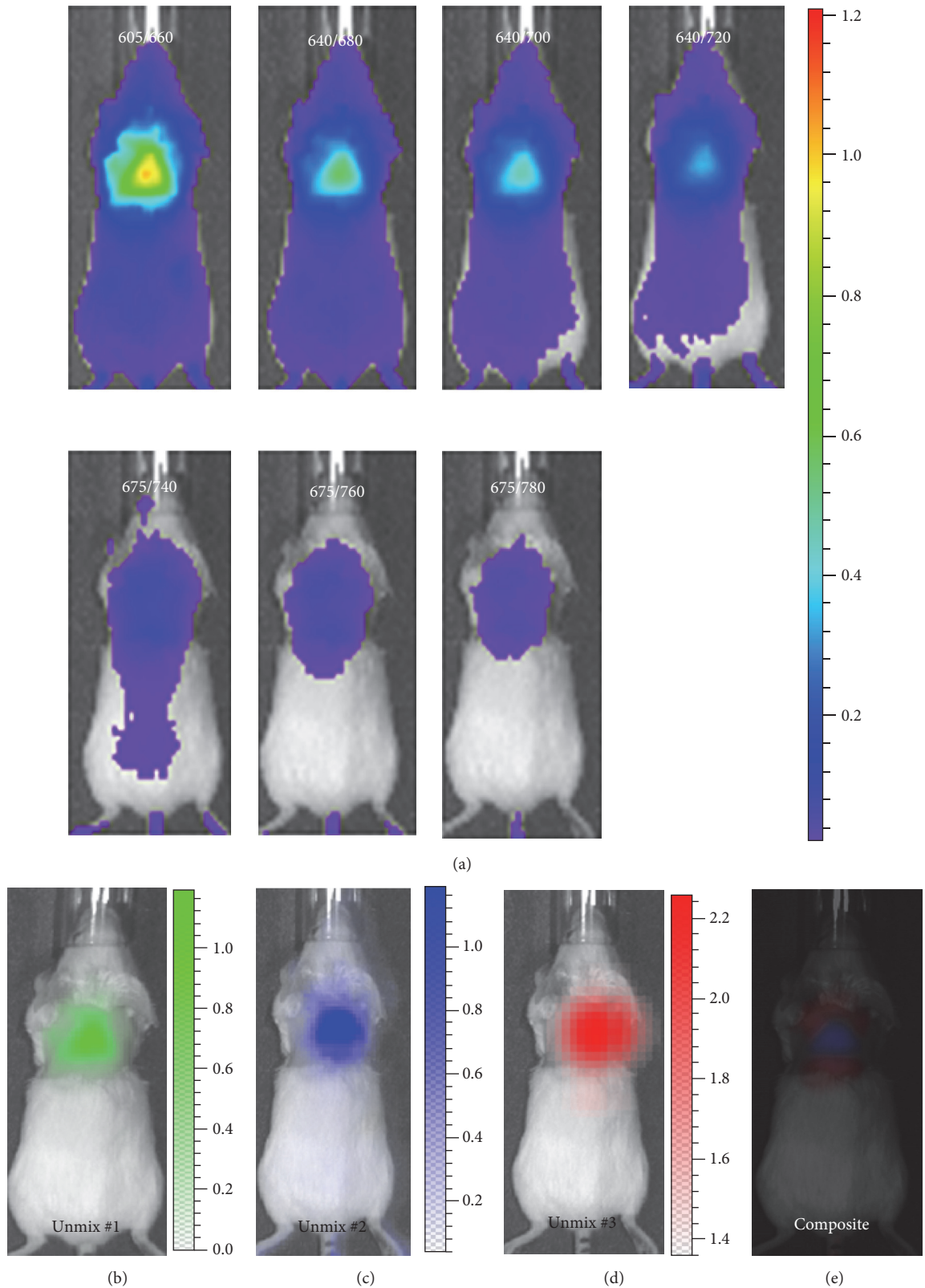


FIGURE 2: Spectral unmixing with CRANAD-29 for in vivo imaging. (a) Raw images of CRANAD-29 before spectral unmixing. (b) Unmixed autofluorescence signal. (c) Unmixed NIRF signal from BAT mass. (d) Unmixed NIRF signal from blood flow. (e) Merged image of unmixed #2 and #3. Note: for clarity, unmixed #1 was not merged.

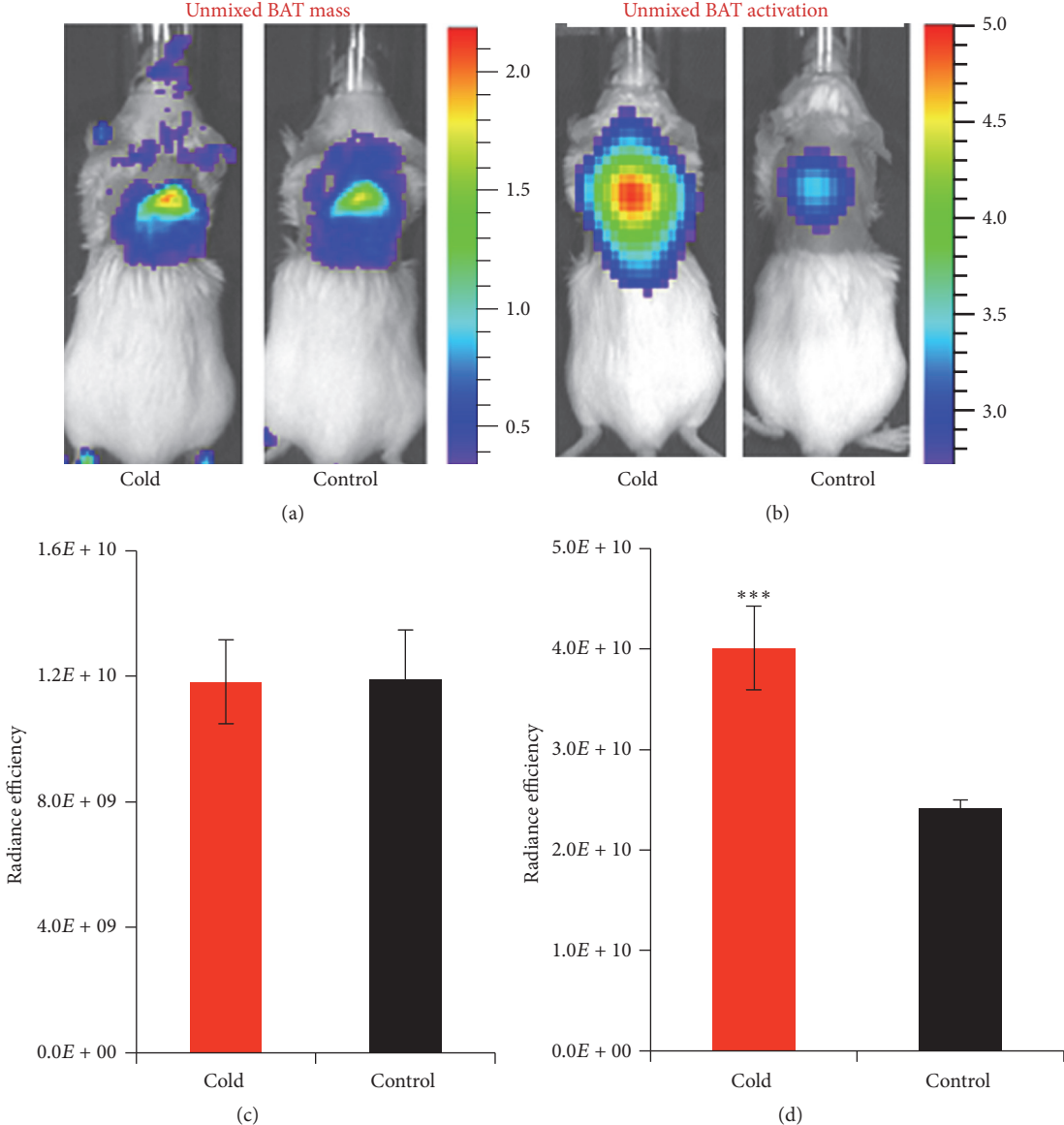


FIGURE 3: Spectral unmixing with CRANAD-29 for in vivo imaging under cold treatment. (a) Unmixed NIRF signal from BAT mass under cold treatment and control condition. (b) Unmixed NIRF signal from blood flow reflecting BAT activation. (c-d) Quantitative analysis of unmixed NIRF signal from BAT mass (c) and blood flow (d) under cold treatment and the control condition. *** $P < 0.005$.

by the well-separated images (Figures 1(a)-1(d)) and spectra from BAT and blood (Figure 1(e)). The spectra generated from this ex vivo unmixing were saved as a spectral library of CRANAD-29, which can be used for in vivo unmixing investigation.

To further validate the feasibility of spectral unmixing for in vivo studies, we acquired sequence images with the same parameters as the above ex vivo experiment with a mouse that was injected CRANAD-29. We used the spectral library of CRANAD-29 to conduct the spectral unmixing. As shown in Figure 2, the autofluorescence, signal of BAT, and blood stream could be well-separated, suggesting that the spectral unmixing is feasible for in vivo imaging.

To investigate spectral unmixing which could be used to dissect the signals from BAT mass and BAT activation, we conducted proof-of-concept experiment with the same group of mice with and without short cold exposure. The group of mice ($n = 5$) were treated with a short cold exposure (2 hours) and injected with CRANAD-29. After 4 hours of the injection. Sequence images were captured with the same parameters as above. After CRANAD-29 totally washing out, the same mice without the cold treatment were imaged again with the probe. We compared the unmixed NIRF signals from BAT and blood flow under cold treatment and without cold exposure. Obviously, with such a short cold exposure, the BAT mass would not change, but the blood flow was

expected to significantly increase under the cold treatment. Indeed, we found that there was no significant NIRF signal difference from BAT mass (Figures 3(a) and 3(c), $p = 0.975$), but an apparent increase of NIRF signal from blood flow from the cold exposure condition, and the increase was about 1.66-fold (Figures 3(b) and 3(d), $p = 0.005$). These results indicated that our method was reliable. Taken together, the above in vitro and in vivo data strongly indicated that spectral unmixing could be used to separate NIRF signal from BAT mass and BAT activation.

4. Conclusion

In this report, we developed a spectral unmixing method that could be, for the first time, to differentiate BAT mass and BAT activation. We believe that our method has the feasibility to reliably report BAT mass changes under different genetic manipulation and drug treatment in preclinical studies. Our cost-efficient NIRF imaging has a potential impact on pre-clinical animal studies and will greatly assist drug discovery and basic research related to BAT.

Conflicts of Interest

The authors declare that there are no conflicts of interest regarding the publication of this paper.

Acknowledgments

This work was supported by NIH/NIDDK R56DK108813 award (Chongzhao Ran). The authors also acknowledge China Scholarship Council of Ministry of Education of China for support (Jing Yang and Jian Yang).

References

- [1] B. Cannon and J. Nedergaard, "Brown adipose tissue: function and physiological significance," *Physiological Reviews*, vol. 84, no. 1, pp. 277–359, 2004.
- [2] D. Richard and F. Picard, "Brown fat biology and thermogenesis," *Frontiers in Bioscience: A Journal and Virtual Library*, vol. 16, no. 4, pp. 1233–1260, 2011.
- [3] V. Ouellet, S. M. Labbé, D. P. Blondin et al., "Brown adipose tissue oxidative metabolism contributes to energy expenditure during acute cold exposure in humans," *The Journal of Clinical Investigation*, vol. 122, no. 2, pp. 545–552, 2012.
- [4] A. M. Cypess, S. Lehman, G. Williams et al., "Identification and importance of brown adipose tissue in adult humans," *The New England Journal of Medicine*, vol. 360, no. 15, pp. 1509–1517, 2009.
- [5] B. P. Leitner, S. Huang, R. J. Brychta et al., "Mapping of human brown adipose tissue in lean and obese young men," *Proceedings of the National Academy of Sciences of the United States of America*, vol. 114, no. 32, pp. 8649–8654, 2017.
- [6] W. D. van Marken Lichtenbelt, J. W. Vanhommerig, N. M. Smulders et al., "Cold-activated brown adipose tissue in healthy men," *The New England Journal of Medicine*, vol. 360, no. 15, pp. 1500–1508, 2009.
- [7] F. S. Celi, "Brown adipose tissue - when it pays to be inefficient," *The New England Journal of Medicine*, vol. 360, no. 15, pp. 1553–1556, 2009.
- [8] K. A. Virtanen, M. E. Lidell, J. Orava et al., "Functional brown adipose tissue in healthy adults," *The New England Journal of Medicine*, vol. 360, no. 15, pp. 1518–1525, 2009.
- [9] T. Yoneshiro, S. Aita, M. Matsushita et al., "Age-related decrease in cold-activated brown adipose tissue and accumulation of body fat in healthy humans," *Obesity*, vol. 19, no. 9, pp. 1755–1760, 2011.
- [10] S. Enerbäck, "The origins of brown adipose tissue," *The New England Journal of Medicine*, vol. 360, no. 19, pp. 2021–2023, 2009.
- [11] S. R. Farmer, "Be cool, lose weight," *Nature*, vol. 458, no. 7240, pp. 839–840, 2009.
- [12] S. Kajimura, P. Seale, K. Kubota et al., "Initiation of myoblast to brown fat switch by a PRDM16-C/EBP-β transcriptional complex," *Nature*, vol. 460, no. 7259, pp. 1154–1158, 2009.
- [13] R. K. Gupta, Z. Arany, P. Seale et al., "Transcriptional control of preadipocyte determination by Zfp423," *Nature*, vol. 464, no. 7288, pp. 619–623, 2010.
- [14] P. Boström, J. Wu, M. P. Jedrychowski et al., "A PGCl-α-dependent myokine that drives brown-fat-like development of white fat and thermogenesis," *Nature*, vol. 481, no. 7382, pp. 463–468, 2012.
- [15] J. A. Timmons, K. Baar, P. K. Davidsen, and P. J. Atherton, "Is irisin a human exercise gene?" *Nature*, vol. 488, no. 7413, pp. E9–E10, 2012.
- [16] T. J. Schulz, P. Huang, T. L. Huang et al., "Brown-fat paucity due to impaired BMP signalling induces compensatory browning of white fat," *Nature*, vol. 495, no. 7441, pp. 379–383, 2013.
- [17] H. Ohno, K. Shinoda, K. Ohyama, L. Z. Sharp, and S. Kajimura, "EHMT1 controls brown adipose cell fate and thermogenesis through the PRDM16 complex," *Nature*, vol. 504, no. 7478, pp. 163–167, 2013.
- [18] T. Gnad, S. Scheibler, I. von Kügelgen et al., "Adenosine activates brown adipose tissue and recruits beige adipocytes via A_{2A} receptors," *Nature*, vol. 516, no. 7531, pp. 395–399, 2014.
- [19] M. Harms and P. Seale, "Brown and beige fat: development, function and therapeutic potential," *Nature Medicine*, vol. 19, no. 10, pp. 1252–1263, 2013.
- [20] Q. A. Wang, C. Tao, R. K. Gupta, and P. E. Scherer, "Tracking adipogenesis during white adipose tissue development, expansion and regeneration," *Nature Medicine*, vol. 19, no. 10, pp. 1338–1344, 2013.
- [21] A. M. Cypess, A. P. White, C. Vernochet et al., "Anatomical localization, gene expression profiling and functional characterization of adult human neck brown fat," *Nature Medicine*, vol. 19, no. 5, pp. 635–639, 2013.
- [22] M. E. Lidell, M. J. Betz, O. D. Leinhard et al., "Evidence for two types of brown adipose tissue in humans," *Nature Medicine*, vol. 19, no. 5, pp. 631–634, 2013.
- [23] K. J. Williams and E. A. Fisher, "Globular warming: how fat gets to the furnace," *Nature Medicine*, vol. 17, no. 2, pp. 157–159, 2011.
- [24] A. Bartelt, O. T. Bruns, R. Reimer et al., "Brown adipose tissue activity controls triglyceride clearance," *Nature Medicine*, vol. 17, no. 2, pp. 200–205, 2011.
- [25] B. Cannon and J. Nedergaard, "Thyroid hormones: igniting brown fat via the brain," *Nature Medicine*, vol. 16, no. 9, pp. 965–967, 2010.
- [26] Y. Qiu, K. D. Nguyen, J. I. Odegaard et al., "Eosinophils and type 2 cytokine signaling in macrophages orchestrate development of functional beige fat," *Cell*, vol. 157, no. 6, pp. 1292–1308, 2014.

- [27] R. R. Rao, J. Long, J. White et al., "Meteorin-like is a hormone that regulates immune-adipose interactions to increase beige fat thermogenesis," *Cell*, vol. 157, no. 6, pp. 1279–1291, 2014.
- [28] A. Fedorenko, P. V. Lishko, and Y. Kirichok, "Mechanism of fatty-acid-dependent UCP1 uncoupling in brown fat mitochondria," *Cell*, vol. 151, no. 2, pp. 400–413, 2012.
- [29] R. Teperino, S. Amann, M. Bayer et al., "Hedgehog partial agonism drives warburg-like metabolism in muscle and brown fat," *Cell*, vol. 151, no. 2, pp. 414–426, 2012.
- [30] L. Qiang, L. Wang, N. Kon et al., "Brown remodeling of white adipose tissue by SirT1-dependent deacetylation of Ppary," *Cell*, vol. 150, no. 3, pp. 620–632, 2012.
- [31] J. Wu, P. Boström, L. M. Sparks et al., "Beige adipocytes are a distinct type of thermogenic fat cell in mouse and human," *Cell*, vol. 150, no. 2, pp. 366–376, 2012.
- [32] A. J. Whittle, S. Carobbio, L. Martins et al., "BMP8B increases brown adipose tissue thermogenesis through both central and peripheral actions," *Cell*, vol. 149, no. 4, pp. 871–885, 2012.
- [33] M. Yudasaka, Y. Yomogida, M. Zhang et al., "Near-infrared photoluminescent carbon nanotubes for imaging of brown fat," *Scientific Reports*, vol. 7, Article ID 44760, 2017.
- [34] J. Nedergaard, T. Bengtsson, and B. Cannon, "Unexpected evidence for active brown adipose tissue in adult humans," *American Journal of Physiology-Renal Physiology*, vol. 293, no. 2, pp. E444–E452, 2007.
- [35] T. T. Tran and C. R. Kahn, "Transplantation of adipose tissue and stem cells: role in metabolism and disease," *Nature Reviews Endocrinology*, vol. 6, no. 4, pp. 195–213, 2010.
- [36] Y.-H. Tseng, E. Kokkotou, T. J. Schulz et al., "New role of bone morphogenetic protein 7 in brown adipogenesis and energy expenditure," *Nature*, vol. 454, no. 7207, pp. 1000–1004, 2008.
- [37] H. Zhang, T. J. Schulz, D. O. Espinoza et al., "Cross talk between insulin and bone morphogenetic protein signaling systems in brown adipogenesis," *Molecular and Cellular Biology*, vol. 30, no. 17, pp. 4224–4233, 2010.
- [38] C. Cohade, K. A. Mourtzikos, and R. L. Wahl, "'USA-Fat': prevalence is related to ambient outdoor temperature-evaluation with 18F-FDG PET/CT," *Journal of Nuclear Medicine: Official Publication, Society of Nuclear Medicine*, vol. 44, no. 8, pp. 1267–1270, 2003.
- [39] P. Lee, K. K. Ho, and M. J. Fulham, "The importance of brown adipose tissue," *The New England Journal of Medicine*, pp. 419–420, 2009.
- [40] M. E. Lidell and S. Enerbäck, "Brown adipose tissue-a new role in humans?" *Nature Reviews Endocrinology*, vol. 6, no. 6, pp. 319–325, 2010.
- [41] A. M. Cypess, C. R. Haft, M. R. Laughlin, and H. H. Hu, "Brown fat in humans: consensus points and experimental guidelines," *Cell Metabolism*, vol. 20, no. 3, pp. 408–415, 2014.
- [42] A. Nakayama, A. C. Bianco, C.-Y. Zhang, B. B. Lowell, and J. V. Frangioni, "Quantification of brown adipose tissue perfusion in transgenic mice using near-infrared fluorescence imaging," *Molecular Imaging*, vol. 2, no. 1, pp. 37–49, 2003.
- [43] A. Azhdarinia, A. C. Daquinag, C. Tseng et al., "A peptide probe for targeted brown adipose tissue imaging," *Nature Communications*, vol. 4, article no. 2472, 2013.
- [44] D. R. Rice, A. G. White, W. M. Leevy, and B. D. Smith, "Fluorescence imaging of interscapular brown adipose tissue in living mice," *Journal of Materials Chemistry B: Materials for Biology and Medicine*, vol. 3, no. 9, pp. 1979–1989, 2015.
- [45] C. Wu, W. Cheng, H. Xing, Y. Dang, F. Li, and Z. Zhu, "Brown adipose tissue can be activated or inhibited within an hour before 18F-FDG injection: a preliminary study with micropet," *Journal of biomedicine & biotechnology*, Article ID 159834, p. 2011, 2011.
- [46] I. Madar, T. Isoda, P. Finley, J. Angle, and R. Wahl, "18F-fluorobenzyl triphenyl phosphonium: a noninvasive sensor of brown adipose tissue thermogenesis," *Journal of Nuclear Medicine*, vol. 52, no. 5, pp. 808–814, 2011.
- [47] H. H. Hu, D. L. Smith Jr., K. S. Nayak, M. I. Goran, and T. R. Nagy, "Identification of brown adipose tissue in mice with fat-water ideal-MRI," *Journal of Magnetic Resonance Imaging*, vol. 31, no. 5, pp. 1195–1202, 2010.
- [48] Y. I. Chen, A. M. Cypess, C. A. Sass et al., "Anatomical and functional assessment of brown adipose tissue by magnetic resonance imaging," *Obesity*, vol. 20, no. 7, pp. 1519–1526, 2012.
- [49] A. Khanna and R. T. Branca, "Detecting brown adipose tissue activity with bold MRI in mice," *Magnetic Resonance in Medicine*, vol. 68, no. 4, pp. 1285–1290, 2012.
- [50] X.-G. Peng, S. Ju, F. Fang et al., "Comparison of brown and white adipose tissue fat fractions in ob, seipin, and Fsp27 gene knockout mice by chemical shift-selective imaging and 1H-MR spectroscopy," *American Journal of Physiology-Endocrinology and Metabolism*, vol. 304, no. 2, pp. E160–E167, 2013.
- [51] R. T. Branca, T. He, L. Zhang et al., "Detection of brown adipose tissue and thermogenic activity in mice by hyperpolarized xenon MRI," *Proceedings of the National Academy of Sciences of the United States of America*, vol. 111, no. 50, pp. 18001–18006, 2014.
- [52] X. Zhang, Y. Tian, H. Zhang et al., "Curcumin analogues as selective fluorescence imaging probes for brown adipose tissue and monitoring browning," *Scientific Reports*, vol. 5, Article ID 13116, 2015.
- [53] X. Zhang, C. Kuo, A. Moore, and C. Ran, "In vivo optical imaging of interscapular brown adipose tissue with 18F-FDG via cerenkov luminescence imaging," *PLoS ONE*, vol. 8, no. 4, Article ID e62007, 2013.
- [54] O. Muzik, T. J. Mangner, and J. G. Granneman, "Assessment of oxidative metabolism in brown fat using PET imaging," *Frontiers in Endocrinology*, vol. 3, Article ID Article 15, 2012.
- [55] M. Clerete, D. M. Baron, P. Brouckaert et al., "Brown adipose tissue blood flow and mass in obesity: a contrast ultrasound study in mice," *Journal of the American Society of Echocardiography: Official Publication of The American Society of Echocardiography*, vol. 26, no. 12, pp. 1465–1473, 2013.
- [56] G. Abreu-Vieira, C. E. Hagberg, K. L. Spalding, B. Cannon, and J. Nedergaard, "Adrenergically stimulated blood flow in brown adipose tissue is not dependent on thermogenesis," *American Journal of Physiology-Endocrinology and Metabolism*, vol. 308, no. 9, pp. E822–E829, 2015.
- [57] J. R. Lakowicz, *Principles of Fluorescence Spectroscopy*, Plenum Publishing Corporation, 1999.
- [58] C. Ran and A. Moore, "Spectral unmixing imaging of wavelength-responsive fluorescent probes: an application for the real-time report of amyloid beta species in alzheimer's disease," *Molecular Imaging and Biology*, vol. 14, no. 3, pp. 293–300, 2012.
- [59] J. Yang, C. Qiao, A. Moore, and C. Ran, "Spectral unmixing imaging for differentiating brown adipose tissue mass and its activation," in *Proceedings of the World Molecular Imaging Congress*, New York , NY, USA, September 7–10, 2016.

Research Article

Associations between ^{18}F -FDG-PET, DWI, and DCE Parameters in Patients with Head and Neck Squamous Cell Carcinoma Depend on Tumor Grading

Leonard Leifels,¹ Sandra Purz,² Patrick Stumpp,¹ Stefan Schob,³ Hans Jonas Meyer,¹ Thomas Kahn,¹ Osama Sabri,² and Alexey Surov¹

¹Department of Diagnostic and Interventional Radiology, University Hospital of Leipzig, Liebigstrasse 20, 04103 Leipzig, Germany

²Department of Nuclear Medicine, University Hospital of Leipzig, Liebigstraße 18, 04103 Leipzig, Germany

³Division of Neuroradiology, University Hospital of Leipzig, Liebigstrasse 20, 04103 Leipzig, Germany

Correspondence should be addressed to Alexey Surov; alexey.surov@medizin.uni-leipzig.de

Leonard Leifels and Sandra Purz contributed equally to this work.

Received 23 June 2017; Revised 31 August 2017; Accepted 12 September 2017; Published 19 October 2017

Academic Editor: Jie Lu

Copyright © 2017 Leonard Leifels et al. This is an open access article distributed under the Creative Commons Attribution License, which permits unrestricted use, distribution, and reproduction in any medium, provided the original work is properly cited.

Our purpose was to analyze associations between positron emission tomography (PET), diffusion weighted imaging (DWI), and dynamic contrast-enhanced (DCE) imaging in patients with head and neck squamous cell carcinoma (HNSCC). The study involved 34 patients (9 women, 25 men, mean age: 56.7 ± 10.2 years). In all patients a simultaneous ^{18}F -FDG-PET/MR was performed. DWI was obtained by using of an axial EPI sequence. Minimal ADC values (ADC_{\min}), mean ADC values (ADC_{mean}), and maximal ADC values (ADC_{\max}) were estimated. DCE MRI was performed by using dynamic T1w DCE sequence. The following parameters were estimated: K_{trans} , V_e , and K_{ep} . Spearman's correlation coefficient was used to analyze associations between investigated parameters. In overall sample, ADC_{mean} correlated significantly with V_e and K_{trans} , ADC_{\min} correlated with V_e , and ADC_{\max} correlated with K_{trans} and V_e . SUV_{mean} tended to correlate slightly with K_{trans} . In G1/2 tumors, only K_{trans} correlated well with ADC_{\max} and SUV_{mean} . In G3 tumors, K_{trans} correlated well with K_{ep} and V_e . V_e showed significant correlations with ADC_{mean} and ADC_{\max} . K_{trans} correlated with ADC_{\max} . K_{ep} was higher in cancers with N2/3 stages. Tumor metabolism, water diffusion, and tumor perfusion have complex relationships in HNSCC. Furthermore, these associations depend on tumor grading. K_{ep} may predict lymphonodal metastasizing.

1. Introduction

Head and neck squamous cell carcinoma (HNSCC) is the most frequent malignancy of the upper aerodigestive tract in humans [1].

Contrast-enhanced computed tomography (CT) and magnetic resonance imaging (MRI) provide the mainstay of imaging for diagnosis, staging, and treatment response assessment in HNSCC [2]. Functional imaging such as positron emission tomography (PET), diffusion weighted imaging (DWI), and dynamic contrast-enhanced (DCE) MRI provide complementary information on the underlying biology such as metabolic activity, cellularity, vascularity, and oxygenation [2, 3].

It has been shown that HNSCC lesions had high standardized uptake values (SUV) and low apparent diffusion coefficient (ADC) values [4, 5]. Furthermore, malignant tumors showed also high perfusion parameters in comparison to benign lesions [6].

Some authors performed multiparametric investigation of HNSCC including ^{18}F fluorodeoxyglucose PET (^{18}F -FDG-PET), DWI, and DCE and attempted to characterize complexity of imaging findings reflecting tumor biology [3, 7, 8]. The reported data, however, were inconsistent. Some authors found significant correlations between analyzed parameters and, therefore, suggested complex interactions among tumor biologic characteristics [7–10]. Thereby, DWI, PET, and DCE parameters were reported to have similar potential to

characterize HNSCC [10]. For example, Nakajo et al. showed that both SUV and ADC values correlated well together and could similarly predict disease-free survival or disease events in HNSCC [10].

However, in other studies, no significant correlations between these parameters were identified [11–13]. Therefore, it has been mentioned that parameters derived from PET, DWI, and DCE are independent biomarkers and complement one another [11–15].

This discrepancy of reported data questions the possibility of using multiparametric imaging findings as surrogate markers of tumor consistency in HNSCC.

The analysis of possible relationships between microcirculation, cellularity, and glucose metabolism has not only scientific importance but also clinical significance. As mentioned previously, an understanding of such complexities could expand the knowledge of tumor characteristics and have clinical implications such as in guidance for treatment planning, early prediction of treatment responses, and evaluation of treatment outcome [3].

The purpose of this study was to analyze possible associations between multiparametric imaging findings of simultaneous ¹⁸F-FDG-PET/MR including DWI and DCE in patients with HNSCC.

2. Materials and Methods

This prospective study was approved by the institutional review board of the University of Leipzig and all patients gave their written informed consent. All methods were performed in accordance with the relevant guidelines and regulations.

2.1. Patients. Overall, 34 patients with primary HNSCC of different localizations were involved in the study (Table 1). There were 9 (26%) women and 25 (74%) men with a mean age of 56.7 ± 10.2 years, range 33–77 years. At initial presentation, the tumors were localized in the tonsil (23.6%), followed by oropharynx (20.6%) and tongue (20.6%), hypopharynx (17.6%), larynx (14.6%), and epipharynx (2.9%). In most cases, high grade lesions (51.8%) were diagnosed. Furthermore, most frequently, the identified lesions were staged as T3 (29.4%) or T4 tumors (47.1%) with additional nodal (91.2%) metastases (Table 1).

2.2. Imaging

2.2.1. Simultaneous PET/MR. In all patients a simultaneous ¹⁸F-FDG-PET/MR (Magnetom Biograph mMR-Biograph, Siemens Healthcare Sector, Erlangen, Germany) was performed from the upper thigh to the skull after a fasting period of at least 6 hours. Application of ¹⁸F-FDG was performed intravenously with a body weight-adapted dose (4 MBq/kg, range: 168–427 MBq, and mean \pm SD: 279 \pm 60 MBq). PET/MR image acquisition started on average 170 minutes (range 60–300 minutes) after ¹⁸F-FDG application. In 28/34 patients a PET/CT scan was performed prior to PET/MRI, which explains the later PET/MRI image acquisition time in these patients. For attenuation correction of the PET data a coronal 3D-encoded gradient-echo sequence

TABLE 1: Localization and stage of the identified tumors.

	n (%)
<i>Diagnosis</i>	
Carcinoma of epipharynx	1 (2.9)
Carcinoma of oropharynx	7 (20.6)
Carcinoma of hypopharynx	6 (17.6)
Carcinoma of larynx	5 (14.7)
Carcinoma of tongue	7 (20.6)
Tonsillar carcinoma	8 (23.6)
<i>Tumor stage</i>	
<i>T stage</i>	
T1	1 (2.9)
T2	7 (20.6)
T3	10 (29.4)
T4	16 (47.1)
<i>N stage</i>	
N0	3 (8.8)
N1	6 (17.7)
N2	22 (64.7)
N3	3 (8.8)
<i>M stage</i>	
M0	30 (88.2)
M1	4 (11.8)
<i>Tumor grading</i>	
G1	1 (2.9)
G2	12 (35.3)
G3	21 (51.8)

(Dixon-VIBE) was used. For each tumor, maximum and mean SUV (SUV_{max}; SUV_{mean}) were determined.

PET images were analyzed by one nuclear medicine physician (S. P.) with 7 years of experience.

2.3. Image Interpretation. PET/MR datasets were evaluated by a board certified nuclear medicine and a board certified radiologist with substantial PET/MR experience in oncological image interpretation. PET/MR image analysis was performed on the dedicated workstation of Hermes Medical Solutions, Sweden.

Tumor margins of the HNSCC were identified on MR images (T1-sequence) and a polygonal volume of interest (VOI) was placed in the fused PET/MR dataset (SUV_{max} threshold 40%) (Figure 1(a)).

2.4. DWI. DWI was obtained by using an axial EPI (echo planar imaging) sequence with *b*-values of 0 and 800 s/mm² (TR/TE: 8620/73 ms, slice thickness 4 mm, and voxel size 3.2 \times 2.6 \times 4.0 mm). ADC maps were automatically generated by the implemented software. DWI images were analyzed by one radiologist (L. L., 2 years of general radiological experience). Polygonal regions of interest (ROI) were manually drawn on the ADC maps along the contours of the tumor on each slice (Figure 1(b)). In all lesions minimal ADC values (ADC_{min}), mean ADC values (ADC_{mean}), and maximal ADC values (ADC_{max}) were estimated (Figure 1(b)).

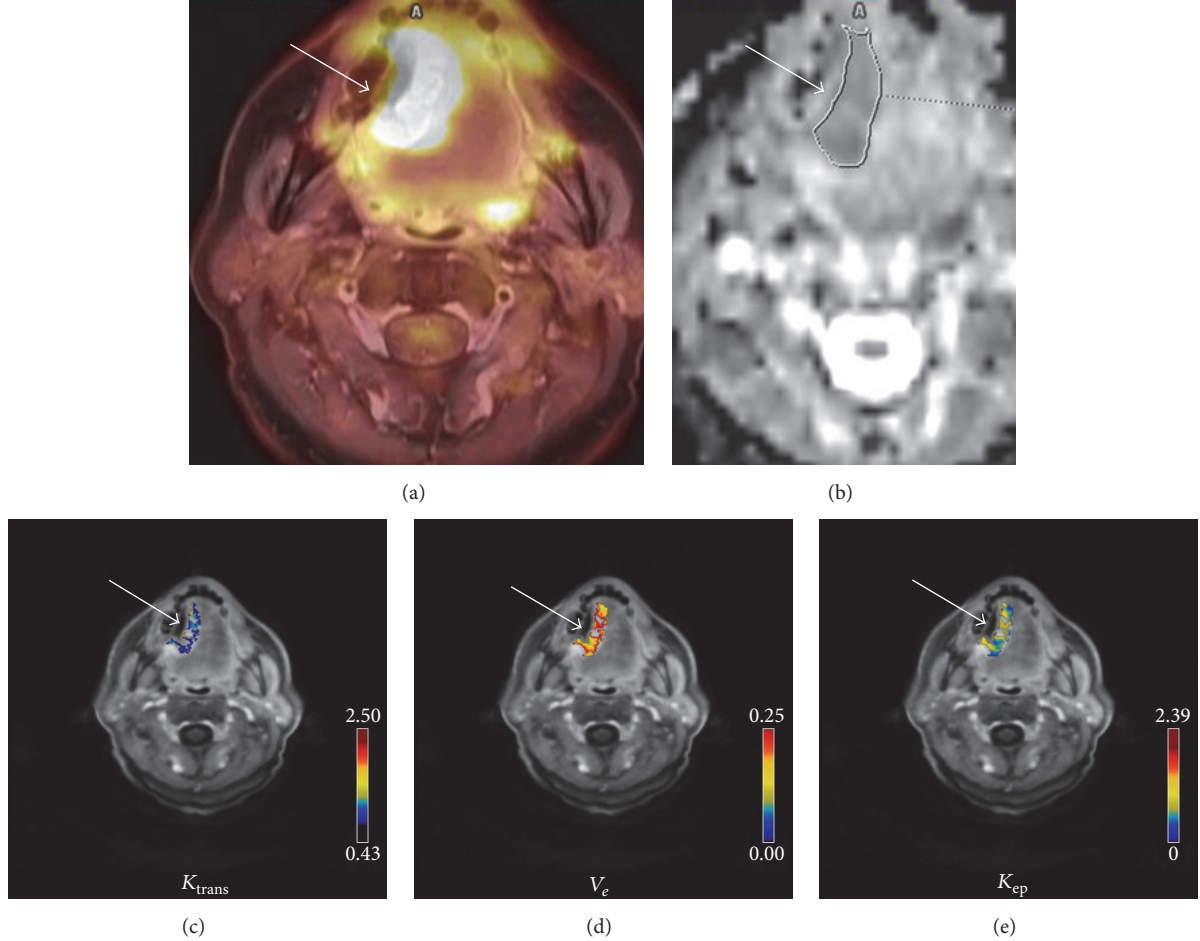


FIGURE 1: Imaging findings in a 58-year-old man with squamous cell carcinoma of the tongue (G1, T4 N2 M0). (a) ^{18}F -FDG-PET imaging (fused image) showing a right sided large lesion of the tongue; $\text{SUV}_{\text{max}} = 24.11$. (b) ADC map. The ADC values ($\times 10^{-3} \text{ mm}^2 \text{s}^{-1}$) of the lesion are as follows: $\text{ADC}_{\text{min}} = 0.68$, $\text{ADC}_{\text{mean}} = 0.97$, and $\text{ADC}_{\text{max}} = 2.1$. (c–e) DCE imaging findings. Estimated DCE parameters are as follows: $K_{\text{trans}} = 0.53 \text{ min}^{-1}$ (c), $V_e = 0.68\%$ (d), and $K_{\text{ep}} = 0.75 \text{ min}^{-1}$ (e).

2.5. DCE. In 31 patients, DCE MRI was performed by using dynamic T1w DCE sequence (TR/TE 2.47/0.97 ms, slice thickness 5 mm, flip angle 8°, and voxel size $1.2 \times 1.0 \times 5.0$ mm) after intravenous application of contrast medium (0.1 mmol Gadobutrol per kg of body weight) (Gadovist®, Bayer Healthcare, Leverkusen, Germany) as reported previously [8, 15]. The acquired images were transferred to a software module for tissue perfusion estimation (Tissue 4D, Siemens Medical Systems, Erlangen, Germany). The software offers a population based approach for the arterial input function (AIF) and the best of three available AIF-options was chosen according to the result of the chi²-parameter, which serves as an error measure for the model fit [7, 8]. The AIF was scaled in relation to the gadolinium dose and modelled according to the biexponential model of Tofts and Kermode [16]. The following pharmacokinetic parameters [7, 8, 15] were automatically calculated for whole lesion in every case (Figures 1(c)–1(e)):

- (i) K_{trans} : volume transfer constant, which estimates the diffusion of contrast medium from the plasma

through the vessel wall into the interstitial space, representing vessel permeability

- (ii) V_e : volume of the extravascular extracellular leakage space (EES)
- (iii) K_{ep} : parameter for diffusion of contrast medium from the EES back to the plasma. It is in close relation with K_{trans} and V_e and is calculated by the formula $k_{\text{ep}} = K_{\text{trans}} \times V_e^{-1}$.

DCE images were analyzed by one radiologist (L. L., 2 years of general radiological experience).

2.6. Statistical Analysis. Statistical analysis and graphics creation were performed using SPSS 20 (IBM SPSS Statistics, Armonk, New York, USA). Collected data were evaluated by means of descriptive statistics (absolute and relative frequencies). Spearman's correlation coefficient (p) was used to analyze associations between investigated parameters. P values < 0.05 were taken to indicate statistical significance.

TABLE 2: DWI, PET, and DCE parameters of HNSCC.

Parameters	M ± SD	Range
SUV _{max}	19.01 ± 9.81	5.81–48.00
SUV _{mean}	8.19 ± 3.55	3.76–17.70
ADC _{mean} × 10 ⁻³ mm ² s ⁻¹	1.14 ± 0.21	0.78–1.68
ADC _{min} × 10 ⁻³ mm ² s ⁻¹	0.71 ± 0.23	0.17–1.24
ADC _{max} × 10 ⁻³ mm ² s ⁻¹	1.77 ± 0.30	1.35–2.39
K _{trans}	0.20 ± 0.12	0.01–0.53
K _{ep}	0.58 ± 0.69	0.16–3.37
V _e	0.51 ± 0.18	0.05–0.79

3. Results

A complete overview of the results including mean values, standard deviation, and ranges is shown in Table 2.

Correlation analysis identified the following: in overall sample, ADC_{mean} correlated significantly well with V_e ($P = 0.0002$) and slightly with K_{trans} (0.04), ADC_{min} correlated with V_e ($P = 0.0007$), and ADC_{max} correlated with K_{trans} (0.0032) and V_e (0.045) (Table 3). K_{trans} correlated well with K_{ep} ($P = 0.0017$) and V_e ($P = 0.0002$).

In addition, SUV_{max} tended to correlate slightly inversely with ADC_{min} ($P = 0.08$) and SUV_{mean} had a tendency to correlate with K_{trans} ($P = 0.08$).

On the next step, the estimated parameters were correlated in different tumor subgroups. In G1/2 tumors, K_{trans} correlated well with ADC_{max} and SUV_{mean} (Table 4). No other significant correlations were identified. SUV_{max} tended to correlate inversely with ADC_{min} ($P = 0.09$). V_e had a tendency to correlate with ADC_{mean} and ADC_{min} (in both cases, $P = 0.08$). In addition, DCE parameters did not correlate together.

However, in G3 tumors, K_{trans} correlated well with K_{ep} ($P = 0.015$) and V_e ($P = 0.003$) (Table 5). V_e showed significant strong correlations with ADC_{mean} ($P = 0.0014$) and ADC_{min} ($P = 0.01$). K_{trans} correlated moderately with ADC_{max} ($P = 0.04$). Finally, SUV values did not correlate with ADC and perfusion parameters.

No significant differences were identified in the analyzed parameters between poorly and moderately/well differentiated tumors (Table 6).

There were no significant differences of the analyzed parameters between several tumor stages (Tables 7(a)–7(c)). Only K_{ep} was higher in cancers with N2/3 stages versus N0/1 stages (Table 7(b)).

4. Discussion

Our study identified several significant associations between PET, DWI, and DCE parameters in primary HNSCC in a complex investigation.

The analysis of previous studies regarding multiparametric imaging findings in HNSCC shows that the reported results are controversial. This applies both comparisons of the investigated parameters in different tumor stages and correlation between the variables. For example, Fruehwald-Pallamar et al. analyzed sequentially acquired ¹⁸F-FDG-PET

and MR images of 31 HNSCC patients and did not observe significant differences in ADC values and SUV_{max} between various T stages of the investigated tumors [11]. However, Kim et al. found that T3/4 tumors had higher SUV_{max} values than T1/2 lesions [17]. In addition, N positive tumors showed also higher SUV_{max} values [17]. According to Zhang et al., T3/4 tumors showed statistically significant higher ADC values in comparison to T1/2 lesions [18]. It has also been reported that DCE parameters correlated well with tumor stage in nasopharyngeal carcinoma [19].

In the present study, we also identified significant differences in analyzed parameters between several tumor stages. Firstly, advanced carcinomas had higher SUV_{max} values. However, there were no significant differences in other investigated parameters between T1/2 and T3/4 tumors. This finding suggests that advanced tumors have higher metabolic activity but not higher cell density or perfusion. Secondly, K_{ep} was higher in N2 tumors. Previously, strong correlations between K_{ep} and microvessel density in HNSCC were reported [15]. Therefore, our findings may indicate that tumor microvessel density might influence lymphatic metastatic spread in HNSCC.

To the best of our knowledge, previously, only two studies investigated associations between imaging findings and tumor grading in HNSCC [11, 12]. So, Choi et al. mentioned that poorly differentiated tumors had statistically significant lower ADC values and higher SUV values than G1/G2 tumors [12]. Other authors, however, reported that SUV and ADC values could not distinguish tumor stages [11]. Also in the present study no significant differences were identified between well/moderately and poorly differentiated carcinomas. Grading system of HNSCC includes the following parameters: degree of keratinization, nuclear pleomorphism, number of mitoses, pattern of invasion, and presence or absence of inflammatory infiltrates [20, 21]. However, this system does not include parameters, such as cell count, cell size, extracellular space, and microvessel density, which are known to influence water diffusion, glucose metabolism, and perfusion. This may explain our negative results regarding associations between tumor grading and multiparametric imaging findings.

According to previous reports, several parameters of tumor perfusion, diffusion, and glucose metabolism were associated together [7–10]. So Bisdas et al. identified significant correlations between SUV values and V_e ($p = 0.42$, $P = 0.03$) [7]. Furthermore, analyzed perfusions parameter (K_{trans}, V_e, and K_{ep}) also correlated well together [7]. In the study of Nakajo et al., a statistically significant inverse correlation between SUV_{max} and ADC_{mean} ($p = -0.566$, $P = 0.005$) was found [10]. Additionally, according to Covello et al., ADC_{mean} correlated inversely with K_{trans} ($p = -0.42$, $P = 0.04$) [9].

However, other authors did not identify significant correlations between analyzed parameters [11–13]. For instance, Rasmussen et al. could not find significant associations between SUV and ADC values [13]. Similar results were also reported in other researches [11, 12, 14]. Furthermore, Han et al. detected no significant associations between DCE and glucose metabolism parameters in HNSCC [3].

TABLE 3: Correlations between DCE, DWI, and PET parameters in all tumors.

Parameters	SUV _{max}	SUV _{mean}	ADC _{mean}	ADC _{min}	ADC _{max}	K _{trans}	K _{ep}	V _e
SUV _{max}	—	p = 0.86 P < 0.0001	p = -0.25 P = 0.15	p = -0.30 P = 0.08	p = 0.18 P = 0.32	p = 0.09 P = 0.63	p = 0.10 P = 0.59	p = -0.07 P = 0.70
	—	—	p = -0.08 P = 0.67	p = -0.15 P = 0.39	p = 0.22 P = 0.22	p = 0.32 P = 0.08	p = 0.26 P = 0.16	p = 0.13 P = 0.49
SUV _{mean}	—	—	—	p = 0.88 P < 0.0001	p = 0.54 P = 0.0009	p = 0.37 P = 0.04	p = -0.10 P = 0.847	p = 0.62 P = 0.0002
	—	—	—	—	p = 0.27 P = 0.12	p = 0.26 P = 0.16	p = -0.08 P = 0.65	p = 0.58 P = 0.0007
ADC _{mean}	—	—	—	—	—	p = 0.51 P = 0.003	p = 0.12 P = 0.52	p = 0.36 P = 0.0445
	—	—	—	—	—	—	p = 0.54 P = 0.0017	p = 0.62 P = 0.0002
ADC _{min}	—	—	—	—	—	—	—	p = -0.12 P = 0.51
	—	—	—	—	—	—	—	—
ADC _{max}	—	—	—	—	—	—	—	—
	—	—	—	—	—	—	—	—
K _{trans}	—	—	—	—	—	—	—	—
	—	—	—	—	—	—	—	—
K _{ep}	—	—	—	—	—	—	—	—
	—	—	—	—	—	—	—	—
V _e	—	—	—	—	—	—	—	—
	—	—	—	—	—	—	—	—

Significant correlations are highlighted in bold.

TABLE 4: Correlations between DCE, DWI, and PET parameters in G1 and 2 tumors.

Parameters	SUV _{max}	SUV _{mean}	ADC _{mean}	ADC _{min}	ADC _{max}	K _{trans}	K _{ep}	V _e
SUV _{max}	—	p = 0.74 P = 0.0041	p = -0.47 P = 0.10	p = -0.49 P = 0.09	p = 0.10 P = 0.75	p = 0.27 P = 0.42	p = 0.16 P = 0.63	p = 0.14 P = 0.69
	—	—	p = -0.23 P = 0.45	p = -0.29 P = 0.34	p = 0.31 P = 0.30	p = 0.65 P = 0.03	p = 0.24 P = 0.48	p = 0.34 P = 0.31
SUV _{mean}	—	—	—	p = 0.68 P = 0.01	p = 0.56 P = 0.046	p = 0.44 P = 0.18	p = -0.10 P = 0.77	p = 0.55 P = 0.08
	—	—	—	—	—	p = -0.08 P = 0.79	p = 0.22 P = 0.52	p = 0.55 P = 0.08
ADC _{mean}	—	—	—	—	—	—	p = 0.65 P = 0.03	p = 0.25 P = 0.45
	—	—	—	—	—	—	—	p = 0.36 P = 0.27
ADC _{min}	—	—	—	—	—	—	—	p = 0.500 P = 0.12
	—	—	—	—	—	—	—	p = -0.37 P = 0.26
ADC _{max}	—	—	—	—	—	—	—	—
	—	—	—	—	—	—	—	—
K _{trans}	—	—	—	—	—	—	—	—
	—	—	—	—	—	—	—	—
K _{ep}	—	—	—	—	—	—	—	—
	—	—	—	—	—	—	—	—
V _e	—	—	—	—	—	—	—	—
	—	—	—	—	—	—	—	—

Significant correlations are highlighted in bold.

TABLE 5: Correlations between DCE, DWI, and PET parameters in G3 tumors.

Parameters	SUV _{max}	SUV _{mean}	ADC _{mean}	ADC _{min}	ADC _{max}	K _{trans}	K _{ep}	V _e
SUV _{max}	—	p = 0.85 P < 0.0001	p = -0.25 P = 0.28	p = -0.26 P = 0.27	p = 0.11 P = 0.65	p = 0.02 P = 0.95	p = 0.15 P = 0.54	p = -0.24 P = 0.33
	—	—	p = -0.11 P = 0.63	p = -0.09 P = 0.71	p = 0.05 P = 0.82	p = 0.10 P = 0.69	p = 0.34 P = 0.16	p = -0.12 P = 0.63
SUV _{mean}	—	—	—	p = 0.94 P < 0.0001	p = 0.60 P = 0.005	p = 0.33 P = 0.17	p = -0.15 P = 0.55	p = 0.68 P = 0.0014
	—	—	—	—	—	p = 0.47 P = 0.04	p = 0.18 P = 0.45	p = 0.57 P = 0.01
ADC _{mean}	—	—	—	—	—	—	p = 0.48 P = 0.04	p = 0.37 P = 0.12
	—	—	—	—	—	—	p = 0.55 P = 0.015	p = 0.65 P = 0.003
ADC _{min}	—	—	—	—	—	—	—	p = -0.06 P = 0.79
	—	—	—	—	—	—	—	—
ADC _{max}	—	—	—	—	—	—	—	—
	—	—	—	—	—	—	—	—
K _{trans}	—	—	—	—	—	—	—	—
	—	—	—	—	—	—	—	—
K _{ep}	—	—	—	—	—	—	—	—
	—	—	—	—	—	—	—	—
V _e	—	—	—	—	—	—	—	—
	—	—	—	—	—	—	—	—

Significant correlations are highlighted in bold.

TABLE 6: Comparison of PET and DWI values between different tumor grades.

Parameters	G1 + 2 Mean ± SD	G3 + 4 Mean ± SD	Mann–Whitney U (<i>p</i> values)
SUV _{max}	21.11 ± 8.37	17.79 ± 9.86	0.20
SUV _{mean}	8.92 ± 3.92	7.75 ± 3.40	0.28
ADC _{min} × 10 ⁻³ mm ² s ⁻¹	0.74 ± 0.15	0.69 ± 0.28	0.65
ADC _{mean} × 10 ⁻³ mm ² s ⁻¹	1.16 ± 0.14	1.13 ± 0.25	0.47
ADC _{max} × 10 ⁻³ mm ² s ⁻¹	1.75 ± 0.25	1.79 ± 0.34	0.96
K _{trans}	0.20 ± 0.13	0.20 ± 0.12	0.93
K _{ep}	0.39 ± 0.16	0.70 ± 0.85	0.22
V _e	0.55 ± 0.19	0.49 ± 0.17	0.37

TABLE 7

(a) Comparison of PET and DWI values between different tumor T stages

Parameters	T1/2 (mean ± SD)	T3/4 (mean ± SD)	Mann–Whitney U (<i>p</i> values)
SUV _{max}	14.98 ± 7.88	20.25 ± 9.34	0.19
SUV _{mean}	6.46 ± 1.60	8.73 ± 3.83	0.17
ADC _{min} × 10 ⁻³ mm ² s ⁻¹	0.64 ± 0.23	0.73 ± 0.23	0.41
ADC _{mean} × 10 ⁻³ mm ² s ⁻¹	1.09 ± 0.17	1.16 ± 0.21	0.56
ADC _{max} × 10 ⁻³ mm ² s ⁻¹	1.73 ± 0.33	1.78 ± 0.30	0.58
K _{trans}	0.17 ± 0.13	0.21 ± 0.11	0.27
K _{ep}	1.05 ± 1.25	0.42 ± 0.17	0.37
V _e	0.41 ± 0.22	0.55 ± 0.15	0.25

(b) Comparison of PET and DWI values between different tumor N stages

Parameters	N 0/1 (mean ± SD)	N 2 (mean ± SD)	Mann–Whitney U (<i>p</i> values)
SUV _{max}	19.72 ± 7.99	18.75 ± 9.72	0.78
SUV _{mean}	8.50 ± 3.88	8.08 ± 3.50	0.97
ADC _{min} × 10 ⁻³ mm ² s ⁻¹	0.78 ± 0.24	0.69 ± 0.23	0.75
ADC _{mean} × 10 ⁻³ mm ² s ⁻¹	1.18 ± 0.24	1.13 ± 0.20	0.64
ADC _{max} × 10 ⁻³ mm ² s ⁻¹	1.78 ± 0.29	1.77 ± 0.31	0.88
K _{trans}	0.16 ± 0.08	0.22 ± 0.13	0.25
K _{ep}	0.32 ± 0.11	0.68 ± 0.79	0.0477
V _e	0.52 ± 0.18	0.50 ± 0.18	0.88

(c) Comparison of PET and DWI values between different tumor M stages

Parameters	M0 (mean ± SD)	M1 (mean ± SD)	Mann–Whitney U (<i>p</i> values)
SUV _{max}	18.98 ± 9.14	16.49 ± 10.06	0.56
SUV _{mean}	8.01 ± 3.40	6.87 ± 1.50	0.60
ADC _{min}	0.68 ± 0.22	0.89 ± 0.28	0.21
ADC _{mean}	1.12 ± 0.19	1.28 ± 0.30	0.33
ADC _{max}	1.76 ± 0.30	1.89 ± 0.37	0.46
K _{trans}	0.21 ± 0.12	0.14 ± 0.08	0.47
K _{ep}	0.62 ± 0.72	0.28 ± 0.17	0.16
V _e	0.50 ± 0.19	0.55 ± 0.10	0.78

It is still unclear why some authors found significant correlations between water diffusion, glucose metabolism, and perfusion parameters in HNSCC while others did not. Presumably, tumor heterogeneity may play a role here. For example, well, moderately, and poorly differentiated tumors

might show also different associations of imaging parameters. In fact, our results confirmed this hypothesis.

In the present study, no significant correlations between different ADC parameters and SUV values were identified in overall sample. Furthermore, SUV_{max} tended to correlate

slightly with K_{trans} and ADC_{min} . All ADC parameters showed significant associations with V_e . In addition, K_{trans} correlated slightly with ADC_{mean} and moderately with ADC_{max} and K_{ep} and well with V_e .

Separate correlation analyses in the G1/2 and G3 tumors showed, however, other associations between the investigated parameters. As seen, perfusion parameters K_{trans} , V_e , and K_{ep} did not significantly correlate together in well and moderately differentiated tumors. However, they correlated well in high grade carcinomas. Additionally, K_{trans} correlated well with SUV_{mean} in G1/2 lesions but not in G3 tumors. Finally, V_e correlated well with ADC_{mean} and ADC_{min} in G3 tumors, but not in G1/2 lesions.

Our data suggest that tumor metabolism, cellularity, and perfusion show complex relationships in HNSCC. Furthermore, these associations depend on tumor grading. Previously, it has been shown that SUV and ADC values as well as perfusion parameters correlated with different histopathological features in HNSCC [14, 15]. We hypothesize on the basis of our findings that tumors with different grading may have also different relationships between cell count, stroma, and microvessel density, that is, different tumor architecture. Furthermore, our data suggest that tissue architecture plays a great role in tumor characteristic. Our findings may also explain controversial data of previous reports. Presumably, previous studies might contain well, moderately, and poorly differentiated lesions in several proportions that may result in different associations between the analyzed parameters.

In conclusion, multiparameter imaging provides information regarding tumor composition. Our study shows that tumor metabolism, water diffusion, and tumor perfusion have complex relationships in HNSCC. Furthermore, these associations depend on tumor grading. Perfusion parameter K_{ep} may predict lymphonodal metastasizing.

Ethical Approval

The study was approved by the institutional review board of the University of Leipzig. All procedures performed in the study were in accordance with the ethical standards of the institutional research committee and with the 1964 Helsinki Declaration and its later amendments or comparable ethical standards.

Consent

For this type of study, informed consent was obtained from all individual participants included in the study.

Conflicts of Interest

The authors declare no conflicts of interest.

Authors' Contributions

Conceptualization was by Alexey Surov. Data curation was performed by Leonard Leifels, Alexey Surov, Hans Jonas Meyer, and Sandra Purz. Formal analysis was conducted by Leonard Leifels, Hans Jonas Meyer, Sandra Purz, and Patrick Stumpp. Investigation was performed by Leonard Leifels,

Alexey Surov, Sandra Purz, and Osama Sabri. Methodology was contributed by Stefan Schob, Alexey Surov, Osama Sabri, Hans Jonas Meyer, Sandra Purz, and Thomas Kahn. Project administration was by Alexey Surov, Osama Sabri, Sandra Purz, and Thomas Kahn. Resources were contributed by Alexey Surov and Hans Jonas Meyer. Software was contributed by Hans Jonas Meyer, Alexey Surov, Stefan Schob, and Sandra Purz. Supervision was by Thomas Kahn, Osama Sabri, Alexey Surov, and Patrick Stumpp. Validation was performed by Alexey Surov, Hans Jonas Meyer, Thomas Kahn, and Osama Sabri. Visualization was performed by Stefan Schob, Alexey Surov, and Leonard Leifels. Writing of original draft was performed by Leonard Leifels and Alexey Surov. Writing in terms of review and editing was performed by Leonard Leifels, Alexey Surov, Hans Jonas Meyer, Thomas Kahn, Osama Sabri, Patrick Stumpp, Sandra Purz, and Stefan Schob.

References

- [1] B. J. M. Braakhuis, C. R. Leemans, and O. Visser, "Incidence and survival trends of head and neck squamous cell carcinoma in the Netherlands between 1989 and 2011," *Oral Oncology*, vol. 50, no. 7, pp. 670–675, 2014.
- [2] C. Powell, M. Schmidt, M. Borri et al., "Changes in functional imaging parameters following induction chemotherapy have important implications for individualised patient-based treatment regimens for advanced head and neck cancer," *Radiotherapy & Oncology*, vol. 106, no. 1, pp. 112–117, 2013.
- [3] M. Han, S. Y. O. Kim, S. J. I. Lee, and J. W. O. Choi, "The correlations between mri perfusion, diffusion parameters, and ¹⁸F-FDG PET metabolic parameters in primary head-and-neck cancer: a cross-sectional analysis in single institute," *Medicine*, vol. 94, no. 47, Article ID e2141, 2015.
- [4] J. Wang, S. Takashima, F. Takayama et al., "Head and neck lesions: characterization with diffusion-weighted echo-planar MR imaging," *Radiology*, vol. 220, no. 3, pp. 621–630, 2001.
- [5] N. Khan, N. Oriuchi, H. Ninomiya, T. Higuchi, H. Kamada, and K. Endo, "Positron emission tomographic imaging with ¹¹C-choline in differential diagnosis of head and neck tumors: Comparison with ¹⁸F-FDG PET," *Annals of Nuclear Medicine*, vol. 18, no. 5, pp. 409–417, 2004.
- [6] D. P. Noij, M. C. De Jong, L. G. M. Mulders et al., "Contrast-enhanced perfusion magnetic resonance imaging for head and neck squamous cell carcinoma: a systematic review," *Oral Oncology*, vol. 51, no. 2, pp. 124–138, 2015.
- [7] S. Bisdas, O. Seitz, M. Middendorp et al., "An exploratory pilot study into the association between microcirculatory parameters derived by MRI-based pharmacokinetic analysis and glucose utilization estimated by PET-CT imaging in head and neck cancer," *European Radiology*, vol. 20, no. 10, pp. 2358–2366, 2010.
- [8] M. Gawlitza, S. Purz, K. Kubiessa et al., "In vivo correlation of glucose metabolism, cell density and microcirculatory parameters in patients with head and neck cancer: initial results using simultaneous PET/MRI," *PLoS ONE*, vol. 10, no. 8, Article ID e0134749, 2015.
- [9] M. Covello, C. Cavaliere, M. Aiello et al., "Simultaneous PET/MR head-neck cancer imaging: preliminary clinical experience and multiparametric evaluation," *European Journal of Radiology*, vol. 84, no. 7, pp. 1269–1276, 2015.

- [10] M. Nakajo, M. Nakajo, Y. Kajiya et al., “FDG PET/CT and diffusion-weighted imaging of head and neck squamous cell carcinoma: comparison of prognostic significance between primary tumor standardized uptake value and apparent diffusion coefficient,” *Clinical Nuclear Medicine*, vol. 37, no. 5, pp. 475–480, 2012.
- [11] J. Fruehwald-Pallamar, C. Czerny, M. E. Mayerhoefer et al., “Functional imaging in head and neck squamous cell carcinoma: correlation of PET/CT and diffusion-weighted imaging at 3 Tesla,” *European Journal of Nuclear Medicine and Molecular Imaging*, vol. 38, no. 6, pp. 1009–1019, 2011.
- [12] S. H. Choi, J. C. Paeng, C.-H. Sohn et al., “Correlation of ¹⁸F-FDG uptake with apparent diffusion coefficient ratio measured on standard and high *b* value diffusion MRI in head and neck cancer,” *Journal of Nuclear Medicine*, vol. 52, no. 7, pp. 1056–1062, 2011.
- [13] J. H. Rasmussen, M. Nørgaard, A. E. Hansen et al., “Feasibility of multiparametric imaging with PET/MR in head and neck Squamous cell carcinoma,” *Journal of Nuclear Medicine*, vol. 58, no. 1, pp. 69–74, 2017.
- [14] A. Surov, P. Stumpp, H. J. Meyer et al., “Simultaneous ¹⁸F-FDG-PET/MRI: associations between diffusion, glucose metabolism and histopathological parameters in patients with head and neck squamous cell carcinoma,” *Oral Oncology*, vol. 58, pp. 14–20, 2016.
- [15] A. Surov, H. J. Meyer, M. Gawlitz et al., “Correlations between DCE MRI and histopathological parameters in head and neck squamous cell carcinoma,” *Translational Oncology*, vol. 10, no. 1, pp. 17–21, 2017.
- [16] P. S. Tofts and A. G. Kermode, “Measurement of the blood-brain barrier permeability and leakage space using dynamic MR imaging. 1. Fundamental concepts,” *Magnetic Resonance in Medicine*, vol. 17, no. 2, pp. 357–367, 1991.
- [17] S. Y. Kim, J.-L. Roh, J. S. Kim et al., “Utility of FDG PET in patients with squamous cell carcinomas of the oral cavity,” *European Journal of Surgical Oncology*, vol. 34, no. 2, pp. 208–215, 2008.
- [18] Y. Zhang, X. Liu, Y. Zhang et al., “Prognostic value of the primary lesion apparent diffusion coefficient (ADC) in nasopharyngeal carcinoma: a retrospective study of 541 cases,” *Scientific Reports*, vol. 5, Article ID 12242, 2015.
- [19] D. Zheng, Y. Chen, Y. Chen et al., “Dynamic contrast-enhanced MRI of nasopharyngeal carcinoma: a preliminary study of the correlations between quantitative parameters and clinical stage,” *Journal of Magnetic Resonance Imaging*, vol. 39, no. 4, pp. 940–948, 2014.
- [20] I. Sawazaki-Calone, A. L. C. A. Rangel, A. G. Bueno et al., “The prognostic value of histopathological grading systems in oral squamous cell carcinomas,” *Oral Diseases*, vol. 21, no. 6, pp. 755–761, 2015.
- [21] G. Anneroth and L. S. Hansen, “A methodologic study of histologic classification and grading of malignancy in oral squamous cell carcinoma,” *European Journal of Oral Sciences*, vol. 92, no. 5, pp. 448–468, 1984.

Research Article

Detecting Triple-Vessel Disease with Cadmium Zinc Telluride-Based Single-Photon Emission Computed Tomography Using the Intensity Signal-to-Noise Ratio between Rest and Stress Studies

**Yu-Hua Dean Fang,¹ Tzu-Pei Su,² Chi-Jen Chang,³ Kung-Chu Ho,⁴
May Su,¹ and Tzu-Chen Yen^{4,5}**

¹Department of Biomedical Engineering, National Cheng Kung University, Tainan, Taiwan

²Department of Nuclear Medicine, Chang Gung Memorial Hospital, Keelung, Taiwan

³Department of Cardiology, Chang Gung Memorial Hospital, Linkou, Taiwan

⁴Department of Nuclear Medicine, Chang Gung Memorial Hospital, Linkou, Taiwan

⁵Center for Advanced Molecular Imaging and Translation & Cyclotron Center, Chang Gung Memorial Hospital, Linkou, Taiwan

Correspondence should be addressed to Tzu-Chen Yen; yentc1110@gmail.com

Received 10 May 2017; Revised 10 August 2017; Accepted 27 August 2017; Published 15 October 2017

Academic Editor: Yun Zhou

Copyright © 2017 Yu-Hua Dean Fang et al. This is an open access article distributed under the Creative Commons Attribution License, which permits unrestricted use, distribution, and reproduction in any medium, provided the original work is properly cited.

The purpose of this study was to investigate if a novel parameter, the stress-to-rest ratio of the signal-to-noise ratio (RSNR) obtained with a cadmium zinc telluride (CZT) SPECT scanner, could be used to distinguish triple-vessel disease (TVD) patients. *Methods.* One hundred and two patients with suspected coronary artery disease were retrospectively involved. Each subject underwent a Tl-201 SPECT scan and subsequent coronary angiography. Subjects were separated into TVD ($n = 41$) and control ($n = 61$) groups based on coronary angiography results using 50% as the stenosis cutoff. The RSNR was calculated by dividing the stress signal-to-noise ratio (SNR) by the rest SNR. Summed scores were calculated using quantitative perfusion SPECT (QPS) for all subjects. *Results.* The RSNR in the TVD group was found to be significantly lower than that in the control group (0.83 ± 0.15 and 1.06 ± 0.17 , resp.; $P < 0.01$). Receiver-operating characteristic (ROC) analysis showed that RSNR can detect TVD more accurately than the summed difference score with higher sensitivity (85% versus 68%), higher specificity (90% versus 72%), and higher accuracy (88% versus 71%). *Conclusion.* The RSNR may serve as a useful index to assist the diagnosis of TVD when a fully automatic quantification method is used in CZT-based SPECT studies.

1. Introduction

Single-photon emission computed tomography (SPECT) myocardial perfusion imaging (MPI) is the most common noninvasive imaging modality used to evaluate myocardial perfusion, with approximately 5 million examinations performed annually in the USA alone [1]. Using perfusion tracers such as Tl-201 and ^{99m}Tc -sestamibi, SPECT MPI is easy to perform at reasonable cost and with satisfactory image quality. However, SPECT MPI has limited ability to detect triple-vessel disease (TVD) [2, 3]. TVD is a high-risk condition found in 5%–10% of patients of coronary

artery disease and often requires immediate intervention with stenting or bypass surgery [4–6]. Tracer uptake is globally and uniformly reduced in patients with TVD and balanced ischemia, leading to a seemingly homogeneous and normal distribution of the tracer in the myocardium, which presents a challenge for visual interpretation. Previous studies of the visual interpretation of SPECT MPI for detecting TVD have reported high false-positive rates in the range of 25% to 35% [7–10]. Currently, summed scores calculated using quantitative perfusion SPECT (QPS) are the most commonly used quantitative parameters in routine SPECT MPI studies. However, reports have also shown that QPS scores perform

only modestly in the diagnosis of TVD. For example, in a recent report by Gimelli et al., it was found that the summed stress score and summed difference score provided areas under the curve (AUCs) of 0.79 and 0.69, respectively, using cadmium zinc telluride- (CZT-) based SPECT cameras [11]. Similar studies have reported QPS scores to have variable and unsatisfactory sensitivity values of 46%–75% [12–14]. Such findings seem reasonable given that QPS computes the summed scores based on a comparison between a specific patient study and a population average. If the tracer uptake appears uniform in the myocardium as often seen in TVD patients, QPS scores would tend to be in the normal range, which would make it difficult to discriminate TVD.

In recent years, CZT has been widely adopted as a scintillation material for SPECT cameras. Use of CZT-based cameras is rapidly expanding because of their unique advantages in terms of sensitivity and because they can significantly reduce the tracer dose and scanning time required. Novel CZT-based cameras dedicated for cardiac applications often have a stationary detector design without moving heads [15, 16], consequently allowing new acquisition modes, such as dynamic acquisition. The dynamic capabilities of CZT-based cameras have been tested for absolute quantification of myocardial blood flow and coronary flow reserve. The SPECT-measured coronary flow reserve has been applied to detect TVD in a recent study, showing improved performance (86% sensitivity, 78% specificity) [13]. However, SPECT-based flow quantification is still under investigation and requires more data to verify its clinical performance. Moreover, current protocols for quantitative SPECT rest/stress studies are quite time-consuming because the tracer injection must be performed on table, which offsets the time-saving advantage of CZT-based cameras. As a result, although several reports have shown the accuracy of measurement of coronary flow reserve with SPECT, the nuclear medicine community may still need some time to adopt such methods for routine studies, hence limiting its contribution in the diagnosis of TVD.

In this study, we took the advantage of the stationary detector design of CZT-based cameras by assuming that such a design would allow us to correlate the local signal-to-noise ratio (SNR) with the amount of acquired counts. In tomographic image reconstruction, the relationship between the local SNR and counts on positron emission tomography has been established [17, 18]. In general, the more the counts that are acquired, the higher the local SNR that can be expected from an area of uniform tracer uptake. On the other hand, for SPECT cameras with rotating heads, counts have been dependent on the rotating mechanism and positions of the camera heads. Therefore, it was traditionally assumed that the SNR cannot be directly correlated with the acquired counts for SPECT. Now that the dedicated CZT-based cameras have a stationary detector arrangement, it is in theory possible to use the local SNR to reflect the counts acquired. Conceptually, the ratio of the stress SNR to the rest SNR should be correlated with the ratio of counts acquired from stress and rest studies. Since the tracer uptake during a stress study is roughly halved in patients with TVD when compared with controls, it may be hypothesized that the SNR

during the stress acquisition would be significantly lower in patients with TVD and therefore own the potential to be a discriminative marker. Accordingly, we hypothesized that the stress-to-rest ratio of the SNR (RSNR) would reflect the difference in myocardial blood flow between the rest and stress conditions and be potentially useful for diagnosis of TVD. To investigate this hypothesis, we used a fully automatic segmentation method to delineate the left ventricle (LV) and calculated the RSNR in control subjects and patients with TVD from their Tl-201 scans. Performance of the calculated parameter was evaluated against the reference from coronary angiography (CAG) findings.

2. Material and Methods

2.1. Acquisition of Clinical Data. This retrospective study was approved by the Institutional Review Board of Chang Gung Memorial Hospital, Linkou, Taiwan. We retrospectively collected clinical data from 102 consecutive subjects. All subjects signed the informed consent for the imaging studies. Due to suspected or preexisting coronary artery disease, these subjects underwent SPECT MPI followed by CAG no later than two months after the initial SPECT scans. The inclusion criterion for the TVD group was at least 50% stenosis in all three major coronary branches or 50% stenosis in the left main stem based on CAG findings [7, 19]. The inclusion criterion for the control group was no more than 50% stenosis in any of the three major coronary branches or in the left main stem. Subjects with previous coronary stenting and those who had previously undergone coronary bypass surgeries were excluded from this cohort. Using these criteria, 61 subjects were allocated to the control group and 41 to the TVD group. The clinical information, including age, gender, New York Heart Association (NYHA) classification, ECG findings, and lab results, was collected for each subject. Left ventricular ejection fraction (LVEF) was measured with echocardiography for all subjects except for one.

SPECT MPI was performed according to the standard stress/rest protocol [20]. Each subject was pharmaceutically stressed with dipyridamole 0.142 mg/kg/min infused slowly over 4 minutes, after which an intravenous injection of 2 mCi of Tl-201 was administered. Five to 10 minutes after injection of the tracer, the subject was scanned using a CZT-based SPECT camera (Discovery NM 530c, GE Healthcare, Little Chalfont, UK) in the supine position. Before starting data acquisition, the technician would use the real-time scintillation images to position the heart as close as possible to the center of the field of view. Once positioning was completed, a gated stress acquisition was started to acquire list-mode data over 5 minutes. The images were reconstructed using three-dimensional iterative Bayesian reconstruction algorithm [21, 22] in a 70×70 matrix with 50 slices. The pixel size was set to 4 mm in all three directions. As our SPECT is not equipped with computed tomography, attenuation correction was not performed. Four hours later, the subject was scanned again for acquisition of data at rest. After manually reorienting the images into long-axis and short-axis views, a board-certified nuclear physician used QPS to calculate the summed rest score (SRS), summed stress score (SSS), and summed

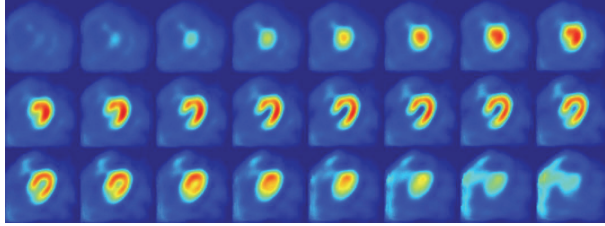


FIGURE 1: Template images generated from ten male subjects.

difference score (SDS) using the built-in software (Myovation for Alcyone, GE Healthcare) [23].

2.2. Segmentation of the LV Myocardium. We used a segmentation method based on spatial normalization that we have described previously [24]. In brief, this approach spatially normalizes the image volume of an individual to a “template” image set precalculated from cohort data. After the transformation relationship is found, the inverse transformation is applied to the predefined LV mask to find the corresponding mask location over the original image volume for the same individual. In this study, we generated the template using the following procedure. The spatial template was generated from images acquired under resting conditions using the same scanner in 20 subjects separate from the study cohort. Average age of them was 63.8 ± 8.9 , 61.8 ± 8.2 , and 62.8 ± 8.4 for female, male, and all subjects, respectively. BMI was 25.0 ± 6.0 , 30.8 ± 4.0 , and 27.9 ± 5.8 for female, male, and all subjects, respectively. These subjects were with negative findings from the SPECT MPI. As none of them underwent further CAG exams, they were not included in the control group of this study. Template images were created separately for men ($n = 10$) and women ($n = 10$). To generate the template for men, one of the ten male subjects was chosen. The images for the other nine subjects were then spatially normalized to this one subject with the software package Statistical Parametric Mapping (SPM, version 8) [25] under MATLAB R2015a (MathWorks Inc., Natick, Massachusetts). The final template for men was generated by averaging all these spatially normalized images, as shown in Figure 1. The template for women was created in the same fashion, using the other ten female subjects. The LV mask was delineated over the template images using the Otsu method [26] separately for male and female subjects.

Segmentation of the LV myocardium for a specific subject was performed as follows. First, the image volume for a specific subject was spatially normalized to the template image for the corresponding sex. The transformation was individually calculated for each subject. Second, this transformation was used to inversely transform the LV mask over the template image into an individual LV mask over the image volume of the specific subject. This inversely transformed LV mask was regarded as the volume of interest (VOI) in the LV myocardium of that subject. All segmentation steps were executed automatically without requiring any manual intervention. The rest and stress images for each subject were segmented to form separate LV VOIs to take into account the

fact that the patient’s position may be different between the rest and stress acquisitions.

2.3. Computation of the RSNR. The RSNR was calculated after the LV myocardial masks were segmented for the rest and stress studies. First, the voxel intensities within the LV VOI of the rest acquisition were taken and used to calculate a mean and standard deviation (SD). SNR_{rest} was then calculated as the mean divided by the SD. $\text{SNR}_{\text{stress}}$ was calculated in the same way, using the stress acquisition and the segmented LV VOI over the stress acquisition. RSNR was calculating by dividing $\text{SNR}_{\text{stress}}$ by SNR_{rest} . These procedures were performed independently and automatically for all subjects.

2.4. Statistical Analysis. As described earlier in this section, the subjects were allocated to the control group or the TVD group groups using the CAG reference criteria for stenosis. The mean (\pm SD) RSNR was calculated for each group. Student’s *t*-test was performed to determine if there was a significant difference in the RSNR between the two groups. Receiver-operating characteristic (ROC) analysis was performed to evaluate the diagnostic performance of RSNR. AUC, accuracy, sensitivity, specificity, and optimal cutoff values were calculated from the ROC curves. A similar statistical analysis was performed for SNR_{rest} , $\text{SNR}_{\text{stress}}$, and the QPS-derived SRS, SSS, and SDS, with mean and SD values calculated for the control group and the TVD groups. ROC analyses were performed for the six parameters (SRS, SSS, SDS, SNR_{rest} , $\text{SNR}_{\text{stress}}$, and RSRN) independent of each other. The parameter (among SRS, SSS, and SDS) with the highest diagnostic accuracy was selected for comparison against the diagnostic performance of RSNR. The sensitivity and specificity of the RSNR and the best-performing score parameter were compared using McNemar’s test. A *P* value < 0.05 was considered to indicate a statistically significant difference between these indices. Univariate logistic regression analysis was used to evaluate how these parameters correlate to disease state (without or with TVD). The statistical analysis was performed with SPSS version 21 (IBM, Armonk, NY).

We also evaluated how age, gender, and body mass index (BMI) affect the diagnostic performances of the SNR-based parameters (SNR_{rest} , $\text{SNR}_{\text{stress}}$, and RSRN) and QPS-based parameters (SRS, SSS, and SDS). To evaluate the effect of age, the subjects were divided into two groups: those with ages less than median age and those with ages greater than or equal to the median age. Using the cutoff values determined from the ROC analysis, we examined what the sensitivity, specificity, and accuracy were obtained from those two age groups. The similar analysis was repeated for the male and female subjects, respectively. Lastly, this analysis was performed using BMI as the grouping criterion which separates the subjects into two groups with the median BMI.

3. Results

In this retrospective study, a total of 102 subjects were involved. 41 subjects were placed in the TVD group, whereas the other 61 subjects were placed in the control group.

TABLE 1: Demographic characteristics of study participants ($n = 102$).

Characteristic	All	Control	TVD
n	102	61	41
Age (yr)	62.6 ± 12.5	60.3 ± 13.3	$66.0 \pm 10.5^*$
Female sex	37	19	18
Hypertension	78	39	39
Body mass index (kg/m^2)	25.9 ± 4.9	26.5 ± 5.2	25.1 ± 4.4
Dyslipidemia	48	24	24
Diabetes	39	15	24
Tobacco use	25	18	7
Angina	74	44	30
LVEF (%)	57.4 ± 17.2	55.7 ± 18.2	59.9 ± 15.4
Arrhythmia	22	16	6
ECG ST change	33	17	16
NYHA class			
I	76	41	35
II	17	14	3
III	6	5	1
IV	3	1	2

TVD, triple-vessel disease; LVEF, left ventricular ejection fraction; ECG, electrocardiography; NYHA, New York Heart Association; * denotes a statistical significance in the mean difference between the control and TVD subjects ($P < 0.05$).

Their demographics and cardiac function parameters were summarized in Table 1. Among these parameters, age was the only parameter that showed a significant difference ($P < 0.05$) between the control and TVD groups. As age was not a specific inclusion or exclusion criterion, this difference might simply be due to the relatively small size of study cohort ($n = 102$).

Using the segmentation method described above, LV VOIs were delineated from the rest and stress acquisitions for all subjects. We confirmed visually that the automatic segmentation appropriately delineated the LV myocardium in all subjects, including those with obvious ischemic defects or dilated myocardium. Figures 2 and 3 showed the segmentation results of two representative cases. The QPS-derived SRS, SSS, and SDS and the proposed SNR_{rest}, SNR_{stress}, and RSNR were calculated from rest/stress Tl-201 images for all subjects in both study groups. The statistics and ROC results of the QPS-derived parameters were summarized in Table 2. The statistics and ROC results of SNR-based parameters were summarized in Table 3. The SSS, SDS, SNR_{stress}, and RSNR values were found to be significantly different between the two study groups ($P < 10^{-5}$). Those four parameters also showed a significant predicting power for TVD subjects ($P < 10^{-3}$) in the simple logistic regression analysis results shown in Table 4. RSNR was lower in patients with TVD (0.83 ± 0.15) than in control subjects (1.06 ± 0.17) as expected because of the reduced uptake during the stress acquisition for patients with TVD. This reduction seemed to be mainly due to the reduction of SNR_{stress} since SNR_{rest} did not show a significant difference between the control and TVD groups.

After we evaluated the statistics of computed parameters, we applied the QPS-based and SNR-based parameters to

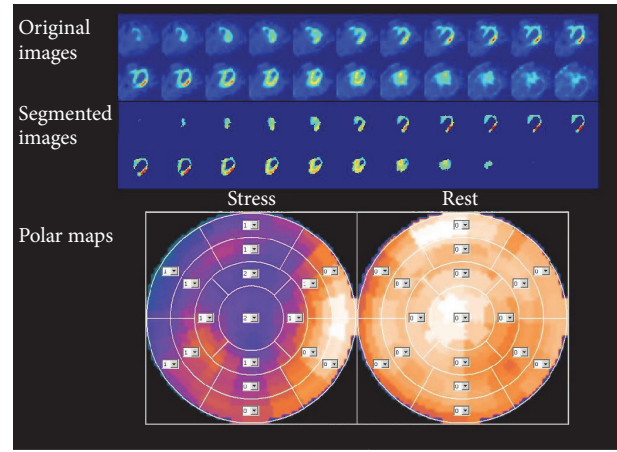


FIGURE 2: The MPI images of a representative TVD case, a 55-year-old man, which showed obvious ischemic deficits. From top to down, the original axial views of the stress acquisition, the segmented axial views of the stress acquisition, and the polar maps were shown. SSS, SRS, and SDS are 14, 0, and 14, respectively. Although the images show ischemic defects in the LAD and LCX, the segmentation was successful to delineate the LV. The SDS was 14 and the RSNR was 0.71. CAG found stenosis of 86% in the LAD, 82% in the LCX, and 68% in the RCA. CAG, coronary angiography; LAD, left anterior descending; LCX, left circumflex; RCA, right coronary artery; RSNR, stress-to-rest ratio of the signal-to-noise ratio; SDS, summed difference score.

discriminate the TVD patients from control subjects. In the results of the ROC analysis shown in Tables 2 and 3, RSNR performed the best in discriminating subjects with and without TVD, with a sensitivity of 85%, a specificity of 90%, an accuracy of 88%, and an AUC of 0.88. The cutoff value for RSNR was found to be 0.94. For QPS scores, the accuracy of the SRS, SSS, and SDS was 59%, 70%, and 71%, respectively. The SDS was found to be the best-performing QPS parameter. McNemar's test showed that, compared to SDS, RSNR had significantly better sensitivity (85% versus 68%, $P < 0.05$) and significantly better specificity (90% versus 72%, $P < 0.05$). The ROC curves for RSNR and SDS are plotted in Figure 4.

We applied the cutoff determined from the ROC analysis to the age-, gender-, and BMI-specific discrimination of the TVD subjects for the QPS-based and SNR-based parameters. The performances in terms of the sensitivity, specificity, and accuracy were summarized in Table 5. For RSNR, age, gender, and BMI did not make much differences in the discrimination performances, in general. Discrimination accuracy with RSNR remained between 86% and 90%. However, we did find that diagnostic sensitivity was lower (75%) in the high-BMI group than the low BMI group (95%).

4. Discussion

In this study, we aimed to address the challenge of detecting multivessel disease using SPECT MPI. The literature indicates that visual interpretation on SPECT may lead to a high false-negative rate and therefore has unsatisfactory sensitivity in detecting TVD. Quantification of absolute flow and flow

TABLE 2: Statistics and the ROC results of the QPS scores.

Parameter	SRS			SSS			SDS		
	All	Control	TVD	All	Control	TVD	All	Control	TVD
Mean	2.12	2.07	2.2	5.44	3.52	8.29	3.28	1.46	6.00
SD	2.67	2.6	2.81	5.24	3.78	5.83	4.62	2.38	5.72
Sensitivity		34			78			68	
Specificity		75			64			72	
Accuracy		59			70			71	
AUC		0.49			0.77			0.75	
Cutoff		2.5			3.5			2.5	
P value		0.81			$P < 10^{-5}$			$P < 10^{-5}$	

P value is derived from the *t*-test of the control versus TVD subjects. ROC, receiver-operating characteristic; QPS, quantitative perfusion single-photon emission computed tomography; SRS, summed rest scores; SSS, summed stress scores; SDS, summed difference scores; AUC, area under the curve.

TABLE 3: Statistics and the ROC results of the image-derived SNR at rest and stress and the ratio of the $\text{SNR}_{\text{stress}}$, SNR_{rest} , and RSNR.

Parameter	SNR_{rest}			$\text{SNR}_{\text{stress}}$			RSNR		
	All	Control	TVD	All	Control	TVD	All	Control	TVD
Mean	4.09	4.03	4.18	3.92	4.24	3.44	0.97	1.06	0.83
SD	0.70	0.73	0.66	0.85	0.83	0.65	0.2	0.17	0.15
Sensitivity		83			76			85	
Specificity		43			75			90	
Accuracy		59			75			88	
AUC		0.57			0.78			0.88	
Cutoff		3.74			3.7			0.94	
P value		0.26			$P < 10^{-5}$			$P < 10^{-5}$	

P value is derived from the *t*-test of the control versus TVD subjects. SNR, signal-to-noise ratio; SNR_{rest} , signal-to-noise ratio at the rest study; $\text{SNR}_{\text{stress}}$, signal-to-noise ratio at the stress study; RSNR, stress-to-rest ratio of the signal-to-noise ratio.

TABLE 4: Univariate logistic regression results of selected parameters.

Variable	Odds ratio	P value	95% CI
Age	1.04	0.03	1.00–1.08
Sex	1.73	0.19	0.76–3.93
BMI	0.94	0.19	0.87–1.03
SRS	1.02	0.81	0.88–1.18
SSS	1.24	<0.001	1.12–1.38
SDS	1.40	<0.001	1.19–1.65
SNR_{rest}	1.39	0.26	0.78–2.46
$\text{SNR}_{\text{stress}}^{\$}$	4.48	<0.001	2.21–9.11
RSNR ^{\$}	33432.17	<0.001	469.91–2378545.76

^{\$}For $\text{SNR}_{\text{stress}}$ and RSNR, since their mean is lower in the TVD group, the logistic regression was performed using ($\text{SNR}_{\text{stress}}$) and (RSNR) against the TVD status.

reserve has been shown to be useful in assisting the diagnosis of TVD with positron emission tomography [27, 28] and magnetic resonance imaging [3, 29]. Although SPECT-based quantification of flow has also been investigated in recent years [13, 19, 30–34], its adoption for routine studies is still limited due to the prolonged acquisition time and other technical difficulties. In the present study, we tested our hypothesis that TVD may be detected with a simple parameter, that is, the ratio between local SNRs in the LV myocardium from the

rest and stress studies. We used Tl-201 images acquired from 102 subjects to evaluate this hypothesis. Our current data support our working hypothesis concerning the usefulness of RSNR. Using our proposed data processing scheme, the RSNR can be calculated automatically with 85% sensitivity, 90% specificity, and 88% accuracy when used to detect TVD. By way of comparison, the SDS was found to be the most accurate parameter among the three summed scores in our data, but even SDS could only discriminate patients with TVD from controls with 68% sensitivity, 72% specificity, and 71% accuracy, which is similar to the performance previously reported for QPS-derived scores [11–14]. Comparing the diagnostic performance of the two parameters, our data show that the proposed RSNR, calculated with a fully automatic procedure, has the potential to advance the sensitivity and accuracy in the diagnosis of TVD.

We have also evaluated whether age, gender, and BMI would affect the diagnostic performances of RSNR. We found that age does not seem to affect the diagnostic performances with the sensitivity/specification/accuracy being 81/91/88 (%) in the lower age group and 88/88/88 (%) in the higher age group. Similarly, the same pattern was observed in the two gender groups. The BMI groups, on the other hand, did show a slightly different pattern than age or gender. We found that, with the median BMI of 25.3 as the cutoff to separate the subjects, the sensitivity/specification/accuracy was found to be 95/87/90 (%) for the lower BMI group and 75/94/86

TABLE 5: Diagnostic performances of QPS scores and SNR parameters in specific age, gender, and BMI groups.

Variable	<i>n</i>	SRS	SSS	SDS	SNR _{rest}	SNR _{stress}	RSNR
Age							
<62.5	51	25/74/59	69/63/65	75/74/75	81/43/55	69/83/78	81/91/88
≥62.5	51	40/71/59	84/65/75	64/69/67	84/42/63	80/66/73	88/88/88
Sex							
Male	65	35/76/62	83/64/71	65/71/69	87/29/49	74/86/82	87/90/89
Female	37	33/74/54	72/63/68	72/74/73	78/74/76	78/53/65	83/89/86
BMI							
<25.3	51	29/70/53	81/63/71	62/73/69	86/43/61	71/83/78	95/87/90
≥25.3	51	40/81/65	75/65/69	75/71/73	80/42/57	80/68/73	75/94/86

Numbers are presented as percentages of sensitivity/specificity/accuracy; for age and BMI, the cutoff for grouping was determined from their medians.

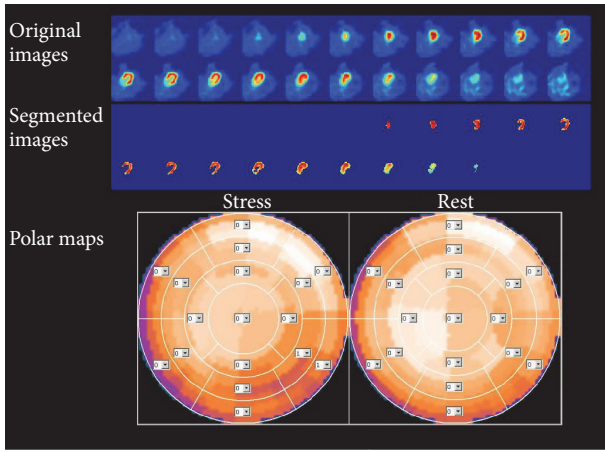


FIGURE 3: The stress MPI images of a representative TVD case, a 64-year-old woman, which showed uniform tracer uptake in the myocardium. From top to down, the original axial views of the stress acquisition, the segmented axial views of the stress acquisition, and the polar maps were shown. SSS, SRS, and SDS are 2, 0, and 2, respectively. The RSNR was 0.91, indicating a low tracer uptake in the stress study and high possibility of present TVD. The CAG identified stenosis of 61% in the LAD, 69% in the LCX, and 62% in the RCA.

(%) for the higher BMI group. Although the accuracy and specificity were not much different than those from the whole study population, there was an obvious drop of sensitivity to 75% in the higher BMI group. We presume that this drop might be due to the lack of attenuation correction in our study. Since the attenuation is dependent on the patient size, BMI may have a nonnegligible effect over the RSNR values. One potential remedy for this is to establish different RSNR cutoff values for low- and high-BMI groups separately, if a larger cohort may be obtained in the future. Alternatively, if computed tomography is available on the SPECT scanner, it would be useful to evaluate how attenuation correction affects the RSNR values and how RSNR performs in diagnosing TVD when attenuation correction is involved in the image reconstruction.

Although our data seem promising, the proposed method still requires further evaluation before it can become a routine diagnostic tool. The study cohort (*n* = 102) was only

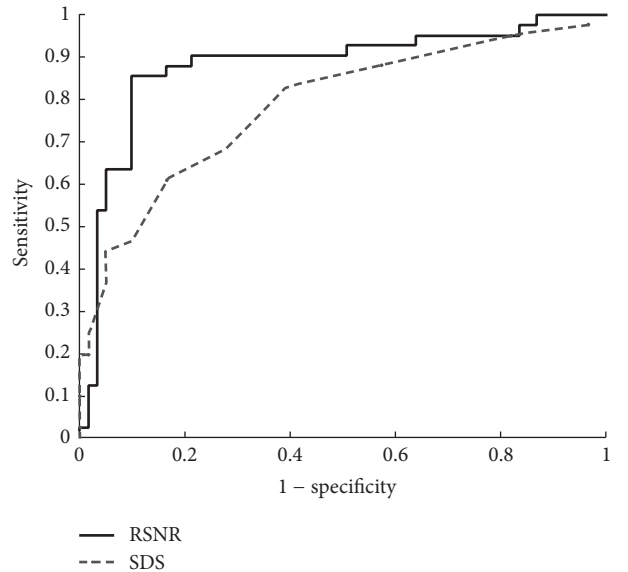


FIGURE 4: ROC analysis. The ROC curves for the proposed parameter RSNR and SDS are shown on the same plot. RSNR provides a better diagnostic performance than the SDS, with AUC of 0.88 versus 0.75. AUC, area under the curve; ROC, receiver-operating characteristic; RSNR, stress-to-rest ratio of the signal-to-noise ratio; SDS, summed difference score.

of a modest size in this work. Data from a larger cohort will be useful to confirm the diagnostic performance of this method. Further, a multicenter trial will be helpful in determining the extent to which the RSNR is dependent on the scanners, protocols, and reconstruction parameters used. The RSNR cutoff for different tracers may also differ and requires further validation. Myocardial segmentation may be conducted differently using other automatic LV segmentation techniques [35–37], so the effects of different segmentation methods also need to be investigated. In the present study, the RSNR cutoff was the same for both sexes in our current study. How RSNR values vary according to race, ethnicity, sex, and age requires more comprehensive evaluation in the future. Lastly, because there is no computed tomography in our SPECT camera, attenuation correction was not performed. Scatter correction was not performed either, as it was not provided by the scanner vendor. A previous report on the

CZT camera performances has shown that the CZT SPECT has a roughly twofold increase in energy resolution that is capable of a better scatter rejection than conventional SPECT cameras [22]. The exact effects of attenuation and scatter correction on the RSNR remain to be studied in the future.

5. Conclusion

A novel parameter based on the stress-to-rest ratio of the SNR, namely, RSNR, has been proposed and shown to be a potentially useful parameter for detecting TVD with CZT-based SPECT MPI. According to our data, this fully automatic method provides a high sensitivity of 85% and high specificity of 90% in discriminating TVD. Patient size does seem to cause a drop in the detection sensitivity with RSNR to 75% in the high-BMI group, but the discrimination accuracy is generally independent of the patient size, age, or gender. Although further studies are required to evaluate the clinical value of RSNR, it points to a robust and quantitative way to assist the diagnosis of TVD with SPECT MPI.

Conflicts of Interest

The authors declare that there are no conflicts of interest regarding the publication of this paper.

Authors' Contributions

Yu-Hua Dean Fang and Tzu-Pei Su contributed equally to this work.

Acknowledgments

This work was financially supported by Ministry of Science and Technology, Taiwan, Research Grant 104-2221-E-006-271-MY2.

References

- [1] E. J. McNulty, Y.-Y. Hung, L. M. Almers, A. S. Go, and R. W. Yeh, "Population trends from 2000–2011 in nuclear myocardial perfusion imaging use," *JAMA - Journal of the American Medical Association*, vol. 311, no. 12, pp. 1248–1249, 2014.
- [2] N. Mahajan, L. Polavaram, H. Vankayala et al., "Diagnostic accuracy of myocardial perfusion imaging and stress echocardiography for the diagnosis of left main and triple vessel coronary artery disease: A comparative meta-analysis," *Heart*, vol. 96, no. 12, pp. 956–966, 2010.
- [3] S.-Y. Chung, K.-Y. Lee, E. J. Chun et al., "Comparison of stress perfusion MRI and SPECT for detection of myocardial ischemia in patients with angiographically proven three-vessel coronary artery disease," *American Journal of Roentgenology*, vol. 195, no. 2, pp. 356–362, 2010.
- [4] "Myocardial Infarction and Mortality in the Coronary Artery Surgery Study (CASS) Randomized Trial," *New England Journal of Medicine*, vol. 310, no. 12, pp. 750–758, 1984.
- [5] E. Varnauskas, S. B. Olsson, and E. Carlstrom, "Long-term results of prospective randomised study of coronary artery bypass surgery in stable angina pectoris," *Lancet*, vol. 2, no. 8309, pp. 1173–1180, 1982.
- [6] J. P. Greenwood, N. Maredia, J. F. Younger et al., "Cardiovascular magnetic resonance and single-photon emission computed tomography for diagnosis of coronary heart disease (CE-MARC): a prospective trial," *The Lancet*, vol. 379, no. 9814, pp. 453–460, 2012.
- [7] R. S. Khattar, R. Senior, and A. Lahiri, "Assessment of myocardial perfusion and contractile function by inotropic stress Tc-99m sestamibi SPECT imaging and echocardiography for optimal detection of multivessel coronary artery disease," *Heart*, vol. 79, no. 3, pp. 274–280, 1998.
- [8] M. Ragosta, A. H. Bishop, L. C. Lipson et al., "Comparison Between Angiography and Fractional Flow Reserve Versus Single-Photon Emission Computed Tomographic Myocardial Perfusion Imaging for Determining Lesion Significance in Patients With Multivessel Coronary Disease," *American Journal of Cardiology*, vol. 99, no. 7, pp. 896–902, 2007.
- [9] N. Melikian, P. De Bondt, P. Tonino et al., "Fractional Flow Reserve and Myocardial Perfusion Imaging in Patients With Angiographic Multivessel Coronary Artery Disease," *JACC: Cardiovascular Interventions*, vol. 3, no. 3, pp. 307–314, 2010.
- [10] S. M. Zaacks, A. Ali, J. E. Parrillo, and J. T. Barron, "How well does radionuclide dipyridamole stress testing detect three-vessel coronary artery disease and ischemia in the region supplied by the most stenotic vessel?" *Clinical Nuclear Medicine*, vol. 24, no. 1, pp. 35–41, 1999.
- [11] A. Gimelli, R. Liga, V. Duce, A. Kusch, A. Clemente, and P. Marzullo, "Accuracy of myocardial perfusion imaging in detecting multivessel coronary artery disease: A cardiac CZT study," *Journal of Nuclear Cardiology*, pp. 1–9, 2016.
- [12] Y. Z. Tan, S. Özdemir, B. Altun, and F. Çelik, "Assessment of Heart Rate Recovery with GATED-Myocardial Perfusion Scintigraphy Outcome in Patients with Coronary Artery Disease: A Retrospective Study and Institutional Experience," *Molecular Imaging and Radionuclide Therapy*, vol. 25, no. 3, pp. 121–127, 2016.
- [13] S. Shiraishi, F. Sakamoto, N. Tsuda et al., "Prediction of left main or 3-vessel disease using myocardial perfusion reserve on dynamic thallium-201 single-photon emission computed tomography with a semiconductor gamma camera," *Circulation Journal*, vol. 79, no. 3, pp. 623–631, 2015.
- [14] S. Hida, T. Chikamori, H. Tanaka et al., "Diagnostic value of left ventricular function after stress and at rest in the detection of multivessel coronary artery disease as assessed by electrocardiogram-gated SPECT," *Journal of Nuclear Cardiology*, vol. 14, no. 1, pp. 68–74, 2007.
- [15] W. Acampa, R. R. Buechel, and A. Gimelli, "Low dose in nuclear cardiology: State of the art in the era of new cadmium-zinc-telluride cameras," *European Heart Journal Cardiovascular Imaging*, vol. 17, no. 6, pp. 591–595, 2016.
- [16] L. Imbert, S. Poussier, P. R. Franken et al., "Compared performance of high-sensitivity cameras dedicated to myocardial perfusion SPECT: A comprehensive analysis of phantom and human images," *Journal of Nuclear Medicine*, vol. 53, no. 12, pp. 1897–1903, 2012.
- [17] T. Chang, G. Chang, J. W. Clark Jr., R. H. Diab, E. Rohren, and O. R. Mawlawi, "Reliability of predicting image signal-to-noise ratio using noise equivalent count rate in PET imaging," *Medical Physics*, vol. 39, no. 10, pp. 5891–5900, 2012.

- [18] C. C. Watson, "Count rate dependence of local signal-to-noise ratio in positron emission tomography," *IEEE Transactions on Nuclear Science*, vol. 51, no. 5, pp. 2670–2680, 2004.
- [19] F. B. Bouallègue, F. Roubille, B. Lattuca et al., "SPECT myocardial perfusion reserve in patients with multivessel coronary disease: Correlation with angiographic findings and invasive fractional flow reserve measurements," *Journal of Nuclear Medicine*, vol. 56, no. 11, pp. 1712–1717, 2015.
- [20] B. Songy, M. Guernou, D. Lussato, M. Queneau, and R. Geronazzo, "Low-dose thallium-201 protocol with a cadmium-zinc-telluride cardiac camera," *Nuclear Medicine Communications*, vol. 33, no. 5, pp. 464–469, 2012.
- [21] T. Hebert and R. Leahy, "A Generalized EM Algorithm for 3-D Bayesian Reconstruction from Poisson Data Using Gibbs Priors," *IEEE Transactions on Medical Imaging*, vol. 8, no. 2, pp. 194–202, 1989.
- [22] M. Bocher, I. M. Blevis, L. Tsukerman, Y. Shrem, G. Kovalski, and L. Volokh, "A fast cardiac gamma camera with dynamic SPECT capabilities: Design, system validation and future potential," *European Journal of Nuclear Medicine and Molecular Imaging*, vol. 37, no. 10, pp. 1887–1902, 2010.
- [23] G. Germano, P. B. Kavanagh, P. J. Slomka, S. D. Van Kriekinge, G. Pollard, and D. S. Berman, "Quantitation in gated perfusion SPECT imaging: The Cedars-Sinai approach," *Journal of Nuclear Cardiology*, vol. 14, no. 4, pp. 433–454, 2007.
- [24] Y.-H. D. Fang, S.-C. Chiu, C.-S. Lu, T.-C. Yen, and Y.-H. Weng, "Fully automated quantification of the striatal uptake ratio of [^{99m}Tc]-TRODAT with SPECT imaging: Evaluation of the diagnostic performance in Parkinson's disease and the temporal regression of striatal tracer uptake," *BioMed Research International*, vol. 2015, Article ID 461625, 2015.
- [25] J. Ashburner and K. J. Friston, "Nonlinear spatial normalization using basis functions," *Human Brain Mapping*, vol. 7, no. 4, pp. 254–266, 1999.
- [26] N. Otsu, "A threshold selection method from gray-level histograms," *Automatica*, vol. 11, pp. 23–27, 1975.
- [27] R. Parkash, R. A. deKemp, T. D. Ruddy et al., "Potential utility of rubidium 82 PET quantification in patients with 3-vessel coronary artery disease," *Journal of Nuclear Cardiology*, vol. 11, no. 4, pp. 440–449, 2004.
- [28] H. R. Schelbert, "Quantification of Myocardial Blood Flow: What is the Clinical Role?" *Cardiology Clinics*, vol. 27, no. 2, pp. 277–289, 2009.
- [29] M. Motwani, N. Maredia, T. A. Fairbairn, S. Kozerke, J. P. Greenwood, and S. Plein, "Assessment of ischaemic burden in angiographic three-vessel coronary artery disease with high-resolution myocardial perfusion cardiovascular magnetic resonance imaging," *European Heart Journal Cardiovascular Imaging*, vol. 15, no. 6, pp. 701–708, 2014.
- [30] S. Ben-Haim and D. Agostini, "Dynamic SPECT: evolution of a widely available tool for the assessment of coronary flow reserve," *European Journal of Nuclear Medicine and Molecular Imaging*, vol. 42, no. 2, pp. 302–304, 2014.
- [31] R. G. Wells, R. Timmins, R. Klein et al., "Dynamic SPECT measurement of absolute myocardial blood flow in a porcine model," *Journal of Nuclear Medicine*, vol. 55, no. 10, pp. 1685–1691, 2014.
- [32] R. Nkoulou, T. A. Fuchs, A. P. Pazhenkottil et al., "Absolute myocardial blood flow and flow reserve assessed by gated SPECT with cadmium-zinc-telluride detectors using ^{99m}Tc-tetrofosmin: Head-to-head comparison with ¹³N-ammonia PET," *Journal of Nuclear Medicine*, vol. 57, no. 12, pp. 1887–1892, 2016.
- [33] S. Ben-Haim, V. L. Murthy, C. Breault et al., "Quantification of myocardial perfusion reserve using dynamic SPECT imaging in humans: A feasibility study," *Journal of Nuclear Medicine*, vol. 54, no. 6, pp. 873–879, 2013.
- [34] Y. D. Fang, Y. Liu, K. Ho et al., "Single-scan rest/stress imaging with ^{99m}Tc-Sestamibi and cadmium zinc telluride-based SPECT for hyperemic flow quantification: a feasibility study evaluated with cardiac magnetic resonance imaging," *PLoS ONE*, vol. 12, no. 8, Article ID e0183402, 2017.
- [35] H. Soneson, J. F. A. Ubachs, M. Ugander, H. Arheden, and E. Heiberg, "An improved method for automatic segmentation of the left ventricle in myocardial perfusion SPECT," *Journal of Nuclear Medicine*, vol. 50, no. 2, pp. 205–213, 2009.
- [36] H. Soneson, H. Engblom, E. Hedström et al., "An automatic method for quantification of myocardium at risk from myocardial perfusion SPECT in patients with acute coronary occlusion," *Journal of Nuclear Cardiology*, vol. 17, no. 5, pp. 831–840, 2010.
- [37] E. Heiberg, J. Sjögren, M. Ugander, M. Carlsson, H. Engblom, and H. Arheden, "Design and validation of segment—freely available software for cardiovascular image analysis," *BMC Medical Imaging*, vol. 10, article 1, 2010.

Research Article

Post Mortem Leukocyte Scintigraphy in Juvenile Pigs with Experimentally Induced Osteomyelitis

Pia Afzelius,¹ Ole Lerberg Nielsen,²
Svend Borup Jensen,^{3,4} and Aage Kristian Olsen Alstrup⁵

¹Department of Diagnostic Imaging, Section of Clinical Physiology and Nuclear Medicine, Copenhagen University Hospital, North Zealand, Hillerød, Denmark

²Department of Veterinary and Animal Sciences, University of Copenhagen, Copenhagen, Denmark

³Department of Nuclear Medicine, Aalborg University Hospital, Aalborg, Denmark

⁴Department of Chemistry and Biosciences, Aalborg University, Aalborg, Denmark

⁵Department of Nuclear Medicine & PET-Centre, Aarhus University Hospital, Aarhus, Denmark

Correspondence should be addressed to Pia Afzelius; pia.afzelius@dadlnet.dk

Received 12 June 2017; Revised 27 July 2017; Accepted 7 August 2017; Published 11 September 2017

Academic Editor: Chongzhao Ran

Copyright © 2017 Pia Afzelius et al. This is an open access article distributed under the Creative Commons Attribution License, which permits unrestricted use, distribution, and reproduction in any medium, provided the original work is properly cited.

We have previously demonstrated that ¹¹¹In-labeled autologous leukocyte scintigraphy is able to detect osteomyelitis in living juvenile pigs. In animal research studies, it may well be an advantage if the animals could be scanned after euthanasia. Applying traditional scanning of living animals to euthanized animals will render anaesthesia unnecessary and be ideal for obtaining good and reliable scans for the correct interpretation of imaging afterwards, since the animals do not move. The autologous leukocytes of the pigs were collected, marked with ¹¹¹In, and reinjected into the pigs and allowed for homing to the site of infections as usual while the pigs were alive. In this study, we demonstrate that it is possible to perform SPECT/CT with ¹¹¹In-labelled autologous leukocytes almost 24 hrs *after* euthanasia with the same detectability of osteomyelitic lesions as in living pigs (78% versus 79%). The pigs in this study had exactly the same experimental conditions as the living pigs and were examined in parallel with the living pigs except for euthanasia prior to the leukocyte scan and that no PET/CT scans were performed.

1. Introduction

Chronic osteomyelitis is a progressive inflammatory process caused most often by *Staphylococcus aureus* (*S. aureus*), resulting in bone destruction and sequestrum formation, which may maintain the infection. The “gold standard” for the diagnosis of chronic osteomyelitis is the presence of positive bone cultures and histopathologic examination of the bone, but noninvasive diagnostic imaging is preferred in humans. We have thus previously refined a pig-model for hematogenous spread of osteomyelitis [1, 2] and used this for examining suitable tracers for better noninvasive imaging [3–5]. In the model, we injected *S. aureus* unilaterally into the femoral artery of female juvenile domestic pigs and tested various radioactive tracers to identify the most useful diagnostic imaging protocol for bone infections. This aim

necessitated a rather busy scanning protocol and prolonged anaesthesia, and due to biological variance and experiment planning we had to infect more pigs that finally were anaesthetized and scanned; the surplus of pigs was euthanized prior to the scans. We, therefore, were curious to see if it was possible to do post mortem scintigraphy of the extra pigs using a tracer with a long half-life injected before euthanasia, thus leaving no pig unused and delaying the scintigraphy to a later and more convenient time.

Naturally occurring *S. aureus* infection in pigs usually manifests as sepsis, which includes development of osteomyelitis. Johansen et al. [6] demonstrated that as in children circulating microorganisms tend to start infections in the metaphyseal ends of the long bones in juvenile pigs. This is probably due to seeding of a septic embolus aided by the slow circulation in the capillary loops in the metaphyseal

growth zone making juvenile pigs particularly susceptible to epiphyseal spread and arthritis of the adjacent joint.

^{111}In -leukocyte scintigraphy is a diagnostic imaging tool that displays the distribution of radiolabelled autologous leukocytes in the body. Regional or whole-body planar and/or single photon emission computed tomography (SPECT) scintigraphy perhaps combined with computed tomography (CT) of specific anatomic regions can be obtained for suspected infection/inflammation. Leukocytes are separated from plasma for labelling with ^{111}In . ^{111}In decays by electron capture emitting two gamma photons of 173 keV and 247 keV. The physical half-life is 67 hrs. ^{111}In is bound to a lipid-soluble complex that chelates metal ions. The ^{111}In -oxine complex diffuses through the cell membrane and once intracellular, the complex dissociates, and ^{111}In binds nuclear and cytoplasmic proteins. After labelling and reinjection radiolabelled leukocytes of humans are distributed to the blood pool, lungs, and the reticuloendothelial system of the liver, spleen, bone marrow, and major blood vessels. Imaging is performed 18–24 hrs after injection when lung, blood pool, bowel, and bladder activity are not normally seen.

We have previously demonstrated by SPECT/CT of living pigs that it is possible to mark porcine leukocytes with ^{111}In , that the marked porcine leukocytes were capable of homing to sites of osteomyelitic lesions, and that the biodistribution is comparable to the human biodistribution [5]. The major difference was the accumulation of activity in the lungs of juvenile pigs, which is only a transient phenomenon in healthy human lungs. The reason for this difference is that the lungs of the pigs are part of the reticuloendothelial system.

2. Materials and Methods

2.1. Pigs and the *S. aureus* Model. Five pigs, all clinically healthy, specific pathogen-free Danish landrace-Yorkshire cross-breed female pigs (approximately 20 kg) aged 8–9 weeks, were purchased from a local commercial pig farmer. All pigs received a restricted pellet diet (DIA plus FI, DLG, Denmark). The environmental conditions were 20°C, 51% relative humidity, 12 : 12 hours light cycles, and 8 air exchanges hourly. The pigs were fasted for 16 h prior to anaesthesia but had free access to tap water. After one week of acclimatization the pigs were, under propofol anaesthesia, inoculated with a suspension of the porcine strain S54F9 [7] of *S. aureus* (10^5 colony forming units per kg in 1.0 to 1.5 mL) into the femoral artery of the right hind limb to induce osteomyelitis, as described elsewhere [1, 2].

We have previously reported that some pigs in this osteomyelitis model will develop haematogenous dissemination of *S. aureus* leading to, for example, embolic pneumonia [3, 4]. In order to reduce the frequency of these additional lesions we used animals aged 8–9 weeks and administered procaine benzyl penicillin intramuscularly as described by Alstrup et al. [2]; after onset of clinical signs, for example, limping of the right hind limb, which occurred in all pigs, the pigs were thus once injected with a single intramuscular (IM) procaine benzyl penicillin 10,000 IE/kg (Penovet, Boehringer Ingelheim, Copenhagen, Denmark). Buprenorphine (45 µg/kg Temgesic

(Reckitt Benckiser, Berkshire, England)) was given three times daily (7 AM, 3 PM, and 11 PM) from time of inoculation until euthanasia. One week after inoculation, the pigs had obtained a body weight of 21–22 kg (Table 1); then anaesthesia was induced, labelling of leukocytes was performed, and then the Indium-111 labelled leukocytes were reinjected. After a various time (Table 1), the pigs were euthanized with an overdose of pentobarbital (100 mg/kg IV), and finally the pigs were scanned at convenient time points (Table 1).

The study was approved by the Danish Animal Experimentation Board (number 2012-15-2934-000123). All facilities were approved by the Danish Occupational Health Surveillance.

2.2. Imaging

2.2.1. Computed Tomography. All examinations at the Positron Emission Centre of Aarhus University Hospital were performed with an integrated PET/computed tomography (CT) system (Siemens Biograph True point 64 PET/CT, Siemens, Erlangen, Germany), one bed position spanning 21 cm. The pigs were anaesthetized with propofol, intubated (for mechanical ventilation), and placed in dorsal recumbence as described by Alstrup and Winterdahl [8]. Initially, a scout view was obtained to secure body coverage from snout to tail.

2.2.2. ^{111}In -Labeled Autologous Leukocytes. After the CT-scan, ^{111}In oxine labelled leukocytes were prepared according to the instructions given by the manufacturer, Mallinckrodt, Pharmaceutical, Copenhagen, Denmark. The ^{111}In -labelling of leukocytes included isolation of the leukocyte fraction from autologous full blood using sedimentation and centrifugation [9]. Visual inspection of the preparation searching for clumps, clots, fibrin, and platelet aggregates was performed throughout the procedure and in particular after resuspension of the pellet of cells after centrifugation. A labelling efficiency between 50% and 80% is expected in human cells in accordance with the European guidelines [9]. We have previously demonstrated that the labelling efficacy of pig leukocytes is similar [5]. Microscopic inspection and trypan blue exclusion test for cell viability were planned if the labelling efficiency was below 50%. The labelling of the leukocyte preparations and the reinjection were performed on day 6 after inoculation (PI), that is, approximately one day before the SPECT and PET scans (day 7 PI). The injected activity of ^{111}In -labelled leukocytes was 18.1–24.7 MBq.

2.2.3. Scintigraphy. In almost all cases the pigs were euthanized in the morning on the day after reinjection of labelled leukocytes and placed in cold environments waiting for the transport together with the living pigs to Aalborg University Hospital as reported previously by [5]. Whole-body planar gamma imaging was then acquired by a dual-headed gamma camera in Aalborg with a medium-energy parallel-hole collimator and using the 2 energy peaks of ^{111}In : 172 and 245 keV, 15% symmetrical windows, and simultaneous two-plane anterior and posterior whole-body acquisition (500,000 counts in a 256×256 matrix for regional and a

TABLE 1: Pig characteristics and time points of scans.

Pig	Body weight (kg)	Time of CT scan the previous day Living pig	Labelling percent (%)	Injected activity (MBq)	Time points ¹¹¹ In-injection the previous day	Time points of death	Injection to death interval (h)	Time points of post mortem SPECT/CT	Death to scan interval (h)
a	21	15:26	76.8%	21.8	16:55	20:40*	3.75	17:55	20.25
b	22	14:57	64.7%	18.1	16:20	9:00	16.67	16:49	7.82
c	22	13:14	78.8%	24.7	16:28	9:30	17.03	16:31	7.02
d	21	9:47	74.6%	24.5	16:26	16:00	23.57	16:56	0.93
e	21.5	15:05	73.8%	24.4	17:50	15:40	21.83	16:13	0.55

*The previous day.

TABLE 2: Number of lesions defined by gross pathology, histopathology, microbiology, and/or CT in 5 juvenile euthanized pigs with haematogenous spread of *S. aureus* osteomyelitis. *S. aureus* culture or immunohistochemistry confirmed at necropsy is summarized in the lower two rows.

CT lesion	a	b	Pig c ¹	d	e
Osteomyelitis	2	4	3	3	6
Sequesters	3	5	6	4	4
Osteolysis of adjacent cortical bone	2	4	6	5	4
Contiguous periosteal abscess	1	3	2	2	2
Arthritis	1 ²			0	
Hematoma/abscess at inoculation site	0	0	1	0	0
Lymph node enlargement	2	2	1	2	2

¹Increased leukocyte accumulation in the growth zone of the left proximal calcaneus area (noninoculated limb). ²Acute fibrinous arthritis in the right hock joint.

256 × 1024 matrix for whole body, zoom 1.0) and supplied with single photon emission computed tomography/high dose computed tomography SPECT/CT using a Symbia T16 SPECT/CT (Siemens Medical Solutions, Hoffman Estates, Illinois, USA). The data were analysed using Philips Medical Systems DICOM Brilliance TM Workspaces, Koninklijke Philips Electronics NV 2007, DA Best, Netherlands. One day prior to the SPECT/CT high dose CT was performed in the PET-Centre of Aarhus with an integrated PET/computed tomography (CT) system (Siemens Biograph True point 64 PET/CT, Siemens, Erlangen, Germany), one bed position spanning 21 cm. The pigs were placed in dorsal recumbence. Initially, a scout view was obtained to secure body coverage from snout to tail.

2.2.4. Images and Interpretation. All images were evaluated by an experienced senior specialist in nuclear medicine and computed tomography. The pigs were inoculated in the right hind limb and the left hind limb served as a healthy control. The lesions seen on CT were registered and counted (Table 2) and examined for leukocyte accumulation as summarized in Table 3. The percentage of osteomyelitic lesions accumulating ¹¹¹In-labelled leukocytes was calculated. Focal ¹¹¹In leukocyte accumulation that was greater than adjacent or contralateral background activity and corresponded to a bone site, or more specifically to a site of increased bone radiopharmaceutical accumulation (but did not have to be of the same intensity), was registered. Very discrete leukocyte

accumulation was seen in some soft tissues and is indicated by an additional number in a parenthesis but was not accepted as an accumulation. All the OM lesions were confirmed by autopsy the following day and supplied with microbiological, immunohistochemistry, and/or microscopy later on.

3. Results

The pigs were scanned 0.55–20.25 hours after euthanasia (Table 1). Diffuse leukocyte accumulation was seen in lungs, liver, and spleen. Prolonged clearance of activity from labelled leukocytes from liver and spleen was in accordance with previous results in living pigs [5]; however, the activity in the liver was lesser when scanning post mortem. As in living pigs, low excretion activity was seen in both faeces and urine. On post mortem CT the lungs were characterized by pulmonary oedema and gas effusion of variable extent was seen in parenchymal organs which are ascribed to the scintigraphy being performed post mortem. The pigs had developed foci of osteomyelitis in the inoculated limbs with insignificant signs of further spread to internal organs (Table 2). An example of ¹¹¹In-marked autologous leukocyte accumulation in an osteomyelitic lesion visualized on post mortem scintigraphy and CT is shown in Figure 1. At autopsy, no extra osteomyelitic lesions apart from the lesions seen on CT were found.

In general, the activity of ¹¹¹In was diffusely increased in the affected hind limb. ¹¹¹In-labeled autologous leukocytes

TABLE 3: ^{111}In -labeled leukocyte accumulation in lesions in the pelvic and right hind limb regions in 5 juvenile pigs with haematogenous *S. aureus* osteomyelitis leukocyte-scanned post mortem.

Pig	Lesion	Total number	^{111}In -leukocytes
a	Osteomyelitic foci	2	1
	Contiguous periosteal abscess	1	1
	Hematoma//abscess at inoculation site	0	0
	Lymph node enlargement	2	0
b	Diffusely increased accumulation in the left limb	—	+
	Osteomyelitic foci	4	3
	Contiguous periosteal abscess	3	0
	Hematoma//abscess at inoculation site	0	—
c	Lymph node enlargement	2	0
	Osteomyelitic foci	3	3
	Contiguous periosteal abscess	2	0
	Hematoma/abscess at inoculation site	1	0
d	Lymph node enlargement	1	0
	Osteomyelitic foci	3	3
	Contiguous periosteal abscess	2	(1)
	Hematoma/abscess at inoculation site	0	—
e	Lymph node enlargement	2	(1)
	Osteomyelitic foci	6	4
	Contiguous periosteal abscess	3	3
	Hematoma/abscess at inoculation site	0	—
Total	Lymph node enlargement	2	0
	Osteomyelitic foci	18	14
	Contiguous periosteal abscess	13	4 (5)
	Hematoma/abscess at inoculation site	1	0
	Lymph node enlargement	9	(1)

accumulated in 78% of the osteomyelitic lesions of the dead pigs (Table 3) which was comparable to the 79% detectability that we previously found in the living juvenile pigs [5].

4. Discussion

The “gold standard” for the diagnosis of chronic osteomyelitis demands invasive procedures confirming the presence of positive bone cultures and histopathologic examination of the bone, but noninvasive diagnostic imaging is preferred in humans. Animal studies can test potential treatments without confounding factors, such as prior drug use and other experiences that complicate human studies. The post mortem examination is possible and important giving a unique opportunity for confirming, for example, assumed noninvasive examination results, as imaging with potential new tracers. Our animal studies address examination of more suitable tracers for noninvasive imaging. At the end of our experiments, all animals are euthanized and the osteomyelitic foci are confirmed at autopsy, microscopically examination, and histopathological examination. We are concerned about the welfare of our research subjects. We constantly strive to minimize the risk to them; however, a surplus of animals inoculated with *S. aureus* was inevitable in our previous studies since biological models are often unpredictable and it

was a necessity for us to have two animals with osteomyelitis available for the long scanning protocol. Thus, we inoculated three pigs at a time but on a few occasions experienced that none of the pigs developed osteomyelitis. In most cases, we did, however, succeed to induce two animals with osteomyelitis; sometimes even all three pigs developed lesions, and we were reluctant to “waste” one of the pigs. In this study, we demonstrated that it was possible to perform SPECT/CT with ^{111}In -labelled autologous leukocytes almost 24 hrs *after* euthanasia with the same detectability of the osteomyelitic lesions as in the living pigs (78% versus 79%) by a simple count of ^{111}In -labelled leukocyte accumulation in the osteomyelitic bone lesions seen on CT. Interpretation of CT, however, still requires careful scrutiny, experience, and time to detect especially small lesions.

Post mortem examination has several advantages, including that it may increase the capacity of trials with many pigs and only a single SPECT scanner is available. Also, the pigs can be euthanized at the scheduled time point and then subsequently scanned at a later time. Furthermore, it opens the possibility of comparing different scanning methods as the pigs can be euthanized immediately after the test scan without risk of continuous changes in pathology. It can also be an animal welfare advantage to scan euthanized pigs, and it does not require staff with experience in anaesthesia and

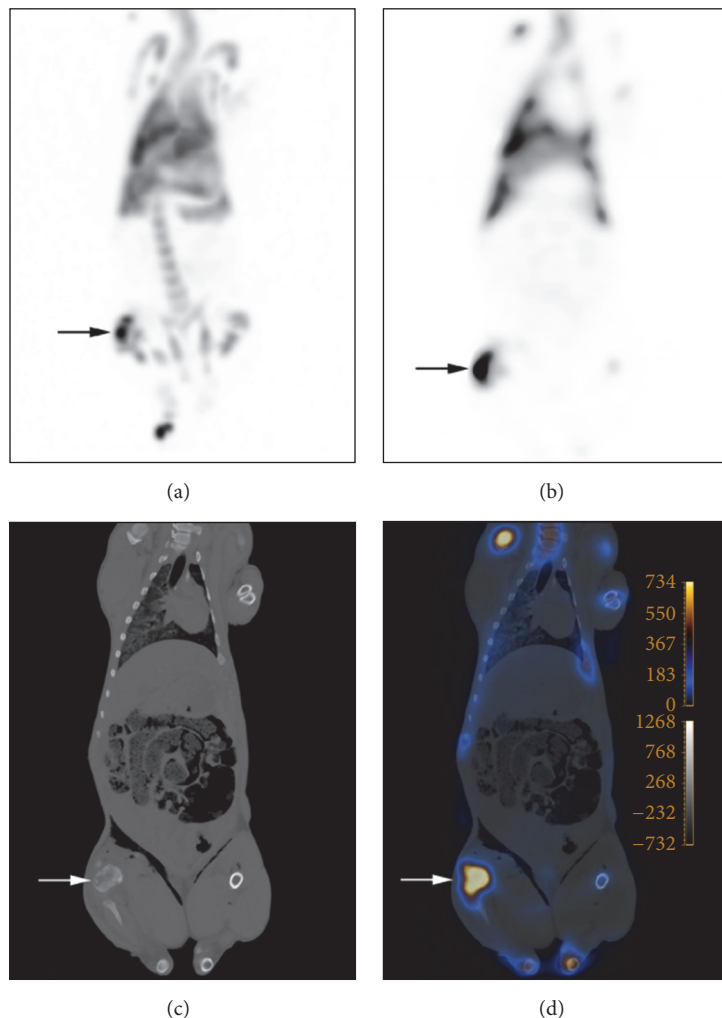


FIGURE 1: Post mortem ^{111}In -leukocyte SPECT (a), ^{111}In -leukocyte scintigraphy in dorsoventral projection (b), CT-scan (c) (bone window), and fused images (d) of a juvenile pig (*pig c*) demonstrating increased leukocyte accumulation in an osteomyelitic lesion in the proximal tibia, indicated by arrows, in the right hind limb. In figure (a), leukocyte accumulation is also seen in the distal femur, and the distal metatarsal bones III and IV.

monitoring of pigs. Finally, it is also an advantage that there are no motion artefacts when the pig is euthanized prior to scanning.

In short, it is possible to perform SPECT/CT with ^{111}In -labelled autologous leukocytes at least up to 20 hrs after euthanasia with the same detectability of osteomyelitic lesions as in living pigs. Scanning post mortem will not hinder imaging and will result in better animal welfare since shorter anaesthesia is needed. It also makes eventual transportation easier, and more pigs can be handled at a time.

Conflicts of Interest

The authors declare that they have no conflicts of interest.

Acknowledgments

This work was supported by Grant no. 0602-01911B (11-107077) from the Danish Council for Independent Research,

Technology and Production Sciences. The authors are grateful for the technical support provided by Dennis Brok, Rikke Skall, Janne Frederiksen, and Lotte S. Meyer.

References

- [1] L. K. Johansen, E. L. Svalastoga, D. Frees et al., "A new technique for modeling of hematogenous osteomyelitis in pigs: Inoculation into femoral artery," *Journal of Investigative Surgery*, vol. 26, no. 3, pp. 149–153, 2013.
- [2] A. K. Alstrup, K. M. Nielsen, H. C. Schønheyder et al., "Refinement of a hematogenous localized osteomyelitis model in pigs," *Scandinavian Journal of Laboratory Animal Science*, vol. 41, pp. 1–4, 2015.
- [3] O. L. Nielsen, P. Afzelius, D. Bender et al., "Comparison of autologous ^{111}In -leukocytes, ^{18}F -FDG, ^{11}C -methionine, ^{11}C -PK11195 and ^{68}Ga -citrate for diagnostic nuclear imaging in a juvenile porcine haematogenous *staphylococcus aureus* osteomyelitis model," *American Journal of Nuclear Medicine and Molecular Imaging*, vol. 5, no. 2, pp. 169–182, 2015.

- [4] P. Afzelius, O. L. Nielsen, A. K. O. Alstrup et al., "Biodistribution of the radionuclides ^{18}F -FDG, ^{11}C -methionine, ^{11}C -PK11195, and ^{68}Ga -citrate in domestic juvenile female pigs and morphological and molecular imaging of the tracers in hematogenously disseminated *Staphylococcus aureus* lesions," *American Journal of Nuclear Medicine and Molecular Imaging*, vol. 6, no. 1, pp. 42–58, 2016.
- [5] P. Afzelius, A. K. O. Alstrup, H. C. Schønheyder et al., "Utility of ^{11}C -methionine and ^{11}C -donepezil for imaging of *Staphylococcus aureus* induced osteomyelitis in a juvenile porcine model: comparison to autologous ^{111}In -labelled leukocytes, ^{99m}Tc -DPD, and ^{18}F -FDG," *American Journal of Nuclear Medicine and Molecular Imaging*, vol. 6, no. 6, pp. 286–300, 2016.
- [6] L. K. Johansen, J. Koch, K. Kirketerp-Møller et al., "Therapy of haematogenous osteomyelitis - a comparative study in a porcine model and Angolan children," *In Vivo*, vol. 27, pp. 305–312, 2013.
- [7] B. Aalbæk, L. K. Jensen, H. E. Jensen, J. E. Olsen, and H. Christensen, "Whole-genome sequence of *Staphylococcus aureus* S54F9 isolated from a chronic disseminated porcine lung abscess and used in human infection models," *Genome Announcements*, vol. 3, no. 5, Article ID e01207-15, 2015.
- [8] A. K. O. Alstrup and M. Winterdahl, "Imaging techniques in large animals," *Scandinavian Journal of Laboratory Animal Sciences*, vol. 36, no. 1, pp. 55–66, 2009.
- [9] M. Roca, E. F. de Vries, F. Jamar, O. Israel, and A. Signore, "Guidelines for the labelling of leucocytes with ^{111}In -oxine. Inflammation/infection task group of the european association of nuclear medicine," *European Journal of Nuclear Medicine and Molecular Imaging*, vol. 37, no. 4, pp. 835–841, 2010.